Advanced atomic force microscopy II

Edited by Milica Todorovic, Mehmet Z. Baykara and Thilo Glatzel

Imprint

Effective sensor properties and sensitivity considerations of a dynamic co-resonantly coupled cantilever sensor

Julia Körner

Full Research Paper

Abstract

Background: Co-resonant coupling of a micro- and a nanocantilever can be introduced to significantly enhance the sensitivity of dynamic-mode cantilever sensors while maintaining the ease of detection. Experimentally, a low-stiffness nanocantilever is coupled to an easy to read out microcantilever and the eigenfrequencies of both beams are brought close to one another. This results in a strong interplay between both beams and, hence, any interaction applied at the nanocantilever alters the oscillatory state of the coupled system as a whole and can be detected at the microcantilever. The amplitude response curve of the microcantilever exhibits two resonance peaks and their response to an interaction applied to the sensor depends on the properties of the individual beams and the degree of frequency matching. Consequently, while an individual cantilever is characterized by its eigenfrequency, spring constant, effective mass and quality factor, the resonance peaks of the co-resonantly coupled system can be described by effective properties which are a mixture of both subsystem's characteristics. These effective properties give insight into the amount of sensitivity of the nanocantilever that can be accessed and, consequently, into the sensitivity gain associated with the co-resonance. In order to design sensors based on the co-resonant principle and predict their behaviour it is crucial to derive a description for these effective sensor properties.

Results: By modeling the co-resonantly coupled system as a coupled harmonic oscillator and using electromechanical analogies, analytical expressions for the effective sensor properties have been derived and discussed. To illustrate the findings, numerical values for an exemplary system based on experimental sensor realizations have been employed. The results give insight into the complex interplay between the individual subsystem's properties and the frequency matching, leading to a rather large parameter space for the co-resonant system's effective properties. While the effective spring constant and effective mass mainly define the sensitivity of the coupled cantilever sensor, the effective quality factor primarily influences the detectability. Hence, a balance has to be found in optimizing both parameters in sensor design which becomes possible with the derived analytic expressions. Besides the description of effective sensor properties, it was studied how the thermal noise and, consequently, minimal detectable frequency shift for the co-resonantly coupled sensor represented by a coupled harmonic oscillator could be derived. Due to the complex

nature of the coupled system's transfer function and the required analysis, it is beyond the scope of this publication to present a full solution. Instead, a simplified approach to estimate the minimal detectable frequency shift for the co-resonant system based on the effective sensor properties is given.

Conclusion: By establishing a theoretical description for the effective sensor properties of a co-resonantly coupled system, the design of such systems is facilitated as sensor parameters can easily be predicted and adapted for a desired use case. It allows to study the potential sensitivity (gain) and detectability capabilities before sensor fabrication in a fast and easy way, even for large parameter spaces. So far, such an analysis of a co-resonantly coupled sensor was only possible with numerical methods and even then only with very limited capability to include and understand the complex interplay between all contributions. The outlined calculation steps regarding the noise considerations in a coupled harmonic oscillator system can provide the basis for a thorough study of that question. Furthermore, in a broader scope, the investigations presented within this work contribute towards extending and completing the already established theoretical basics of this novel co-resonant sensor concept and open up new ways of studying the coupled system's behaviour.

Introduction

Dynamic-mode cantilever sensors are used for many different applications which include the detection of smallest masses [1,2], in situ observation of the growth of biological films [3], detection of trace analytes in gases ("artificial nose") [4] and the investigation of properties of novel (nano)materials by scanning probe methods or magnetometry [5-7]. In contrast to static-mode operation, where the static bending of cantilever sensors is used as a measurement signal, the dynamic mode is based on exciting the beam to vibrations and monitoring its amplitude, resonance frequency and phase shift. These properties can be altered either due to a change of the cantilever's properties (spring constant, mass) or an external force gradient. The oscillation detection is usually realized by laser-optical methods such as interferometry or deflectometry [8].

In many cases, the shift of the cantilever's resonance frequency ω_0 is measured and, hence, the sensitivity of a cantilever sensor can be defined as the obtainable frequency shift with respect to an external interaction. This interaction can either be a force gradient represented by Δk or a mass change Δm (either point mass at the beam's end or distributed mass) which alters the cantilever spring constant k and/or its effective mass m_{eff}. The frequency shift $\Delta\omega$ is then given by:

$$\Delta\omega = \sqrt{\frac{k + \Delta k}{m_{\text{eff}} + \Delta m}} - \sqrt{\frac{k}{m_{\text{eff}}}} \, . \tag{1}$$

Assuming negligible mass change Δm compared to the effective mass, the frequency shift becomes (see Supporting Information File 1 for details):

$$\frac{\Delta\omega}{\omega_0} \approx \frac{\Delta k}{2k} \, , \tag{2}$$

and for negligible change of the spring constant Δk and a homogeneously distributed mass change:

$$\frac{\Delta\omega}{\omega_0} \approx -\frac{\Delta m}{2m_{\text{eff}}} \, . \tag{3}$$

Please note that Equation 3 is derived from Equation 1 by a Taylor series expansion for small Δm (see Supporting Information File 1 for details). From Equation 2 and Equation 3 it is evident that a small spring constant, small effective mass and high resonance frequency of the cantilever are favorable, especially for small interactions. Therefore, a common measure to increase the sensitivity of a cantilever sensor with regard to force gradients is the use of very soft beams which is typically achieved by reducing the cantilever dimensions, in particular the thickness. In this regard, attonewton force sensitivity has been demonstrated for very thin ($\approx$100 nm) cantilever structures with a correspondingly low spring constant in the order of few μN/m [5]. Size reduction is also a favorable approach in terms of decreasing the effective cantilever mass. Another approach of reaching femtonewton force sensitivity has been demonstrated for optomechanical cantilever sensors by optimizing cantilever design for high quality factors (in the order of 10^6). Consequently, cantilevers with rather high stiffness (kN/m) can be used, avoiding the snap-to-contact instability of very soft beams [9]. However, this experiment requires a highly specialized setup to drive the cantilever by optical means. In case of the typically used micromechanical cantilever sensors with piezo-actuator excitation, the low force sensitivity is achieved by reducing the beam's size.

This reduction of the cantilever's dimensions creates new challenges, not only for fabrication but also for oscillation detection [10]. Although sophisticated setups exist which allow the detection of the oscillatory state of a nanocantilever [11,12], these

challenge hinders the widespread use of highly sensitive cantilevers with state-of-the-art equipment. Therefore, new concepts which access the high sensitivity of a nanocantilever but at the same time preserve the ease of oscillation detection need to be explored.

One approach is a recently introduced co-resonant measurement principle which combines the ease of detection at a microcantilever with the high sensitivity of a nanocantilever. The co-resonance is introduced by coupling these two beams and matching of their eigenfrequencies, i.e., they are brought close to one another, resulting in a strong interplay between both cantilevers. Thus, any interaction applied at the highly sensitive nanocantilever alters the oscillatory state of the coupled system as a whole and can be detected by measuring the coupled system's amplitude response curve at the microcantilever [13,14]. Details about the basic underlying sensing principle as well as sensor fabrication with regard to coupling and eigenfrequency matching can for example be found in [13] and [15].

The sensor concept was tested experimentally in magnetic measurements. In cantilever magnetometry, individual Co_2FeGa Heusler nanoparticles were studied with respect to their magnetic properties. This led to the first time observation of magnetic switching of these individual Heusler nanoparticles at room temperature and with a comparatively simple setup (laser-deflection detection) [16]. Other experiments in magnetic force microscopy showed a likewise increase in sensitivity [17,18].

These first proof-of-principle experiments and applications demonstrate the immense potential of the co-resonant sensor concept but they also indicate that a further study of the implications of the co-resonance is necessary.

As Equation 2 and Equation 3 indicate, the frequency shift response of an individual cantilever to an external interaction depends on the cantilever's properties, i.e., its resonance frequency f, spring constant k, effective mass m_{eff} and also quality factor Q (with regard to detectability [19]).

While a single cantilever only exhibits one resonance peak for each of its oscillation modes, the coupled system's amplitude response curve features two resonance peaks which show a differing frequency shift response to external influences on the system, depending on the degree of eigenfrequency matching. Furthermore, the frequency shift is always greater than that of the individual microcantilever and smaller than that of the individual nanocantilever. Consequently, the observation of the coupled system's behavior leads to the conclusion that each resonance peak of the coupled system can be described by a set of effective sensor properties which are influenced by the char-

acteristics of both individual beams and depend on the degree of eigenfrequency matching. These effective properties ultimately define the capabilities of the co-resonantly coupled system in terms of sensitivity and detectability. It is therefore crucial in view of sensor design and for evaluating sensor performance to derive ways of describing these effective properties and their dependence on the individual beam's properties and the degree of eigenfrequency matching. Here, we present the derivation of simplified analytical formulas for the effective sensor properties of co-resonantly coupled sensor systems which will allow an accurate and fast way of determining prospective sensor performance. Furthermore, noise considerations within the coupled system and implications of the effective properties on the sensitivity and detectability of a co-resonantly coupled sensor are outlined.

In the following, first the sensitivity definition of a cantilever sensor will briefly be discussed and it will be evaluated how this can be used to estimate the sensitivity of a co-resonantly coupled cantilever system. This will allow to identify which effective properties of the coupled system are important in addition to the effective spring constant and effective mass which are already indicated by Equation 2 and Equation 3. In the next section, the modelling approach will be introduced. Then, the derivation of effective properties based on that model as well as the resulting expressions will be presented. These allow to estimate the potential performance and limitation of the system (e.g., sensitivity for a given task) before fabricating it and give new insights into the behaviour of co-resonantly coupled oscillating systems. Additionally, the treatment of thermal noise within the coupled system will be outlined.

Sensitivity of a Cantilever Sensor

The sensitivity of a cantilever sensor is given by its minimal detectable frequency shift with respect to an external interaction. It is influenced by various noise contributions which are due to the cantilever itself (e.g., thermal noise, thermal frequency drift noise), the measurement principle (e.g., magnetic noise in case of magnetic measurements) and the excitation and detection setup (e.g., oscillator noise, detector noise) [8,20]. However, the lowest limit for a cantilever's sensitivity is given by its thermal fluctuations leading to a thermally induced average frequency shift. This results in a minimal detectable frequency shift signal that is usually given in terms of a minimal detectable force gradient [5,8,21,22] or minimal detectable mass [23]. The following discussion will therefore be focused on the thermal noise limit and the minimal detectable frequency shift as a representation for sensitivity.

A cantilever can be described by a harmonic oscillator model with varying parameters for each of its eigenfrequencies [24]

which is the basis used for the sensitivity considerations. The minimal detectable frequency shift $\partial\omega_{\text{th}}$ of an individual cantilever represented by a harmonic oscillator is given by [8]:

$$\frac{\partial\omega_{\text{th}}}{\omega_0} = \sqrt{\frac{2k_{\text{B}}TB_{\text{w}}}{k\omega_0 QA^2}} \qquad (4)$$

with the Boltzman constant k_{B}, temperature T, measurement bandwidth B_{w} and the cantilever parameters spring constant k, quality factor Q, eigenfrequency ω_0 and oscillation amplitude A.

Equation 4 is derived based on the equipartition theorem for a harmonic oscillator with one degree of freedom as outlined in [25] and [26]. It may also be applied to estimate the minimal detectable frequency shift and, hence, sensitivity of the coupled system based on the hypothesis that each of the resonance peaks of the coupled system can be represented by an effective harmonic oscillator with effective properties as outlined in [14]. Consequently, that requires the derivation of expressions for effective spring constant, resonance frequency and quality factor and a discussion about the oscillation amplitude of the co-resonant system.

Modelling Approach

The derivation of analytical expressions for the effective properties of the co-resonant system will be based on a modelling approach which has been discussed extensively in [13] and [14] and will therefore only briefly be outlined here. As mentioned above, the co-resonant cantilever system can be described as a coupled harmonic oscillator, consisting of a damping element $d_{1,2}$, spring $k_{1,2}$ and effective mass $m_{1,2}$ for each subsystem. Please note that $m_{1,2}$ still denotes the effective mass but the subscript *eff* was omitted to keep the descriptions short. The model furthermore allows to study external interactions on the coupled system and in Figure 1 a force gradient represented by an additional spring k_3 is exemplarily considered.

By employing electromechanical analogies and the conventions force $F \equiv$ current I and velocity $v \equiv$ voltage U, the mechanical model can be transformed into an electric circuit [14]. The respective models are depicted in Figure 1 together with an experimental sensor representation. The circuit model gives the opportunity to utilize analytical (e.g., Laplace-space analysis) and simulation tools (e.g., Spice) to study the system's behaviour.

All following considerations will be based on this model. In order to present some graphic representations of the analytical formulas derived below, the exemplary parameters given in Table 1 for a micro- and a nanocantilever will be used. They are based on sensor parameters which have been observed for experimental realizations of the co-resonantly coupled system such as depicted in Figure 1a.

Furthermore, please note that the following naming convention will be used to distinguish between the properties of the individual subsystems and those of the coupled system. For the individual subsystem, the indices 1 and 2 indicate micro- and nanocantilever, respectively. Indices a and b will be employed for the coupled system's parameters, where a always refers to the left resonance peak (the one with the lower resonance frequency) and b to the right resonance peak (higher resonance frequency). To visualize these definitions, Figure 2 shows the amplitude response curve of the coupled system calculated for the microcantilever based on the circuit model from Figure 1c and for the values in Table 1 and +2% eigenfrequency deviation between micro- and nanocantilever. Additionally, most expressions will be derived in dependence on the angular frequency ω but in some cases this will be recalculated into the frequency f by $\omega = 2\pi f$.

Results and Discussion
Derivation of effective sensor properties

The effective sensor properties which characterize each resonance peak are the resonance frequency $f_{\text{a,b}}$, the effective spring

Table 1: Numerical values for micro- (1) and nanocantilevers (2) based on experimental implementations of co-resonantly coupled sensors. Please note that the values are given for the initial state before frequency matching for the individual subsystems (columns 2 and 3). The two right-hand side columns summarize the values for both resonance peaks (*a* - left peak, *b* - right peak) of the coupled system in case of +2% eigenfrequency deviation Δf_e between micro- and nanocantilever (f_1 = 200 kHz, f_2 = 204 kHz) and have been calculated based on the model in Figure 1c.

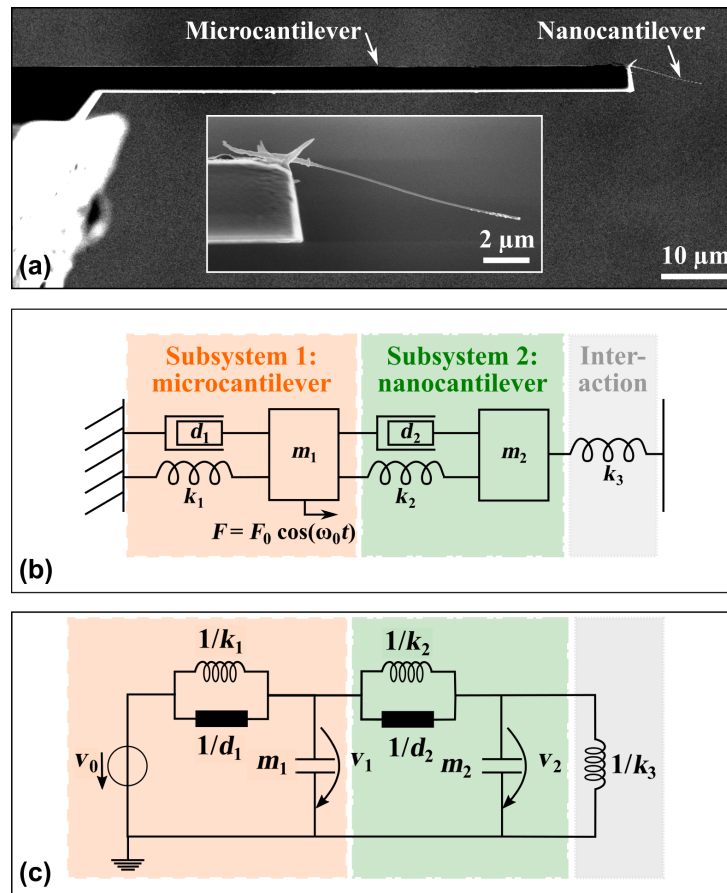|	Individual subsystems		Coupled system, Δf_e = +2%	
Parameter	Micro (1)	Nano (2)	Left peak (a)	Right peak (b)
Frequency f	200.0 kHz	400.0 kHz	198.3 kHz	205.8 kHz
Spring constant k	1 N/m	0.001 N/m	0.0044 N/m	0.0013 N/m
Quality factor Q	10000	800	2670	1008
Effective mass m_{eff}	6.33×10^{-13} kg	6.09×10^{-16} kg	2.83×10^{-15} kg	7.77×10^{-16} kg

Figure 1: (a) Scanning electron microscopy image of a sensor realization consisting of a silicon microcantilever and a carbon nanotube nanocantilever. (b) Sensor's representation by a coupled harmonic oscillator model and (c) corresponding electric circuit model. $m_{1,2}$ denote the effective mass, $d_{1,2}$ the damping and $k_{1,2}$ the spring constant of each individual beam. The potential external interaction applied at the nanocantilever is modelled by an additional spring k_3 (representing a force gradient) [14]. The system is excited via a periodic force F applied at the microcantilever.
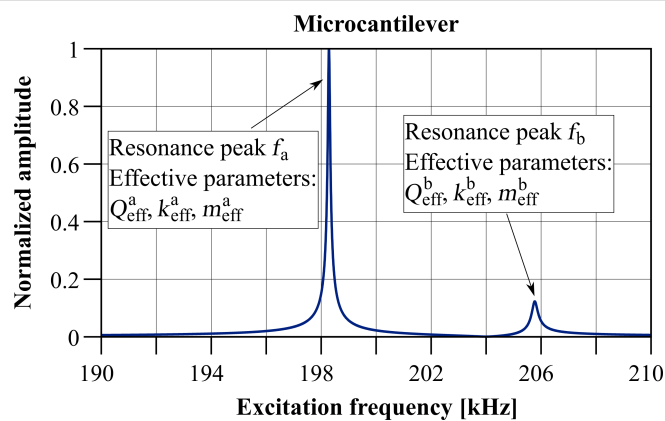

Figure 2: Calculated microcantilever amplitude response curve of the co-resonantly coupled system based on the values in Table 1 and for +2% eigenfrequency deviation between micro- and nanocantilever. The amplitude has been normalized to the maximum value of the curve.

constant $k_{\mathrm{eff}}^{\mathrm{a,b}}$ and effective quality factor $Q_{\mathrm{eff}}^{\mathrm{a,b}}$. Furthermore, as described above, the relevant measured amplitude A of the coupled system has to be defined in order to employ the known sensitivity definition. This additionally warrants a discussion of

thermal noise in the coupled system and an evaluation of how the thermally induced amplitude noise may be amplified due to the co-resonance and how that may affect the detection limit. In the following, the derivation of the effective properties

based on the coupled harmonic oscillator model will be outlined and the implication on sensitivity and detectability will be discussed.

Resonance frequencies of a co-resonantly coupled system

To analytically derive the resonance frequencies for the co-resonantly coupled system, the circuit model in Figure 1c is considered. The resonance frequencies are found by determining the frequencies where the maxima of the amplitude response curve for subsystem 1 (microcantilever) $A_1(\omega) = |\underline{v}_1/\underline{v}_0|$ and/or subsystem 2 (nanocantilever) $A_2(\omega) = |\underline{v}_2/\underline{v}_0|$ occur. Previous investigations have shown that both amplitude response curves exhibit the same resonance frequencies, hence, only subsystem 1 will be considered in the following. Please note that the derivations are exactly the same if subsystem 2 is used [14]. Considering the damped coupled harmonic oscillator results in very complex expressions for the amplitude response curves (see [14]). Analytical calculation of the resonance frequencies would involve the derivative of the amplitude response curve to be zero which results in a sixth degree polynomial expression that can only be solved numerically.

Consequently, for an estimate of the resonance frequencies, we consider the model from Figure 1c without the damping elements $d_{1,2}$. The validity of this assumption is supported by comparison of simulation results for the damped and undamped circuit model which show that the position of the resonance frequencies is only minimally influenced, even for high damping, i.e., low quality factors [14].

This can be understood by following the reasoning of [27]. In case of viscous damping, one has to distinguish between the angular natural frequency (eigenfrequency) ω_0 and the angular frequency of damped vibration (resonance frequency) ω_d. The former remains unchanged in case of damping as it only depends on the properties spring constant k and effective mass m_{eff} of the system itself, i.e., $\omega_0^2 = k/m_{\text{eff}}$. The resonance frequency ω_d is shifted compared to the eigenfrequency, depending on damping, hence $\omega_d = \sqrt{\omega_0^2 - n^2}$. Thereby, n denotes the ratio between damping coefficient d and effective mass m_{eff}, i.e., $n = d/2m_{\text{eff}}$. Employing this together with $d = \sqrt{m_{\text{eff}}k}/Q$ leads to:

$$\omega_d = \omega_0 \cdot \sqrt{1 - \frac{1}{4Q^2}}. \tag{5}$$

From Equation 5 it can be concluded that, even for low quality factors, the assumption from above gives a good approximation for the resonance frequencies of the coupled system.

In that case, the expressions for the amplitude response curves of micro- and nanocantilever read:

$$A_1(\omega) = \frac{k_1\left(k_2 + k_3 - \omega^2 \cdot m_2\right)}{k_1\left(k_2 + k_3 - \omega^2 \cdot m_2\right)\cdot\left(1 - \left(\frac{\omega}{\omega_1}\right)\right) + k_2 \cdot \left(k_3 - m_2 \cdot \omega^2\right)} \tag{6}$$

$$A_2(\omega) = \frac{1}{1 + \frac{k_3}{k_2} - \left(\frac{\omega}{\omega_2}\right)^2} \cdot A_1(\omega) = B(\omega) \cdot A_1(\omega) \tag{7}$$

Here, $B(\omega)$ denotes an amplification factor between the amplitude of micro- and nanocantilever which is also frequency-dependent.

The corresponding resonance frequencies $\omega_{a,b}$ for left a and right peak b, respectively, are found by determining the poles of Equation 6, resulting in [13,28]:

$$\omega_{a,b}^2 = \frac{\omega_{12}^2 + \omega_{23}^2}{2} \mp \sqrt{\left(\frac{\omega_{12}^2 - \omega_{23}^2}{2}\right)^2 + \frac{k_2^2}{m_1 m_2}} \tag{8}$$

with the squared combined frequencies:

$$\omega_{12}^2 = \frac{k_1 + k_2}{m_1} \tag{9}$$

$$\omega_{23}^2 = \frac{k_2 + k_3}{m_2}. \tag{10}$$

Please note that the radical term in Equation 8 is subtracted to calculate the left resonance peak a and the plus sign refers to resonance peak b with the higher resonance frequency. This is to ensure consistency with the definition of the resonance peaks given above.

By employing the relation $\omega^2 = k/m$, Equation 8 can be expressed by the eigenfrequencies $\omega_{1,2}$ of micro- and nanocantilever:

$$\omega_{a,b}^2 = \frac{1}{2}\left(K_{12}\omega_1^2 + K_{23}\omega_2^2\right) \mp \sqrt{\frac{1}{4}\left(K_{12}\omega_1^2 - K_{23}\omega_2^2\right)^2 + \frac{k_2}{k_1}\omega_1^2\omega_2^2} \tag{11}$$

with

$$K_{12} = 1 + \frac{k_2}{k_1} \tag{12}$$

$$K_{23} = 1 + \frac{k_3}{k_2}. \qquad (13)$$

By assuming a constant eigenfrequency of subsystem 1, i.e., $\omega_1 = \text{const}$, and that only the eigenfrequency of subsystem 2 is varied, the coupled resonance frequencies can be derived in dependence on the degree of eigenfrequency matching $\Delta\omega_{\text{eigen}}$ (see Supporting Information File 1 for details):

$$\Delta\omega_{\text{eigen}} = \frac{\omega_2 - \omega_1}{\omega_1}. \qquad (14)$$

Please note that $\Delta\omega_{\text{eigen}}$ is a dimensionless quantity which will be used to generate all following graphs. Figure 3 depicts
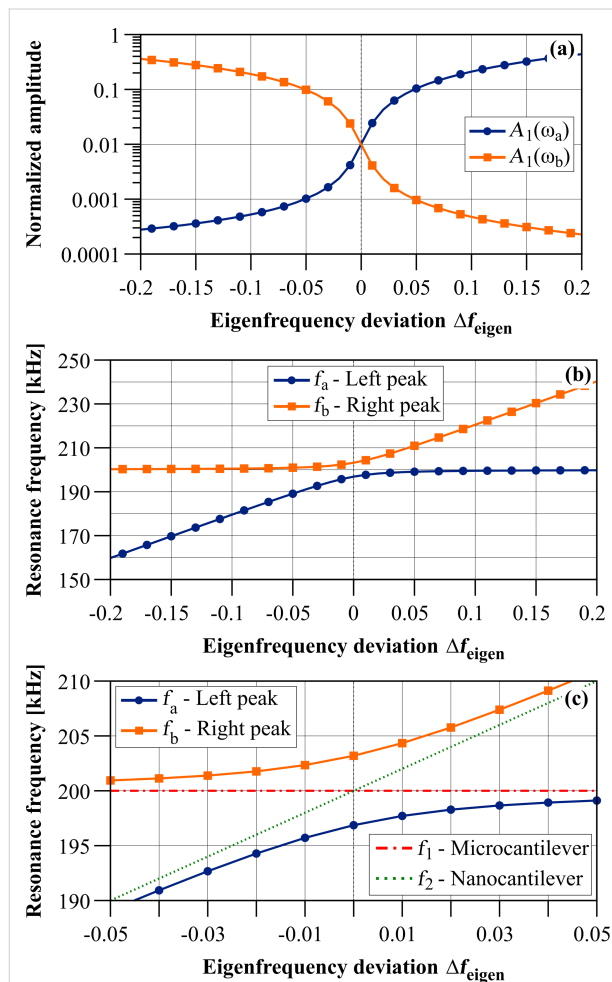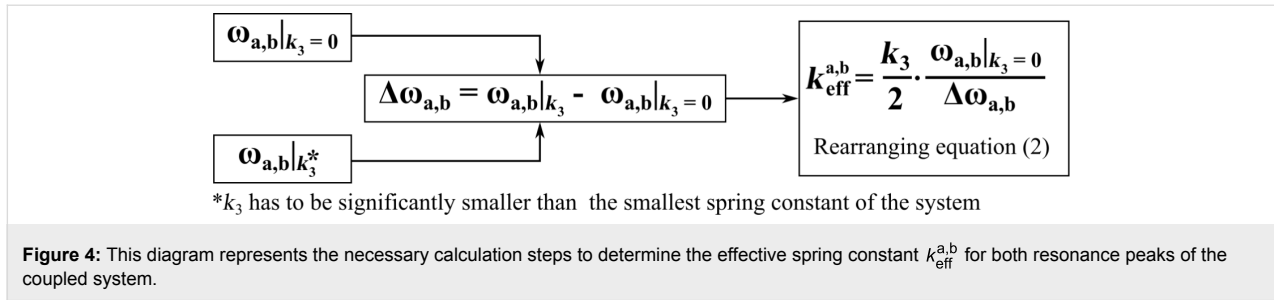

Figure 3: (a) Resonance amplitudes of both resonance peaks of the coupled system calculated for the microcantilever (index 1) and (b) resonance frequencies of both resonance peaks of the coupled system in dependence on the eigenfrequency deviation $\Delta f_{\text{eigen}} = \Delta\omega_{\text{eigen}}/2\pi$ based on Equation 11 for the values given in Table 1. (c) Magnification of the resonance frequencies of both resonance peaks of the coupled system for small eigenfrequency deviation with added eigenfrequencies of micro- and nanocantilever to illustrate the effect of the co-resonance.

the resonance frequencies for both resonance peaks of the coupled system in dependence on the eigenfrequency deviation $\Delta f_{\text{eigen}} = \Delta\omega_{\text{eigen}}/2\pi$ based on Equation 11 as well as the amplitudes of the resonance peaks. In case of negative eigenfrequency deviation, i.e., $f_2 < f_1$, the lower left branch corresponds to the left resonance peak a which has a small amplitude and whose resonance frequency is changing because it corresponds to the nanocantilever. The upper left branch corresponds to the resonance peak b which has a high amplitude and is mainly corresponding to the microcantilever. For $f_2 \approx f_1$ (see magnification in Figure 3c), the resonance frequencies for the coupled system clearly deviate from the eigenfrequencies of micro- and nanocantilever, which is also the region where the interplay between both beams is strongest. Hence, in that region, the effective properties of the coupled system's resonance peaks will have a significant contribution of both individual beam's properties. Please note that this is also the region where the so called "avoided crossing" of the resonance frequencies is clearly visible which has already been described for coupled oscillating systems [29] and for the co-resonant approach in particular in [14]. In case of positive eigenfrequency deviation, i.e., $f_2 > f_1$, the upper right branch in Figure 3a corresponds to the left resonance peak a which now has the higher amplitude and is approaching the eigenfrequency of and mainly corresponding to the properties of the microcantilever. The lower right branch in Figure 3a corresponds to the right resonance peak b whose amplitude is decreasing with increasing eigenfrequency deviation and whose properties increasingly correspond to that of the nanocantilever. Please note that the discussion of the amplitudes is only valid if the amplitude response curve of the microcantilever is studied. If the nanocantilever would be considered, the amplitude of the smaller resonance peak would be significantly increased but the conclusions regarding coupled resonance frequencies and effective properties are the same as for the microcantilever's amplitude response curve.

Effective spring constant

Based on the expressions for the resonance frequencies of the coupled system, the effective spring constants for both resonance peaks $k_{\text{eff}}^{\text{a,b}}$ can easily be derived by using Equation 2. Figure 4 gives an overview of the calculation steps.

Equation 2 is originally given for a single cantilever (harmonic oscillator) but can be employed for a coupled harmonic oscillator by using the resonance frequencies of the coupled system and the effective spring constants $k_{\text{eff}}^{\text{a,b}}$ instead of k. The first step is the calculation of both resonance frequencies $\omega_{\text{a,b}}$ of the coupled system, with and without an interaction $\Delta k = k_3$. As shown in [15], it is crucial to choose k_3 to be much smaller (at least two orders of magnitude) than the smallest spring constant of the coupled system. Otherwise, the effective spring constant

Figure 4: This diagram represents the necessary calculation steps to determine the effective spring constant $k_{eff}^{a,b}$ for both resonance peaks of the coupled system.

will strongly depend on k_3 [30]. Please note that this is the case for any cantilever sensor and not a feature of the co-resonantly coupled system.

Rearranging Equation 2 results in:

$$k_{eff}^{a,b} = \frac{k_3}{2} \frac{\omega_{a,b}|_{k_3=0}}{\Delta\omega_{a,b}} \qquad (15)$$

with

$$\Delta\omega_{a,b} = \omega_{a,b}|_{k_3} - \omega_{a,b}|_{k_3=0} \cdot \qquad (16)$$

By substituting ω_2 as given in Equation 14, the effective spring constants for the co-resonantly coupled system can be given as a function of the degree of eigenfrequency matching (see Supporting Information File 1 for details). Figure 5 depicts the effective spring constants for left (a) and right (b) resonance peak of the coupled system based on Equation 15 for the values given in Table 1.

In Figure 5, different sections can be identified which are summarized in Table 2. These sections are of general nature and not specific for the exemplary values given in Table 1. However, it is important to note that the width of the sections depends on
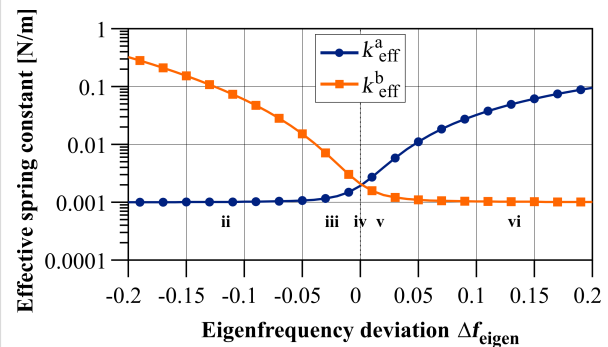

Figure 5: Effective spring constants for both resonance peaks of the coupled system in dependence on the eigenfrequency deviation $\Delta f_{eigen} = \Delta\omega_{eigen}/2\pi$ based on Equation 15 for the values given in Table 1. Different sections can be identified which are summarized in Table 2 and sections ii to vi are depicted in the graph.

the properties of both subsystems and that the slope of the transition region, i.e., sections ii, iii, v and vi is dependent on the ratio of the individual beam's spring constants. The greater the difference between the individual spring constants, the steeper the slope.

Furthermore, a slight asymmetry can be found in the curve which is due to the very different properties of the individual subsystems, and, consequently, leads to an asymmetric energy distribution in the coupled system which is reflected in the

Table 2: Overview of amplitude and effective spring constants of both resonance peaks of the coupled system in dependence on the eigenfrequency deviation. Seven general sections of the curve depicted in Figure 5 can be identified. Please note that the result for section iv has already been described by T. Mühl [31] and in [8].

Section	Frequency relation	Amplitude relation	Left peak k_{eff}^a	Right peak k_{eff}^b
i	$f_2 \ll f_1$	$A_a \ll A_b$	$= k_2$	$= k_1$
ii	$f_2 < f_1$	$A_a < A_b$	$\approx k_2$	$2k_2 < k_{eff}^b < k_1$
iii	$f_2 \approx f_1$	$A_a < A_b$	$k_2 < k_{eff}^a < 2k_2$	$2k_2 < k_{eff}^b < k_1$
iv	$f_2 = f_1$	$A_a \approx A_b$	$= 2 \cdot k_2$	$= 2 \cdot k_2$
v	$f_2 \approx f_1$	$A_a > A_b$	$2k_2 < k_{eff}^a < k_1$	$k_2 < k_{eff}^b < 2k_2$
vi	$f_2 > f_1$	$A_a > A_b$	$2k_2 < k_{eff}^a < k_1$	$\approx k_2$
vii	$f_2 \gg f_1$	$A_a \gg A_b$	$= k_1$	$= k_2$

effective sensor properties. That is not only the case for the effective spring constants but also for the effective quality factor as well as amplitude considerations.

Although the expressions without damping have been used, a comparison of effective spring constants obtained by Spice simulations of the damped co-resonantly coupled system and the undamped analytical calculations based on Equation 15 shows a good agreement, even for rather large damping, i.e., low quality factors. For the exemplary values given in Table 1 and with quality factors below 100 for both subsystems, the deviation between the effective spring constants for undamped and damped case was less than 5%. Experimentally, the spring constant of a cantilever can be determined by various approaches such as thermal noise, Sader, Cleveland (added mass) methods [32,33] but they all have an uncertainty of at least 10% [33]. These comparisons indicates that the simplified expressions based on the undamped case give a good estimate for the effective spring constants of the coupled system.

Effective quality factor

The quality factor can either be defined as the ratio of total energy to dissipated energy per oscillation period [34] or as the bandwidth of the resonance curve. In the latter case, the bandwidth is given by the difference of the two frequencies at which the amplitude has been decreased to $1/\sqrt{2}$ times the resonance amplitude [35]. Both definitions are equivalent for sufficiently low damping [36]. However, for the following derivation of the effective quality factor $Q_{\text{eff}}^{\text{a,b}}$ for both resonance peaks a, b of the co-resonantly coupled system, the definition based on energy dissipation will be used, hence:

$$Q_{\text{eff}}^{\text{a,b}} = 2\pi \frac{E_{\text{a,b}}}{\left| \Delta E_{\text{a,b}} \right|} \qquad (17)$$

with $E_{\text{a,b}}$ denoting the total energy stored in the system and $\Delta E_{\text{a,b}}$ the dissipated energy per oscillation period. Please note that the absolute value for the dissipated energy (often considered with a negative sign) is used as only the relation between total and dissipated energy is relevant for the quality factor.

Based on the coupled harmonic oscillator representation, the total energy of the system can be approximated by the potential energy given by [37]:

$$E_{\text{a,b}} = \frac{1}{2} \left[k_1 \cdot A_1^2 \left(\omega_{\text{a,b}} \right) + k_2 \cdot \left(A_2 \left(\omega_{\text{a,b}} \right) - A_1 \left(\omega_{\text{a,b}} \right) \right)^2 \right], \quad (18)$$

depending on the spring constants $k_{1,2}$ and the amplitudes $A_{1,2}(\omega_{\text{a,b}})$ at the resonance frequencies $\omega_{\text{a,b}}$.

The dissipated energy per oscillation cycle is defined by the damping coefficient $d_{1,2}$ which contains all intrinsic and extrinsic damping contributions, and the oscillation speed $v_{1,2}(t)$:

$$\Delta E_{\text{a,b}} = \int_0^T -d_1 \cdot v_1^2 \left(t \right) \mathrm{d}t + \int_0^T -d_2 \cdot v_2^2 \left(t \right) \mathrm{d}t . \qquad (19)$$

Assuming a deflection of $u_{1,2}(t) = A_{1,2} \cdot \cos(\omega t)$, the velocity of each oscillator is given by:

$$v_{1,2} \left(t \right) = -\omega \cdot A_{1,2} \cdot \sin \left(\omega t \right), \qquad (20)$$

and hence, the dissipated energy is:

$$\Delta E_{\text{a,b}} = -\omega_{\text{a,b}} \pi \left(d_1 A_1^2 \left(\omega_{\text{a,b}} \right) + d_2 A_2^2 \left(\omega_{\text{a,b}} \right) \right). \qquad (21)$$

Employing $d_{1,2} = \sqrt{m_{1,2} \cdot k_{1,2}} / Q_{1,2}$, $m_{1,2} = k_{1,2} / \omega_{1,2}^2$ and the amplitude relation $A_2(\omega_{\text{a,b}}) = B_{\text{a,b}} \cdot A_1(\omega_{\text{a,b}})$ results in an effective quality factor for each resonance peak:

$$Q_{\text{eff}}^{\text{a,b}} = \frac{1}{\omega_{\text{a,b}}} \cdot \frac{\left(k_1 + \left(B_{\text{a,b}} - 1 \right)^2 \cdot k_2 \right) \cdot \omega_1 \omega_2 Q_1 Q_2}{k_1 \omega_2 Q_2 + k_2 \omega_1 Q_1 B_{\text{a,b}}^2} . \qquad (22)$$

At this point it is necessary to discuss the factor $B_{\text{a,b}}$ in more detail. It relates the amplitudes A_1 and A_2 of both subsystems as discussed above and for a model with integrated damping would be a complicated expression, resulting in a complex formula for the effective quality factor. To give a simplified estimate for the effective quality factor, the undamped relation is assumed which has been shown to be a reasonably good estimate. Therefore, $B_{\text{a,b}}$ can be derived from Equation 7 for $k_3 = 0$ and at the two resonance frequencies $\omega_{\text{a,b}}$:

$$B_{\text{a,b}} \approx \frac{1}{1 - \left(\frac{\omega_{\text{a,b}}}{\omega_2} \right)^2} . \qquad (23)$$

Equation 22 can also be expressed as a function of the eigenfrequency deviation $\Delta\omega_{\text{eigen}}$ by substituting ω_2 with the expression given in Equation 14, leading to:

$$Q_{\text{eff}}^{\text{a,b}} \left(\Delta\omega_{\text{eigen}} \right) = \frac{1}{\omega_{\text{a,b}}} \cdot \frac{\left(k_1 + \left(B_{\text{a,b}} - 1 \right)^2 \cdot k_2 \right) \cdot \left(1 + \Delta\omega_{\text{eigen}} \right) \cdot \omega_1 Q_1 Q_2}{\left(1 + \Delta\omega_{\text{eigen}} \right) \cdot k_1 Q_2 + k_2 Q_1 B_{\text{a,b}}^2} . \qquad (24)$$

Figure 6 depicts the effective quality factors for both resonance peaks of the coupled system based on Equation 24 for the values given in Table 1. It shows a similar behaviour as the effective spring constants, leading to comparable sections as identified in Table 2.

Figure 6: Effective quality factor for both resonance peaks of the coupled system in dependence on the eigenfrequency deviation $\Delta f_{\text{eigen}} = \Delta\omega_{\text{eigen}}/2\pi$ based on Equation 24 for the values given in Table 1.
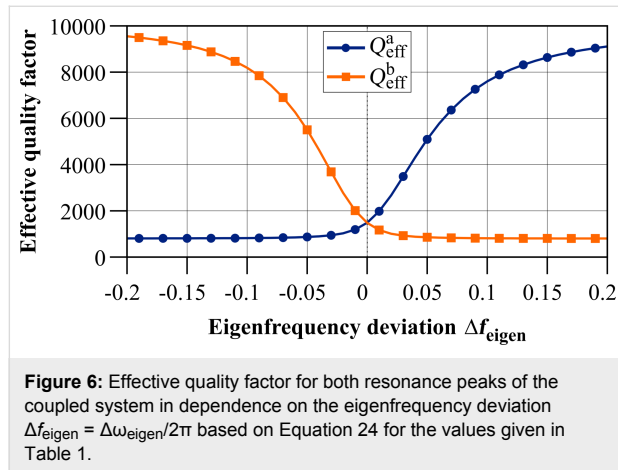
In order to better understand the behaviour of the system in terms of the effective quality factor, it is instructive to make some assumptions. Two subsystems with the same quality factor, i.e., $Q_1 = Q_2 = Q$, are considered. This results in the following expression for the effective quality factor $Q_{\text{eff}}^{\text{a,b}}$:
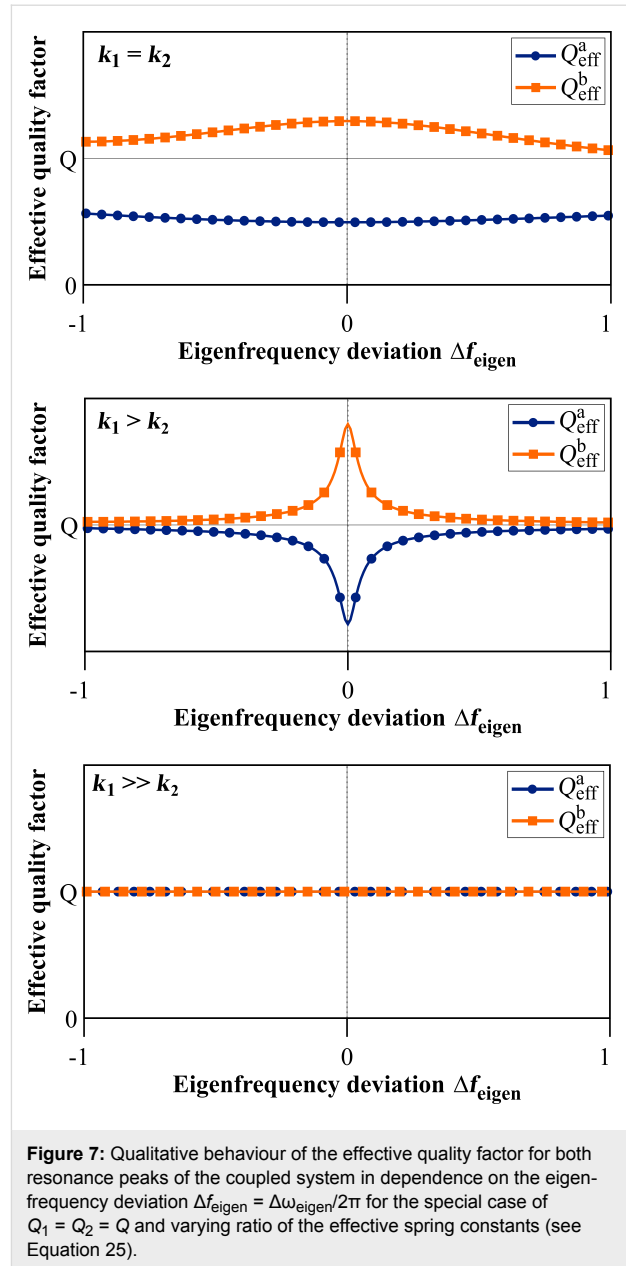
$$Q_{\text{eff}}^{\text{a,b}} = Q \cdot \frac{\omega_1\omega_2}{\omega_{\text{a,b}}} \cdot \frac{1 + \frac{k_2}{k_1}\left(B_{\text{a,b}}-1\right)^2}{\omega_2 + \frac{k_2}{k_1}\omega_1 B_{\text{a,b}}^2} \qquad (25)$$

with

$$\omega_{\text{a,b}}^2 = \frac{1}{2}\left(\omega_1^2 + \frac{k_2}{k_1}\omega_1^2 + \omega_2^2\right)$$
$$\mp \sqrt{\frac{1}{4}\left(\omega_1^2 + \frac{k_2}{k_1}\omega_1^2 - \omega_2^2\right)^2 + \frac{k_2}{k_1}\omega_1^2\omega_2^2} \qquad (26)$$

$$B_{\text{a,b}} = \frac{1}{1 - \left(\frac{\omega_{\text{a,b}}}{\omega_2}\right)^2}. \qquad (27)$$

All expressions in that case show a dependence on the ratio of the individual subsystem's spring constants k_2/k_1 and Figure 7 illustrates the general behaviour of the effective quality factor of the co-resonantly coupled system's resonance peaks for varying ratios of k_1 and k_2 and within an eigenfrequency deviation range of ±100%.

Figure 7: Qualitative behaviour of the effective quality factor for both resonance peaks of the coupled system in dependence on the eigenfrequency deviation $\Delta f_{\text{eigen}} = \Delta\omega_{\text{eigen}}/2\pi$ for the special case of $Q_1 = Q_2 = Q$ and varying ratio of the effective spring constants (see Equation 25).

The case $k_2/k_1 = 1$ results in two different effective quality factors, one of which is smaller than Q and the other one is greater than Q:

$$Q_{\text{eff}}^{\text{a,b}} = Q \cdot \frac{\omega_1\omega_2}{\omega_{\text{a,b}}} \cdot \frac{1 + \left(B_{\text{a,b}}-1\right)^2}{\omega_2 + B_{\text{a,b}}^2\omega_1} \qquad (28)$$

$$B_{\text{a,b}} = \frac{1}{1 - \frac{1}{\omega_2^2}\left(\omega_1^2 + \frac{1}{2}\omega_2^2 \mp \sqrt{\frac{1}{4}\left(2\omega_1^2 - \omega_2^2\right)^2 + \omega_1^2\omega_2^2}\right)}. \qquad (29)$$

For $k_2/k_1 < 1$ the clearly separated lines from $k_2/k_1 = 1$ start to approach each other for greater frequency deviation but have a minimum/maximum respectively around zero eigenfrequency deviation. These extrema vanish for $k_2/k_1 \ll 1$ resulting in the two effective quality factors being identical and equal to Q. This particular result has also been described by T. Mühl [31]. For the reversed case of $k_2/k_1 > 1$ the same behaviour as for $k_2/k_1 = 1$ is found but with increasing spacing between the two almost parallel lines when the difference between the two spring constants increases.

In general, i.e., without any assumptions for the individual subsystem's properties, the slope of the curves for the effective quality factor depends on the ratio of the spring constants as well as the quality factors of the individual subsystems and different curve shapes can be found by varying the relations between all these parameters.

Furthermore, the effective quality factors calculated by the derived analytical expression from Equation 22 have been compared to values obtained by numerical circuit simulations of the coupled system with the software LTSpice. Thereby, a two step approach was used where first the amplitude response curve of the coupled system was simulated for varying properties of the subsystems and degree of frequency matching. In a second step, the quality factor of each resonance peak was determined by the definition based on the bandwidth. A wide range of parameters was simulated, for both, quality factors and spring constants of the subsystems and in all cases, a very good agreement was found between the analytical solution and the simulation.

Although the comparison between an analytical formula and simulations is somewhat limited by the parameter space covered in the simulation, the results strongly indicate that the derived analytical expression gives a very good estimate for the effective quality factors of a co-resonantly coupled system. Another conclusion drawn from the above discussion is that a more thorough study of the effective quality factor of co-resonantly coupled systems based on the obtained analytical expression will be necessary, especially with regard to tuning parameters for a sensor application. Here, only the case of $Q_1 = Q_2$ was discussed in detail and other relations will lead to a different behaviour compared to what is described above for this specific case. However, this is beyond the scope of this publication which aims at giving the basic relations for describing the coupled system's effective properties.

Measured amplitude and thermal noise

Equation 4 contains another parameter which is the oscillation amplitude A of the cantilever. The amplitude response curve of the coupled system is still measured at the microcantilever as in the case of an individual cantilever sensor. Therefore, no "effective" value is required and the actual oscillation amplitude of the microcantilever can be used for the coupled system.

At this point, all effective properties of the coupled system have been derived and can be used to estimate the minimal detectable frequency shift for each resonance peak of the co-resonantly coupled system based on Equation 4. The important point which needs to be stressed here is that this approach is only valid under the assumption that each resonance peak of the co-resonant system can be modelled as an effective harmonic oscillator with effective properties.

While this is a reasonable assumption as shown in [14], the sensitivity discussion inevitably leads to the question of how the co-resonance is actually affecting thermal noise distribution in the coupled system and how that may affect the minimal detectable frequency shift. Finding an answer to that requires a derivation based on the equipartition theorem and transfer function for the coupled harmonic oscillator in a similar way as it is outlined in [25] for the individual harmonic oscillator. However, for the coupled system it has to be noted that while the complete system has to be considered in the derivation, any oscillation detection takes place at the microcantilever and therefore its amplitude is the quantity of interest.

The equipartition theorem states that, in thermal equilibrium, each independent quadratic term in the system's total energy (i.e., each degree of freedom) equals a mean value of thermal energy $1/2k_\mathrm{B}T$ [26]. The coupled harmonic oscillator constitutes a two-degree of freedom system, hence the equipartition theorem in that case is:

$$2 \cdot \frac{1}{2} k_\mathrm{B} T = \frac{1}{2} k_1 \tilde{A}_1^2 + \frac{1}{2} k_2 \left(\tilde{A}_2 - \tilde{A}_1 \right)^2 \qquad (30)$$

with the mean square displacement noise amplitudes $\tilde{A}_{1,2}$ and spring constants $k_{1,2}$ of subsystem 1 and 2. Rearranging Equation 30 and substituting $\tilde{A}_2 = \Lambda_{1,2} \tilde{A}_1$, the mean square thermal noise amplitude of the microcantilever becomes:

$$\tilde{A}_1^2 = \frac{2 k_\mathrm{B} T}{k_1 + \left(\Lambda_{12} - 1 \right)^2 k_2} . \qquad (31)$$

Please note that Λ_{12} is only equal to the previously used amplitude amplification factor $B_\mathrm{a,b}$ between micro- and nanocantilever in case of neglected damping. If the complete coupled harmonic oscillator model including damping is considered, the amplification factor becomes more complicated and a derivation thereof can be found in [14].

Following the reasoning of [25], the next steps involve the calculation of the white thermal noise density and the mean square displacement noise by integrating over the coupled system's transfer function $G(f) = A_1/A_0$. By using the electric circuit model from Figure 1, $G(f) = v_1/v_0$ which can be found in [14]. The ansatz to be used for the noise calculation is:

$$N_{\text{th,osci}} = N_{\text{th,exc}} \cdot G(f) \qquad (32)$$

with the thermal oscillator noise density $N_{\text{th,osci}}$ and the excitation white thermal noise density $N_{\text{th,exc}}$. This represents the filtering of the excitation white thermal noise due to the resonance characteristics of the coupled harmonic oscillator system.

Integration of the squared thermal oscillator noise density from Equation 32 over the complete frequency range $[0,\infty]$ and relating that to the expression for the mean square amplitude noise obtained from the equipartition theorem (Equation 31 for the coupled harmonic oscillator) allows to derive the excitation white thermal noise density according to:

$$N_{\text{th,exc}}^2 = \frac{\tilde{A}_1^2}{\int_0^\infty G^2(f)\mathrm{d}f}. \qquad (33)$$

However, this involves solving the integral for the squared transfer function $G^2(f)$. While an antiderivative exists for the single harmonic oscillator, no solution is available for the coupled harmonic oscillator. Hence, numerical treatment is required and, based on this, it has to be studied if it is possible at all to find an approximation for an antiderivative for the given boundary conditions in the coupled case.

Integrating the oscillator noise over the relevant measurement bandwidth from f_{low} to f_{high} finally gives the mean square displacement noise according to

$$\tilde{A}_1^2\left(f_{\text{low}},f_{\text{high}}\right) = N_{\text{th,exc}}^2 \cdot \int_{f_{\text{low}}}^{f_{\text{high}}} G^2(f)\mathrm{d}f. \qquad (34)$$

In case of a dynamic-mode cantilever which is excited at or close to its resonance frequency f_0, the transfer function becomes $G^2(f_0) = Q^2$ for a single harmonic oscillator. Again there is no solution for the co-resonantly coupled harmonic oscillator available yet.

The final derivation of the minimal detectable frequency shift is based on the ansatz:

$$\frac{\Delta f}{f_0} = \frac{\Delta f}{f_0} \cdot \frac{\Delta A}{\Delta A}. \qquad (35)$$

For a sensor working point close to the resonance frequency, the inverse slope of the amplitude response curve can be approximated by $\Delta A/\Delta f_0 \approx f_0/QA$ for a single harmonic oscillator [25]. It has to be studied in more detail but it is likely that this approximation still holds for the coupled harmonic oscillator since the resonance peaks in that case are measured in the same way as for the single harmonic oscillator. However, in this case Q would have to be replaced by the effective quality factor for the resonance peak measured and $A = A_1$ since the amplitude of subsystem 1 (microcantilever) is used. Furthermore $\Delta A = \sqrt{\tilde{A}_1^2\left(f_{\text{low}},f_{\text{high}}\right)}$, and hence:

$$\frac{\Delta f_{\text{a,b}}}{f_{\text{a,b}}} = \frac{1}{Q_{\text{eff}}^{\text{a,b}} A_1} \cdot N_{\text{th,exc}} \cdot \sqrt{\int_{f_{\text{low}}}^{f_{\text{high}}} G^2(f)\mathrm{d}f}$$

$$= \frac{1}{Q_{\text{eff}}^{\text{a,b}} A_1} \cdot \sqrt{\tilde{A}_1^2 \cdot \frac{\int_{f_{\text{low}}}^{f_{\text{high}}} G^2(f)\mathrm{d}f}{\int_0^\infty G^2(f)\mathrm{d}f}}. \qquad (36)$$

As Equation 36 and the above considerations show, two main questions have to be studied in order to derive an expression for the minimal detectable frequency shift of a co-resonantly coupled cantilever sensor represented by a damped coupled harmonic oscillator:

1. Derivation of an antiderivative or approximation formula thereof for the coupled system's squared transfer function $G^2(f)$, including incorporation of the relevant boundary conditions
2. Approximation of inverse slope of the amplitude response curve close to the resonance frequency for each resonance peak

By solving these questions and following the steps outlined above, a complete analytical solution for the minimal detectable frequency shift and, consequently, the sensitivity of a co-resonantly coupled cantilever sensor may be derived. However, due to the co-resonantly coupled system constituting a two-degree of freedom system with a complex transfer function, the actual solution goes far beyond the scope of this publication which aims at providing simplified expressions for relevant sensor properties. The sensitivity calculation of a system represented by a coupled harmonic oscillator will therefore have to be part of future work as it will potentially involve numerical solutions and elaborate approximations and assumptions. Nonetheless,

the steps outlined here can provide the basis for such an investigation.

Implications on sensor sensitivity and detectability

Until a solution for the above open questions is found, the sensitivity based on the minimal detectable frequency shift of the co-resonantly coupled system can be estimated by using Equation 4 for each resonance peak based on the derived expressions for effective sensor properties. That furthermore allows to analyze the sensitivity gain induced by the co-resonant coupling in comparison to an individual cantilever sensor. For the exemplary values given in Table 1, the minimal detectable frequency shift can be calculated and consequently the minimal detectable force gradient and mass load for both individual subsystems as well as the resonance peaks of the coupled systems, in that case for +2% eigenfrequency deviation. For the calculations, Equation 2 and Equation 3 have been used with $\Delta f / f_0$ being substituted by the expression in Equation 4. The results are listed in Table 3 and illustrate how the co-resonant concept allows to access the high sensitivity of the nanocantilever.

Please note that the estimates presented here are very conservative, as for example a rather high stiffness of the nanocantilever and room temperature were assumed. A decrease in stiffness, especially of the nanocantilever, and low temperatures will lead to much more gain in sensitivity. With the derived expressions within this work, a fast and easy way to estimate the potential sensitivity is given.

However, the co-resonantly coupled system's frequency shift response to an external interaction is only one aspect. The other equally important aspect is the detectability, i.e., how well the oscillatory state of a dynamic-mode cantilever sensor can be detected. That is limited by the signal-to-noise ratio (SNR) for frequency, amplitude and phase measurements. It mainly depends on the cantilever's quality factor which directly influences the phase noise and resolution of the resonance peak [19]. With decreasing cantilever dimensions, the quality factor usually decreases, hence, detectability deteriorates [38]. As the considerations for the effective quality factor of the co-resonantly coupled system show, this effect is, at least partly, counteracted by the co-resonance. While the high sensitivity of the nanocantilever is accessible, the usually higher quality factor of the microcantilever becomes beneficial for detectability. Hence, if always the resonance peak with the higher amplitude is measured, the effective quality factor will never be below approximately twice the smallest individual quality factor of the system. Furthermore, as the graphs for effective quality factor and spring constant show, the regions of small eigenfrequency deviation (not perfectly matched) might be the most promising in terms of sensor design as the effective quality factor can be relatively high, i.e., ensure good detectability, while still very good sensitivity is achieved by a low effective spring constant. A more detailed study of the relation between detectability and sensitivity of the co-resonant system based on the derived expressions is necessary in order to fully understand the behaviour of the coupled system in this regard. That will eventually lead to design criteria with respect to different sensor applications.

Conclusion

Coupling and eigenfrequency matching of a micro- and nanocantilever has experimentally been demonstrated to lead to a significant increase in sensitivity of cantilever sensors while maintaining the ease of detection. This co-resonant measurement principle allows to access the high sensitivity of a nanocantilever as it induces a strong interplay between both individual beams, resulting in an amplitude response curve comprised of two resonance peaks which can be measured at the microcantilever. It was found that these two resonance peaks can be described by effective sensor properties which depend on the individual beam's properties and the degree of eigenfrequency matching. Consequently, a small eigenfrequency deviation between micro- and nanocantilever results in effective properties for both resonance peaks that are strongly influenced by the nanocantilever's characteristics. With increasing eigenfrequency deviation, the effective properties of the resonance peaks start to approach those of the individual beams,

Table 3: Minimal detectable frequency shift and related force gradient and mass load for individual micro- and nanocantilever and both resonance peaks of the coupled system represented by effective properties. For the calculation, Equation 4 has been used, assuming measurement bandwidth B_w = 1 Hz and room temperature T = 293 K.

	Individual subsystems		Coupled system, Δf_e = +2%	
Parameter	Micro (1)	Nano (2)	Left peak (a)	Right peak (b)
Amplitude A	100 nm	1000 nm	100 nm	100 nm
Freq. shift Δf_{therm}	1.6 mHz	18.1 mHz	46.6 mHz	142.2 mHz
Min. force gradient k_{min}	1.6×10^{-8} N/m	1.8×10^{-10} N/m	2.1×10^{-9} N/m	1.8×10^{-9} N/m
Min. mass m_{min}	1.0×10^{-20} kg	1.1×10^{-22} kg	1.3×10^{-21} kg	1.1×10^{-21} kg

i.e., one peak is becoming increasingly similar to the single microcantilever while the other one is approaching the nanocantilever's characteristics. When measuring the coupled system's amplitude response curve at the microcantilever, this secondly mentioned resonance peak will eventually not be detectable anymore. For sensor design and evaluation of prospective sensor performance it is therefore crucial to analyze and understand the effective sensor properties in order to advance the measurement principle towards sensor implementations for different applications. In this publication, the derivation of analytical expressions for the effective sensor properties resonance frequency, spring constant and quality factor were presented for both resonance peaks of the coupled system based on the coupled harmonic oscillator model. These expressions, in combination with considerations for resonance amplitude amplification between micro- and nanocantilever, allow to easily estimate the prospective sensor performance and gain in sensitivity due to co-resonant coupling based on the parameters of micro- and nanocantilever. This is a crucial contribution for advancing the co-resonant measurement principle and can be the basis for further investigations and applications of co-resonantly coupled systems. Furthermore, it was studied how the thermal noise and consequently the derivation of a minimal detectable frequency shift has to be treated for a co-resonantly coupled system represented by a coupled harmonic oscillator. While calculation steps could be outlined, the solutions are rather complicated due to the complex transfer function of this two-degree of freedom system and will potentially require numerical treatment and elaborate assumptions and approximations. This will be the subject of future investigations and here, a simplified approach to estimate the minimal detectable frequency shift based on the effective sensor properties was shown.

Supporting Information

Supporting Information File 1
Details on mathematical derivations.
[https://www.beilstein-journals.org/bjnano/content/supplementary/2190-4286-9-237-S1.pdf]

Acknowledgements

References

1. Martínez-Martín, D.; Fläschner, G.; Gaub, B.; Martin, S.; Newton, R.; Beerli, C.; Mercer, J.; Gerber, C.; Müller, D. J. *Nature* **2017,** *550,* 500–505. doi:10.1038/nature24288

2. Johnson, B. N.; Mutharasan, R. *Biosens. Bioelectron.* **2012,** *32,* 1. doi:10.1016/j.bios.2011.10.054

3. Gfeller, K. Y.; Nugaeva, N.; Hegner, M. *Biosens. Bioelectron.* **2005,** *21,* 528–533. doi:10.1016/j.bios.2004.11.018

4. Baller, M. K.; Lang, H. P.; Fritz, J.; Gerber, C.; Gimzewski, J. K.; Drechsler, U.; Rothuizen, H.; Despont, M.; Vettiger, P.; Battiston, F. M.; Ramseyer, J. P.; Fornardo, P.; Meyer, E.; Güntherodt, H.-J. *Ultramicroscopy* **2000,** *82,* 1–9. doi:10.1016/s0304-3991(99)00123-0

5. Stowe, T. D.; Yasumura, K.; Kenny, T. W.; Botkin, D.; Wago, K.; Rugar, D. *Appl. Phys. Lett.* **1997,** *71,* 288–290. doi:10.1063/1.119522

6. Gross, B.; Weber, D. P.; Rüffer, D.; Buchter, A.; Heimbach, F.; Fontcuberta i Morral, A.; Grundler, D.; Poggio, M. *Phys. Rev. B* **2016,** *93,* 064409. doi:10.1103/physrevb.93.064409

7. Gysin, U.; Rast, S.; Aste, A.; Speliotis, T.; Werle, C.; Meyer, E. *Nanotechnology* **2011,** *22,* 285715. doi:10.1088/0957-4484/22/28/285715

8. Giessibl, F. J.; Pielmeier, F.; Eguchi, T.; An, T.; Hasegawa, Y. *Phys. Rev. B* **2011,** *84,* 125409. doi:10.1103/PhysRevB.84.125409

9. Melcher, J.; Stirling, J.; Cervantes, F. G.; Pratt, J. R.; Shaw, G. A. *Appl. Phys. Lett.* **2014,** *105,* 233109. doi:10.1063/1.4903801

10. Li, M.; Tang, H. X.; Roukes, M. L. *Nat. Nanotechnol.* **2007,** *2,* 114–120. doi:10.1038/nnano.2006.208

11. Gil-Santos, E.; Ramos, D.; Martínez, J.; Fernández-Regúlez, M.; García, R.; San Paulo, Á.; Calleja, M.; Tamayo, J. *Nat. Nanotechnol.* **2010,** *5,* 641–645. doi:10.1038/nnano.2010.151

12. Nichol, J. M.; Hemesath, E. R.; Lauhon, L. J.; Budakian, R. *Appl. Phys. Lett.* **2008,** *93,* 193110. doi:10.1063/1.3025305

13. Reiche, C. F.; Körner, J.; Büchner, B.; Mühl, T. *Nanotechnology* **2015,** *26,* 335501. doi:10.1088/0957-4484/26/33/335501

14. Körner, J.; Reiche, C. F.; Büchner, B.; Mühl, T.; Gerlach, G. *J. Sens. Sens. Syst.* **2016,** *5,* 245–259. doi:10.5194/jsss-5-245-2016

15. Körner, J.; Reiche, C. F.; Gemming, T.; Büchner, B.; Gerlach, G.; Mühl, T. *Beilstein J. Nanotechnol.* **2016,** *7,* 1033–1043. doi:10.3762/bjnano.7.96

16. Körner, J.; Reiche, C. F.; Ghunaim, R.; Fuge, R.; Hampel, S.; Büchner, B.; Mühl, T. *Sci. Rep.* **2017,** *7,* 8881. doi:10.1038/s41598-017-08340-z

17. Reiche, C. F.; Körner, J.; Büchner, B.; Mühl, T. Bidirectional scanning force microscopy probes with co-resonant sensitivity enhancement. In *Proceedings of IEEE 15th International Conference on Nanotechnology,* 2015; pp 1222 ff.

18. Körner, J.; Reiche, C. F.; Büchner, B.; Mühl, T. *tm - Technisches Messen* **2018,** *85,* 410–419. doi:10.1515/teme-2017-0139

19. Lochon, F.; Dufour, I.; Rebière, D. *Sens. Actuators, B* **2005,** *108,* 979–985. doi:10.1016/j.snb.2004.11.086

20. Martin, Y.; Williams, C. C.; Wickramasinghe, H. K. *J. Appl. Phys.* **1987,** *61,* 4723–4729. doi:10.1063/1.338807

21. Jenkins, N. E.; DeFlores, L. P.; Allen, J.; Ng, T. N.; Garner, S. R.; Kuehn, S.; Dawlaty, J. M.; Marohn, J. A. *J. Vac. Sci. Technol., B: Microelectron. Nanometer Struct.–Process., Meas., Phenom.* **2004,** *22,* 909. doi:10.1116/1.1695336

22. Gysin, U.; Rast, S.; Ruff, P.; Meyer, E.; Lee, D. W.; Vettiger, P.; Gerber, C. *Phys. Rev. B* **2004,** *69,* 045403. doi:10.1103/physrevb.69.045403

23. Ilic, B.; Yang, Y.; Craighead, H. G. *Appl. Phys. Lett.* **2004,** *85,* 2604–2606. doi:10.1063/1.1794378

24. Rast, S.; Wattinger, C.; Gysin, U.; Meyer, E. *Rev. Sci. Instrum.* **2000,** *71,* 2772–2775. doi:10.1063/1.1150690

25. Voigtländer, B. *Scanning Probe Microscopy,* 1st ed.; Springer: Berlin, Germany, 2015. doi:10.1007/978-3-662-45240-0

26. Butt, H.-J.; Jaschke, M. *Nanotechnology* **1995,** *6,* 1–7. doi:10.1088/0957-4484/6/1/001

27. Weaver, W. J.; Timoshenko, S. P.; Young, D. H. *Vibration Problems in Engineering,* 5th ed.; Wiley: New York, NY, U.S.A., 1990.

28. Novotny, L. *Am. J. Phys.* **2010,** *78,* 1199–1202. doi:10.1119/1.3471177

29. Rubbmark, J. R.; Kash, M. M.; Littman, M. G.; Kleppner, D. *Phys. Rev. A* **1981,** *23,* 3107–3117. doi:10.1103/physreva.23.3107

30. Lang, H. P.; Hegner, M.; Gerber, C. Nanomechanical cantilever array sensors. In *Springer Handbook of Nanotechnology;* Bhushan, B., Ed.; Springer: Berlin, Germany, 2007; pp 427–452. doi:10.1007/978-3-642-02525-9_15

31. T. Mühl, personal communication, 24th August 2017.

32. Pirzer, T.; Hugel, T. *Rev. Sci. Instrum.* **2009,** *80,* 035110. doi:10.1063/1.3100258

33. Gibson, C. T.; Smith, D. A.; Roberts, C. J. *Nanotechnology* **2005,** *16,* 234–238. doi:10.1088/0957-4484/16/2/009

34. Morita, S.; Giessibl, F. J.; Wiesendanger, R., Eds. *Noncontact Atomic Force Microscopy;* NanoScience and Technology; Springer Berlin: Berlin, Germany, 2009. doi:10.1007/978-3-642-01495-6

35. Sarid, D. *Scanning Force Microscopy - With Applications to Electric, Magnetic and Atomic Forces,* 1st ed.; Oxford Series in Optical and Imaging Sciences; Oxford University Press: Oxford, United Kingdom, 1994.

36. Blanter, M. S.; Golovin, I. S.; Neuhäuser, H.; Sinning, H.-R. *Internal Friction in Metallic Materials - A Handbook;* Springer: Berlin, Germany, 2007. doi:10.1007/978-3-540-68758-0

37. Jazar, R. N. *Advanced Vibrations;* Springer US: Boston, MA, U.S.A., 2013. doi:10.1007/978-1-4614-4160-1

38. Yasumura, K. Y.; Stowe, T. D.; Chow, E. M.; Pfafman, T.; Kenny, T. W.; Stipe, B. C.; Rugar, D. *J. Microelectromech. Syst.* **2000,** *9,* 117–125. doi:10.1109/84.825786

Nitrous oxide as an effective AFM tip functionalization: a comparative study

Taras Chutora[1], Bruno de la Torre[*1,2], Pingo Mutombo[2], Jack Hellerstedt[2], Jaromír Kopeček[2], Pavel Jelínek[1,2] and Martin Švec[*1,2]

Abstract

We investigate the possibility of functionalizing Au tips by N_2O molecules deposited on a Au(111) surface and their further use for imaging with submolecular resolution. First, we characterize the adsorption of the N_2O species on Au(111) by means of atomic force microscopy with CO-functionalized tips and density functional theory (DFT) simulations. Subsequently we devise a method of attaching a single N_2O to a metal tip apex and benchmark its high-resolution imaging and spectroscopic capabilities using FePc molecules. Our results demonstrate the feasibility of high-resolution imaging. However, we find an inherent asymmetry of the N_2O probe-particle adsorption on the tip apex, in contrast to a CO tip reference. These findings are consistent with DFT calculations of the N_2O- and CO tip apexes.

Introduction

Frequency-modulated atomic force microscopy (AFM) has become the tool of choice for the characterization of molecules on the atomic scale. Functionalization of a metallic tip apex with a single carbon monoxide molecule (CO) was the key to achieve submolecular resolution for the first time, on a pentacene molecule [1]. This milestone initiated a vigorous development of the technique that now serves a variety of purposes. For example, it can identify molecular structures of natural and pure compounds [2-5], determine the bond order in conjugated systems [6], visualize intramolecular charge distributions [7-9], image three-dimensional molecular structures [10-12], discern complex molecular mixtures [13,14], resolve the intermediate states of chemical reactions [15-19] or discriminate the spin state of single molecules [20].

In most of these cases, the functionalized tip is routinely obtained by picking up a single CO molecule from the substrate. Applying an analogous approach, atomically sharp metal apexes can be also decorated either by different molecular species such as C_{60} [21], naphthalenetetracarboxylic diimide (NTCDI) [22], NO [23] or single atoms such as Xe [24,25], Br [24], Kr [24], O [26], and Cl [1,27]. Such tip terminations have proved to be fairly stable and therefore capable of achieving submolecular resolution. The characteristics of each type of tip termination, such as chemical structure or internal charge distribution, are extremely important for the AFM contrast, distortions in the molecule images, and spatial resolution [8,27,28]. The tip-terminating particle also significantly affects the spectroscopy measurements, i.e., the interaction energy toward different atomic species in force spectroscopy, the contact potential difference in Kelvin probe force microscopy (KPFM) [9,29] and vibrational levels of inelastic tunneling spectroscopy (IETS) [30,31]. A particular termination of the tip may be bound to certain types of substrates, and better suited for a limited range of investigated objects, such as molecules with specific functional groups or atomic impurities with characteristic charge distribution. Therefore it is of utmost importance to search for new potentially practical molecules for tip functionalization and describe their unique properties.

Here we present a process in which N_2O was deposited on a Au(111) substrate and characterized. Subsequently we functionalized the Au tip with N_2O and benchmarked its capabilities by imaging a FePc molecule and performing force–distance spectroscopy. The data is compared to equivalent measurements done with a Au tip functionalized with CO.

Results and Discussion

A clean Au(111) surface was inserted into the microscope head and cooled to 5 K before exposing it to N_2O gas. Figure 1a shows a characteristic constant-current image of the N_2O/Au(111) system, revealing the formation of small 2D clusters, preferentially located at the kinks of the characteristic herringbone structure. Their variable size is typically a few nanometers in diameter. The estimated average apparent height of the cluster formations was 70 pm.

After the N_2O cluster formation, the metallic tip (pre-treated by a gentle indentation into the substrate) was functionalized by an impurity CO molecule, which significantly improved the resolution in both STM and AFM. We performed high-resolution AFM/STM measurements on various clusters (comparable to the inset of Figure 1a), which revealed elongated structures; we attribute these to individual flat-lying N_2O molecules. In a cluster, typically composed of 5–25 molecules, the N_2O molecules have a preferential short-range arrangement of rotation-
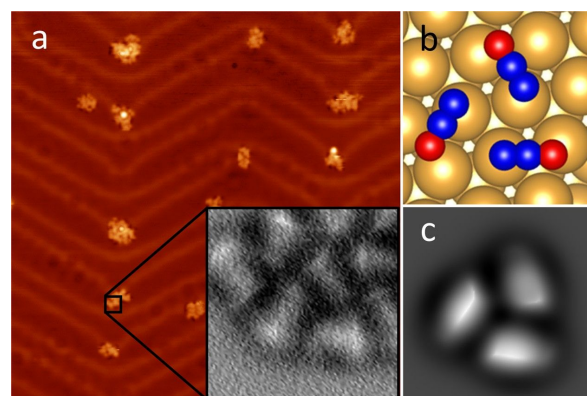

Figure 1: Adsorption of N_2O molecules on the Au(111) substrate. (a) Overview STM image (100 mV, 10 pA, 50 × 50 nm^2) of a sample after N_2O deposition. Inset: a close-up AFM image (1.5 × 1.5 nm^2) of the N_2O cluster adsorbed on the herringbone elbow, scanned with a CO-functionalized tip. (b) Top view of the calculated adsorption geometry of a N_2O trimer. (c) Simulated AFM image (1.5 × 1.5 nm^2) of a N_2O trimer on Au (111) using the probe-particle model [32].

ally symmetrical trimers, with intermolecular distances of about 4.3 Å. A DFT calculation of a single N_2O molecule on the surface confirms that its adsorption configuration on Au(111) is primarily driven by a non-covalent dispersion interaction and prefers to orient its longer axis parallel to the $[2\,\overline{1}\,\overline{1}]$ axis of the surface. The vertical distance between the single molecule and the surface was estimated to be 3.5 Å. Based on this finding, we construct an atomic model of the three flat-lying N_2O molecules on Au(111) and optimize it with total-energy DFT calculations. We find that the trimer is stabilized by electrostatic interactions between the N and O atoms of adjacent N_2O molecules, due to their slightly different polarization. The calculations reveal that the preferred orientation of the N_2O molecules in the clusters is with the O atoms outward (Figure 1b), being 17 meV more stable than the opposite arrangement.

Using the optimized geometry of the cluster obtained from DFT calculations, as an input for the probe-particle model [32], we simulated the AFM images to determine the atomic contrast of the N_2O trimer (Figure 1c). Note that the probe–particle was mimicking a CO molecule. We found good agreement between theory and experiment.

We were able to functionalize the tip with a N_2O molecule. In various attempts to adsorb N_2O onto the tip, we discovered that by intentionally reducing the bias to 50–100 mV for several seconds in constant-current mode while scanning an area containing a cluster of N_2O molecules, a sudden improvement of the resolution occurred (as shown in Figure 2a). This event is characteristic for the tip picking up a molecule from the surface [33,34] and therefore can be attributed to a transfer of a N_2O
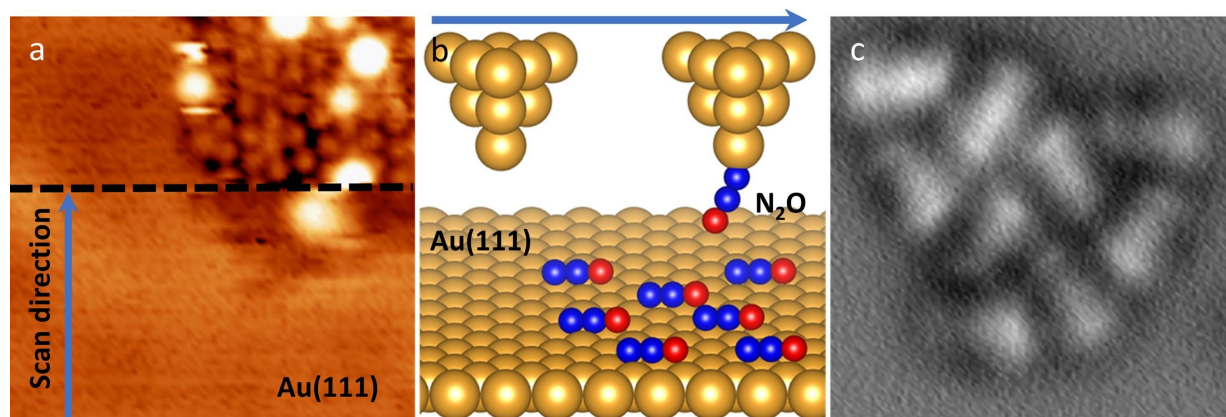
Figure 2: Tip functionalization with a N_2O molecule. (a) STM image (100 mV, 10 pA, 6 × 6 nm^2) demonstrating a spontaneous enhancement of the resolution while scanning over the N_2O-covered surface. (b) Schematic representation of the functionalization process (blue arrow indicates the scan direction). (c) Constant-height AFM image (2 × 2 nm^2) of a single N_2O cluster obtained with a N_2O-functionalized tip.

molecule from the surface to the tip apex, as schematically shown in Figure 2b. We propose that the N_2O molecule is attached to the tip apex through the terminal N (Figure 2b), which has a more reactive character compared to the O atom [35]. In this manner, the O atom would be responsible for the majority of interaction with the substrate.

After functionalization of the tip apex with a single N_2O molecule, we obtained a high-resolution AFM image of the N_2O cluster (Figure 2c). The N_2O tip exhibits good stability during the measurement, allowing us to scan at smaller tip–sample separations and to enter the Pauli repulsion regime. The AFM image of the N_2O cluster Figure 2c shows a remarkably similar resolution to the images acquired with a CO-decorated tip.

In order to understand the chemical behavior of the N_2O tips and compare them to the CO tips, we carried out DFT calculations of their electrostatic potential and total densities (see Methods for more detail). Figure 3 shows the calculated electrostatic potential (ESP) map for CO and N_2O attached to a Au pyramid, projected onto isosurfaces of their respective total electron densities (cut at 0.03 e/A^3). The spatial ESP variation is an important factor for the determination of the molecular reactivity and can be interpreted as the static distribution of the charge around the molecule [36].

The ESP maps of the CO and the N_2O molecule attached to the gold tip (Figure 3) possess some similar characteristics. Both molecules have similar variation of the potential along the probe molecule, i.e., the regions with negative values around the C–O and N–O bonds (electron-rich area, colored in blue) and regions with positive values at the terminal O atoms (electron-poor area, colored in red). This indicates that the N_2O tip is
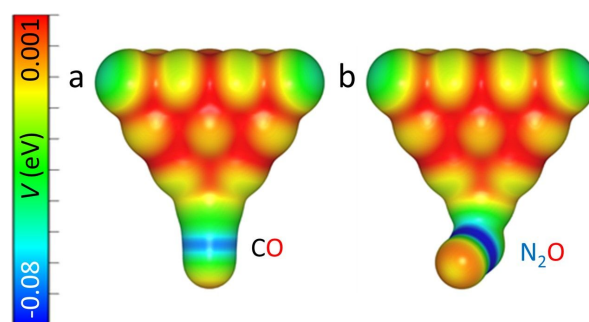

Figure 3: Comparison of the calculated electrostatic potential projections of the CO (a) and N_2O (b) tips obtained through DFT calculations.

very similar to the CO tip in terms of spatial charge distribution. However, the Hirschfeld analysis [37] of atomic charge at the O apex atom gives $-0.077e$ for the N_2O tip, compared to $-0.055e$ for the CO tip. This can result in a larger electrostatic interaction of the N_2O probe with a charged atom or molecule. Also, the geometry of the probe particles on the tip is remarkably different. The CO molecule is attached to the Au pyramid almost perfectly on its axis, whereas N_2O is bent strongly. The bent adsorption configuration of the N_2O molecule is caused by electrostatic interactions between the molecule and the Au tip, which arise from the mutual dipole–dipole interaction. Furthermore, the calculated adsorption energies of the two molecules on the tip differ as well. We have found a value of -0.840 eV for CO, compared to -0.156 eV for N_2O. So while a N_2O tip might still provide the resolution and sensitivity needed for submolecular imaging, an asymmetry is expected in the images made by the N_2O tips and interaction forces may have a larger electrostatic contribution.

To benchmark the performance of the N_2O-decorated tip experimentally, we used it to obtain high-resolution STM/AFM images of a single FePc molecule, which is suitable as a standard due to its planar shape and the flat adsorption geometry on Au(111) [31]. A submonolayer coverage of FePc molecules was deposited on Au(111) at room temperature, and the FePc/Au(111) surface was subsequently cooled down in the microscope and exposed to N_2O. Figure 4 shows an overview STM image of the obtained sample, where the FePc molecules predominantly occupy the fcc-stacked Au regions and the kinks of the Au(111) herringbone reconstruction. The N_2O species adsorbs planarly as in the previous experiment, clustering in the vicinity of single FePc molecules. To functionalize the tip with a single N_2O molecule on such a sample we used the procedure described above. We scan a small region around a single FePc molecule that is surrounded by N_2O molecules, at a setpoint of 50 mV and 20 pA until the characteristic change in the contrast, which is associated with the functionalization, occurs (inset of Figure 4).

With this functionalized tip, we performed imaging with submolecular resolution on one of the FePc molecules, surrounded by the N_2O species. Figure 5a shows the corresponding set of constant-height STM/AFM maps, along with the reference data acquired with a CO tip on a single FePc molecule on Au(111).
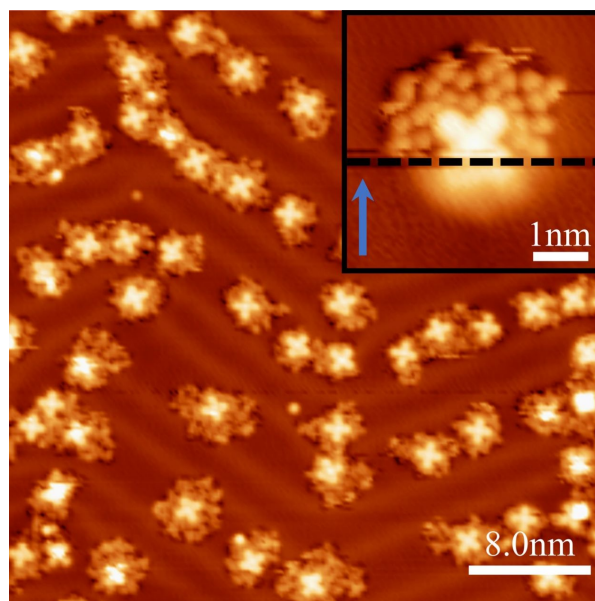

Figure 4: Constant-current STM images of the co-adsorption of FePc and N_2O molecules on a Au(111) surface (200 mV, 20 pA, 40 × 40 nm^2), imaged with a N_2O-functionalized tip. Inset: STM image (50 mV, 20 pA, 5 × 5 nm^2) of a FePc molecule surrounded by N_2O species, demonstrating a tip-functionalization event (on the scan line marked by the dashed line). The scan direction is indicated by a blue arrow.
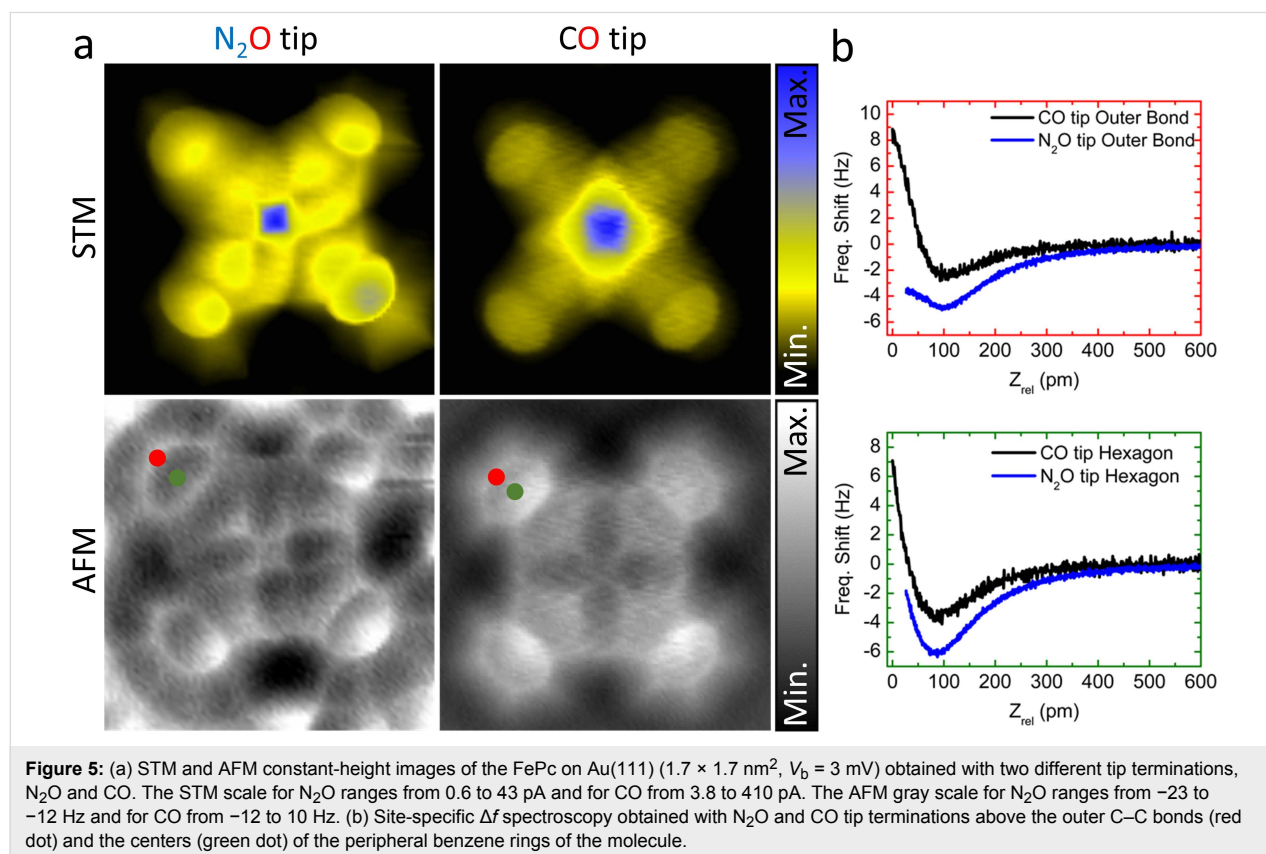

Figure 5: (a) STM and AFM constant-height images of the FePc on Au(111) (1.7 × 1.7 nm^2, V_b = 3 mV) obtained with two different tip terminations, N_2O and CO. The STM scale for N_2O ranges from 0.6 to 43 pA and for CO from 3.8 to 410 pA. The AFM gray scale for N_2O ranges from −23 to −12 Hz and for CO from −12 to 10 Hz. (b) Site-specific Δ*f* spectroscopy obtained with N_2O and CO tip terminations above the outer C–C bonds (red dot) and the centers (green dot) of the peripheral benzene rings of the molecule.

The observed AFM contrast for both the tips generally corresponds to the FePc backbone structure; it shows the four peripheral benzene rings, the inner pyrrole groups and a signature of the metal atom at the center. In the STM images both tips detect a dominating electron tunneling contribution of the central Fe molecular orbital at the Fermi level [31] and also the overall shape of the molecule.

The AFM image taken with the N_2O tip exhibits slightly lower resolution, in comparison to the CO tip termination, with a strong directionality of the submolecular features within the peripheral benzene rings. The tunneling current image also reveals a significant shadow cast in the same direction as the asymmetric features in AFM. These features are indicative of a general probe asymmetry, consistent with the theoretical calculations, which shows a strongly bent adsorption configuration of the N_2O molecule on the tip apex.

For a quantitative comparison of the interaction energy of the two tip terminations with FePc, we performed site-specific frequency-shift spectroscopy $\Delta f(z)$ measurements on the outer C–C bonds and centers of the peripheral benzene molecules indicated by the red and green dots in Figure 5a. In Figure 5b, the short-range Δf curves recorded with N_2O and CO tips are shown (after subtracting the background measured on clean Au [38]). The $\Delta f(z)$ dependence recorded for the N_2O tips is considerably different from the one obtained with a CO tip, both qualitatively and quantitatively. The value of the maximum attractive force [39] for the N_2O tip (Figure S1, Supporting Information File 1) on both spectroscopy sites (outer C–C bond, $F_{N_2O} \approx -125$ pN, and hollow site, $F_{N_2O} \approx -132$ pN) are significantly higher in comparison to the CO tip (outer C–C bond, $F_{CO} \approx -30$ pN, and hollow site, $F_{CO} \approx -56$ pN). Consequently, the interaction energies (Figure S1, Supporting Information File 1) measured with the N_2O tip (outer C–C bond, $E_{N_2O} \approx -156$ meV, and hollow site, $E_{N_2O} \approx -167$ meV) are substantially greater in comparison to the values measured by the CO tip (outer C–C bond, $E_{CO} \approx -43$ meV, and hollow site, $E_{CO} \approx -75$ meV). This difference can be understood as a result of stronger electrostatic interaction of the molecule with the N_2O tip, which is consistent with the DFT calculations of the two different tip terminations.

Conclusion

We have investigated the behavior of N_2O molecules on the surface of Au(111) and determined that they adsorb parallel to the surface, forming typical triangular clusters. We were able to readily functionalize a metallic tip with a single N_2O molecule by picking it up from the Au(111) substrate and demonstrated that the functionalization of the tip can be achieved even when N_2O is co-adsorbed on the surface with other species, in this case FePc molecules. We evaluated the performance of the N_2O tips in submolecular imaging of FePc and site-specific $\Delta f(z)$ spectroscopies. We reproducibly achieved a resolution qualitatively equivalent to the resolution otherwise routinely observed with CO tips, distinguishable by a noticeable asymmetry and higher interaction energies, indicative of a bent adsorption geometry of the N_2O on the tip and more electrostatic charge relative to CO. These observations were corroborated by DFT calculations.

Methods
Experimental

Experiments were carried out in an ultra-high vacuum STM/AFM system (Createc) operated at 5 K. The Au(111) sample (Mateck) was cleaned by repeated cycles of sputtering (1 keV) and subsequent annealing to 600 °C. FePc molecules (Sigma Aldrich, evaporation temperature ca. 250 °C) were directly evaporated onto a clean Au(111) surface at room temperature. N_2O was adsorbed onto the Au(111) surface at temperatures below 12 K with exposures of 0.5–1.7 L. AFM measurements were performed with a qPlus sensor (resonance frequency ca. 30 kHz; $k \approx 1800$ N/m), using an oscillation amplitude of 50 pm. Prior to functionalization, the Pt tip was repeatedly indented into the Au(111) substrate several nanometers deep for sharpening and coating with Au. Experimental data were analyzed using WSxM software [40]; all models were visualized using Vesta software [41].

DFT calculations

We performed density functional theory calculations using the FHI-AIMS code [42] to study the interaction of N_2O with the Au(111) surface. We have used a 6×6 supercell, composed of three Au layers to represent the Au(111) surface. Both a single molecule and trimer clusters were initially placed on the surface according to experimental findings. The structural optimization of the slab was carried out, except for the two bottom Au layers, until the remaining atomic forces and the total energy were found to be below 10^{-2} eV/Å and 10^{-5} eV, respectively. A Monkhorst–Pack grid of $3 \times 3 \times 1$ was used for integration in the Brillouin zone.

DFT calculations were performed at the GGA-PBE level including the Tkatchenko–Scheffler treatment of the van der Waals interactions [43]. The scaled zeroth-order regular approximation [44] was applied to take into account the relativistic effects. The total density and the Hartree potential were calculated to determine the electronic interactions between the surface and the molecules.

AFM images were simulated based on the probe-particle model [32,45], which takes into account van der Waals (vdW) and

electrostatic interactions between the tip and the sample. The calculations were performed varying the effective charge of the probe particle in order to obtain the best possible agreement between the experimental findings and the simulated AFM images. The lateral stiffness was set to $k = 0.25$ N/m. The correlation of the experimental evidence and theory permit us to understand the nature and origin of the chemical contrast.

Supporting Information

Supporting Information File 1
Additional computational data.
[https://www.beilstein-journals.org/bjnano/content/
supplementary/2190-4286-10-30-S1.pdf]

ORCID® iDs
Pingo Mutombo - https://orcid.org/0000-0002-8175-7587
Jack Hellerstedt - https://orcid.org/0000-0003-2282-8223
Jaromír Kopeček - https://orcid.org/0000-0002-9337-4639
Martin Švec - https://orcid.org/0000-0003-0369-8144

References
1. Gross, L.; Mohn, F.; Moll, N.; Liljeroth, P.; Meyer, G. *Science* **2009,** *325,* 1110–1114. doi:10.1126/science.1176210
2. Gross, L.; Mohn, F.; Moll, N.; Meyer, G.; Ebel, R.; Abdel-Mageed, W. M.; Jaspars, M. *Nat. Chem.* **2010,** *2,* 821–825. doi:10.1038/nchem.765
3. Hanssen, K. Ø.; Schuler, B.; Williams, A. J.; Demissie, T. B.; Hansen, E.; Andersen, J. H.; Svenson, J.; Blinov, K.; Repisky, M.; Mohn, F.; Meyer, G.; Svendsen, J.-S.; Ruud, K.; Elyashberg, M.; Gross, L.; Jaspars, M.; Isaksson, J. *Angew. Chem., Int. Ed.* **2012,** *51,* 12238–12241. doi:10.1002/anie.201203960
4. Schuler, B.; Collazos, S.; Gross, L.; Meyer, G.; Pérez, D.; Guitián, E.; Peña, D. *Angew. Chem.* **2014,** *126,* 9150–9152. doi:10.1002/ange.201403707
5. Pavliček, N.; Schuler, B.; Collazos, S.; Moll, N.; Pérez, D.; Guitián, E.; Meyer, G.; Peña, D.; Gross, L. *Nat. Chem.* **2015,** *7,* 623–628. doi:10.1038/nchem.2300
6. Gross, L.; Mohn, F.; Moll, N.; Schuler, B.; Criado, A.; Guitian, E.; Pena, D.; Gourdon, A.; Meyer, G. *Science* **2012,** *337,* 1326–1329. doi:10.1126/science.1225621
7. Mohn, F.; Gross, L.; Moll, N.; Meyer, G. *Nat. Nanotechnol.* **2012,** *7,* 227–231. doi:10.1038/nnano.2012.20
8. Hapala, P.; Švec, M.; Stetsovych, O.; van der Heijden, N. J.; Ondráček, M.; van der Lit, J.; Mutombo, P.; Swart, I.; Jelínek, P. *Nat. Commun.* **2016,** *7,* 11560. doi:10.1038/ncomms11560
9. Albrecht, F.; Repp, J.; Fleischmann, M.; Scheer, M.; Ondráček, M.; Jelínek, P. *Phys. Rev. Lett.* **2015,** *115,* 076101. doi:10.1103/physrevlett.115.076101
10. Moreno, C.; Stetsovych, O.; Shimizu, T. K.; Custance, O. *Nano Lett.* **2015,** *15,* 2257–2262. doi:10.1021/nl504182w
11. Albrecht, F.; Pavliček, N.; Herranz-Lancho, C.; Ruben, M.; Repp, J. *J. Am. Chem. Soc.* **2015,** *137,* 7424–7428. doi:10.1021/jacs.5b03114
12. Albrecht, F.; Bischoff, F.; Auwärter, W.; Barth, J. V.; Repp, J. *Nano Lett.* **2016,** *16,* 7703–7709. doi:10.1021/acs.nanolett.6b03769
13. Schuler, B.; Meyer, G.; Peña, D.; Mullins, O. C.; Gross, L. *J. Am. Chem. Soc.* **2015,** *137,* 9870–9876. doi:10.1021/jacs.5b04056
14. Schuler, B.; Fatayer, S.; Meyer, G.; Rogel, E.; Moir, M.; Zhang, Y.; Harper, M. R.; Pomerantz, A. E.; Bake, K. D.; Witt, M.; Peña, D.; Kushnerick, J. D.; Mullins, O. C.; Ovalles, C.; van den Berg, F. G. A.; Gross, L. *Energy Fuels* **2017,** *31,* 6856–6861. doi:10.1021/acs.energyfuels.7b00805
15. Riss, A.; Paz, A. P.; Wickenburg, S.; Tsai, H.-Z.; De Oteyza, D. G.; Bradley, A. J.; Ugeda, M. M.; Gorman, P.; Jung, H. S.; Crommie, M. F.; Rubio, A.; Fischer, F. R. *Nat. Chem.* **2016,** *8,* 678–683. doi:10.1038/nchem.2506
16. de Oteyza, D. G.; Gorman, P.; Chen, Y.-C.; Wickenburg, S.; Riss, A.; Mowbray, D. J.; Etkin, G.; Pedramrazi, Z.; Tsai, H.-Z.; Rubio, A.; Crommie, M. F.; Fischer, F. R. *Science* **2013,** *340,* 1434–1437. doi:10.1126/science.1238187
17. Shiotari, A.; Nakae, T.; Iwata, K.; Mori, S.; Okujima, T.; Uno, H.; Sakaguchi, H.; Sugimoto, Y. *Nat. Commun.* **2017,** *8,* 16089. doi:10.1038/ncomms16089
18. Rogers, C.; Chen, C.; Pedramrazi, Z.; Omrani, A. A.; Tsai, H.-Z.; Jung, H. S.; Lin, S.; Crommie, M. F.; Fischer, F. R. *Angew. Chem., Int. Ed.* **2015,** *54,* 15143–15146. doi:10.1002/anie.201507104
19. Stetsovych, O.; Švec, M.; Vacek, J.; Chocholoušová, J. V.; Jančařík, A.; Rybáček, J.; Kosmider, K.; Stará, I. G.; Jelínek, P.; Starý, I. *Nat. Chem.* **2017,** *9,* 213–218. doi:10.1038/nchem.2662
20. de la Torre, B.; Švec, M.; Hapala, P.; Redondo, J.; Krejčí, O.; Lo, R.; Manna, D.; Sarmah, A.; Nachtigallová, D.; Tuček, J.; Błoński, P.; Otyepka, M.; Zbořil, R.; Hobza, P.; Jelínek, P. *Nat. Commun.* **2018,** *9,* 2831. doi:10.1038/s41467-018-05163-y
21. Hauptmann, N.; Mohn, F.; Gross, L.; Meyer, G.; Frederiksen, T.; Berndt, R. *New J. Phys.* **2012,** *14,* 073032. doi:10.1088/1367-2630/14/7/073032
22. Sweetman, A. M.; Jarvis, S. P.; Sang, H.; Lekkas, I.; Rahe, P.; Wang, Y.; Wang, J.; Champness, N. R.; Kantorovich, L.; Moriarty, P. *Nat. Commun.* **2014,** *5,* 3931. doi:10.1038/ncomms4931
23. Shiotari, A.; Odani, T.; Sugimoto, Y. *Phys. Rev. Lett.* **2018,** *121,* 116101. doi:10.1103/physrevlett.121.116101
24. Mohn, F.; Schuler, B.; Gross, L.; Meyer, G. *Appl. Phys. Lett.* **2013,** *102,* 073109. doi:10.1063/1.4793200

25. Schuler, B.; Liu, W.; Tkatchenko, A.; Moll, N.; Meyer, G.; Mistry, A.; Fox, D.; Gross, L. *Phys. Rev. Lett.* **2013,** *111,* 106103. doi:10.1103/physrevlett.111.106103

26. Mönig, H.; Hermoso, D. R.; Díaz Arado, O.; Todorović, M.; Timmer, A.; Schüer, S.; Langewisch, G.; Pérez, R.; Fuchs, H. *ACS Nano* **2016,** *10,* 1201–1209. doi:10.1021/acsnano.5b06513

27. Peng, J.; Guo, J.; Hapala, P.; Cao, D.; Ma, R.; Cheng, B.; Xu, L.; Ondráček, M.; Jelínek, P.; Wang, E.; Jiang, Y. *Nat. Commun.* **2018,** *9,* 122. doi:10.1038/s41467-017-02635-5

28. Jelínek, P. *J. Phys.: Condens. Matter* **2017,** *29,* 343002. doi:10.1088/1361-648x/aa76c7

29. Wagner, C.; Green, M. F. B.; Leinen, P.; Deilmann, T.; Krüger, P.; Rohlfing, M.; Temirov, R.; Tautz, F. S. *Phys. Rev. Lett.* **2015,** *115,* 026101. doi:10.1103/physrevlett.115.026101

30. Chiang, C.-l.; Xu, C.; Han, Z.; Ho, W. *Science* **2014,** *344,* 885–888. doi:10.1126/science.1253405

31. de la Torre, B.; Švec, M.; Foti, G.; Krejčí, O.; Hapala, P.; Garcia-Lekue, A.; Frederiksen, T.; Zbořil, R.; Arnau, A.; Vázquez, H.; Jelínek, P. *Phys. Rev. Lett.* **2017,** *119,* 166001. doi:10.1103/physrevlett.119.166001

32. Hapala, P.; Kichin, G.; Wagner, C.; Tautz, F. S.; Temirov, R.; Jelínek, P. *Phys. Rev. B* **2014,** *90,* 085421. doi:10.1103/physrevb.90.085421

33. Temirov, R.; Soubatch, S.; Neucheva, O.; Lassise, A. C.; Tautz, F. S. *New J. Phys.* **2008,** *10,* 053012. doi:10.1088/1367-2630/10/5/053012

34. Wagner, C.; Temirov, R. *Prog. Surf. Sci.* **2015,** *90,* 194–222. doi:10.1016/j.progsurf.2015.01.001

35. Kokalj, A.; Matsushima, T. *J. Chem. Phys.* **2005,** *122,* 034708. doi:10.1063/1.1829652

36. Murray, J. S.; Politzer, P. *Wiley Interdiscip. Rev.: Comput. Mol. Sci.* **2011,** *1,* 153–163. doi:10.1002/wcms.19

37. Hirshfeld, F. L. *Theor. Chim. Acta* **1977,** *44,* 129–138. doi:10.1007/bf00549096

38. Lantz, M. A. *Science* **2001,** *291,* 2580–2583. doi:10.1126/science.1057824

39. Giessibl, F. J. *Appl. Phys. Lett.* **2001,** *78,* 123–125. doi:10.1063/1.1335546

40. Horcas, I.; Fernández, R.; Gómez-Rodríguez, J. M.; Colchero, J.; Gómez-Herrero, J.; Baro, A. M. *Rev. Sci. Instrum.* **2007,** *78,* 013705. doi:10.1063/1.2432410

41. Momma, K.; Izumi, F. *J. Appl. Crystallogr.* **2011,** *44,* 1272–1276. doi:10.1107/s0021889811038970

42. Blum, V.; Gehrke, R.; Hanke, F.; Havu, P.; Havu, V.; Ren, X.; Reuter, K.; Scheffler, M. *Comput. Phys. Commun.* **2009,** *180,* 2175–2196. doi:10.1016/j.cpc.2009.06.022

43. Tkatchenko, A.; Scheffler, M. *Phys. Rev. Lett.* **2009,** *102,* 073005. doi:10.1103/physrevlett.102.073005

44. van Lenthe, E.; van Leeuwen, R.; Baerends, E. J.; Snijders, J. G. *Int. J. Quantum Chem.* **1996,** *57,* 281–293. doi:10.1002/(sici)1097-461x(1996)57:3<281::aid-qua2>3.0.co;2-u

45. Hapala, P.; Temirov, R.; Tautz, F. S.; Jelínek, P. *Phys. Rev. Lett.* **2014,** *113,* 226101. doi:10.1103/physrevlett.113.226101

Review of time-resolved non-contact electrostatic force microscopy techniques with applications to ionic transport measurements

Aaron Mascaro[*], Yoichi Miyahara, Tyler Enright, Omur E. Dagdeviren and Peter Grütter

Abstract

Recently, there have been a number of variations of electrostatic force microscopy (EFM) that allow for the measurement of time-varying forces arising from phenomena such as ion transport in battery materials or charge separation in photovoltaic systems. These forces reveal information about dynamic processes happening over nanometer length scales due to the nanometer-sized probe tips used in atomic force microscopy. Here, we review in detail several time-resolved EFM techniques based on non-contact atomic force microscopy, elaborating on their specific limitations and challenges. We also introduce a new experimental technique that can resolve time-varying signals well below the oscillation period of the cantilever and compare and contrast it with those previously established.

Introduction

Since the inception of the atomic force microscope (AFM) a variety of techniques have been developed aimed at measuring local electronic and ionic properties on a wide range of samples. By carefully controlling the electric field between the tip and sample many properties can be measured with high spatial resolution including static properties such as local contact potential difference (which can be used to extract the local work function) [1] and local piezoelectric response [2], and dynamic properties such as the charging and decay times of photoexcited carriers [3-6], and local activation energies for ionic transport [7,8]. These measurements play a crucial role in understanding local charge dynamics and composition of numerous materials

with applications across many fields including energy generation and storage. Capturing time-resolved dynamic processes at ever-decreasing time and length scales has become of increased interest in recent years due to the importance of understanding transport properties of real-world, often heterogeneous materials relevant for energy generation and storage. A number of AFM techniques have been developed to study relevant materials including time-resolved EFM to measure photoexcited charge accumulation and charge transfer [6,9-11], time-domain EFM to measure ionic transport [7,12], time-resolved electrochemical strain microscopy (ESM) to measure ionic transport [8,13], various time-resolved Kelvin probe force microscopy

(KPFM) techniques that utilize either optical pump-probe or advanced signal processing to measure time-resolved surface potentials [14-18], and other techniques that exploit non-linear signal mixing or heterodyning to extract the time evolution of the tip–sample interaction [19,20]. All of these techniques share a common goal of furthering the understanding of charge generation and transport processes to develop a clear picture of the underlying mechanisms that govern them. This requires an extensive toolbox of experimental techniques of which EFM-based ones will most certainly play an essential role.

In this review we explore in detail several techniques that allow for time-resolved electrostatic force measurements to probe ionic transport. More specifically, these techniques are able to capture time-varying changes in the tip–sample coupling due to the movement of mobile ions within the sample in the sample volume directly underneath the probe tip. The ionic motion is initiated by an electric potential applied across the sample; the movement of mobile ions leads to a change in the tip–sample capacitance and, thus, to a change in the electrostatic force acting on the cantilever probe tip. The electrostatic tip–sample force is proportional to the capacitance gradient $\partial C/\partial z$ times the square of the applied potential $V(t)^2$, i.e.,

$$F \sim \frac{\partial C(t)}{\partial z} V(t)^2 .$$

In ionic transport measurements it is the time-dependence of the capacitance $C(t)$ that is to be measured; however, this is not usually a known quantity. In order to validate a technique for suitability in measuring this quantitatively, a known time-varying voltage with the same functional time-dependence that mimics the expected $C(t)$ can be used instead. This allows for a quantitative assessment of the extracted parameters and is the method used to validate each technique discussed herein.

Since there is a multitude of similar techniques, each with their own clever implementations and analyses, we have restricted our review to exclude all pump–probe and KPFM techniques as these are generally unsuitable for probing ionic transport. For a recent review of all KPFM and related techniques, we refer the reader to [21].

We begin by describing the direct time-domain method and its limitations, we then introduce a new technique we refer to as voltage-pulse averaging EFM, and then continue to explain and examine three other techniques with applications to ionic transport measurements, specifically fast free time-resolved EFM [22], phase-kick EFM [23], and intermodulation spectroscopy [20]. Table 1 lists these techniques along with their respective time resolutions (smallest value demonstrated), limitations, and strengths.

Review
Direct time-domain EFM
Background
Direct time-domain EFM measurements are the most straightforward methods of measuring time-varying interactions. In the

Table 1: Overview of the five techniques explored in this review. Time resolution is the smallest demonstrated value.

technique	time resolution	limitations	strengths
direct time-domain	above 2 µs	– resonance frequency and detection bandwidth limit time resolution	– simple implementation
voltage-pulse averaging EFM	ca. 200 ns	– significant averaging time	– simple implementation
		– difficulty in extracting stretched exponential	– time resolution not limited by detection bandwidth
		– functional form of $C(t)$ must be known	
fast free time-resolved EFM [22]	ca. 10 ns	– slowly varying relationship between τ and extracted signal t_{fp} for sub-cycle time constants	– excellent spatial resolution
		– difficulty in extracting stretched exponential for small time constants	– fast imaging times with simultaneous acquisition and analysis
phase-kick EFM [23]	ca. 35 ns	– requires precisely phase-locked excitation signals	– strong signal-to-noise ratio due to averaging
		– tip–sample force gradient must be approximately constant over oscillation cycle	– time resolution not limited by detection bandwidth
intermodulation spectroscopy [20]	ca. 30 ns	–high Q-factor cantilevers result in lower signal-to-noise ratio	– time resolution theoretically only limited by measurement time
		– a time dependent capacitance will likely lead to a complicated analytic representation needed to extract the time-evolution of the system	– full time-evolution can be captured using only a single measurement

commonly used frequency-modulated AFM configuration, the resonance frequency of an oscillating cantilever is measured while the probe tip interacts with a surface [24]. The interactions are purely electrostatic – in other words, the tip and sample form a capacitor. The oscillation of the cantilever can therefore be modulated by the electric field between the tip and sample, which may vary with time. The first use of an AFM to measure the time evolution of sample charge carriers was reported by Schönenberger and Alvarado [25]. They first applied a voltage pulse between the tip and sample to inject charge into the sample. They subsequently measured the (ac) electrostatic force as a function of time using a lock-in amplifier where the observed force decayed over several seconds.

In the case of photovoltaic samples, simply shining light on them photoexcites charge carriers, which can result in charge build-up in the sample at the location of the AFM tip if an appropriate voltage is applied across the tip–sample gap. Measuring the resonance frequency shift as a function of time after the light is turned on/off then allows for the charging/ discharging time to be directly acquired, revealing information about charge generation and transport in the sample. This was first performed by Krauss et al. who observed charging of photoexcited CdSe nanocrystals by direct frequency shift measurements after illumination [26].

The concept outlined above can be applied to measure ionic transport in ionic conducting materials as well. To probe ionic transport a step potential is applied between the AFM tip and a conducting back electrode, creating an electric field across the tip–sample gap and through the sample, illustrated in Figure 1b. The mobile ions inside the sample move in response to this field over time, resulting in a change in the field (and field gradient) at the tip as illustrated in Figure 1c. This changing electric field as a result of screening by the mobile ions leads to a shift of the cantilever resonance frequency as a function of time, which can

be directly measured, typically by using a phase-locked loop (PLL). This was first performed by Bennewitz et al. to measure the mobility of F^- vacancies in a CaF_2 crystal [27]. Schirmeisen et al. later improved the technique by performing the measurements at various temperatures to extract the activation energy for ionic transport in Li^+ conducting glasses [7]. To further expand the power of the technique, Mascaro et al. developed a real-time averaging system used in conjunction with a fast (high-bandwidth) PLL to improve the time resolution [12]. This enabled ionic transport measurements to be performed on lithium iron phosphate ($LiFePO_4$), a relevant lithium-ion battery cathode material. In this configuration the time resolution (and thus the fastest ionic conductor that can be measured) is limited by the time response of the PLL, which depends on many parameters including the free resonance frequency of the cantilever as well as the various PLL settings.

Limitation: direct frequency detection

A critically damped second-order PLL (i.e., optimized settings) has an exponentially decaying time response to abrupt changes in the frequency being tracked (the center frequency, f_0) [28]. The response time-constant of the phase detector is determined directly by the center frequency: $\tau_{PD} = 1/f_0$. Thus, the theoretical minimum response time to achieve more than 95% tracking is three cycles. This is difficult to realize in practice as it neglects amplification/filtering before and after the phase detector and other non-ideal effects such as jitter and noise. The overall response time of the system (τ_{PLL}, inversely proportional to the overall bandwidth) serves as a more practical metric as it takes all contributions into account. This can either be measured by stepping the frequency of a known signal and measuring the response time or in the case of some digital PLLs by a built-in function that models the response [29].

In general, ionic transport in solid ionic conductors follows a stretched-exponential time response to applied electric fields:
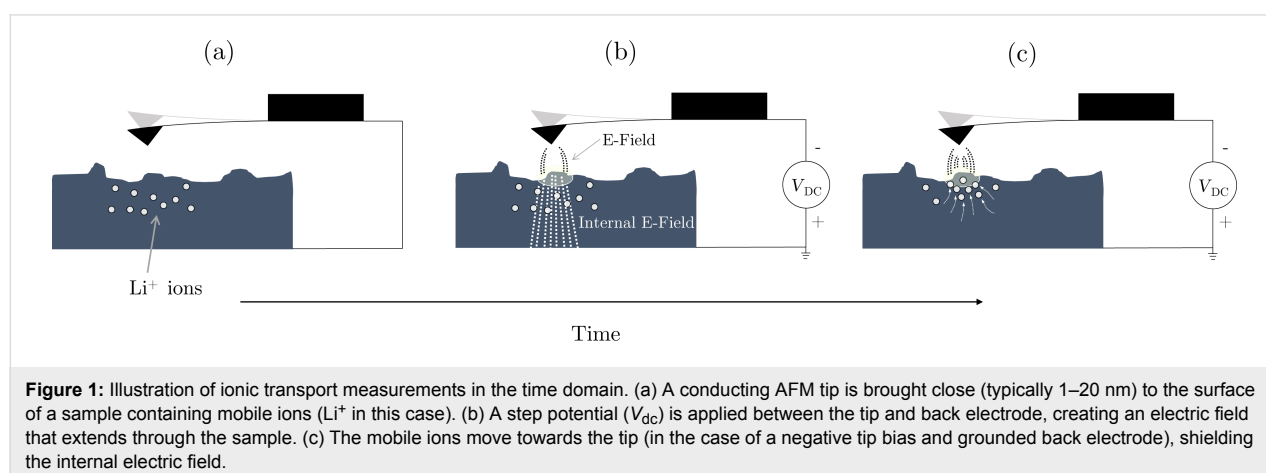
Figure 1: Illustration of ionic transport measurements in the time domain. (a) A conducting AFM tip is brought close (typically 1–20 nm) to the surface of a sample containing mobile ions (Li^+ in this case). (b) A step potential (V_{dc}) is applied between the tip and back electrode, creating an electric field that extends through the sample. (c) The mobile ions move towards the tip (in the case of a negative tip bias and grounded back electrode), shielding the internal electric field.

$$\phi(t) = \phi_0 \exp\left[-\left(t / \tau^* \right)^\beta \right]; \quad 0 < \beta < 1, \qquad (1)$$

where ϕ represents the internal electric field, ϕ_0 is the initial field strength, β is the stretching factor, and τ^* is the collective (or overall) time constant for the response [30]. Note that this stretched exponential behaviour is due to the correlated nature of ion transport, which depends on the atomic and electronic structure of the material, and not necessarily due to a distribution of relaxation times [31]. Nonetheless, this complicates time-domain measurements of ionic transport as the functional form of the relaxation must be fully captured in order to reliably extract the relevant parameters, namely τ^* and β. With slow ionic relaxation times (longer than milliseconds) and typical operating (scanning) parameters (bandwidth of ca. 100 Hz) the PLL response will not affect the extracted values obtained from directly fitting the data. However, as the relaxation time approaches the response time of the PLL, the output signal will become a convolution of the PLL response function and the ionic relaxation. This makes any quantification of the transport properties challenging.

To investigate the effect of τ_{PLL} on the ability to extract parameters from measured signals, a digitially synthesized voltage waveform varying in time as a stretched exponential (Equation 1, $\beta = 0.7$) was applied between a Pt-coated AFM tip and a gold substrate (separated by about 20 nm) under high vacuum (ca. 10^{-6} mbar, Jeol JSPM-5200) to simulate ionic transport in the sample with a known decay time constant. Note that a separation ≥ 1 nm is necessary in general to ensure that no charge is injected into the sample. In this case, the electric field follows the applied voltage instantaneously on the relevant time scales. For each programmed time constant (from 0.1 to 10 ms), the voltage was varied from 0 V initially to 5 V; the measured response is shown in Figure 2a where the blue curve is the result of the smoothly varying stretched-exponential applied voltage. The orange curve is the result of applying an initial instantaneous jump from 0 to 2.5 V followed by a stretched-exponential increase to 5 V. This is intended to mimic experimental conditions as the step voltage applied causes an initial jump in the resonance frequency (due to the stepped electric field between the tip and sample before the ions respond) followed by the slow sample relaxation (as the ions move to shield the initial electric field). Since the actual time constant is given by the synthesized voltage waveform, the percent error can be directly calculated from the fit results. Note that since the frequency shift is quadratic in voltage and it is the voltage being changed here, we must first take the square root of the data before fitting. The results are shown in Figure 2b where the shaded area is the region for which $\tau^* < \tau_{PLL} \approx 600$ µs. To replicate measurement conditions, 100 waveforms were applied as a pulse train (50%

duty cycle) and the response signals were averaged together using our realtime averaging system to reduce noise (described in [12]). In both cases (with and without the initial jump) we are able to accurately extract the relaxation time constant; the initial jump only leads to a higher statistical uncertainty, which is due to the slow initial response of the PLL relative to the fast jump from 0 to 2.5 V. This becomes especially apparent for $\tau^* \approx \tau_{PLL}$. The stretching factor displays exactly the same behaviour (not shown).
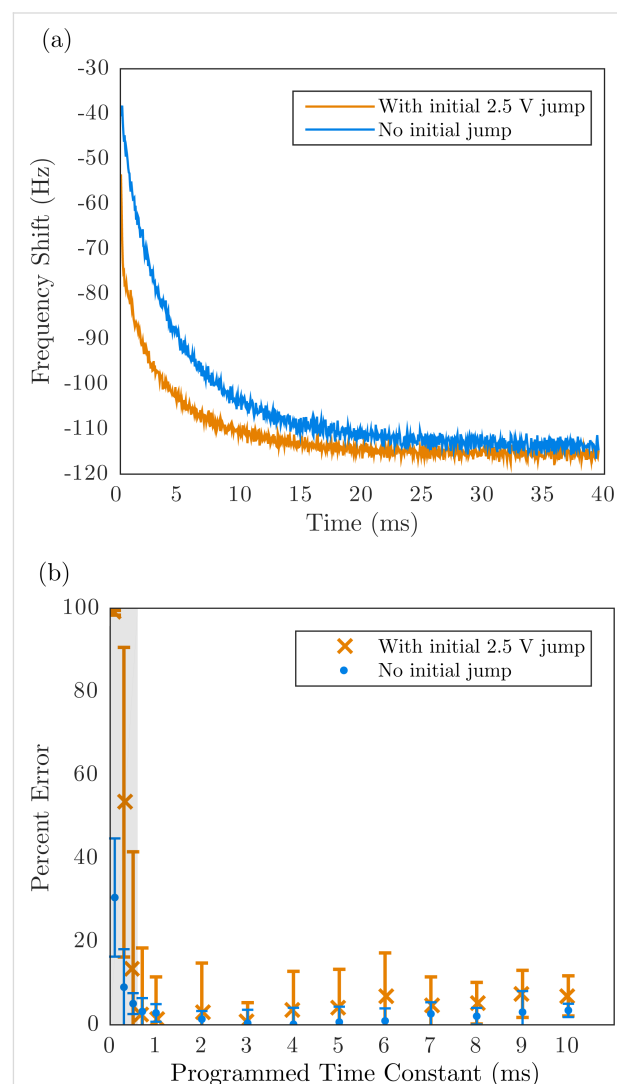
Figure 2: (a) AFM frequency shift response to stretched-exponential voltage pulses (from 0 to 5 V) with and without an intial 2.5 V jump. (b) Percent error of fitted relaxation time constant (τ^*) as a function of relaxation time constant of applied voltage pulse for fixed PLL response time (τ_{PLL}). Shaded region shows where $\tau^* < \tau_{PLL}$.

Clearly the practical limitation for high-fidelity measurements is determined by τ_{PLL} as the percent error increases drastically for $\tau^* < \tau_{PLL}$. Simply increasing the PLL bandwidth will decrease τ_{PLL} although this will result in higher noise due to the less

aggressive filtering. By taking a larger number of averages, the same signal-to-noise ratio can be achieved, however the cantilever resonance frequency will ultimately determine the minimum τ_{PLL}. Empirically we have found that the minimum PLL response time achievable is $\tau_{PLLmin} \approx 10 \times 1/f_0$. The highest resonance frequency cantilevers currently commercially available have frequencies of $f_0 \approx 5$ MHz, thus the realistic minimum measurable relaxation time of this technique is ca. 2 µs.

Voltage-pulse averaging EFM
Motivation
Improving the time resolution beyond the limitations of direct time-domain measurements is possible in several ways using careful instrumentation and signal analysis. The basic concept is to detect (using a slow detector) the change in average response of the sample due to a change in the frequency (or, e.g., repetition rate or delay time) of an excitation signal. This is also the basis for pump–probe spectroscopy, which is routinely employed to measure ultrafast dynamics of condensed matter systems using a variety of pulsed light sources [32-35]. In some systems the probe pulse is not even necessary as the pump both excites the response being investigated and engages the probing behaviour simultaneously. One example of this is in time-resolved Kelvin probe force microscopy (KPFM) experiments that measure the surface photovoltage of a sample as a function of time after a light source is pulsed. This was first implemented by Takihara et al. to measure the photovoltage dynamics of a sample at time scales faster than the KPFM feedback loop can track [36]. In this measurement mode, the tip–sample coupling is in an 'always-on' state and the time resolution is achieved by modulating the length of time the system is allowed to decay (i.e., the pulse-off time). The minimum time resolution is no longer limited by the detection electronics, but instead is theoretically limited only by the thermal noise of the cantilever [18]. This principle can be easily extended to ionic systems (such as those discussed previously) by simply replacing the pulsed light source with a pulsed voltage. In this case, the electric field engages the tip–sample coupling and simultaneously moves the mobile ions in the substrate, which leads to a changing tip–sample capacitance. Since the applied voltage controls the tip–sample coupling, turning the voltage off decouples the tip from changes occurring in the sample, thus the ionic transport is only probed during the pulse-on time, which can be directly controlled. Finding a relationship between the average frequency shift $\langle f_0 \rangle$ and the relaxation time constant of the sample τ^* as a function of the pulse width T then allows for sample transport dynamics to be extracted beyond the time resolution of the detection electronics. To relate the frequency shift of a cantilever to the tip–sample forces for FM-AFM, we turn to canonical perturbation theory using action-angle variables similar to the work done by Giessibl [37].

Derivation using canonical perturbation theory
Starting with the Hamiltonian for a harmonic oscillator and using a capacitive force perturbation Hamiltonian ($\Delta H = (1/2)CV^2$), we transform the momentum and position variables to action and angle variables: $(p,q) \rightarrow (\alpha,\beta)$, where the first-order perturbation solution for the angle variable β_1 (not to be confused with the earlier use of β as the exponential stretching factor) has the property:

$$\dot{\beta}_1 = \left.\frac{\partial \Delta H(\alpha,\beta,t)}{\partial \alpha}\right|_0, \tag{2}$$

where the dot denotes the time derivative and the subscript 0 indicates that α and β are to be replaced with their unperturbed, constant values (α_0,β_0) after differentiation [38].

Writing q in terms of the action and angle variables explicitly:

$$q = \sqrt{\frac{2\alpha}{m\omega^2}} \sin(\omega t + \beta), \tag{3}$$

we see that $\dot{\beta}$ is the time derivative of the phase change due to the perturbing force. Taking the average therefore gives us the steady-state frequency shift $\langle \Delta f \rangle = \langle \dot{\beta} \rangle$, which can easily be measured. Re-writing:

$$\left.\frac{\partial \Delta H(\alpha,\beta,t)}{\partial \alpha}\right|_0 = \left.\frac{\partial \Delta H(\alpha,\beta,t)}{\partial q}\frac{\partial q}{\partial \alpha}\right|_0, \tag{4}$$

it can be easily shown that

$$\frac{\partial q}{\partial \alpha} = \frac{q}{2\alpha_0}, \tag{5}$$

and $\alpha_0 = kA_0^2/2f_0$ where A_0 is the oscillation amplitude, k is the spring constant, and f_0 is the resonance frequency of the oscillator. In the simplest experiment where a time-varying voltage is applied between a conducting tip and sample, C has only an explicit dependence on q and V only an explicit dependence on t:

$$\left.\frac{\partial \Delta H(\alpha,\beta,t)}{\partial \alpha}\right|_0 = \left.\frac{\partial}{\partial q}\left[\frac{1}{2}C(q)V(t)^2\right]\right|_0 \frac{qf_0}{kA_0^2}. \tag{6}$$

However, C does have an implicit time-dependence because the position q is not constant. The capacitance $C(q)$ between a conducting sphere and conducting plane is approximated by [39]:

$$C \approx 4\pi\varepsilon_0 R \left[1 + \frac{1}{2}\log\left(1 + \frac{R}{q'}\right) \right], \qquad (7)$$

where R is the radius of the sphere and q' is the sphere-plane (tip–sample) separation, which changes as the (tip) position, q, oscillates. In other words: $q' = A_0 + d + A_0\sin(\omega_0 t + \phi_0)$, where ϕ_0 is the initial cantilever phase, ω_0 is the free resonance frequency, A_0 is the amplitude, and d is the closest tip–sample separation of the oscillating cantilever. Assuming this is an acceptable approximation for an AFM tip and conducting sample, the average frequency shift can be written as follows:

$$\langle \Delta f \rangle = \langle \dot{\beta} \rangle = \frac{2\pi\varepsilon_0 \left(R/A_0\right)^2}{k} \frac{1}{1/f_0} \int_0^{1/f_0} \frac{V(t)^2}{q' + R}\,\mathrm{d}t, \qquad (8)$$

with the integral taken over one cycle ($1/f_0$). Thus far we have only made an assumption regarding the functional form of the tip–sample capacitance. This relation (Equation 8) is thus valid for arbitrary oscillation amplitudes and timescales as long as the tip–sample interaction remains a small perturbation to the overall mechanical energy of the cantilever oscillation. This condition is fulfilled for a periodic voltage pulse with its frequency, f_V, away from any of the mechanical resonances of the cantilever ($f_V < f_{i+1}$ and $f_V > f_i$ where f_i is the i-th mechanical eigenfrequency of the cantilever). This is due to the large quality factor enhancement present on resonance, which would lead to a significant contribution to the total mechanical energy from even a small voltage (and thus field) applied near resonance, invalidating the perturbation approach to derive Equation 8.

Validation measurement

To demonstrate the time resolution of this technique a validation measurement was performed using a cantilever with a low resonance frequency (16.7 kHz) and a conducting tip over a gold sample. The tip was retracted a short distance (ca. 20 nm) with the z-feedback turned off and a train of exponential voltage pulses was applied, resulting in a change in the average frequency shift as a function of the width of the voltage pulse (T), illustrated in Figure 3a. The frequency shift was averaged over several seconds for each value of T, and T was then stepped as illustrated in Figure 3b. This full measurement was repeated 20 times with the z-feedback turned on and then back off between each measurement to minimize drift. Each pulse had the form $V(t) = V_0 + \Delta V(1 - \exp[-t/\tau])$ during the pulse-on period and $V(t) = V_0$ during the pulse-off period with a duty cycle of 20%. To fit the data, the integral in Equation 8 was performed piecewise over the corresponding on and off time periods for one full cantilever oscillation: ($0{\to}T/5$, $T/5{\to}T$), ($T{\to}6T/5$,
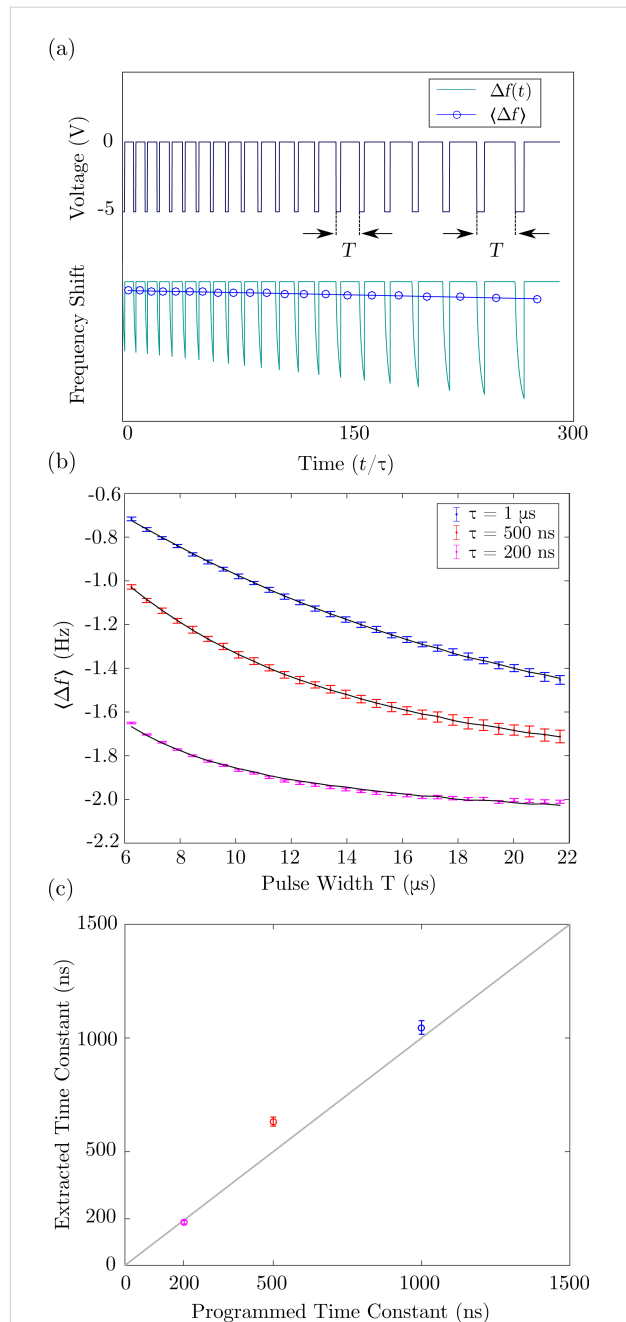
Figure 3: (a) Schematic illustration of the voltage-pulse averaging EFM technique: the top shows the applied voltage pulses with different pulse width (T), while the bottom shows the (simulated) instantaneous (Δf) and average ($\langle \Delta f \rangle$) frequency shift due to an exponentially varying sample response. (b) Measured average frequency shift response as a function of the pulse width (T) for exponential voltage pulses with 1 µs (blue), 500 ns (red) and 200 ns (purple) time constants (τ), cantilever f_0 = 16.7 kHz, 2 s averaging per measurement, 20 measurements per point. Error bars are the standard deviation of 20 measurements, and the black lines show fits to Equation 8. (c) Extracted time constant, (τ), as a function of the programmed time constant for the three measurements in (b); the solid gray line has a slope of unity to illustrate where points would lie for a perfect 1:1 relationship. Measured values: τ = 1.05 ± 0.03 µs, τ = 633 ± 20 ns, τ = 192 ± 3 ns. Note that a decay time of 190 ns is ca. 300-times faster than the cantilever oscillation period.

$6T/5{\rightarrow}2T)$, … , $(…, (5N − 4)T/5{\rightarrow}NT)$, where $NT \approx 1/f_0$ (note that $NT \neq 1/f_0$ because the pulse width cannot be an integer multiple of the oscillation period as discussed above). This integral has no closed-form solution and therefore must be computed numerically in order to fit the data. Since the phase between the applied pulses and the cantilever oscillation is arbitrary, the integral must be computed for many oscillation cycles (starting with an arbitrary phase) and then averaged to minimize the effect of the initial relative phase.

The results are shown in Figure 3 along with the fits to Equation 8 where we set: $V(t) = A + B{\cdot}\exp(−t/\tau)$, giving three fit parameters: A, B, and the time constant τ. The effect of the finite number of oscillation cycles appears in the fitted curves (black lines in Figure 3) as small deviations from a perfectly smooth function. This can be minimized by integrating over more cycles at the expense of increased computation time, which can be significant and has a negligible effect on the extracted fit parameters. The extracted time constants are plotted as a function of the programmed time constants in Figure 3c.

Extending this technique to ionic transport systems requires only the insertion of an explicit time dependence of the capacitance $C(t)$ in place of the time-dependent voltage in Equation 8. The capacitance follows the time dependence of the system after a bias is applied, which is typically a stretched exponential as in Equation 1. Although this is in principle feasible, the main challenge is to perform the fitting. We attempted to fit the data in Figure 3 to a stretched exponential with an additional parameter, β, which should result in an extracted value of $\beta = 1$ since this is a 'pure' exponential decay. The fitting was very problematic due to the dependence of the fit results on the chosen initial conditions. This is a general challenge when using functions with numerous fit parameters, in accordance with the famous quote about fitting an elephant by John Von Neumann [40].

Assumptions and limitations

As shown by this validation measurement, this technique can be used to measure transport processes occurring faster than the period of the cantilever. Fundamentally, the time resolution should only be limited by the minimum electrical pulse width that can be reliably applied to the sample (which is likely much larger than the theoretical limit [18]). The only assumption used that may not be true for all cases is the functional form of the tip–sample capacitance (Equation 7). To test the accuracy of this assumption we investigated both a conducting sample and a thick dielectric sample (200 µm thick sapphire, $\varepsilon_r = 11.3$) by measuring the frequency shift as a function of the distance with a constant applied bias. The force was then extracted from the frequency shift using the Sader–Jarvis method [41] while taking

care to ensure that the inversion procedure is mathematically well-posed for this particular experiment [42,43].

The results are shown in Figure 4 where the black lines are fits to the approximate force between a conducting sphere held at a constant potential and a conducting plane:

$$F \approx \tilde{F}\left[\frac{1}{\left(z/\tilde{R}\right)+\left(z/\tilde{R}\right)^2}\right], \qquad (9)$$

where $\tilde{F}$ and $\tilde{R}$ are fit parameters. Theoretically, $\tilde{F} = 4\varepsilon V^2$, where ε is the permittivity and V is the applied voltage, and $\tilde{R}$ is the effective tip radius. The oscillation amplitude for both experiments was 6 nm, thus the x-axis is the average tip–sample separation and the zero-point was chosen as the point when the oscillation stopped due to contact with the sample. The resulting values for $\tilde{F}$ were 0.6 nN for gold and 38.5 nN for sapphire and the effective tip radii obtained were $\tilde{R} = 4.3$ nm and 0.23 nm for gold and sapphire, respectively. The $\tilde{F}$ value obtained for gold is very close to the theoretical value of 0.53 nN, but the value for sapphire is off by approximately a factor of 5, while the tip radii are significantly smaller than the true tip radius (ca. 30 nm). These results are not surprising as there are many potential sources of error that can affect the absolute value of the force including the calibration of the cantilever spring constant, background forces from the conical probe and the cantilever itself, and uncertainty in the zero-point for both the tip–sample separation and the force itself, which are typically chosen arbitrarily [44-49]. Note that this experiment aims
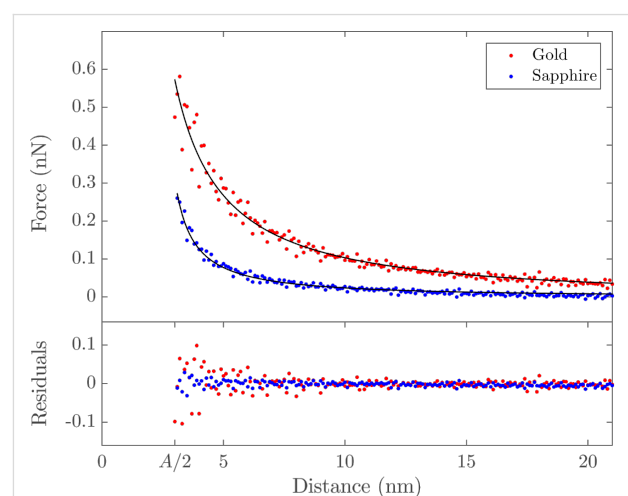

Figure 4: Measured tip–sample force as a function of the distance for a gold-coated tip over a grounded gold substrate (red) and a grounded 200 µm thick sapphire substrate (blue) with 4 V applied to the tip. Cantilever parameters: $f_0 = 295.621$ kHz, $k = 27$ N/m, $A = 6$ nm (Mikromasch NSC15/CR-AU).

only to demonstrate the validity of the functional form of the relationship and not as a quantitative measurement of these parameters. Better approximations than the simple sphere–plane one used here have been developed, but would introduce significant challenges in computing the integral in Equation 8. Using this simple approximation for both gold and sapphire substrates, the residuals are normally distributed to within experimental uncertainty (i.e., the χ^2 goodness of fit test performed on the residuals does not reject the null hypothesis to 0.05 significance [50]). This demonstrates that the functional form of this approximation is valid with this particular probe type on samples of two extremes (a smooth conductor and a thick dielectric material). However, it is not necessarily valid in all cases and should therefore be verified through spectroscopy measurements such as this on a case-by-case basis.

Sapphire was chosen for its high dielectric constant ($\varepsilon_r > 10$), which is similar to those found in many solid ionic conductors such as $LiFePO_4$ and $LiCoO_2$, and for its low electronic conductivity and lack of mobile ions. This experiment is therefore a reliable validation of the *z*-dependence of the tip–sample capacitance expected for actual ionic transport measurements on relevant samples.

Fast free time-resolved EFM
Motivation
It is clear that there are challenges in using time-averaged AFM signals to extract fast sample dynamics, namely a priori knowledge or assumptions of the specific temporal functional form of the dynamics. Some techniques have sought to avoid this by directly capturing the deflection signal using high-speed data acquisition systems and performing offline analysis to reconstruct the sample response. One such technique is fast free time-resolved electrostatic force microscopy (FF-trEFM), first proposed by Giridharagopal and co-workers [22]. FF-trEFM captures the full dynamics of an oscillating cantilever when an interaction force between the tip and sample is turned on. An overview of this technique is shown in Figure 5 (reproduced from [51]).

Description and implementation
To implement FF-trEFM requires the addition of a high-speed data acquisition system to a standard AFM, which is not overly expensive or onerous. Acquiring the raw deflection signal in the time-domain precludes the necessity for expensive detection electronics that are commonly used to acquire and demodulate the oscillation of the cantilever. The only limitation on standard AFM systems are the photodetectors, which typically have bandwidths of 1–2 MHz, although faster photodiodes are available. The raw signal can then be filtered and postprocessed using a Hilbert transform to extract the analytical signal and

what is known as the 'instantaneous frequency' (the time derivative of the instantaneous phase). Examining the extracted instantaneous frequency after applying a voltage with an exponential rise time τ (shown in Figure 5b for simulated data), it is clear that the response shows observable differences as a function of τ. Since the cantilever is continuously driven throughout the experiment, the instantaneous frequency shows a fast transient response to the applied pulse, followed by a slow relaxation towards a new steady-state value. This leads to a clear initial peak in the frequency shift, which is defined as the 'time to first frequency shift peak' (t_{FP}) by Giridharagopal and co-workers [22]. The authors demonstrated that simulated results (both numerical simulations of a damped-driven harmonic oscillator and finite element simulations) and their experimental results show excellent agreement given the same parameters and subject to the same postprocessing (windowing, filtering, and analytical signal extraction).

It is instructive to note that the extracted instantaneous frequency contains a time delay introduced by the bandpass filter used in the processing to smooth the response, which cannot be completely corrected for. This leads to the attenuation of high-frequency components, especially for decay times faster than the oscillation period. Because of this attenuation, the extracted signal is a representation of the true 'instantaneous frequency', leading to difficulties in determining the full functional form of the time-dependent tip–sample interaction.

Application to ionic transport measurements
To accurately quantify ionic transport requires the capability to fully resolve the functional form of a stretched exponential response to extract the two main parameters of interest, τ and β. To test the suitability of FF-trEFM for these measurements, we performed numerical simulations (of a damped driven harmonic oscillator, see Supporting Information File 1 for MATLAB code) similar to those performed by Karatay and co-workers [51], using instead a resonance frequency varying in time as a stretched exponential and a stretched exponential electrostatic force term:

$$\omega_0\left(t \geq 0\right) = \omega_0\left(t = 0\right) + \Delta\omega\left[1 - e^{-(t/\tau)^\beta}\right] \qquad (10)$$

and

$$F_e\left(t\right) = F_{e0}\left[1 - e^{-(t/\tau)^\beta}\right]. \qquad (11)$$

The parameters employed were $\omega_0 = 2\pi \times 277$ kHz, $\Delta\omega = 2\pi \times 277$ Hz, and $F_{e0} = 3$ nN, similar to those used in [22]. The results after windowing, filtering, and performing the

Figure 5: "(a) Schematic of the experimental setup: (i) Computer requests a trigger at a defined phase of the oscillation, (ii) trigger circuitry triggers the digitizer and the excitation source accordingly, and (iii) the digitizer transfers the acquired signals to computer. (b) Flow diagram of the data analysis procedure after the acquisition: (iv) signals are averaged together, (v) windowed and filtered, and (vi) demodulated via Hilbert transform to find the instantaneous frequency of the cantilever (instantaneous frequency curves for excitations with time constants of 25 ns and 100 μs are shown)." Reproduced with permission from [51], copyright 2016 AIP Publishing.

Hilbert transform are shown in Figure 6. The colours denote different time constants and the β values are shown by different line styles. For slower time constants ($\tau \geq 10$ μs) the different values of β are visually distinct; however, at much smaller timescales these distinctions are no longer visible, making ionic transport measurements using FF-trEFM challenging and possibly no more advantageous than direct time-domain EFM.

Demonstration of spatial resolution

In more recent work by Karatay and co-workers, they analyzed how a variety of factors including noise and the phase difference between the cantilever oscillation and the applied pulses affect the achievable time resolution [51]. They presented guidelines for implementation of their technique, in particular the use of photothermal excitation to reduce other sources of mechanical noise. To study the relationship between the system dynamics and the measured t_{FP} response they mapped t_{FP} as a function of true exponential time constant τ to generate a calibration curve (Figure 7a). They observed statistically significant differences in the measured signal in differences in τ down
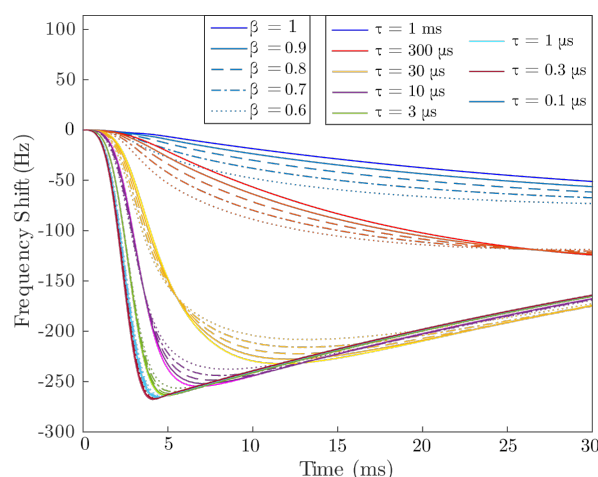

Figure 6: Extracted FF-trEFM signals from numerical simulations of tip–sample interactions with a stretched-exponential time response (Equation 1) with various relaxation time constants, τ, and stretching factors, β.
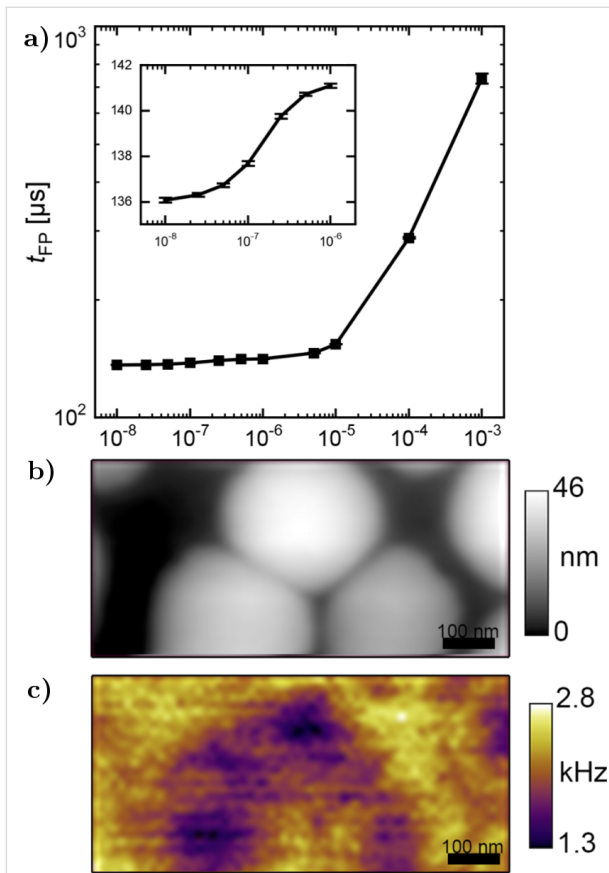
Figure 7: "(a) Calibration curve for a range of characteristic times of exponential decay (τ) (inset shows a zoom-in for shorter times). (b) Topography and (c) inverse τ_{FP} (τ_{FP}^{-1}) images of a 1:4 ratio MDMO-PPV:PCBM thin film photovoltaic device cast from toluene. Excitation wavelength is 488 nm and intensity at the tip is ~290 W/cm^2. Data are acquired at 10 nm lift height, 10 V bias between the cantilever and the sample, with 60 averages per pixel." Adapted with permission from [51], copyright 2016 AIP Publishing.

to 10 ns, which they designated as the minium attainable time resolution. The authors then utilized t_{FP} to study differences in local charging times of an organic photovoltaic thin film (MDMO-PPV:PCBM), shown in Figure 7, and demonstrated the ability of the technique to spatially resolve heterogeneities. Due to the difficulty in quantitatively extracting τ from the measured τ_{FP}, spatially resolved measurements are limited to relative charging rates presented as spatial mapping of τ_{FP}. These results can still provide useful insight into sample dynamics (in this case the quantum efficiency of the photovoltaic material) even though direct quantitative measurements of decay time constants may not always be possible.

Phase-kick EFM
Background and implementation
Another technique recently developed by Dwyer and co-workers, referred to as "phase-kick" EFM (pk-EFM), uses an indirect measurement of the cumulative change of a cantilever

parameter (phase or amplitude) in order to reconstruct a time-varying signal [23]. One implementation of pk-EFM utilizes a carefully timed voltage pulse applied between tip and sample that controls the tip–sample coupling while a light pulse is also applied, as illustrated in Figure 8 (reproduced from [23]). Initially, the cantilever is driven on resonance at a steady-state amplitude and a voltage is applied. The voltage engages the tip–sample coupling and leads to an initial frequency shift, which can be seen at $t = -50$ ms in Figure 8F. A short time later the drive is turned off so that the cantilever is freely oscillating; practically, this removes the drive signal as a source of noise in the experiment. At $t = 0$ a light pulse is then applied and the capacitance varies temporally as the sample charges due to the photoexcitation. By then abruptly turning off the tip–sample coupling (by setting the voltage back to 0) the total photocapacitance change measured by the cantilever can be controlled. The applied voltage therefore acts as a gate that controls the cumulative sample response that is captured in the cumulative change in the cantilever oscillation. The total phase shift $\Delta\phi$ from the time the light pulse is applied ($t = 0$) to the time when the voltage is returned to 0 ($t = t_p$) is then proportional to the integrated photocapacitance since the voltage is held constant over this time:

$$\Delta\phi = -\frac{f_0 V^2}{4k_0} \int_0^{t_p} C_t''(t)\, \mathrm{d}t, \tag{12}$$

where C_t'' is the is the second derivative of the tip–sample capacitance with respect to vertical separation, f_0 is the resonance frequency, and k_0 is the spring constant. This result is derived from the relationship between the frequency shift and the capacitive force between the tip and sample:

$$\delta f(t) = -\frac{f_0}{4k_0} C_t''(t) V^2, \tag{13}$$

which is a valid approximation in the limiting case of small oscillation amplitudes [37]. More specifically, this approximation is only valid if the force gradient is constant over one full oscillation of the tip [52]. This can be achieved under typical experimental conditions (1–5 nm oscillation amplitude) by simply performing the measurement with a larger tip–sample separation, but this comes at the cost of degraded spatial resolution. Achieving smaller oscillation amplitudes (much smaller than 1 nm) is possible using more sensitive detection methods (interferometry, for example [53]) and cleaner excitation schemes such as photothermal excitation [54]. Using probes of higher stiffness, however, is not expected to be advantageous due to the inverse relationship between the measured phase shift and cantilever spring constant.
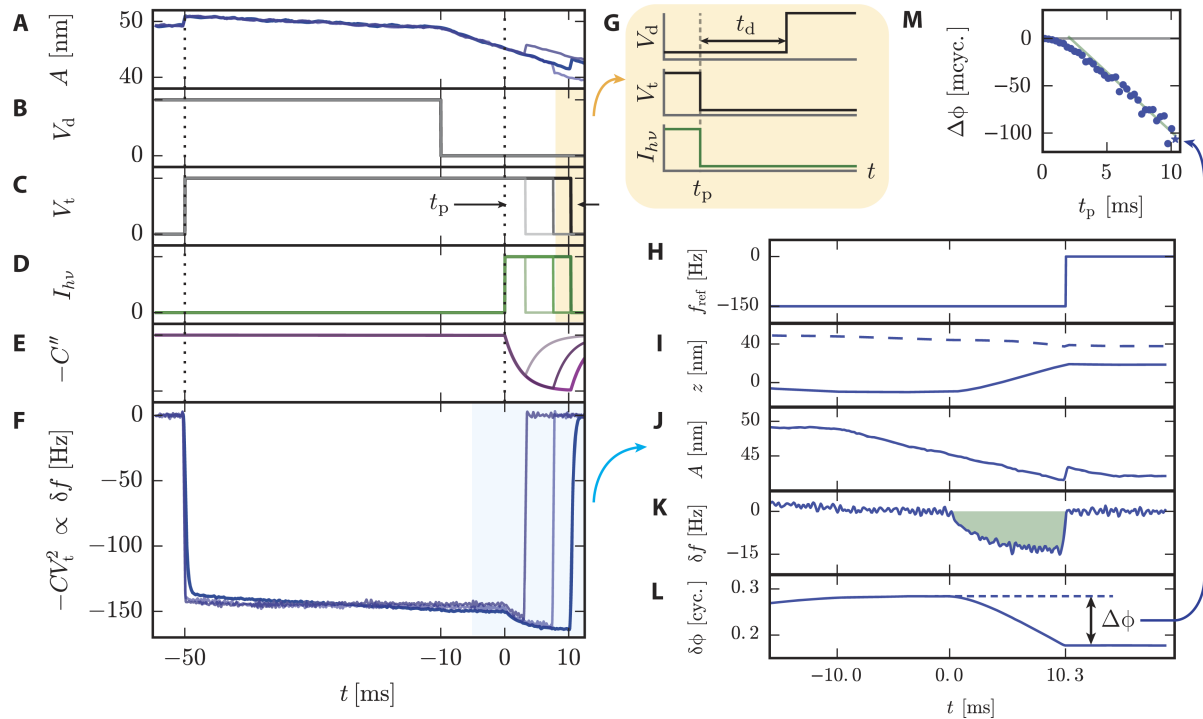
Figure 8: "For three representative pulse times, we plot (A) cantilever amplitude; (B) cantilever drive voltage, turned off at $t = -10$ ms; (C) tip voltage, with the pulse time t_p indicated; (D) sample illumination intensity, turned on at $t = 0$; (E) sample capacitance; and (F) cantilever frequency shift. (G) Timing of applied voltages and light pulses. The voltage and light turn off simultaneously at $t = t_p$. After a delay t_d (typically 5 to 15 ms), the cantilever drive voltage is turned back on. Next, we illustrate how the phase shift $\Delta\phi$ is calculated using the $t_p = 10.3$ ms data. We process the cantilever displacement data using a software lock-in amplifier. (H) The software lock-in amplifier reference frequency changes at $t = t_p$. The software lock-in amplifier outputs (I) the in-phase (solid) and out-of-phase (dashed) components of the cantilever displacement; (J) cantilever amplitude; (K) frequency shift; and (L) phase shift. The total phaseshift $\Delta\phi$ is equal to the highlighted area under the cantilever frequency shift curve. (M) The voltage- and light-induced phase shift $\Delta\phi$ is measured as a function of the pulse time t_p. We show only every other data point for clarity. The $t_p = 10.3$ ms data point is denoted with a star. Experimental parameters: PFB:F8BT on indium tin oxide (ITO) film, $h = 250$ nm, $V_t = 10$ V, $I_{h\nu} = 0.3$ kW m^{-2}, delay time between pulses = 1.5 s." The cantilever used had a resonance frequency of 62 kHz. Reproduced with permission from [23].

Validation measurement

To demonstrate the sub-cycle time resolution of this technique, Dwyer et al. used the Magnus expansion in order to solve the system of linear differential equations describing the cantilever motion [23]. Modelling the photocapacitance as a single exponential with a risetime of τ,

$$C_t''(t) = C_t''(0) + \Delta C_{h\nu}''\left(1 - e^{-t/\tau}\right),$$

resulted in two expressions relating the cumulative amplitude (ΔA) and phase shifts ($\Delta\phi$) to the time constant:

$$\Delta A \approx \delta x h\nu \frac{\omega_0}{1 + \tau^2\omega_0^2}\left[t_p - \tau + \tau e^{-t_p/\tau}\right]\sin\phi_p, \quad (14)$$

$$\Delta\phi \approx \frac{\delta x h\nu}{A_0}\frac{\omega_0}{1 + \tau^2\omega_0^2}\left[t_p - \tau + \tau e^{-t_p/\tau}\right]\cos\phi_p, \quad (15)$$

where $\delta x_{h\nu} = V^2\Delta C_{h\nu}'/(2k_0)$ ($\delta x_{h\nu}$ is the dc deflection due to the photocapacitive force). This result is valid for very short times after the voltage is abruptly returned to 0. It is especially interesting as it relates the change in amplitude and phase with the phase of the cantilever when the voltage is turned off, $\phi_p = \theta(t = t_p)$. By tuning t_p, a phase shift, an amplitude change, or a combination of both can be induced. The technique is fully illustrated in Figure 9 where the amplitude data in Figure 9E (ΔA) was obtained by voltage pulses alone. The voltage pulses resulted in charging/discharging of the sample (PFB:F8BT on ITO), which was also modelled as a single exponential in time: $V_t(t) = V[1 - \exp(-t/\tau_c)]$. This allowed for the amplitude to be written as a function of t_p and τ_c where it again displayed a sinusoidal dependence on ϕ_p. Note that t_p in Figure 9 refers to the width of the voltage pulse, whereas t_p used in the derivation was the time at which the voltage was returned to zero. Relabelling the width of the voltage pulses as t_p', this yields $t_p = t_p' + t_d$; in other words the t_p in Equation 14 and Equation 15 can be tuned by changing the delay time t_d. This is shown in Figure 9E where the sinusoidal behaviour of ΔA as a
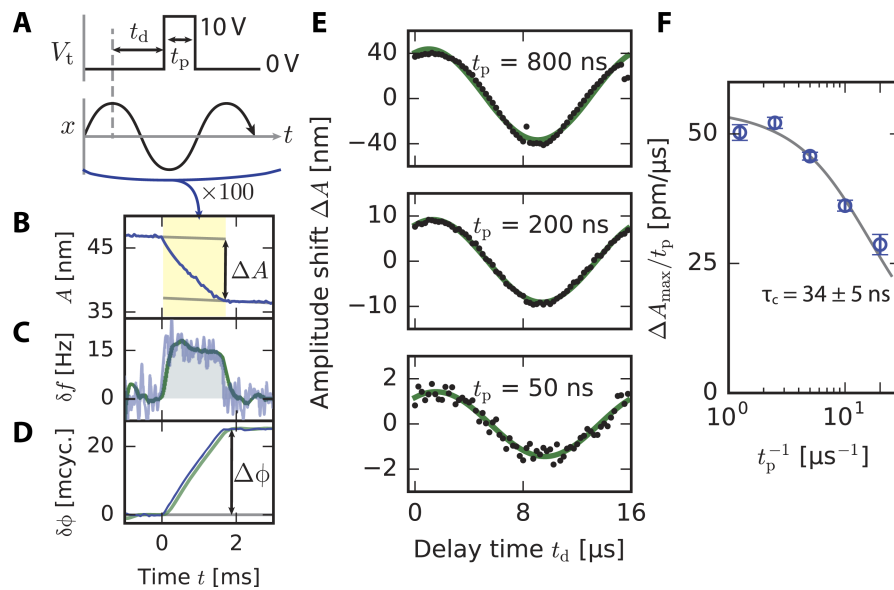
Figure 9: "Experiments and simulations demonstrating subcycle time resolution in pk-EFM. (A) Subcycle voltage-pulse control experiment (PFB:F8BT on ITO, h = 250 nm). A voltage pulse of length t_p is applied to the cantilever tip (top) at a delay of t_d relative to the cantilever oscillation (middle) for 100 consecutive cantilever oscillations. (B) The pulses shift the cantilever amplitude by ΔA.(C) Measured frequency shift and (D) phase shift, demodulated with a 3-dB bandwidth of 4.8 kHz (blue) and 1.5 kHz (green). (E) The amplitude shift ΔA versus delay time t_d for three representative pulse lengths. (F) The normalized response $\Delta A_{max}/t_p$ obtained by fitting data in (E) shows the cantilever wiring attenuating the response at short pulse times. The gray line is a fit to a single-exponential cantilever charging transient." Adapted with permission from [23].

function of t_d is clear. Figure 9F shows the maximum amplitude change ΔA_{max} as a function of the inverse pulse width $1/t_p'$. An exponentially decreasing amplitude change at smaller pulse widths is clearly visible, which the authors explain by the charge being unable to get in and out of the sample on these fast timescales. The extracted time constant for the charging time, τ_c, was 34 ± 5 ns.

Application to ionic transport measurements

From this voltage-pulse measurement it is clear that this technique can easily be extended to measure ionic transport. In fact, it may even be best suited to this application as it requires only a precisely timed voltage pulse instead of phase-locked voltage and light pulses. This technique operates in much the same way as the voltage-pulse averaging method previously described: A parameter of the cantilever oscillation (be it phase, frequency shift, or amplitude) is averaged over a long time period while a coherent (i.e., phase-locked with respect to cantilever oscillation) repeating signal is applied over a much smaller time period that induces a change in the measured parameter. By changing the length of time that the 'fast' signal is allowed to interact with the cantilever it can then be reconstructed by relating the slowly varying parameter to the fast dynamics. Although similar to pump–probe style measurements, these techniques are unique in that they operate by changing the cumulative interaction time between the probe and the sample instead of simply capturing 'snapshots' of the evolution of the sample

dynamics as a function of time. This allows for sample dynamics that are driven only while the tip–sample coupling is engaged to be measured, such as ionic transport, for example. Directly applying this technique to measure ionic transport, however, would require the addition of a stretching factor, β, into the exponential as previously discussed. The main complication in this case is performing the time-integral over the capacitive gradient, which was assumed to be a simple exponential in Equation 14 and Equation 15. The integral will not have a closed-form solution, which would require either a series expansion approximation or a numerical approximation in order to extract useful information from the data. This will likely result in the same challenge as we encountered with the voltage-pulse averaging technique where the least-squares fitting has many local minima for the fit parameters resulting in a strong dependence of the fit results on the initial conditions. Nonetheless, this technique is promising in terms of achieving better time-resolution in EFM-based measurements.

Intermodulation spectroscopy
Background and implementation

Significant progress has clearly been made in measuring electrostatic force microscopy signals in the time domain. The main challenges of the techniques discussed thus far have been the detection methods (specifically, bandwidth limitations) and various assumptions and approximations that have been made, which limit the useful parameter space of some experiments.

Looking instead in the frequency domain, one very recent method of extracting fast sample dynamics appears to be a promising alternative to many of these challenges. Intermodulation spectroscopy, developed by Borgani and Haviland [20], utilizes the spectral response of a cantilever near resonance due to an applied pulse train (optical or electrical) in order to probe sample dynamics. This technique exploits the non-linear tip–sample interaction due to the applied pulse train that results in a spectrum of peaks at various sum and difference frequencies, illustrated in Figure 10. Each of these frequency components (referred to as intermodulation products, or IMPs) contains information about the interaction, which can be extracted by looking at the Fourier series expansion of the tip–sample interaction. Since the interaction is purely capacitive, the force is given by

$$F = \frac{1}{2}\frac{\partial C}{\partial z}V^2,$$

which contains two separate variables each with their own periodicity: the capacitive gradient $\partial C/\partial z$, and the voltage V. Since V is controlled by the applied excitation, it is periodic in ω_E, the repetition rate of the applied pulses. The Fourier series for $V^2(t)$ is therefore given by:

$$V^2(t) = \sum_{j=-\infty}^{+\infty} v_j e^{i\left(j\omega_E t + \theta_j\right)}. \tag{16}$$

In the case where the sample capacitance remains constant (in a conducting sample, for example), the capacitance gradient has the same periodicity as the cantilever oscillation since the cantilever sweeps through the gradient as it oscillates. The Fourier series expansion for

$$\frac{1}{2}\frac{\partial C}{\partial z}\big[z(t)\big]$$

can then be written as

$$\frac{1}{2}\frac{\partial C}{\partial z}\big[z(t)\big] = \sum_{k=-\infty}^{+\infty} c_k e^{i\left(k\omega_D t + \phi_k\right)}. \tag{17}$$

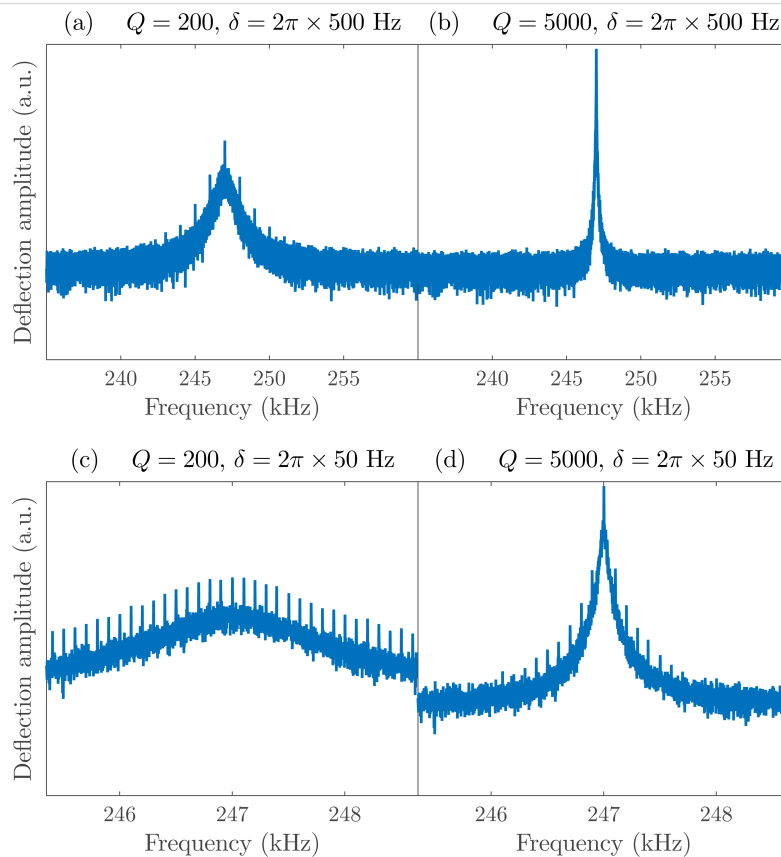**Figure 10:** Synthetic data of cantilever deflection spectrum around the fundamental resonance frequency, $\omega_0 = 2\pi \times 247$ kHz, with: (a) $\delta = 2\pi \times 500$ Hz and a quality factor typical for ambient measurements, $Q = 200$; (b) $\delta = 2\pi \times 500$Hz and $Q = 5000$, typical of vacuum measurements; (c) $\delta = 2\pi \times 50$ Hz and $Q = 200$; and (d) $\delta = 2\pi \times 50$ Hz and $Q = 5000$.

The authors proposed three distinct excitation schemes based on the frequency of the applied pulses, ω_E, relative to the mechanical drive frequency ω_D: resonant excitation, where $\omega_E = \omega_D + \delta$, with $\delta \ll \omega_0$; sub-resonant excitation, where $\omega_E = \delta \ll \omega_D$; and super-resonant excitation, where $\omega_E = 2\omega_D + \delta$. For each excitation scheme they showed the Fourier coefficients for the first six IMPs, which have the form

$$\hat{F}_{\pm n} = c_k v_j e^{i\left(\phi_k \pm \theta_j\right)}.$$

For resonant excitation, they determined that taking the ratio and product of certain pairs ($\hat{F}_{n+2}$ and $\hat{F}_{-n}$) yields quantities that depend only on the electrical response, which completely eliminates the dependence on the capacitance gradient. Thus, to extract information about the system using these quantities does not require any assumptions about the functional form of the capacitance gradient. The only (major, and possibly limiting) assumption is that the sample is metallic (see discussion below). The authors also derived similar ratios for both the sub-resonant and super-resonant schemes, allowing them to directly compare the time resolution and signal-to-noise ratio of each.

Validation measurement

As a validation measurement, they applied electrical pulses with known exponential charging times between a conducting tip and sample and extracted the rise and fall time constants, τ_r and τ_f, using an analytical model for $V^2(t)$. This allows for a high-fidelity reconstruction of the true signal using only a few

Fourier coefficients. Using the resonant excitation scheme, they accurately extracted the time constants down to ca. 20 ns, approaching the theoretical limit they derived for the technique. Their results are shown in Figure 11 for each of the three excitation schemes. Both the resonant and super-resonant schemes allowed signals more than an order of magnitude faster than the oscillation period of the cantilever to be extracted.

They report that mapping of system dynamics can be done even at standard imaging speeds due to the simultaneous acquisition at multiple frequencies using a multi-frequency lock-in amplifier. This is a drastic improvement over many other time-resolved EFM variations that require lengthy averaging times, which makes spatial mapping difficult and time consuming.

Challenges and application to ionic transport measurements

Thus far, measurements using this technique have only been performed under ambient conditions and on a conducting sample with known voltage pulses. One foreseeable challenge will be in performing measurements under vacuum conditions, which is typically beneficial due to the large increase in quality factor that leads to a greater force sensitivity. However, for intermodulation spectroscopy measurements, this will lead to a smaller frequency window in which quality factor enhancement will be available to boost the relative amplitudes of the IMPs. This is illustrated in Figure 10 where panel (a) shows synthetic data for a standard cantilever in ambient ($Q = 200$) with several IMPs clearly visible above the noise. Figure 10b shows the exact same simulated experiment with a much higher quality
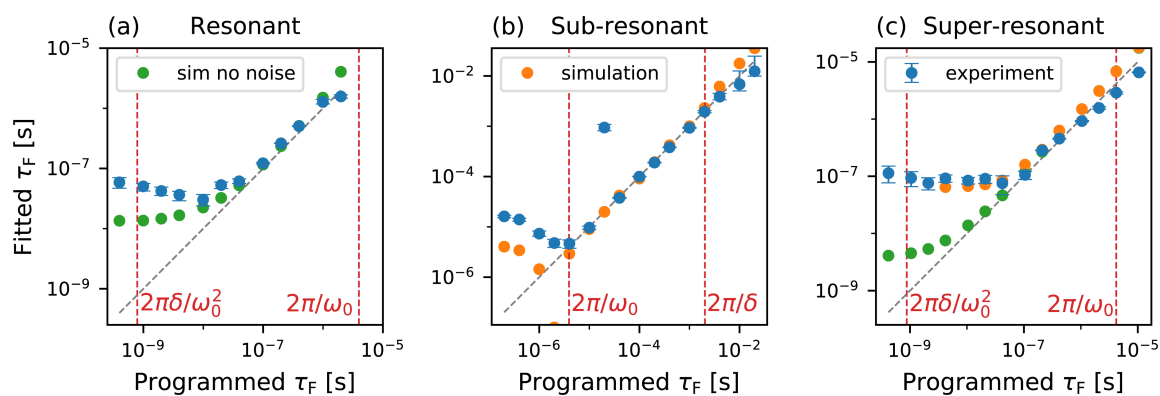

Figure 11: "Results from simulations and from the experimental validation for the proposed excitation schemes: (a) resonant, (b) sub-resonant and (c) super-resonant. The cantilever has a resonance frequency of about $2\pi \times 250$ kHz, a value of $\delta = 2\pi \times 500$ Hz is used in the sub-resonant scheme and $\delta = 2\pi \times 50$ Hz in the resonant and super-resonant schemes. The fittted values τ_F are plotted versus the value programmed in the simulation and in the MLA. The gray dashed lines have slope unity and indicate where a perfect data point would be. For the experimental data, a series of 256 measurements is performed at each value of programmed τ_F: the blue dots indicate the median of the reconstructed values, and the error bars indicate the inter-quartile range. The vertical red dashed lines mark the time resolution calculated in Sec. IV." of [20]. "(a) in the resonant scheme, both simulations without noise (green dots) and experiments fail to reach the predicted time-resolution, due to the violation of Eq. (7). (b) in the sub-resonant scheme, simulations with detector and force noise (orange dots) and experiments show the predicted time resolution. (c) in the super-resonant scheme, simulations without noise approach the predicted time resolution, while experiments are limited to about 50 ns. Simulations with detector and force noise reproduce the experimental data." Reproduced with permission from [20], copyright 2019 AIP Publishing.

factor ($Q = 5000$), which is typical for vacuum applications. In both cases $\delta = 2\pi \times 500$ Hz. Reducing δ to 50 Hz, as was done for the resonant and super-resonant experiments, yields many more IMPs above the noise level as shown in Figure 10c. Simultaneously demodulating several of these components allows for accurate reconstruction of the time-varying voltage. However, in the case of high Q, we see that many of the peaks are now well below the noise level due to the size of the resonance peak compared to the IMP spacing (δ). The signal-to-noise ratio is significantly lower in this case, requiring a much smaller value of δ and, in turn, longer averaging times. Note that since the time resolution is proportional to δ (Equations 15 and 16 in [20]), using a smaller δ values actually results in better time resolution, at the expense of longer measurement times.

Another complication that may be encountered will be observed when performing measurements on samples with non-static capacitance gradients. For the analysis performed in this case the capacitance was assumed to have only the periodicity of the cantilever oscillation, ω_D, which is, of course, valid because the sample is a conductor. This will not be the case when the capacitance gradient has an explicit time-dependence, as with many photovoltaic and ionic conductors. In these samples, the tip–sample capacitance gradient will evolve with time after the application of the pulse (be it optical or electronic) and will therefore have a frequency component matching that of the applied pulses, ω_E. This is due to sample dynamics such as photoexcitation or ionic transport [12,23,55]. This may make extracting the time response of the sample much more difficult if the capacitive Fourier coefficients cannot be eliminated by taking ratios of certain components. There may be methods of minimizing this effect, especially in the case of optical pulses for measuring time-resolved photocapacitance similar to the pk-EFM method discussed previously [23]. In this implementation, Dwyer et al. applied a large bias between the tip and sample to engage the coupling, having the fortunate side-effect of rendering the measurement insensitive to small variations in surface potential as the sample charges. This results in a response that is only sensitive to the time-varying capacitance, simplifying the analysis significantly. Similar techniques may be required to extract information from samples where large time-dependent changes in capacitance and surface potential are expected.

Conclusion

We have reviewed several established techniques that achieve time resolution using EFM and examined their assumptions, limitations, and potential applications. Direct time-domain EFM is the most straightforward to implement, but is limited to measuring on timescales much slower than the cantilever oscillation. The new technique we have demonstrated – voltage-

pulse averaging EFM – allows for time resolution much faster than the cantilever oscillation period, but requires a priori knowledge of the time-evolution of the signal and the functional form of the tip–sample capacitance. FF-trEFM, which uses post-processing to extract the instantaneous frequency of the cantilever, allows for rapid data acquisition while scanning and high spatial resolution, but suffers from a nonlinear variation of the measured signal with the time constant of the sample response for fast responses. Phase-kick EFM provides a pathway to extract sample dynamics indirectly by observing cumulative changes in the cantilever oscillation, but relies on the assumption that the oscillation amplitude is small with regards to the capacitance gradient, which can be violated for large amplitudes and/or small tip–sample separations. Finally, we have looked in detail at intermodulation spectroscopy, which exploits the non-linear signal mixing of the cantilever oscillation and an applied pulse train by recording the various frequency components corresponding to specific Fourier coefficients. This technique may encounter difficulties in extracting information for measurements where the tip–sample capacitance also changes as a result of the applied pulse train.

Despite many of these assumptions and potential limitations, all of these techniques represent great strides in the advancement of time-resolution in EFM. With the need for measurements of faster and faster dynamics with higher spatial resolution, the role of time-resolved EFM as a key tool is more significant than ever.

Supporting Information

Supporting Information File 1
MATLAB code to simulate FF-trEFM measurements with a stretched exponential response.
[https://www.beilstein-journals.org/bjnano/content/supplementary/2190-4286-10-62-S1.m]

ORCID® iDs
Aaron Mascaro - https://orcid.org/0000-0003-2402-8115
Yoichi Miyahara - https://orcid.org/0000-0002-9514-9603
Peter Grütter - https://orcid.org/0000-0003-1719-8239

References

1. Nonnenmacher, M.; O'Boyle, M. P.; Wickramasinghe, H. K. *Appl. Phys. Lett.* **1991,** *58,* 2921–2923. doi:10.1063/1.105227

2. Güthner, P.; Dransfeld, K. *Appl. Phys. Lett.* **1992,** *61,* 1137–1139. doi:10.1063/1.107693

3. Hamers, R.; Cahill, D. G. *J. Vac. Sci. Technol., B: Microelectron. Nanometer Struct.–Process., Meas., Phenom.* **1991,** *9,* 514–518. doi:10.1116/1.585559

4. Krauss, T. D.; Brus, L. E. *Phys. Rev. Lett.* **1999,** *83,* 4840. doi:10.1103/physrevlett.83.4840

5. Chen, L.; Cherniavskaya, O.; Shalek, A.; Brus, L. E. *Nano Lett.* **2005,** *5,* 2241–2245. doi:10.1021/nl051567m

6. Coffey, D. C.; Ginger, D. S. *Nat. Mater.* **2006,** *5,* 735–740. doi:10.1038/nmat1712

7. Schirmeisen, A.; Taskiran, A.; Fuchs, H.; Roling, B.; Murugavel, S.; Bracht, H.; Natrup, F. *Appl. Phys. Lett.* **2004,** *85,* 2053–2055. doi:10.1063/1.1790034

8. Guo, S.; Jesse, S.; Kalnaus, S.; Balke, N.; Daniel, C.; Kalinin, S. V. *J. Electrochem. Soc.* **2011,** *158,* A982–A990. doi:10.1149/1.3604759

9. Reid, O. G.; Rayermann, G. E.; Coffey, D. C.; Ginger, D. S. *J. Phys. Chem. C* **2010,** *114,* 20672–20677. doi:10.1021/jp1056607

10. Cox, P. A.; Glaz, M. S.; Harrison, J. S.; Peurifoy, S. R.; Coffey, D. C.; Ginger, D. S. *J. Phys. Chem. Lett.* **2015,** *6,* 2852–2858. doi:10.1021/acs.jpclett.5b01360

11. Alexe, M. *Nano Lett.* **2012,** *12,* 2193–2198. doi:10.1021/nl300618e

12. Mascaro, A.; Wang, Z.; Hovington, P.; Miyahara, Y.; Paolella, A.; Gariepy, V.; Feng, Z.; Enright, T.; Aiken, C.; Zaghib, K.; Bevan, K. H.; Grutter, P. *Nano Lett.* **2017,** *17,* 4489–4496. doi:10.1021/acs.nanolett.7b01857

13. Jesse, S.; Balke, N.; Eliseev, E.; Tselev, A.; Dudney, N. J.; Morozovska, A. N.; Kalinin, S. V. *ACS Nano* **2011,** *5,* 9682–9695. doi:10.1021/nn203141g

14. Murawski, J.; Graupner, T.; Milde, P.; Raupach, R.; Zerweck-Trogisch, U.; Eng, L. M. *J. Appl. Phys.* **2015,** *118,* 154302. doi:10.1063/1.4933289

15. Shao, G.; Glaz, M. S.; Ma, F.; Ju, H.; Ginger, D. S. *ACS Nano* **2014,** *8,* 10799–10807. doi:10.1021/nn5045867

16. Collins, L.; Ahmadi, M.; Wu, T.; Hu, B.; Kalinin, S. V.; Jesse, S. *ACS Nano* **2017,** *11,* 8717–8729. doi:10.1021/acsnano.7b02114

17. Fernández Garrillo, P. A.; Borowik, Ł.; Caffy, F.; Demadrille, R.; Grévin, B. *ACS Appl. Mater. Interfaces* **2016,** *8,* 31460–31468. doi:10.1021/acsami.6b11423

18. Schumacher, Z.; Spielhofer, A.; Miyahara, Y.; Grutter, P. *Appl. Phys. Lett.* **2017,** *110,* 053111. doi:10.1063/1.4975629

19. Garrett, J. L.; Munday, J. N. *Nanotechnology* **2016,** *27,* 245705. doi:10.1088/0957-4484/27/24/245705

20. Borgani, R.; Haviland, D. B. *Rev. Sci. Instrum.* **2019,** *90,* 013705. doi:10.1063/1.5060727

21. Sadewasser, S.; Glatzel, T., Eds. *Kelvin Probe Force Microscopy: From Single Charge Detection to Device Characterization;* Springer Series in Surface Sciences, Vol. 65; Springer International Publishing: Cham, Switzerland, 2018. doi:10.1007/978-3-319-75687-5

22. Giridharagopal, R.; Rayermann, G. E.; Shao, G.; Moore, D. T.; Reid, O. G.; Tillack, A. F.; Masiello, D. J.; Ginger, D. S. *Nano Lett.* **2012,** *12,* 893–898. doi:10.1021/nl203956q

23. Dwyer, R. P.; Nathan, S. R.; Marohn, J. A. *Sci. Adv.* **2017,** *3,* e1602951. doi:10.1126/sciadv.1602951

24. Albrecht, T. R.; Grütter, P.; Horne, D.; Rugar, D. *J. Appl. Phys.* **1991,** *69,* 668–673. doi:10.1063/1.347347

25. Schönenberger, C.; Alvarado, S. F. *Phys. Rev. Lett.* **1990,** *65,* 3162–3164. doi:10.1103/physrevlett.65.3162

26. Krauss, T. D.; O'Brien, S.; Brus, L. E. *J. Phys. Chem. B* **2001,** *105,* 1725–1733. doi:10.1021/jp0023415

27. Bennewitz, R.; Reichling, M.; Matthias, E. *Surf. Sci.* **1997,** *387,* 69–77. doi:10.1016/s0039-6028(97)00268-9

28. Kroupa, V. F. *Phase Lock Loops and Frequency Synthesis;* John Wiley & Sons, Ltd: Chichester, United Kingdom, 2003. doi:10.1002/0470014105

29. HF2LI lock-in amplifier, Rev. 42300.

30. Ngai, K. L.; Kanert, O. *Solid State Ionics* **1992,** *53–56,* 936–946. doi:10.1016/0167-2738(92)90275-t

31. Funke, K. *Prog. Solid State Chem.* **1993,** *22,* 111–195. doi:10.1016/0079-6786(93)90002-9

32. Woutersen, S.; Emmerichs, U.; Bakker, H. J. *Science* **1997,** *278,* 658–660. doi:10.1126/science.278.5338.658

33. Pfeifer, T.; Spielmann, C.; Gerber, G. *Rep. Prog. Phys.* **2006,** *69,* 443–505. doi:10.1088/0034-4885/69/2/r04

34. Cavalieri, A. L.; Müller, N.; Uphues, T.; Yakovlev, V. S.; Baltuška, A.; Horvath, B.; Schmidt, B.; Blümel, L.; Holzwarth, R.; Hendel, S.; Drescher, M.; Kleineberg, U.; Echenique, P. M.; Kienberger, R.; Krausz, F.; Heinzmann, U. *Nature* **2007,** *449,* 1029–1032. doi:10.1038/nature06229

35. Cooke, D. G.; Hegmann, F. A.; Young, E. C.; Tiedje, T. *Appl. Phys. Lett.* **2006,** *89,* 122103. doi:10.1063/1.2349314

36. Takihara, M.; Takahashi, T.; Ujihara, T. *Appl. Phys. Lett.* **2008,** *93,* 021902. doi:10.1063/1.2957468

37. Giessibl, F. J. *Phys. Rev. B* **1997,** *56,* 16010–16015. doi:10.1103/physrevb.56.16010

38. Goldstein, H. *Classical Mechanics;* Pearson Education India, 2011.

39. Crowley, J. M. Simple expressions for force and capacitance for a conductive sphere near a conductive wall. In *Proceedings of the ESA Annual Meeting on Electrostatics 2008.* http://www.electrostatics.org/images/ESA_2008_D1.pdf

40. Dyson, F. *Nature* **2004,** *427,* 297. doi:10.1038/427297a

41. Sader, J. E.; Jarvis, S. P. *Appl. Phys. Lett.* **2004,** *84,* 1801–1803. doi:10.1063/1.1667267

42. Sader, J. E.; Hughes, B. D.; Huber, F.; Giessibl, F. J. *Nat. Nanotechnol.* **2018,** *13,* 1088–1091. doi:10.1038/s41565-018-0277-x

43. Dagdeviren, O. E.; Zhou, C.; Altman, E. I.; Schwarz, U. D. *Phys. Rev. Appl.* **2018,** *9,* 044040. doi:10.1103/physrevapplied.9.044040

44. Hudlet, S.; Saint Jean, M.; Guthmann, C.; Berger, J. *Eur. Phys. J. B* **1998,** *2,* 5–10. doi:10.1007/s100510050219

45. Sader, J. E.; Borgani, R.; Gibson, C. T.; Haviland, D. B.; Higgins, M. J.; Kilpatrick, J. I.; Lu, J.; Mulvaney, P.; Shearer, C. J.; Slattery, A. D.; Thorén, P.-A.; Tran, J.; Zhang, H.; Zhang, H.; Zheng, T. *Rev. Sci. Instrum.* **2016,** *87,* 093711. doi:10.1063/1.4962866

46. Butt, H.-J.; Cappella, B.; Kappl, M. *Surf. Sci. Rep.* **2005,** *59,* 1–152. doi:10.1016/j.surfrep.2005.08.003

47. Colchero, J.; Gil, A.; Baró, A. M. *Phys. Rev. B* **2001,** *64,* 245403. doi:10.1103/physrevb.64.245403

48. Schirmeisen, A.; Cross, G.; Stalder, A.; Grütter, P.; Dürig, U. *New J. Phys.* **2000,** *2,* 29. doi:10.1088/1367-2630/2/1/329

49. Güntherodt, H. J.; Anselmetti, D.; Meyer, E., Eds. *Forces in Scanning Probe Methods;* Nato Science Series E, Vol. 286; Springer Netherlands: Dordrecht, Netherlands, 1995. doi:10.1007/978-94-011-0049-6

50. Cochran, W. G. *Biometrics* **1954,** *10,* 417–451. doi:10.2307/3001616

51. Karatay, D. U.; Harrison, J. S.; Glaz, M. S.; Giridharagopal, R.;
    Ginger, D. S. *Rev. Sci. Instrum.* **2016,** *87,* 053702.
    doi:10.1063/1.4948396
52. Weymouth, A. J.; Giessibl, F. J. The Phantom Force. In *Noncontact*
    Atomic Force Microscopy; Morita, S.; Giessibl, F. J.; Meyer, E.;
    Wiesendanger, R., Eds.; NanoScience and Technology, Vol. 3;
    Springer International Publishing: Cham, Switzerland, 2015; pp 71–92.
    doi:10.1007/978-3-319-15588-3_5
53. Rugar, D.; Mamin, H. J.; Guethner, P. *Appl. Phys. Lett.* **1989,** *55,*
    2588–2590. doi:10.1063/1.101987
54. Kiracofe, D.; Kobayashi, K.; Labuda, A.; Raman, A.; Yamada, H.
    Rev. Sci. Instrum. **2011,** *82,* 013702. doi:10.1063/1.3518965
55. Schumacher, Z.; Miyahara, Y.; Spielhofer, A.; Grutter, P.
    Phys. Rev. Appl. **2016,** *5,* 044018.
    doi:10.1103/physrevapplied.5.044018

License and Terms

Comparing a porphyrin- and a coumarin-based dye adsorbed on NiO(001)

Sara Freund[1], Antoine Hinaut[1], Nathalie Marinakis[2], Edwin C. Constable[2], Ernst Meyer[1], Catherine E. Housecroft[2] and Thilo Glatzel[*1]

Full Research Paper

`Open Access`

Address:
[1]Department of Physics, University of Basel, Klingelbergstrasse 82, 4056 Basel, Switzerland and [2]Department of Chemistry, University of Basel, BPR 1096, Mattenstrasse 24a, 4058 Basel, Switzerland

Email:
Thilo Glatzel[*] - thilo.glatzel@unibas.ch

* Corresponding author

Abstract

Properties of metal oxides, such as optical absorption, can be influenced through the sensitization with molecular species that absorb visible light. Molecular/solid interfaces of this kind are particularly suited for the development and design of emerging hybrid technologies such as dye-sensitized solar cells. A key optimization parameter for such devices is the choice of the compounds in order to control the direction and the intensity of charge transfer across the interface. Here, the deposition of two different molecular dyes, porphyrin and coumarin, as single-layered islands on a NiO(001) single crystal surface have been studied by means of non-contact atomic force microscopy at room temperature. Comparison of both island types reveals different adsorption and packing of each dye, as well as an opposite charge-transfer direction, which has been quantified by Kelvin probe force microscopy measurements.

Introduction

With regard to its use in dye-sensitized solar cells (DSSCs), the wide-bandgap n-type semiconductor TiO_2 has become one of the most extensively studied metal oxides, especially in the context of scanning probe microscopy (SPM) [1]. The working principle of an n-type DSSC, which is shown in Figure 1a, relies on the functionalization of TiO_2 surfaces with dye molecules enabling the absorption of light in the visible region of the sun spectrum. The photons are absorbed by the dye molecules leading to the excitation of an electron from the highest occupied molecular orbital (HOMO) to the lowest unoccupied molecular orbital (LUMO) of the dye and subsequent injection into the conduction band (CB) of the semiconductor [2]. This charge transfer, which occurs from the dye molecules towards the surface of the semiconductor, offers the possibility of designing specific hybrid devices with photoactive anodes consisting of functionalized TiO_2.
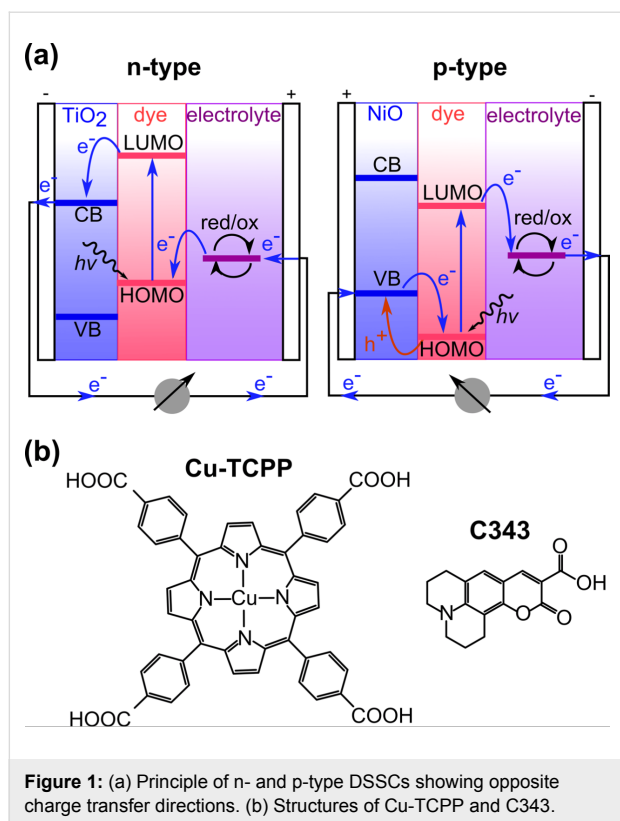
Figure 1: (a) Principle of n- and p-type DSSCs showing opposite charge transfer directions. (b) Structures of Cu-TCPP and C343.

In this paper, non-contact atomic force microscopy (nc-AFM) is used at room temperature (RT) to compare the properties of the two dyes deposited on a NiO(001) single-crystal surface. Under ultrahigh vacuum (UHV) conditions, the adsorption modes of both molecules on the surface of NiO(001) are studied and their charge state upon adsorption are investigated by Kelvin probe force microscopy (KPFM) [25]. This technique is used to observe and quantify the contact potential difference (CPD) changes between the metal oxide surface and the molecular layers and to determine the corresponding dipole moments.

Results and Discussion

Atomically clean NiO surfaces, mandatory for reliable SPM studies, are difficult to prepare because of the hardness of the material and its high reactivity [12-15,26-34]. Figure 2a shows a topographic image measured by nc-AFM of the bare NiO(001) surface that was prepared by in situ cleavage and annealing. The surface shows extended terraces separated by monoatomic steps that are 210 pm in height. Additionally, some line-shaped defects are observed all over the terraces. These defects, thought to be due to segregation of bulk impurities, were not further investigated in the present study and do not influence the reported results.

In contrast to TiO_2 [3-11], wide-bandgap p-type semiconductors, such as NiO, and their functionalization with sensitizers, have been less extensively studied by using SPM [12-15]. NiO was the first reported p-type wide-bandgap semiconductor [16], and can be used for the fabrication of p-type DSSCs with photoactive cathodes, a first step towards the design of tandem solar cells with two photoactive electrodes [17,18]. In p-type DSSCs, the charge transfer is in the opposite direction to that in n-type devices. Holes are injected from the highest occupied molecular orbital (HOMO) of the dye to the valence band (VB) of the semiconductor after photon absorption [17,19,20], resulting in an electron transfer from the surface of the semiconductor towards the dyes (see Figure 1a).

In other terms, the direction of charge transfer relies on the electron affinity of the dyes and on their HOMO and LUMO levels compared to the CB and VB of the semiconductor. Typically, dyes are specifically designed to be compatible with one or the other type of device. Consequently, the careful choice of the dye is crucial for the optimal function of n- or p-type DSSCs. Because of its electron-donor character, copper(II) *meso*-tetrakis(4-carboxyphenyl)porphyrin (Cu-TCPP) has been studied for the fabrication of n-type DSSCs [21,22]. In contrast, Coumarin 343 (C343) is an electron acceptor and is used for the design of p-type devices [23,24]. Both molecules structures are shown in Figure 1b.

Figure 2: The surface of NiO(001). (a) Large-scale topographic image of the NiO(001) crystal showing clean terraces running along the [110] direction of the surface (scan parameters: A_{f_1} = 4 nm, Δf_1 = −9 Hz). (b) Frequency-shift (Δf_1) signal of the same surface at atomic resolution, recorded in the second line scan of the multipass technique with following scan parameters: A_{f_1} = 4 nm, Δf_1 = −42 Hz) and z_{offset} = −700 pm.

Figure 2b shows the frequency-shift signal acquired using the multipass imaging technique [14,15,35,36] clearly showing atomic resolution of the NiO(001) surface. Employing this method, the crystallographic directions of the substrate are

resolved with atomic accuracy, and upon comparing them with the large-scale image, one can deduce that the step edges of NiO(001) as well as the observed defects run along the [110] direction (see violet dotted lines in Figure 2). With this physical image of the atomically resolved structure of the clean NiO(001) surface in mind, the adsorption properties of the Cu-TCPP and the C343 dye molecules were investigated.

Cu-TCPP islands formed on NiO(001)

In a first experiment, Cu-TCPP molecules were deposited at RT on a freshly cleaved NiO(001) surface. Figure 3a shows a large-scale topographic image of the molecules adsorbed on the substrate, where it can be seen that Cu-TCPP exhibits either the tendency to aggregate in small clusters at step edges and defects, or to form large molecular islands (up to 70 nm in width). The fact that the island formation takes place at RT indicates a relatively high diffusion rate of the molecules on NiO(001). The emergence of numerous clusters is related to the presence of various defects on the surface that act as anchoring sites for the dyes.

Concentrating on the islands and measuring their heights (250–300 pm), we can conclude that the molecules are lying flat on the substrate. Interestingly, only two types of islands (type 1 and type 2) were found on the sample surface. In both types, molecular rows are aligned with two distinguishable angles (α and β) with respect to the [010] direction of the substrate (see red and blue dotted lines in Figure 3a–c.

Both molecular alignments are shown in more detail in the close-up topographic images displayed in Figure 3b,c recorded

on type-1 and type-2 islands, respectively. The angles α and β are measured to be $10 \pm 1°$ and $20 \pm 1°$ with respect to the [010] direction, respectively. The lattice parameters were measured and it was observed that a_1, b_1, a_2 and b_2 are similar in the range of 1.5 ± 0.1 nm, while the angles θ_1 and θ_2 of the unit cells clearly differ ($88 \pm 1°$ and $82 \pm 1°$, respectively). The molecular densities of both types are measured to be $D_1 = D_2 = 0.46 \pm 0.02$ nm^{-2}.

Based on these high-resolution images and on the measured mesh parameters, the corresponding models in Figure 3d,e can be established. Knowing that Cu-TCPP has a fourfold symmetrical structure with four equivalent anchoring groups, it is assumed, that Cu-TCPP lies flat and is commensurate with the surface of NiO(001). Considering the partial charge distribution of the surface (Ni is δ^+ and O is δ^-), it is thought that the metallic core of the molecule is likely to be located above an O atom. In addition, it is expected, that the molecules adopt the same adsorption configuration, independent of the island type, triggered by the formation of H-bonds between the carboxylic groups of adjacent molecules. This results in model values for all the parameters that have been calculated and are presented in Table 1. These values are in very good agreement with the experimental results.

C343 islands formed on NiO(001)

In a second experiment, the absorption of C343 on a clean NiO(001) surface was studied. In the large-scale topographic image shown in Figure 4a, it can be seen that C343 also forms molecular islands on the clean terraces of NiO with a typical size of 20–40 nm. The height of the C343 islands (250–300 pm)

Figure 3: (a) Large-scale topographic image showing that Cu-TCPP molecules form islands on the surface of NiO(001) (scan parameters: $A_{f_1} = 7$ nm, $\Delta f_1 = -7$ Hz). (b, c) Close-up topographic images recorded on a type-1 and a type-2 island, respectively (scan parameters: $A_{f_1} = 4$ nm, $\Delta f_1 = -38$ Hz and $A_{f_1} = 7$ nm, $\Delta f_1 = -8$ Hz); (d, e) Models corresponding to (b) and (c).
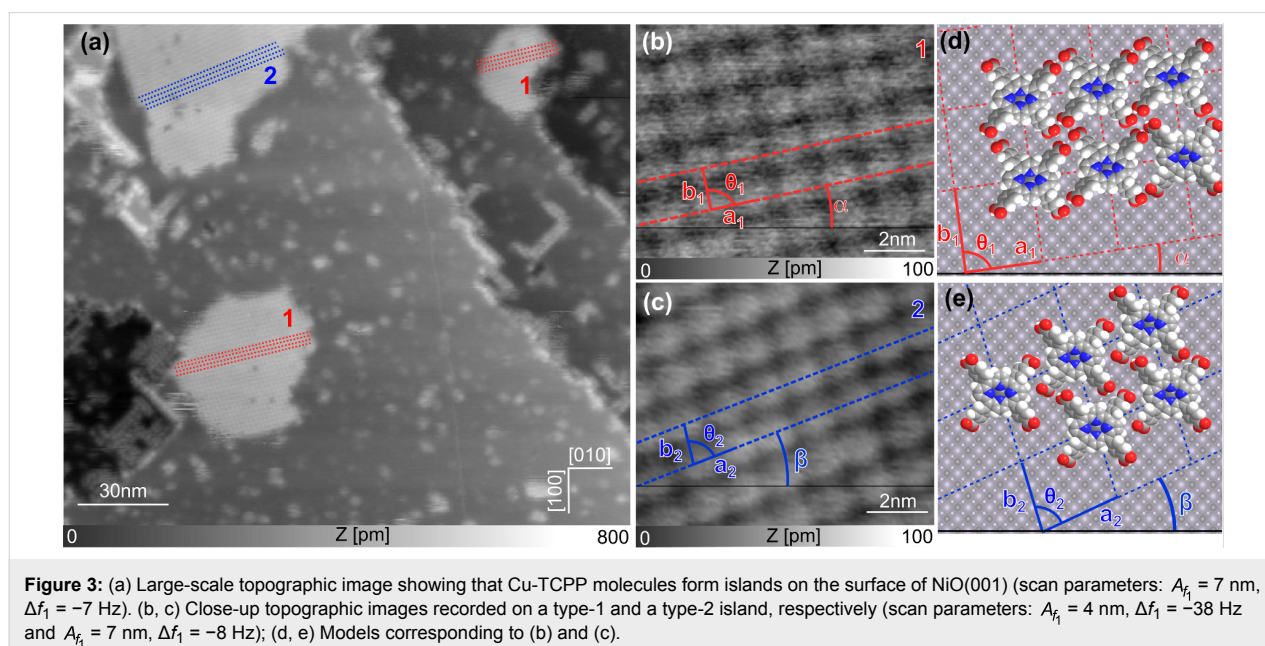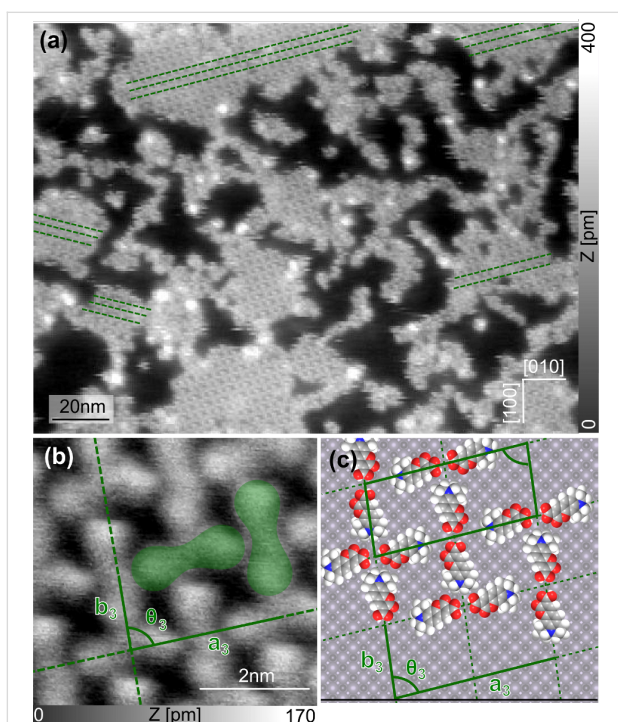
Table 1: Experimental values and model parameters of both types of Cu-TCPP islands.

island type	mesh parameters		molecular density	
	experiment	model	experiment	model
type 1	a_1 = 1.5 ± 0.1 nm	a_1 = 1.47 nm	D_1 = 0.46 ± 0.2 nm^{-2}	D_1 = 0.46 nm^{-2}
	b_1 = 1.5 ± 0.1 nm	b_1 = 1.47 nm		
	θ_1 = 88 ± 1°	θ_1 = 90°		
type 2	a_2 = 1.5 ± 0.1 nm	a_2 = 1.62 nm	D_2 = 0.46 ± 0.2 nm^{-2}	D_2 = 0.48 nm^{-2}
	b_2 = 1.5 ± 0.1 nm	b_2 = 1.32 nm		
	θ_2 = 82 ± 1°	θ_2 = 85.2°		

Figure 4: (a) Large-scale topographic image showing that C343 molecules form islands on the surface of NiO(001). (b) Close-up topographic image taken on top of one of these islands. One unit cell corresponds to four molecules arranged in two different pairs of molecules shown in green. (c) Corresponding model reproducing the mesh motive (scan parameters: A_{f_1} = 7 nm, Δf_1 = −7 Hz).

one angle ±(15 ± 1°) with respect to the [010] direction. More precise information, including the mesh parameters a_3 and b_3 and the angle θ_3 between these vectors can be determined from the close-up high-resolution nc-AFM topographic image shown in Figure 4b. In this image it can be seen (in green) that the mesh motive is composed of two different pairs of dyes, implying that a unit cell is composed of four molecules. The first pair of molecules has the molecular axis aligned along vector a_3, whereas the second pair is oriented along b_3 and an angle θ_3 of 86 ± 1° is measured between these vectors. The lattice parameters a_3 and b_3 lie in the range of 3.5 ± 0.1 nm and 1.5 ± 0.1 nm, respectively and the molecular density is measured to be D_3 = 0.74 ± 0.2 nm^{-2}.

The model depicted in Figure 4c reproduces the mesh motive observed in the topographic image. It can clearly be seen that the pairs are composed of two molecules facing each other, stabilized via H-bonds between the carboxylic acid groups. This model delivers values for the mesh parameters that are compared to the experimental results in Table 2. The data demonstrate that the parameters correspond nicely, highlighting the accuracy of the model.

Charge-transfer direction studied by KPFM

KPFM is an analytical method that can be applied to examine the change of the work function induced by the adsorption of organometallic complexes on surfaces at the nanoscale. Using this method, the CPD between the surface of NiO and the different molecular islands was measured. Depending on the tip, it has been observed, that the absolute CPD values recorded on

is comparable to the height of Cu-TCPP islands suggesting, again, flat lying adsorbed dye molecules. In contrast to the Cu-TCPP islands, the molecular rows are aligned only along

Table 2: Experimental and model parameters, respectively measured and calculated on C343 islands.

mesh parameters		molecular density	
experiment	model	experiment	model
a_3 = 3.5 ± 0.1 nm	a_3 = 3.44 nm	D_3 = 0.74 ± 0.2 nm^{-2}	D_3 = 0.79 nm^{-2}
b_3 = 1.5 ± 0.1 nm	b_3 = 1.47 nm		
θ_3 = 86 ± 1°	θ_3 = 84.1°		

NiO can vary by roughly ±100 mV. Therefore, in order to facilitate the comparison between Cu-TCPP and C343, the CPD of NiO was set as reference (0 V) and all CPD values given below are relative values. The values of the CPD between the surface and the molecular islands measured by using KPFM [25] are given in Figure 5a and Figure 5b. These large-scale KPFM images were acquired simultaneously with the topographic images presented in Figure 3a and Figure 4a, respectively.

In Figure 5a, as well as in the profile recorded along the red line present in this image and displayed in Figure 5c, it can be seen that the CPD, and hence the work function, is decreased above the islands in comparison to the surface of NiO. This effect can be related to a more positively charged island compared to the substrate. This is attributed to the creation of a surface dipole moment p (see Figure 5c). In the present case, the positive end of the dipole moment is pointing towards the molecular layer. Consequently, this results in an electron transfer from the molecules to the surface of NiO, which is expected for a dye such as Cu-TCPP originally designed for an n-type semiconductor. The value of the dipole moment as well as the partial charge transfer can be calculated from the measured CPD values [37,38] (see Supporting Information File 1). On type-1 and type-2 islands, the average CPD difference between the molecular layer and the surface is $\Delta V_{CPD} = -400 \pm 50$ mV. Considering a flat-lying adsorption geometry of the molecules and knowing that the molecular densities of both types of islands are in the same range, this is attributed to an average dipole moment of −2.2 D/mole-

cule independent of the island type. This, in turn, corresponds to a partial charge transfer of $+0.35e^-$/molecule. Calculated as a function of the active area, this corresponds to a value $+0.16e^-$/nm^2.

The adsorption KPFM measurement of C343, which is designed to be implemented in a p-type device, is shown in Figure 5b. In this image it can be seen that, at a large scale, the CPD contrast is slightly modulated. This is attributed to variations of surface charges resulting from the cleavage process. To get a clear and unambiguous CPD contrast one has to focus on smaller areas where long-range charge variations do not interfere with the determination of the relative CPD between NiO and molecular islands (see Supporting Information File 1). Nevertheless, Figure 5b, as well as the profile recorded along the green line and displayed in Figure 5d, show that the CPD, and therefore also the work function, is locally increased above the molecular layer compared to the surface of NiO. Thus, in contrast to Cu-TCPP, the electron transfer occurs from the substrate towards the molecules (see schematic in Figure 5d). The average CPD change between the islands and the surface is measured to be $\Delta V_{CPD} = +150 \pm 30$ mV. Based on a flat-lying adsorption geometry of the molecules, an average dipole moment of $+0.5$ D/molecule is calculated. This corresponds to a partial charge transfer of $-0.08e^-$/molecule occurring in the opposite direction to Cu-TCPP, and that C343 is compatible with application in a p-type device. Furthermore, this also implies that, in terms of charge transfer, C343 is about four times less efficient than Cu-TCPP. However, because C343 has

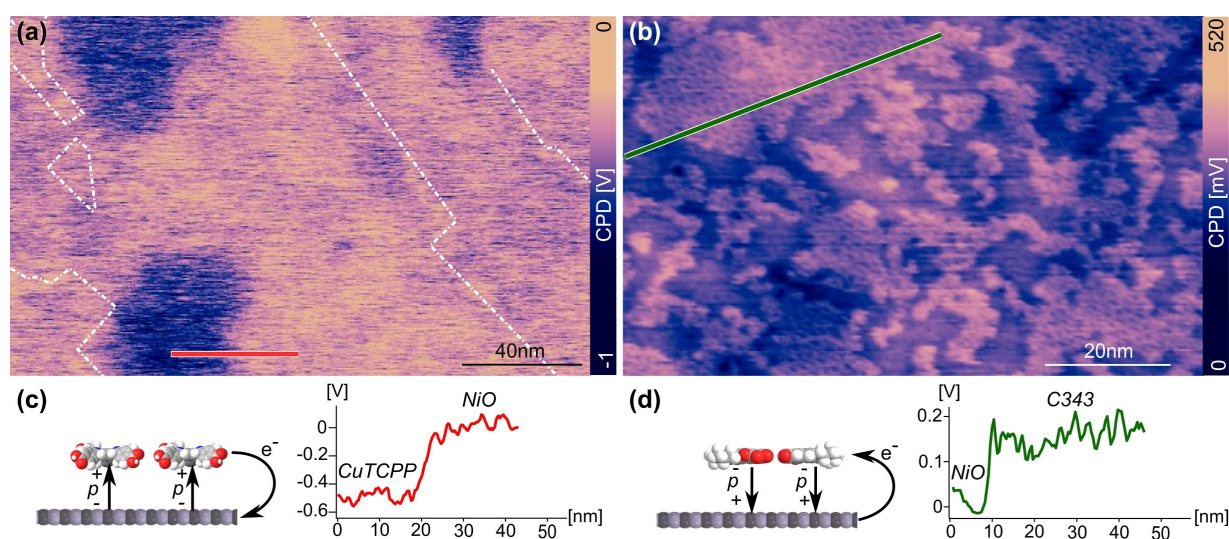**Figure 5:** (a, b) CPD measurements of Cu-TCCP and C343 islands on the NiO(001) substrate, respectively (scan parameters: A_{f_1} = 7 nm; Δf_1 = −7 Hz, V_{ac} = 800 mV, and f_{ac} = 1 kHz or f_{ac} = 250 Hz, respectively). (c, d) Profiles recorded in (a) and (b), respectively, and models highlighting the direction of the dipole moment p and the corresponding charge transfer.

Table 3: Comparison between Cu-TCPP and C343 adsorbed on NiO(001).

molecules	ΔV_{CPD}	dipole moment	partial charge transfer	
		molecule^{-1}	molecule^{-1}	nm^{-2}
Cu-TCPP	−400 ± 50 mV	−2.2 D	+0.35e^-	+0.16e^-
C343	+150 ± 30 mV	+0.5 D	−0.08e^-	−0.06e^-

a larger molecular density than Cu-TCCP, the charge transfer intensity appears to be roughly equal to $-0.06e^-/\text{nm}^2$ when calculated as a function of active area instead of single molecules. Consequently, if we think about building a DSSC device, this implies that C343 will result in active electrodes that would be 2.5-times less efficient in terms of charge injection compared to Cu-TCPP.

To summarize the results, a comparison of Cu-TCPP and C343 is given in Table 3.

Conclusion

The adsorption of Cu-TCPP molecules on the surface of NiO(001) was investigated by nc-AFM and compared to that of C343 molecules. Using high-resolution topographic measurements, it was shown that both molecules lie flat on the surface and form islands. Different types of islands, where molecules are aligned with different angles with respect to the crystallographic directions of the surface, are observed. Using these topographic measurements as well as appropriate models reproducing accurately the mesh motives, the molecular densities from both molecules could be estimated. By combining these results with KPFM measurements, the average dipole moment of both molecular assemblies were determined. Comparing the two molecules adsorbed on NiO, their charge transfer directions are found to be opposite: Cu-TCPP is observed to be an electron acceptor whereas C343 is an electron donor, meaning that the latter is effectively more suitable for the design of p-type DSSCs. However, it has also been shown that, active areas composed of Cu-TCPP molecules are about 2.5-times more efficient in terms of charge transfer compared to C343 domains ($+0.16e^-/\text{nm}^2$ vs $-0.06e^-/\text{nm}^2$).

Experimental
Sample preparation
The NiO(001) crystals used in this study were purchased from SurfaceNet. They consist of a rectangular rod with dimensions $2 \times 2 \times 7$ mm^3 and a long axis in the [001] direction. The NiO(001) surface was prepared by in situ cleavage with prior and subsequent annealing (at 600 °C and 500 °C, respectively) resulting in an atomically clean surface. Molecules were then thermally evaporated, from commercially avail-

able molecular powders, at RT and under UHV conditions ($p < 1 \times 10^{-10}$ mbar) on the clean surface of NiO. Different deposition parameters were used for Cu-TPP and C343. **Cu-TCPP:** $T_{evaporation} = 315$ °C, $t_{deposition} = 5$ min and a rate of 0.5 Å/min; **C343:** $T_{evaporation} = 150$ °C $t_{deposition} = 5$ min and a rate of 0.5 Å/min. After C343 deposition, the sample was annealed for 30 min at 80 °C.

Scanning probe microscopy
All measurements were carried out in dark using a custom-built atomic force microscope operating under UHV at RT. All AFM images were recorded in the non-contact mode, using silicon cantilevers (Nanosensors PPP-NCL, stiffness $k = 20$–30 N/m, resonance frequency $f_1 \approx 165$ kHz, quality factor $Q_{f1} \approx 30000$) with compensated contact potential difference. Kelvin probe force microscopy was performed in frequency-modulation mode using a voltage modulation applied together with the dc compensation voltage to the sample ($V_{ac} = 800$ mV and $f_{ac} = 1$ kHz or 250 Hz).

Supporting Information

The Supporting Information discusses the determination method of the average CPD difference and shows that the CPD can be determined locally when C343 is adsorbed on NiO.

Supporting Information File 1
Additional experimental data.
[https://www.beilstein-journals.org/bjnano/content/supplementary/2190-4286-10-88-S1.pdf]

ORCID® iDs
Sara Freund - https://orcid.org/0000-0003-2053-2568
Antoine Hinaut - https://orcid.org/0000-0002-2608-2564
Nathalie Marinakis - https://orcid.org/0000-0003-3978-5178

Edwin C. Constable - https://orcid.org/0000-0003-4916-4041
Ernst Meyer - https://orcid.org/0000-0001-6385-3412
Catherine E. Housecroft - https://orcid.org/0000-0002-8074-0089
Thilo Glatzel - https://orcid.org/0000-0002-3533-4217

References

1. Diebold, U. *Surf. Sci. Rep.* **2003,** *48,* 53–229.
   doi:10.1016/s0167-5729(02)00100-0
2. O'Regan, B.; Grätzel, M. *Nature* **1991,** *353,* 737–740.
   doi:10.1038/353737a0
3. Matthey, D.; Wang, J. G.; Wendt, S.; Matthiesen, J.; Schaub, R.;
   Laegsgaard, E.; Hammer, B.; Besenbacher, F. *Science* **2007,** *315,*
   1692–1696. doi:10.1126/science.1135752
4. Ikeda, M.; Koide, N.; Han, L.; Sasahara, A.; Onishi, H. *Langmuir* **2008,**
   24, 8056–8060. doi:10.1021/la8010019
5. Schütte, J.; Bechstein, R.; Rahe, P.; Rohlfing, M.; Kühnle, A.;
   Langhals, H. *Phys. Rev. B* **2009,** *79,* 045428.
   doi:10.1103/physrevb.79.045428
6. Setvin, M.; Buchholz, M.; Hou, W.; Zhang, C.; Stöger, B.; Hulva, J.;
   Simschitz, T.; Shi, X.; Pavelec, J.; Parkinson, G. S.; Xu, M.; Wang, Y.;
   Schmid, M.; Wöll, C.; Selloni, A.; Diebold, U. *J. Phys. Chem. C* **2015,**
   119, 21044–21052. doi:10.1021/acs.jpcc.5b07999
7. Jöhr, R.; Hinaut, A.; Pawlak, R.; Sadeghi, A.; Saha, S.; Goedecker, S.;
   Such, B.; Szymonski, M.; Meyer, E.; Glatzel, T. *J. Chem. Phys.* **2015,**
   143, 094202. doi:10.1063/1.4929608
8. Zajac, L.; Olszowski, P.; Godlewski, S.; Bodek, L.; Such, B.; Jöhr, R.;
   Pawlak, R.; Hinaut, A.; Glatzel, T.; Meyer, E.; Szymonski, M.
   Appl. Surf. Sci. **2016,** *379,* 277–281. doi:10.1016/j.apsusc.2016.04.069
9. Prauzner-Bechcicki, J. S.; Zajac, L.; Olszowski, P.; Jöhr, R.; Hinaut, A.;
   Glatzel, T.; Such, B.; Meyer, E.; Szymonski, M.
   Beilstein J. Nanotechnol. **2016,** *7,* 1642–1653.
   doi:10.3762/bjnano.7.156
10. Pawlak, R.; Sadeghi, A.; Jöhr, R.; Hinaut, A.; Meier, T.; Kawai, S.;
    Zajac, Ł.; Olszowski, P.; Godlewski, S.; Such, B.; Glatzel, T.;
    Goedecker, S.; Szymoński, M.; Meyer, E. *J. Phys. Chem. C* **2017,** *121,*
    3607–3614. doi:10.1021/acs.jpcc.6b11873
11. Jöhr, R.; Hinaut, A.; Pawlak, R.; Zajac, Ł.; Olszowski, P.; Such, B.;
    Glatzel, T.; Zhang, J.; Muntwiler, M.; Bergkamp, J. J.; Mateo, L.-M.;
    Decurtins, S.; Liu, S.-X.; Meyer, E. *J. Chem. Phys.* **2017,** *146,* 184704.
    doi:10.1063/1.4982936
12. Schwarz, A.; Gao, D. Z.; Lämmle, K.; Grenz, J.; Watkins, M. B.;
    Shluger, A. L.; Wiesendanger, R. *J. Phys. Chem. C* **2013,** *117,*
    1105–1112. doi:10.1021/jp311702j
13. Gao, D. Z.; Grenz, J.; Watkins, M. B.; Federici Canova, F.;
    Schwarz, A.; Wiesendanger, R.; Shluger, A. L. *ACS Nano* **2014,** *8,*
    5339–5351. doi:10.1021/nn501785q
14. Freund, S.; Hinaut, A.; Marinakis, N.; Constable, E. C.; Meyer, E.;
    Housecroft, C. E.; Glatzel, T. *Beilstein J. Nanotechnol.* **2018,** *9,*
    242–249. doi:10.3762/bjnano.9.26
15. Freund, S.; Pawlak, R.; Moser, L.; Hinaut, A.; Steiner, R.; Marinakis, N.;
    Constable, E. C.; Meyer, E.; Housecroft, C. E.; Glatzel, T. *ACS Omega*
    2018, *3,* 12851–12856. doi:10.1021/acsomega.8b01792
16. Sato, H.; Minami, T.; Takata, S.; Yamada, T. *Thin Solid Films* **1993,**
    236, 27–31. doi:10.1016/0040-6090(93)90636-4
17. He, J.; Lindström, H.; Hagfeldt, A.; Lindquist, S.-E. *J. Phys. Chem. B*
    1999, *103,* 8940–8943. doi:10.1021/jp991681r
18. Nattestad, A.; Mozer, A. J.; Fischer, M. K. R.; Cheng, Y.-B.; Mishra, A.;
    Bäuerle, P.; Bach, U. *Nat. Mater.* **2010,** *9,* 31–35.
    doi:10.1038/nmat2588
19. Odobel, F.; Pellegrin, Y.; Gibson, E. A.; Hagfeldt, A.; Smeigh, A. L.;
    Hammarström, L. *Coord. Chem. Rev.* **2012,** *256,* 2414–2423.
    doi:10.1016/j.ccr.2012.04.017
20. Wood, C. J.; Summers, G. H.; Clark, C. A.; Kaeffer, N.; Braeutigam, M.;
    Carbone, L. R.; D'Amario, L.; Fan, K.; Farré, Y.; Narbey, S.;
    Oswald, F.; Stevens, L. A.; Parmenter, C. D. J.; Fay, M. W.;
    La Torre, A.; Snape, C. E.; Dietzek, B.; Dini, D.; Hammarström, L.;
    Pellegrin, Y.; Odobel, F.; Sun, L.; Artero, V.; Gibson, E. A.
    Phys. Chem. Chem. Phys. **2016,** *18,* 10727–10738.
    doi:10.1039/c5cp05326a
21. Rochford, J.; Chu, D.; Hagfeldt, A.; Galoppini, E. *J. Am. Chem. Soc.*
    2007, *129,* 4655–4665. doi:10.1021/ja068218u
22. Imahori, H.; Kang, S.; Hayashi, H.; Haruta, M.; Kurata, H.; Isoda, S.;
    Canton, S. E.; Infahsaeng, Y.; Kathiravan, A.; Pascher, T.;
    Chábera, P.; Yartsev, A. P.; Sundström, V. *J. Phys. Chem. A* **2011,**
    115, 3679–3690. doi:10.1021/jp103747t
23. Morandeira, A.; Boschloo, G.; Hagfeldt, A.; Hammarström, L.
    J. Phys. Chem. B **2005,** *109,* 19403–19410. doi:10.1021/jp053230e
24. Morandeira, A.; Boschloo, G.; Hagfeldt, A.; Hammarström, L.
    J. Phys. Chem. C **2008,** *112,* 9530–9537. doi:10.1021/jp800760q
25. Sadewasser, S.; Glatzel, T., Eds. *Kelvin Probe Force Microscopy:*
    Measuring and Compensating Electrostatic Forces; Springer Series in
    Surface Sciences, Vol. 48; Springer Berlin: Berlin, Germany, 2012.
    doi:10.1007/978-3-642-22566-6
26. Castell, M. R.; Wincott, P. L.; Condon, N. G.; Muggelberg, C.;
    Thornton, G.; Dudarev, S. L.; Sutton, A. P.; Briggs, G. A. D.
    Phys. Rev. B **1997,** *55,* 7859–7863. doi:10.1103/physrevb.55.7859
27. Hosoi, H.; Sueoka, K.; Hayakawa, K.; Mukasa, K. *Appl. Surf. Sci.* **2000,**
    157, 218–221. doi:10.1016/s0169-4332(99)00529-2
28. Hosoi, H.; Kimura, M.; Hayakawa, K.; Sueoka, K.; Mukasa, K.
    Appl. Phys. A: Mater. Sci. Process. **2001,** *72* (Suppl. 1), S23–S26.
    doi:10.1007/s003390100722
29. Allers, W.; Langkat, S.; Wiesendanger, R.
    Appl. Phys. A: Mater. Sci. Process. **2001,** *72* (Suppl. 1), S27–S30.
    doi:10.1007/s003390100731
30. Langkat, S. M.; Hölscher, H.; Schwarz, A.; Wiesendanger, R. *Surf. Sci.*
    2003, *527,* 12–20. doi:10.1016/s0039-6028(03)00076-1
31. Hosoi, H.; Sueoka, K.; Mukasa, K. *Nanotechnology* **2004,** *15,* 505–509.
    doi:10.1088/0957-4484/15/5/018
32. Kaiser, U.; Schwarz, A.; Wiesendanger, R. *Nature* **2007,** *446,* 522–525.
    doi:10.1038/nature05617
33. Schmid, M.; Mannhart, J.; Giessibl, F. J. *Phys. Rev. B* **2008,** *77,*
    045402. doi:10.1103/physrevb.77.045402
34. Pielmeier, F.; Giessibl, F. J. *Phys. Rev. Lett.* **2013,** *110,* 266101.
    doi:10.1103/physrevlett.110.266101
35. Moreno, C.; Stetsovych, O.; Shimizu, T. K.; Custance, O. *Nano Lett.*
    2015, *15,* 2257–2262. doi:10.1021/nl504182w
36. Müller, V.; Hinaut, A.; Moradi, M.; Baljozovic, M.; Jung, T. A.;
    Shahgaldian, P.; Möhwald, H.; Hofer, G.; Kröger, M.; King, B. T.;
    Meyer, E.; Glatzel, T.; Schlüter, A. D. *Angew. Chem.* **2018,** *130,*
    10744–10748. doi:10.1002/ange.201804937
37. Milde, P.; Zerweck, U.; Eng, L. M.; Abel, M.; Giovanelli, L.; Nony, L.;
    Mossoyan, M.; Porte, L.; Loppacher, C. *Nanotechnology* **2008,** *19,*
    305501. doi:10.1088/0957-4484/19/30/305501
38. Glatzel, T.; Zimmerli, L.; Koch, S.; Kawai, S.; Meyer, E.
    Appl. Phys. Lett. **2009,** *94,* 063303. doi:10.1063/1.3080614

Influence of dielectric layer thickness and roughness on topographic effects in magnetic force microscopy

Alexander Krivcov[1], Jasmin Ehrler[1], Marc Fuhrmann[1], Tanja Junkers[2,3] and Hildegard Möbius[*1]

Abstract

Magnetic force microscopy (MFM) has become a widely used tool for the characterization of magnetic properties. However, the magnetic signal can be overlapped by additional forces acting on the tip such as electrostatic forces. In this work the possibility to reduce capacitive coupling effects between tip and substrate is discussed in relation to the thickness of a dielectric layer introduced in the system. Single superparamagnetic iron oxide nanoparticles (SPIONs) are used as a model system, because their magnetic signal is contrariwise to the signal due to capacitive coupling so that it is possible to distinguish between magnetic and electric force contributions. Introducing a dielectric layer between substrate and nanoparticle the capacitive coupling can be tuned and minimized for thick layers. Using the theory of capacitive coupling and the magnetic point dipole–dipole model we could theoretically explain and experimentally prove the phase signal for single superparamagnetic nanoparticles as a function of the layer thickness of the dielectric layer. Tuning the capacitive coupling by variation of the dielectric layer thickness between nanoparticle and substrate allows the distinction between the electric and the magnetic contributions to the MFM signal. The theory also predicts decreasing topographic effects in MFM signals due to surface roughness of dielectric films with increasing film thickness.

Introduction

MFM has become an important tool for studying magnetic properties of surface structures with submicrometer resolution [1-8]. Although the MFM signals in the so-called interleave mode are taken at a certain distance (lift height) from the sam-

ple, following the topography of the sample measured in a first scan, a total force is measured with unknown contributions from different forces. Therefore, the quantitative analysis of magnetic properties is still an issue especially because of contributions

from electrostatic forces leading to topographic features in the MFM phase images [7,9-14]. Yu et al. [9] explained the topographic artifacts by electrostatic interactions. Origin of these artifacts is the work-function difference between tip and sample material. Yu et al. [10] demonstrated that topographic features can be avoided by combining MFM with electrostatic force microscopy (EFM) compensating the contact potential difference by an appropriate tip bias. Kim et al. [11] used a capacitive coupling of electrostatic force modulation to separate the magnetic from the topographic signal. In our previous paper [14], we demonstrated that Kelvin force probe microscopy (KPFM) measurements as proposed by Jaafar et al. [13] show no difference between measurements above SPIONs and measurements above the substrate. The combination of KPFM and MFM can only eliminate the electrostatic contributions for structures larger than the tip size [13]. Measuring structures with dimensions similar or smaller than the tip size KPFM does not reduce the capacitive coupling effect. During the imaging of nanoparticles a mirroring of the topography is often observed in MFM phase images [15-18]. Neves et al. [15] distinguished between magnetic and nonmagnetic nanoparticles by applying an external bias to the tip minimizing the topographical influence of the sample. Without an external tip bias a positive phase shift in the MFM image was reported for the nonmagnetic nanoparticles. Passeri et al. [19] also observed a positive phase shift for nonmagnetic niosomes in the MFM phase image. Angeloni et al. [16] discussed the topography-induced positive phase shift for small SPIONs aggregates by capacitive coupling effects. In order to distinguish electrostatic and magnetic forces Angeloni et al. [18] employed a controlled change of the tip magnetization. They demonstrated this new method by measuring superparamagnetic nanoparticles but also discussed current limitations of this technique such as artifacts in the magnetic image due to instrumental parameters as well as incomplete demagnetization of the probe. In our previous work, we theoretically explained and experimentally proved that the positive phase shift above nanoparticles derives from capacitive coupling between tip and substrate [14]. The increase of the tip–substrate distance in the interleave mode above the nanoparticle leads to a reduction of the electrostatic forces resulting in a positive phase shift. Furthermore methods to reduce the capacitive coupling were discussed, e.g., measurements on substrates with a minimized work-function difference between tip and substrate or the usage of a tip with smaller radius. In [20] we demonstrated that capacitive coupling effects vanish investigating nanoparticles embedded in a polymer matrix.

In this work we show that capacitive coupling effects can be reduced by using a dielectric layer between substrate and nanoparticles. Magnetic nanoparticles in the superparamagnetic state are used in this work in order to distinguish between electro-static and magnetic signal. The magnetic vector of the superparamagnetic nanoparticle is aligned along the field of the probe resulting in an attractive force. In contrast, the electrostatic force due to topography changes is a repulsive force.

Simulations as well as experiments show that an increase of the dielectric layer thickness between nanoparticle and substrate leads to a decrease of the capacitive coupling.

The theoretical model described in this paper also predicts decreasing topographic effects in MFM signals due to surface roughness of dielectric films with increasing film thickness.

Theory
Capacitive coupling effects in MFM on nanoparticles

In our previous work we proposed a theory of a capacitive coupling between tip and substrate explaining the mirroring of the topography in MFM phase images, and thus a positive phase shift, when measuring nanoparticles [14]. While measuring in interleave mode the distance z between the probe and the substrate increases above the nanoparticles ($z + d$, with d nanoparticle diameter) resulting in a positive phase shift:

$$\Delta\varphi_{el} = -\frac{Q}{k}\varepsilon_0\left[\frac{A}{(z+d)^3}\left(V_{CPD}\right)^2 - \frac{A}{z^3}\left(V_{CPD}\right)^2\right], \quad (1)$$

with A being the effective capacitive area, z the lift height, d the nanoparticle diameter, V_{CPD} the contact potential difference between tip and substrate, Q the quality factor, k the spring constant of the cantilever, and ε_0 the dielectric constant of vacuum. The effective area of the capacitor is calculated taking the curvature of the tip into account [14]. $\Delta\varphi_{el}$ represents the difference in phase shift above and beside the nanoparticle. As the effective interaction area of the tip and the single nanoparticle is less than 2% of the interaction area between tip and substrate the contribution of the capacitance between tip and SPION and the self-capacitance of the SPION can be neglected [14]. The capacitive coupling significantly increases the phase shift for small lift heights as shown in Figure 1.

The capacitive coupling is decreasing with increasing lift height (Figure 1). However, in order to measure the magnetic signal of single SPIONs, the distance between nanoparticle and tip has to be in the range of 10 to 30 nm in order to get a magnetic interaction above the detection limit [14]. At this range the attractive magnetic interactions of SPIONs are often hidden by repulsive electrostatic interactions due to the changes in capacitive coupling. In [14] possibilities are discussed to minimize the

Figure 1: Phase shift as a function of the tip–substrate distance z; calculated for a silicon substrate with V_{CPD} = 0.35 V, a tip radius of 84 nm and a nanoparticle diameter of 10 nm on a flat substrate.
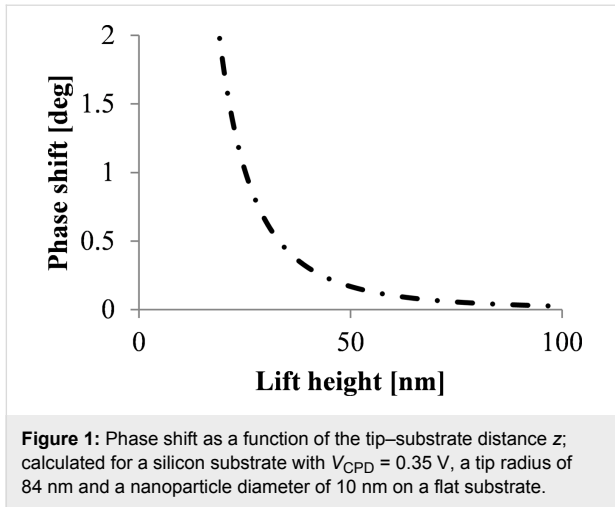
capacitive coupling, e.g., by using a substrate with minimized work-function difference between tip and substrate or by using a sharper tip.

Another possibility to minimize the capacitive coupling is the use of a dielectric layer between substrate and nanoparticle, as shown in Figure 2. This results in a reduction of capacitive coupling due to the larger distance between tip and substrate even for small lift heights above the nanoparticles assuring a strong magnetic interaction between nanoparticle and tip.

Figure 2: Substrate without dielectric layer and with dielectric layer. The dielectric layer allows the tip to get closer to the nanoparticle without disturbing capacitive coupling due to interaction of tip and substrate.
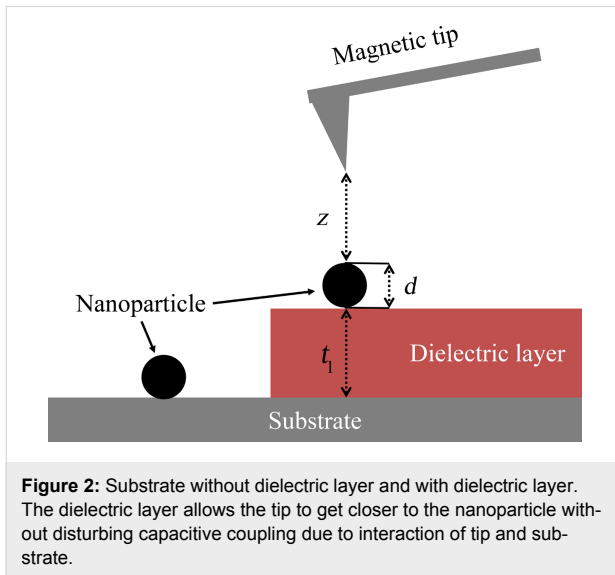
Taking into account a dielectric layer the formula for capacitive coupling can be modified as follows:

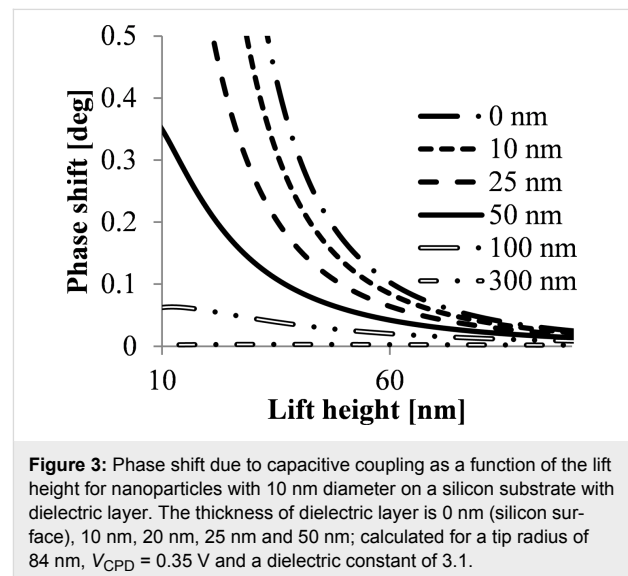$$\Delta\varphi_{el} = -\frac{Q}{k}\varepsilon_0 \left[\frac{A}{\left(z+d+t_{eff}\right)^3}\left(V_{CPD}\right)^2 - \frac{A}{\left(z+t_{eff}\right)^3}\left(V_{CPD}\right)^2 \right] \cdot \quad (2)$$

The effective film thickness t_{eff} of the dielectric layer is included in the distance between tip and substrate to calculate the capacitive coupling of the tip with the substrate beneath the dielectric layer. The effective thickness is calculated as follows:

$$t_{eff} = \frac{t_l}{\varepsilon_r}. \quad (3)$$

ε_R represents the dielectric constant and t_l the real film thickness of the dielectric layer. The dielectric constant for the layer used in this work is 3.1 [21].

Figure 3 compares the phase shift due to capacitive coupling of a nanoparticle lying on a flat substrate with the phase shift for a nanoparticle lying on dielectric layers with different layer thicknesses. All simulations were carried out assuming the absence of trapped charges on the dielectric layer.

Figure 3: Phase shift due to capacitive coupling as a function of the lift height for nanoparticles with 10 nm diameter on a silicon substrate with dielectric layer. The thickness of dielectric layer is 0 nm (silicon surface), 10 nm, 20 nm, 25 nm and 50 nm; calculated for a tip radius of 84 nm, V_{CPD} = 0.35 V and a dielectric constant of 3.1.

Introducing a dielectric layer in the system the capacitive coupling effect is significantly reduced for lift heights below 40 nm. It can therefore be concluded that dielectric layer thicknesses larger than 100 nm allow the detection of weak magnetic signals with reduced overlaying electrostatic effects.

Capacitive coupling effects in MFM on rough surfaces

The considerations about capacitive coupling effects on nanoparticles can be generalized assuming rough surfaces depicted in Figure 4a.

The distance changes between tip and substrate in the interleave mode due to the surface roughness (measured in the first scan) also lead to capacitive coupling effects and positive phase
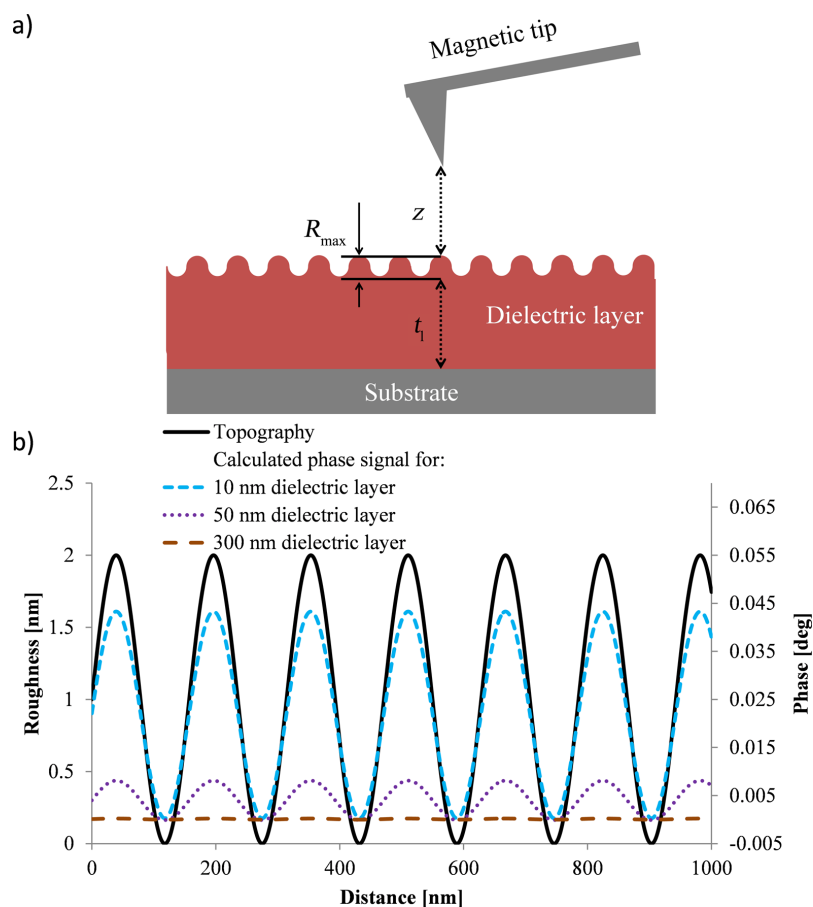
Figure 4: a) Sketch of a MFM measurement of a dielectric layer with defined roughness (R_{max}); b) Simulation for rough surfaces using a sine wave depicting the roughness and assuming a peak to peak distance, R_{max} in Figure 4a, of 2 nm; calculated for a silicon substrate with V_{CPD} of 0.35 V, tip radius of 84 nm, 20 nm lift height and dielectric constant of the dielectric layer of 3.1.

shifts in the MFM image as shown in Figure 4b. For dielectric layer with a thickness on the silicon substrate in the range of 10 nm the capacitive coupling due to the roughness leads to topographical mirroring in the MFM signal whereas the roughness of layers of several 100 nm thickness has no influence on the MFM phase signal. Although the idealized calculations neglect trapped charges on the dielectric layer the simulations reveal a significant reduction of capacitive coupling using a dielectric layer.

Magnetic forces between tip and SPION

Single SPIONs are chosen as a model system to investigate the superposition of magnetic and electrostatic contributions in the MFM phase shift. Theoretical estimates based on vibrating sample magnetometer (VSM) measurements (Figure S2, Supporting Information File 1) reveal that the magnetic field of the probe with a magnetic moment of $3 \cdot 10^{-16}$ A·m^2 is sufficient to induce a magnetic moment at lift heights up to 150 nm in superparamagnetic nanoparticles with 10 nm diameter. This results in attractive forces and, thus, negative phase shifts in MFM mea-

surements. Therefore the magnetic signal is contrariwise to the signal of capacitive coupling described above.

The magnetic point dipole–dipole approximation is used to calculate the magnetic force gradient acting on the tip due to the interaction between a spherical superparamagnetic nanoparticle and the tip, approximated by a uniform magnetized sphere [20,22,23]:

$$\Delta\varphi_{mag} = -\frac{Q}{k}\frac{\partial F}{\partial z} = -\frac{Q}{k}\frac{6\mu_0 m_p m_{tip}}{\pi(a)^5}, \qquad (4)$$

where Q is the quality factor of the cantilever, k is the spring constant, μ_0 is the vacuum permeability, m_p is the magnetic moment of the nanoparticle, m_{tip} is the magnetic moment of the tip, and a is the distance between the two dipoles and is shown schematically in Figure 5. The position of the tip dipole is assumed to be at the half radius of the tip [17].
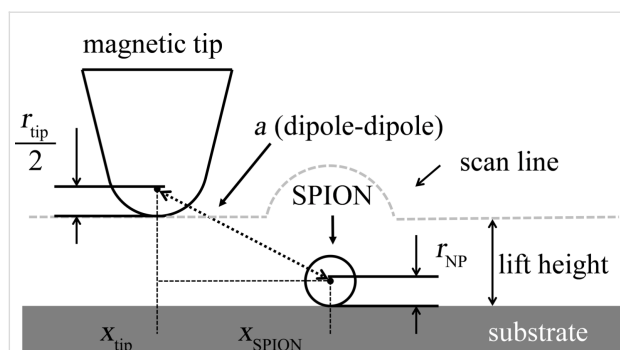
Figure 5: Schematic representation of the distance between tip and nanoparticle dipole during the interleave measurements.

Cross section simulation of MFM phase

The first scan of MFM measurements provides a topographic image displaying a convolution of the tip and the nanoparticle [24]. The topographic cross section is simulated by using a Gaussian profile at the position of the nanoparticle (black line in Figure 6). The width of the Gaussian profile is much broader than the width of the nanoparticle (assumed to be 12 nm) because of the convolution with the tip with a radius of 84 nm. Both magnetic and electric forces for a single SPION can be calculated as a function of the horizontal position of the tip corresponding to a cross section of the MFM image. The vertical distance changes in the second scan (interleave scan with a certain lift height following the topography of the first scan) lead to a positive phase shift due to capacitive coupling and can be calculated by Equation 1 for each horizontal position of the tip. In order to determine the negative phase shift due to the magnetic interaction between tip and nanoparticle according to Equation 4, the distance *a* between the point dipole representing the tip and the point dipole representing the nanoparticle can be calculated for each horizontal position of the tip as follows:

$$a = \sqrt{\left[\left(h + z + \frac{r_{\text{tip}}}{2}\right) - r_{\text{SPION}}\right]^2 + \left(x_{\text{tip}} - x_{\text{SPION}}\right)^2}, \quad (5)$$

where *a* is the distance between the dipoles, *h* is the height of the topography and *z* is the lift height. Figure 6 shows a simulation of both forces, capacitive (dotted purple line in Figure 6) and magnetic (dashed light blue line in Figure 6), for a single nanoparticle with 12 nm diameter on a silicon substrate. The dashed-dotted dark blue line presents the overall signal comprising electrostatic and magnetic interaction.

Electrostatic forces are stronger than the magnetic forces resulting in a positive phase shift above the nanoparticle. However, weak attractions are expected in a ring around the nanoparticles because the magnetic signal is broader than the topographical signal (the half width of the magnetic signal is ca. 100 nm and that of the electric signal is ca. 60 nm in this simulation).

When a dielectric layer is introduced the capacitive coupling can be reduced so that the overall phase signal becomes negative. Thus, tuning the phase shift due to capacitive coupling by introducing a dielectric layer suppresses the electrostatic interaction and allows the visualization of magnetic contributions to the MFM phase signal.

Results and Discussion
Minimization of capacitive coupling through dielectric layer

According to theory the capacitive coupling can be reduced by increasing the distance between tip and substrate. This can be achieved by adding a dielectric layer between substrate surface and SPION. Figure 7 shows the phase shift as a function of lift height for substrates with different dielectric layer thicknesses ranging from 0 nm (no layer) up to 380 nm. The measurements

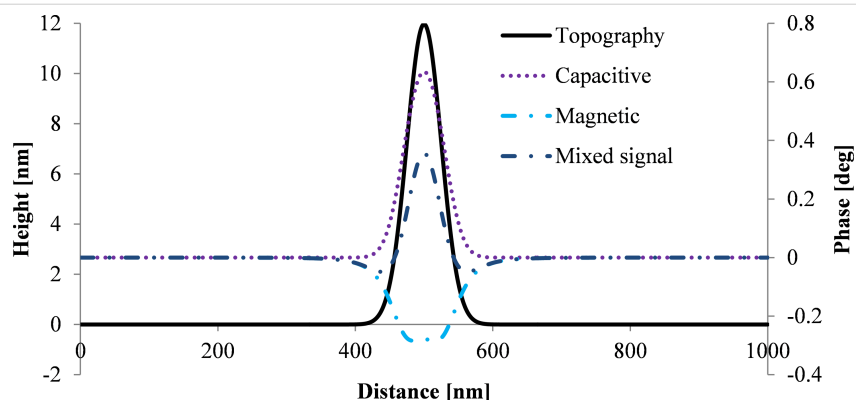**Figure 6:** Simulation of the MFM phase for a single SPION using a Gaussian topographic profile corresponding to a SPION with a diameter of 12 nm and a lift height of 20 nm. V_{CPD} for the electrostatic force is 0.35 V. A tip volume magnetization of $4.5 \cdot 10^{-15}$ A·m^2 and a specific magnetization of the SPION of 80 A·m^2·kg^{-1} were used for calculations of the magnetic force.
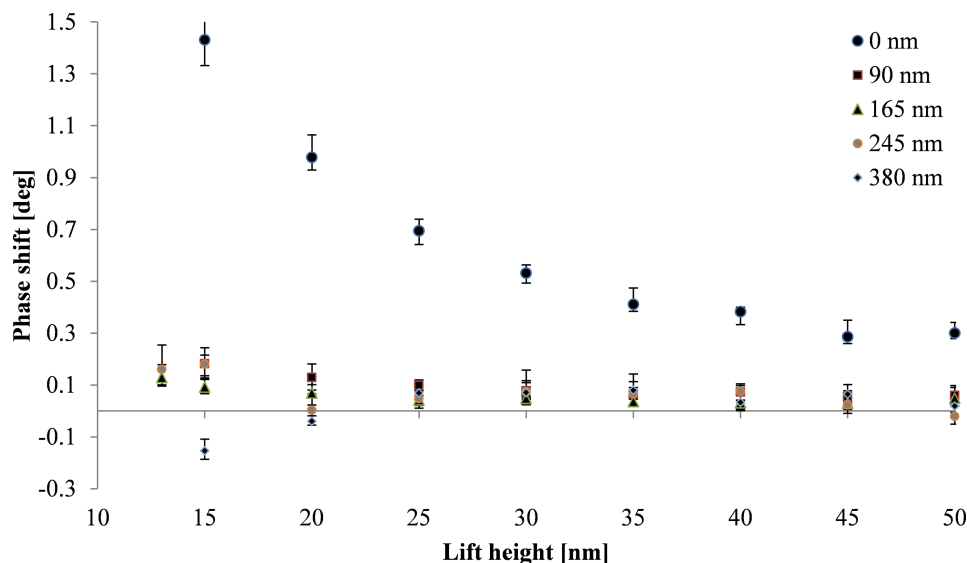
Figure 7: Phase shift above nanoparticles (10 ± 2 nm) on dielectric layers of various thicknesses as a function of the lift height. The measurements were carried out using a tip with high magnetic moment (ASYMFM-HM) to assure magnetic sensitivity.

are carried out with a tip with high magnetic moment (ASYMFM-HM tip) in order to obtain a strong magnetic interaction between tip and SPIONs. In case of SPIONs lying directly on the silicon substrate the capacitive coupling is dominant and completely hides the magnetic signal. Adding a dielectric layer between silicon substrate and the nanoparticle, the capacitive coupling is reduced. The capacitive coupling is significantly decreasing with increasing layer thickness of the dielectric layer. For a dielectric layer with 380 nm layer thickness the magnetic interaction is dominating the phase signal for small lift heights resulting in attraction and, therefore, negative phase shift for lift heights of 15 and 20 nm.

Figure 8 shows the phase shift as a function of the effective tip–substrate distance, ($z + t_{eff}$, Figure 2) for samples with layer thicknesses varying from 0 to 380 nm. For each layer thickness the phase shift above the nanoparticle has been measured as a function of the lift height z (Figure 2). The black line shows the theoretical phase shift for capacitive coupling with a silicon substrate indicating the decrease of the capacitive coupling with increasing dielectric layer thickness as discussed above.

We observe a significant decrease of the capacitive coupling between tip and substrate with increasing layer thickness. The positive phase shift above the nanoparticles can be reduced by a
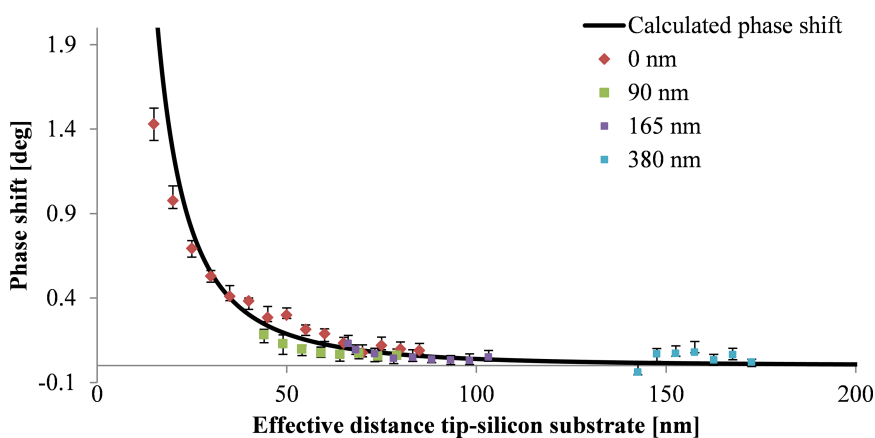
Figure 8: Calculated ($\Delta\varphi_{el}$; black line) and measured phase shift for single nanoparticles with 10 ± 2 nm diameter on silicon substrates with dielectric layers of different thicknesses of 0, 90, 165 and 380 nm; calculated for a silicon substrate with V_{CPD} of 0.35 V, and a tip radius of 84 nm taking into account the dielectric constant of 3.1 of the dielectric layer. The effective distance is determined by lift height z, particle diameter d and t_{eff}.

factor of about seven introducing dielectric layers with thicknesses of 90 nm and more. Trapped charges on the surface of the dielectric layer might limit the minimization of the capacitive coupling and result in a weak capacitive coupling between tip and dielectric layer. Figure 9 shows magnetic nanoparticles on a silicon substrate with a spin-coated dielectric layer of 380 nm thickness. The repulsive force of capacitive coupling is reduced significantly. However, an increase of the phase shift can still be observed directly above the nanoparticles indicating a remaining weak capacitive coupling.

Figure 10 shows a cross section of the topography image as well as of the phase image for a single SPION on a silicon substrate. For the single SPION lying directly on the silicon surface a strong repulsion indicated by a positive phase shift is measured for lift heights of 50 nm or less. Additionally, a negative phase shift is observed around the nanoparticle indicating an attractive magnetic force. This magnetic aureole around the nanoparticle is due to the broader magnetic signal compared to the electrostatic signal from capacitive coupling. This behavior is in accordance with our simulations combining magnetic and
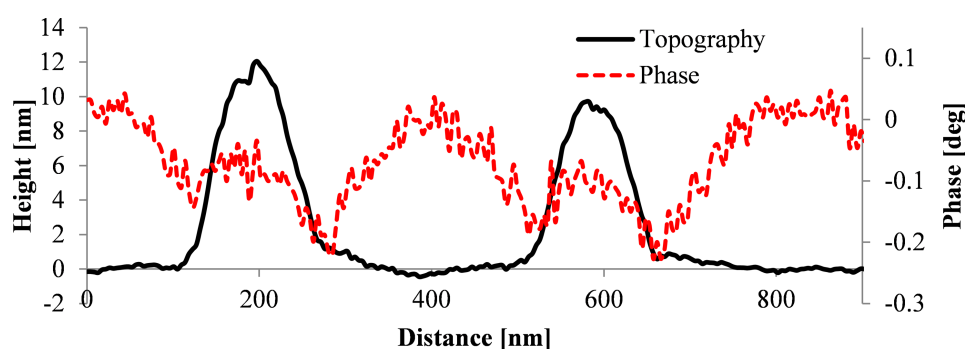
Figure 9: Measurement of a single SPION with 10 ± 2 nm diameter on a silicon substrate with a dielectric layer (380 nm layer thickness) recorded with an ASYMFM-HM tip at a lift height of 20 nm.

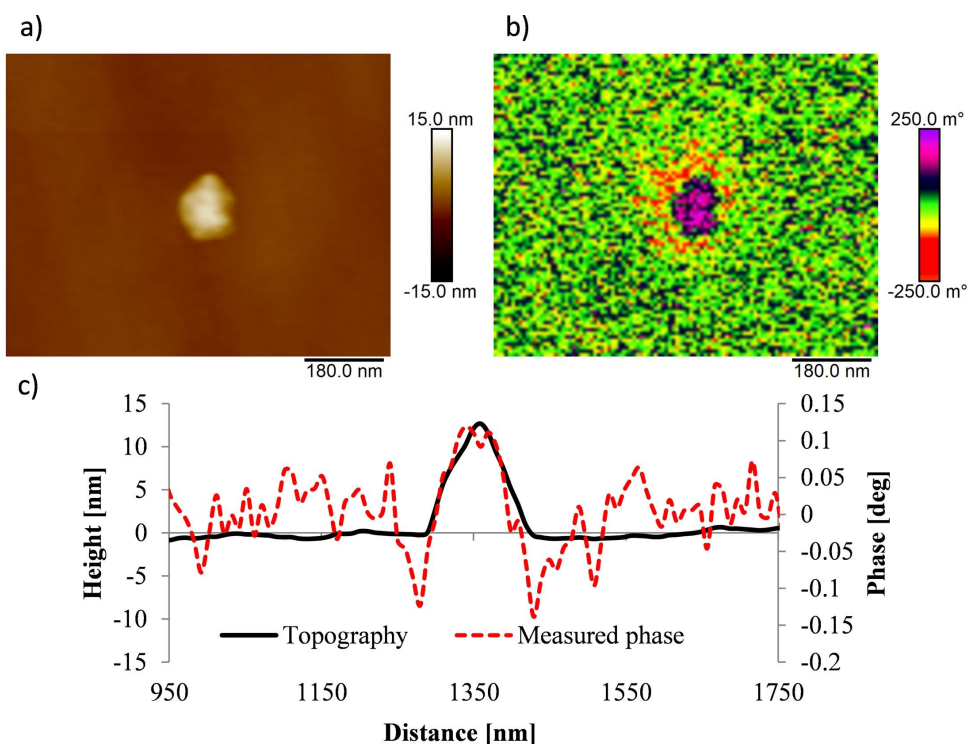**Figure 10:** Measurement of a single SPION with 12 ± 1 nm diameter on a silicon substrate recorded with an ASYMFM-HM tip. a) Topography image, b) phase image at 20 nm lift height and c) cross section of topography image (black line) and of phase image (red line).

electrostatic interactions resulting in a ring of negative phase shift (Figure 6).

Hence, MFM measurements on single SPIONs reveal contributions of electrostatic forces in form of a positive phase shift above the nanoparticles as well as contributions of magnetic forces observed as a ring, a magnetic aureole, of negative phase shift around the nanoparticle.

Conclusion

In summary we could explain the specific MFM phase characteristic often seen in measurements of SPIONS. The phase image arising due to interplay of electrostatic and magnetic forces could be explained. We showed that capacitive coupling effects can be reduced by including a dielectric layer between substrate and nanoparticle. The capacitive coupling decreases with increasing layer thickness since the distance between tip and substrate is increased. The theoretical model described in this paper also predicts decreasing topographic effects in MFM signals due to surface roughness of dielectric films with increasing film thickness.

Experimental

The MFM measurements in this work were carried out under ambient conditions using a Bruker Dimension Icon atomic force microscope. The topography of the samples was measured in tapping mode and the phase images in interleave mode at a certain lift height. The changes in amplitude indicate the topography changes in tapping mode. The amplitude of the tip oscillation is 50 nm in order to increase the signal-to-noise ratio. The resolution of the images is 254 measuring points per line, and the scan speed is 0.9 Hz. The force gradient is detected by phase shifts in interleave mode. A magnetic ASYMFM-HM tip was used for all measurements in order to assure a high magnetic sensitivity. The ASYMFM-HM tip has a resonance frequency of 75 kHz, a radius of 84 nm and a magnetic moment of $3 \cdot 10^{-16}$ A·m^2 due to the magnetic CoCr coating. The MFM measurements were processed using the NanoScope analysis software. A flatten command of 1st order was used on topography and phase images shown in this paper to remove offset and slope of the measured data.

The SPIONs with 10 ± 2 nm diameter with oleic acid as stabilizing ligand were used as received (Merck). A single-crystal silicon substrate with <100> orientation (Siegert Wafer) was cut in 2 cm^2 squares. The dielectric layers were spin-coated on silicon substrates at 3000 rpm using a closed-system spin-coater with rotating lid (BLE). Bisphenol A-epichlorohydrin resin was used as dielectric layer. The resin is the hard component of AR-P 5910 resist (Allresist) with a dielectric constant of 3.1 [21]. The thickness was varied by different dilutions of the

resist using the AR 300-12 thinner (Allresist). The layer thickness and the degree of dilutions are shown in Table S1 (Supporting Information File 1). The thickness of the layers was measured using the AFM tip-scratch method.

Supporting Information

Supporting Information File 1
Additional experimental details.
[https://www.beilstein-journals.org/bjnano/content/supplementary/2190-4286-10-106-S1.pdf]

ORCID® iDs

Alexander Krivcov - https://orcid.org/0000-0001-7741-6571
Jasmin Ehrler - https://orcid.org/0000-0002-6335-5867
Tanja Junkers - https://orcid.org/0000-0002-6825-5777
Hildegard Möbius - https://orcid.org/0000-0003-2725-9752

References

1. Kim, D.; Chung, N.-K.; Allen, S.; Tendler, S. J. B.; Park, J. W. *ACS Nano* **2012,** *6,* 241–248. doi:10.1021/nn203464g
2. Schreiber, S.; Savla, M.; Pelekhov, D. V.; Iscru, D. F.; Selcu, C.; Hammel, P. C.; Agarwal, G. *Small* **2008,** *4,* 270–278. doi:10.1002/smll.200700116
3. Körnig, A.; Hartmann, M. A.; Teichert, C.; Fratzl, P.; Faivre, D. *J. Phys. D: Appl. Phys.* **2014,** *47,* 235403. doi:10.1088/0022-3727/47/23/235403
4. Moya, C.; Iglesias-Freire, Ó.; Batlle, X.; Labarta, A.; Asenjo, A. *Nanoscale* **2015,** *7,* 17764–17770. doi:10.1039/c5nr04424c
5. Torre, B.; Bertoni, G.; Fragouli, D.; Falqui, A.; Salerno, M.; Diaspro, A.; Cingolani, R.; Athanassiou, A. *Sci. Rep.* **2011,** *1,* 202. doi:10.1038/srep00202
6. Sievers, S.; Braun, K.-F.; Eberbeck, D.; Gustafsson, S.; Olsson, E.; Schumacher, H. W.; Siegner, U. *Small* **2012,** *8,* 2675–2679. doi:10.1002/smll.201200420
7. Li, J.-R.; Lewandowski, B. R.; Xu, S.; Garno, J. C. *Anal. Chem. (Washington, DC, U. S.)* **2009,** *81,* 4792–4802. doi:10.1021/ac900369v
8. Li, X.; Lu, W.; Song, Y.; Wang, Y.; Chen, A.; Yan, B.; Yoshimura, S.; Saito, H. *Sci. Rep.* **2016,** *6,* 22467. doi:10.1038/srep22467
9. Yu, J.; Ahner, J.; Weller, D. *J. Appl. Phys.* **2004,** *96,* 494–497. doi:10.1063/1.1757029
10. Yu, J.; Ahner, J.; Weller, D. *Appl. Phys. Lett.* **2003,** *83,* 4208–4210. doi:10.1063/1.1627940
11. Kim, B. I. *Rev. Sci. Instrum.* **2009,** *80,* 23702. doi:10.1063/1.3077151
12. Schwarz, A.; Wiesendanger, R. *Nano Today* **2008,** *3,* 28–39. doi:10.1016/s1748-0132(08)70013-6

13. Jaafar, M.; Iglesias-Freire, O.; Serrano-Ramón, L.; Ibarra, M. R.; de Teresa, J. M.; Asenjo, A. *Beilstein J. Nanotechnol.* **2011,** *2,* 552–560. doi:10.3762/bjnano.2.59
14. Krivcov, A.; Junkers, T.; Möbius, H. *J. Phys. Commun.* **2018,** *2,* 075019. doi:10.1088/2399-6528/aad3a4
15. Neves, C. S.; Quaresma, P.; Baptista, P. V.; Carvalho, P. A.; Araújo, J. P.; Pereira, E.; Eaton, P. *Nanotechnology* **2010,** *21,* 305706. doi:10.1088/0957-4484/21/30/305706
16. Angeloni, L.; Passeri, D.; Reggente, M.; Rossi, M.; Mantovani, D.; Lazzaro, L.; Nepi, F.; De Angelis, F.; Barteri, M. *AIP Conf. Proc.* **2015,** *1667,* 020010. doi:10.1063/1.4922566
17. Raşa, M.; Kuipers, B. W. M.; Philipse, A. P. *J. Colloid Interface Sci.* **2002,** *250,* 303–315. doi:10.1006/jcis.2002.8345
18. Angeloni, L.; Passeri, D.; Reggente, M.; Mantovani, D.; Rossi, M. *Sci. Rep.* **2016,** *6,* 26293. doi:10.1038/srep26293
19. Passeri, D.; Dong, C.; Reggente, M.; Angeloni, L.; Barteri, M.; Scaramuzzo, F. A.; De Angelis, F.; Marinelli, F.; Antonelli, F.; Rinaldi, F.; Marianecci, C.; Carafa, M.; Sorbo, A.; Sordi, D.; Arends, I. W.; Rossi, M. *Biomatter* **2014,** *4,* e29507. doi:10.4161/biom.29507
20. Krivcov, A.; Schneider, J.; Junkers, T.; Möbius, H. *Phys. Status Solidi A* **2018,** 1800753. doi:10.1002/pssa.201800753
21. Technical Data Sheet for AR-P 3100 Resist by Allresist. https://www.allresist.com/wp-content/uploads/sites/2/2015/08/allresist_produktinfos_ar-p5900_englisch.pdf (accessed March 19, 2019).
22. Hartmann, U. *Phys. Lett. A* **1989,** *137,* 475–478. doi:10.1016/0375-9601(89)90229-6
23. Edwards, B. F.; Riffe, D. M.; Ji, J.-Y.; Booth, W. A. *Am. J. Phys.* **2017,** *85,* 130–134. doi:10.1119/1.4973409
24. Serem, W. K.; Lusker, K. L.; Garno, J. C. Using Scanning Probe Microscopy to Characterize Nanoparticles and Nanocrystals. *Encyclopedia of Analytical Chemistry;* John Wiley & Sons, Ltd: Chichester, United Kingdom, 2010. doi:10.1002/9780470027318.a9155

Kelvin probe force microscopy work function characterization of transition metal oxide crystals under ongoing reduction and oxidation

Dominik Wrana[*1], Karol Cieślik[1], Wojciech Belza[1], Christian Rodenbücher[2], Krzysztof Szot[3,4] and Franciszek Krok[1]

Full Research Paper

Address:
[1]Marian Smoluchowski Institute of Physics, Jagiellonian University, Lojasiewicza 11, 30-348 Krakow, Poland, [2]Institute of Energy and Climate Research (IEK-3), Forschungszentrum Jülich GmbH, 52425 Jülich, Germany, [3]Peter Grünberg Institute (PGI-7), Forschungszentrum Jülich GmbH, 52425 Jülich, Germany and [4]August Chelkowski Institute of Physics, University of Silesia, 40–007 Katowice, Poland

Email:
Dominik Wrana[*] - dominik.wrana@uj.edu.pl

* Corresponding author

Abstract

Controlling the work function of transition metal oxides is of key importance with regard to future energy production and storage. As the majority of applications involve the use of heterostructures, the most suitable characterization technique is Kelvin probe force microscopy (KPFM), which provides excellent energetic and lateral resolution. In this paper, we demonstrate precise characterization of the work function using the example of artificially formed crystalline titanium monoxide (TiO) nanowires on strontium titanate ($SrTiO_3$) surfaces, providing a sharp atomic interface. The measured value of 3.31(21) eV is the first experimental work function evidence for a cubic TiO phase, where significant variations among the different crystallographic facets were also observed. Despite the remarkable height of the TiO nanowires, KPFM was implemented to achieve a high lateral resolution of 15 nm, which is close to the topographical limit. In this study, we also show the unique possibility of obtaining work function and conductivity maps on the same area by combining noncontact and contact modes of atomic force microscopy (AFM). As most of the real applications require ambient operating conditions, we have additionally checked the impact of air venting on the work function of the $TiO/SrTiO_3(100)$ heterostructure, proving that surface reoxidation occurs and results in a work function increase of 0.9 eV and 0.6 eV for $SrTiO_3$ and TiO, respectively. Additionally, the influence of adsorbed surface species was estimated to contribute 0.4 eV and 0.2 eV to the work function of both structures. The presented method employing KPFM and local conductivity AFM for the characterization of the work function of transition metal oxides may help in understanding the impact of reduction and oxidation on electronic properties, which is of high importance in the development of effective sensing and catalytic devices.

Introduction

Transition metal oxides are viewed today as some of the most promising materials in various fields, ranging from (photo)catalysis [1], hydrogen production [2], resistive switching [3] and organic electronics [4,5] to so-called thermoelectric power generators [6]. The performance of all of the abovementioned applications is extremely sensitive to the work function (WF) of the active oxide layer. As a vast majority of applications are nowadays based on oxide heterostructures, not only is macroscopic information of the work function needed (which may be provided by averaging techniques such as ultraviolet photoelectron spectroscopy (UPS)) but also spatial resolution on the nanoscale. Driven by its remarkable lateral and energetic resolution, Kelvin probe force microscopy (KPFM, also known as scanning Kelvin probe microscopy, SKPM) is the tool of choice for the precise measurement of the WF across oxide heterostructures, which is a technique that has not been fully exploited to date. In recent years, KPFM has proved to be superior for many cases in both fundamental research and applications, such as the identification of adsorption geometries of molecules on oxide surfaces [7], probing energetics of electron transfer within single molecules [8] and operation of prototypical electronic devices, such as perovskite solar cells [9] or Ti/TiO$_x$/Ti memristive devices [10]. Of the two KPFM operation modes, frequency modulation (FM) has proven to be more suitable for the investigation of oxide nanostructures (due to the higher lateral resolution) as compared to amplitude modulation (AM) [11]. Therefore, in our study, we present the advantages and limitations of the FM-KPFM technique using the example of a newly discovered TiO/SrTiO$_3$(100) (metal/insulator) heterostructure, which has potentially high technological relevance [12].

Now it would be justified to introduce both TiO and SrTiO$_3$ oxides, highlighting the differences and similarities between those two structures. Based on the electronic conduction, most transition metal oxides could be classified as insulators or semiconductors. However, due to the plethora of available valence states in which a cation can be, many transition metal oxides may also exhibit metallic conductivity. Here, a huge advantage over other materials is the possibility of oxides that self-dope via the introduction of oxygen vacancies [13], which is also a reason why there are not many reliable experimental studies on the work function of transition metal oxides (with one notable exception [14]). Strontium titanate, SrTiO$_3$, is a perfect example of a semiconductor with a wide bandgap of 3.2 eV and also a model perovskite oxide. Ti^{4+} cations provide no electrons for the d-band, which can participate in conductivity. Strontium titanate finds many applications as a dielectric ceramic material [15] but also in various heterostructures, with exotic electronic states, e.g., a two-dimensional electron gas (2DEG) on the interface with LaAlO$_3$ [16,17]. On the other side of the transition

metal oxides spectrum lies titanium monoxide, TiO, in which the titanium atoms adopt the valence state 2+, contributing to the formation of d^2 electrons. Hence, TiO is a d-band conductor with a room temperature conductivity of 3500 Ω^{-1} cm^{-1}, which slowly decreases with temperature [18]. There is a growing interest in such metallic oxides, not only as oxide electrodes but also in medicine, since reduced TiO nanostructures exhibit a strong absorbance of light over a broad spectrum, which is of potential use in novel tumor therapy [19]. In addition, in the previous year, a profound interest was focused on the superconductivity of various TiO structures [20,21]. According to those, rock-salt TiO is a type-II superconductor with a superconductivity transition temperature (T_c) of 5.5 K, which is higher than previously reported results [22]. As a result of its electronic structure, titanium monoxide nanoparticles find further application in heterogeneous catalysis, e.g., for the hydrogenation of styrene [1].

Here we show the properties of a bulk-like crystalline rock-salt TiO phase, unlike previous studies on the crystallography and electronic structure of TiO, which were based on defective thin films formed on various surfaces, e.g., TiC(100) [23] or TiO$_2$(110) [24]. γ-TiO is the high-temperature phase with a NaCl-type (rock-salt-type, B1) cubic structure (*Fm−3m*, *a* = 4.184 Å), displaying a wide range of nonstoichiometric values [25]. Our study contains first measurements of electrical conductivity and the work function of crystalline TiO and its response to the ambient air reoxidation. This is all compared to the work function of another relevant oxide, SrTiO$_3$(100), showing similarities and differences.

The present manuscript is organized as follows: after the introduction of our TiO/SrTiO$_3$(100) system, a combined conductivity and work function study from the same surface area is presented, showing the possibility of obtaining full information on the electronic properties when the KPFM technique is accompanied by local conductivity atomic force microscopy (LC-AFM). This is followed by a discussion of the significant variations of the WF within cubic TiO nanowires, the estimation of the KPFM resolution and the differences between TiO$_2$ and SrO terminations of SrTiO$_3$(100). The last part of the study is dedicated to the discussion of the work function response of both TiO and SrTiO$_3$ surfaces upon oxidation via ambient air exposure, in order to provide insight into the effect of oxygen, water, and carbon dioxide interaction and therefore mimic the operation conditions in real life applications.

Results and Discussion

The thermal reduction of a SrTiO$_3$(100) crystal under reduced oxygen partial pressure (UHV conditions + an oxygen getter),

assured by the extremely low oxygen partial pressure (ELOP) process, results in the formation of a network of ordered TiO nanowires on the (100) surface as shown in Figure 1. Heavily reducing conditions enable not only the removal of oxygen from the crystal but additionally trigger an incongruent sublimation of strontium, resulting in the titanium enrichment of the surface [26]. This general process has also been observed for the broader class of transition metal oxides, such as $CaTiO_3$ or $BaTiO_3$. The titanium monoxide surface layer crystallizes in the form of nanowires oriented along the main crystallographic directions of $SrTiO_3$(100), with a length of up to 10 μm, a width of a few hundred nanometers and a height of tens of nanometers – see Figure 1. Their size could be easily tuned either by the temperature or time of reduction [12]. The perfect crystallographic order of TiO nanostructures is confirmed by the transmission electron microscopy (TEM) measurements in the high-angle annular dark-field imaging scanning transmission electron microscope (HAADF-STEM) mode as we have recently shown in [12]. A closer look at TiO reveals the γ-TiO structure in a Fm-3m space group and 2.1 Å unit cell, which stands in perfect agreement with subject literature values [27]. The high level of crystallinity of these nanowires is the result of the formation mechanism, which comprises incongruent strontium effusion from $SrTiO_3$ and then a TiO structure growth via crystallographic shearing and diffusion (more details can be found in [12]). The abrupt $TiO/SrTiO_3$ interface and the Ti^{2+} to Ti^{4+} transition thereof make such a transition metal oxide heterostructure a promising candidate for various electronic properties and charge transfer investigations.
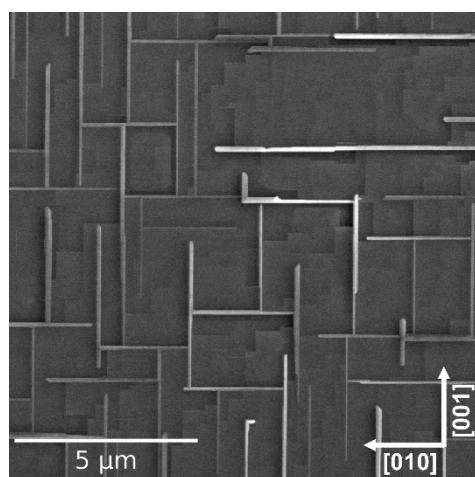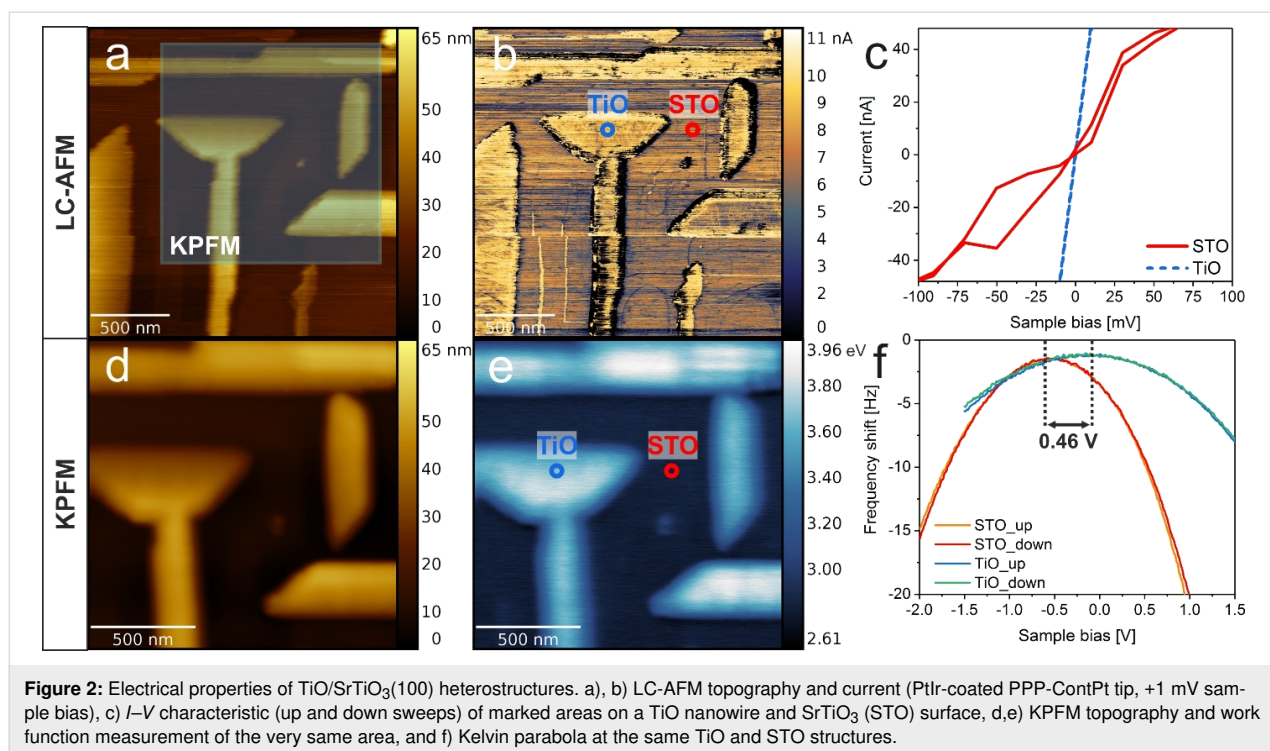

Figure 1: SEM images of an oriented network of titanium monoxide (TiO) nanowires on $SrTiO_3$(100). In between the terrace structure of $SrTiO_3$(100) can be seen.

Despite the similarities (both structures have a cubic crystallographic phase), there are profound differences in the electronic structure between the band insulator $SrTiO_3$ and metallic TiO. Here there are two 3d electrons per one Ti^{2+} divalent titanium ion, partially filling the metallic d-band in the energy diagram. From the orbital perspective, high conductivity is a consequence of the d-orbital overlap from the neighboring Ti sites. In the case of cubic TiO, the Ti–Ti distance is slightly above 2 Å, which is enough to have a significant overlap given the d-orbital extension. On the other hand, in the ideal $SrTiO_3$ perovskite there are no d-electrons on Ti sites. Thus a TiO network on $SrTiO_3$ constitutes a metallic nanowire array embedded in an insulator matrix, and to properly disentangle the electronic properties of both structures a technique with nanoscale resolution is needed. Indeed with the use of the LC-AFM technique, the conductivity of the developed nanostructures at the nanoscale can be characterized, providing the possibility of obtaining current maps as well as *I*–*V* characteristics at a given spot. Figure 2a and Figure 2b show the topography and current maps of the TiO nanowire network on $SrTiO_3$(100). TiO has a higher conductivity than the surrounding $SrTiO_3$ (STO) surface (the no current areas at nanowire edges are due to technical artefacts, such as wear of the coating of the conductive probe). To better illustrate the differences, *I*–*V* characteristics of TiO and STO were collected and are presented in Figure 2c. Given the ohmic behavior at the TiO nanowire, the conductance of the whole system (tip + contact + TiO nanowire + interface + STO bulk + bottom electrode) can be estimated to G_{LCAFM} = 10 μS. In contrast, the STO surface exhibits a one order of magnitude lower current of a rather semiconducting nature. It is noteworthy that the STO(100) surface had been thermally reduced up to 1150 °C in UHV beforehand, resulting in the formation of a high concentration of oxygen vacancies. Therefore, the conductivity is much higher than that of a pristine single crystal, which has been estimated via a comparable LC-AFM study to be around 10^{-16} S [28]. Here the observed changes of conductivity on the surface correlate directly with the work function differences as provided by the KPFM measurements taken at the very same area. This was possible by forcing the same conductive contact AFM tip to oscillate at higher harmonics to enter the FM-KPFM mode (more details can be found in [29]). Figure 2d,e presents the topography and work function of the same area. Differences in the WF are as high as 900 meV between TiO and $SrTiO_3$, in favor of TiO. However, there is also a certain variation within the TiO and $SrTiO_3$ structures, which will be discussed later. The bias sweep measurements presented in Figure 2f show reproducible Kelvin parabola with negative curvature for both structures. As up and down bias sweeps appear to follow the same curve, and there is no sign of charging or charge transfer. A comparative study of LC-AFM and KPFM of the $TiO/SrTiO_3$ structure enables a clear distinction between two materials of comparable conductivity but notably different work functions. The reason behind this is that

Figure 2: Electrical properties of TiO/SrTiO$_3$(100) heterostructures. a), b) LC-AFM topography and current (PtIr-coated PPP-ContPt tip, +1 mV sample bias), c) *I–V* characteristic (up and down sweeps) of marked areas on a TiO nanowire and SrTiO$_3$ (STO) surface, d,e) KPFM topography and work function measurement of the very same area, and f) Kelvin parabola at the same TiO and STO structures.

although undoped SrTiO$_3$(100) is a band insulator, it could be easily self-doped with oxygen vacancies upon thermal reduction [28,30]. Reduction preferentially occurs at the surface, resulting in the reconstruction transformation from (1×1) to ($\sqrt{5}\times\sqrt{5}$)R26.6°, and in the vicinity of extended defects in a crystal (dislocations) which act as easy conduction paths for electrons. Oxygen vacancy formation, and therefore Ti^{3+} valence, results in the appearance of new t$_{2g}$ electron states within Ti 3d, which are below the conduction band of SrTiO$_3$(100) [31]. Consequently, a decrease of the WF is expected, as it was previously reported for 900 °C thermal

annealing under UHV, where the WF of SrTiO$_3$(100) yielded 3.478(64) eV [30]. Hence, here a high conductivity of the reduced SrTiO$_3$(100) is measured and a work function of 3.12(18) eV, which is almost 1 eV lower than previous X-ray photoemission electron microscopy (XPEEM) and UPS studies (4.13 and 4.2 eV) for untreated oxide [32,33].

As stated before, KPFM investigations reveal certain variations in the work function value of TiO nanostructures. To illustrate this properly a 3D topography overprinted image with color scale representing the WF is shown in Figure 3a. The WF of

Figure 3: TiO facets influence the work function (WF) on the nanoscale. a) 3D view of the combined topography and the WF of TiO/SrTiO$_3$. b,c) Topography and work function profiles of two areas on the same TiO nanowire.
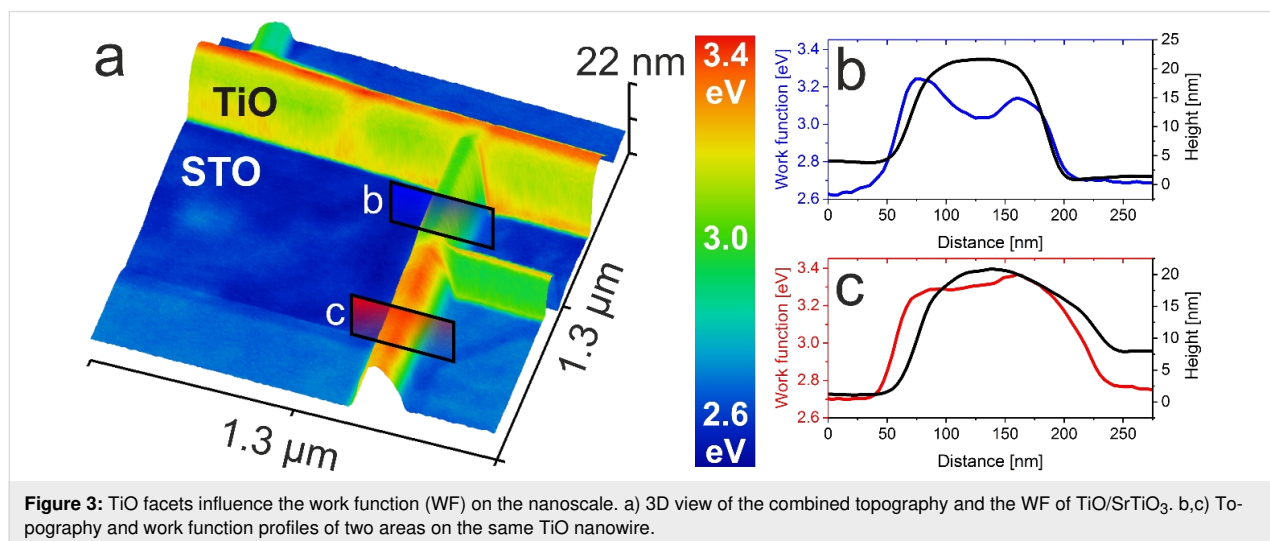
titanium monoxide varies to as high as 300 meV, even within one nanowire. This is not an imaging artifact but rather a morphological-related feature, which is proved by the two profiles obtained for the same nanowire and shown in Figure 3b,c. The edges of the nanowires have a different work function from the top surface. This could be a consequence of the different facets of the cubic TiO crystal being exposed. Such an effect of facets having different WFs has to date been observed for many structures – the differences could be as high as 255 meV measured in the case of $(\overline{1}\,\overline{1}\,2)$ and (110) surfaces of $CuGaSe_2$ [34]. For the case of transition metal oxide crystals, XPEEM studies have proved that the WF of the $SrTiO_3(111)$ face is higher than that of the (100) face by no less than 210 meV [32]. Smaller differences in the range of 70 meV were reported in the case of titanium dioxide (110) and (100) faces [35]. In the present case, the differences could be higher because the whole sample with TiO nanostructures was annealed up to 1150 °C and thus a possible reduction-driven non-stoichiometry occurs. From a geometrical perspective, the low index faces of cubic TiO, like (100), (110) or (210), have an equal number of protruding oxygen and titanium atoms, in contrast to the (111) face, where a whole plane

is formed by either titanium or oxygen. To our knowledge, there are no subject literature studies on the stability or work function on such faces, but it is justified to assume certain differences may be present between those facets, which are also influenced by the preferential removal of oxygen during thermal reduction. As TiO nanowires have a height of tens of nanometers and tip convolution may play a role, a precise evaluation of the steep facets of a higher WF, as seen in Figure 3, is difficult. Based on the relative slope of a TiO surface it seems that the top surface typically adopts a (100) plane, though this requires further investigation.

An overlay of the work function on the topography map shown in Figure 3a provides additional information on the high lateral contrast of KPFM. The WF and morphology match almost completely, although height variations are of tens of nanometers. To investigate the resolution limits of KPFM imaging of oxide heterostructures with a complex topography, a set of images of parallel TiO nanowires was investigated, and the results are presented in Figure 4. As a measure of the potential resolution, we have used the ratio between the measured con-
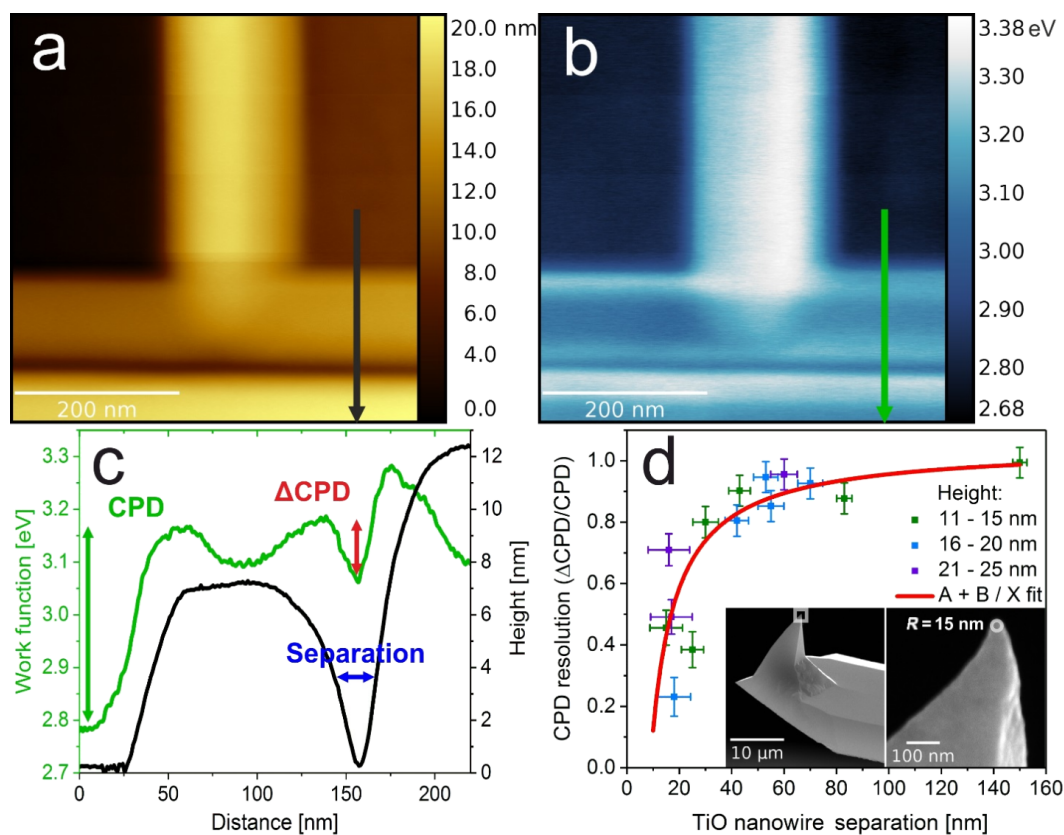
Figure 4: KPFM lateral resolution on high TiO/STO structures. a) Topography and b) work function of TiO nanowire array on $SrTiO_3(100)$. c) Height (black line) and work function (green line) profiles of two adjacent TiO nanowires, showing high KPFM contrast. d) Dependence of the CPD resolution (estimated as ΔCPD/CPD, see c) on the separation between TiO nanowires, with A + B/X asymptote fit. Insets show the SEM images of the actual PtSi cantilever used in the experiments with a tip radius of 15 nm.

tact potential difference (CPD) decrease in between the TiO nanowires and the full CPD of TiO with respect to STO. For an ideal case, when the CPD reaches the value of STO in the gap between parallel nanowires, this measure adopts 1, and 0 if there is no drop in CPD. The dependence of this value on the TiO nanowire separation (plotted in Figure 4d) provides information on the resolution limit. It follows an asymptotic behavior, with the correct CPD values measured when TiO nanowires are separated by more than 40 nm. This stands in perfect agreement with the real tip radius of 15 nm, which was measured for the same cantilever in high-resolution SEM (see Figure 4d insets). Here, the use of uniformly PtIr-coated tips enables topography correlated artifacts to be avoided, unlike with some previous studies [36]. Taking into account the opening angle of about 40° and the average nanowire height of 18(8) nm, the tip diameter at the level of the top surface of the nanowire would be about 40 nm, meaning that the CPD resolution approaches the topography resolution, which is the ultimate physical limit of the FM-KPFM technique [11]. Similar results were obtained for the resolution estimation for KBr nanoislands of monoatomic thickness, where a resolution of 0.5 was obtained for 20 nm separation, as is the case in the following study [37]. The CPD resolution at the $TiO/SrTiO_3$ transition is insensitive to the nanowire height, following the same asymptotic behavior (see Figure 4d), unlike the situation for C_{60} islands on HOPG, where a spread of 50 nm was reported, while the topography resolution was 10 nm [38]. From our results, we can set the limit of the smallest separation of oxide nanostructures at 15 nm to obtain any CPD difference. As for the CPD resolution, the estimated value would be below 5 meV, due to the high mechanical stability and good conductivity of both platinum silicide and PtIr-coated tips.

Apart from the work function difference between the TiO and STO materials, we also found that the CPD/WF mapping of the STO(100) itself exhibits a nonuniform nature. This could be associated with two different exposed surfaces, as $SrTiO_3(100)$ perovskite structure has two stable nonpolar terminations, SrO and TiO_2, which both are present on the pristine surface, although TiO_2 is more stable [39]. When annealed under reducing conditions, the TiO_2 termination is promoted. Upon heavy reduction, there is further oxygen depletion which results in the formation of the $(\sqrt{5}\times\sqrt{5})R26.6°$ reconstruction, which we recently proved to be a Ti-enriched layer on TiO_2-terminated $SrTiO_3(100)$ [30,40]. The electronic structures of both terminations are much different – the DFT calculated work function values are 1.92 eV and 4.48 eV for SrO and TiO_2, respectively [14], obtained for the pure surfaces without vacancies.

In the present case of thermally reduced $SrTiO_3(100)$, the dominant reconstruction is $(\sqrt{5}\times\sqrt{5})R26.6°$, which forms on the TiO_2 termination, as proved by the scanning tunneling microscopy (STM) and low-energy electron diffraction (LEED) investigations (see Figure 5g,h). The surface is composed of two equiprobable orientations of $(\sqrt{5}\times\sqrt{5})R26.6°$ domains, both rotated with respect to the (1×1) surface by 26.6 degrees. Those two domains are labeled A and B, both in LEED and STM images. Bright protrusions seen in the STM picture, which also decorate domain boundaries, are either oxygen vacancies/vacancy clusters or Sr adatoms, according to the model [30]. The KPFM map reveals a non-homogeneous landscape of the work function – higher values are measured on terraces, whereas areas near the edges a reduced work function is observed (see Figure 5b). This could be directly represented by the histogram shown in Figure 5c. A clear difference of ≈23 meV could be measured between the two areas. This effect is not purely topographical, since the WF differences are similar in the cases of a single step and multistep (12 atomic layers), as shown in Figure 5d–f. Three possible mechanisms are possible to cause such difference: termination-, reconstruction- or reduction-related. The first would be the termination variation within one terrace, with the higher WF values related to the TiO_2 termination, which is dominant, and the lower to the SrO-enriched terrace edges, as previous KPFM studies showed the difference between air-annealed $SrTiO_3$ terminations of ≈10 meV [41]. However, for the case of heavily reduced $SrTiO_3(100)$ the only observed termination is TiO_2, given the step uniform heights of ≈4 Å. The second possible origin of the observed variation is the presence of multiple surface reconstructions, notwithstanding that the recorded LEED patterns and STM maps do not support such claims, showing clear $(\sqrt{5}\times\sqrt{5})R26.6°$ surfaces, even near the step edges (see Figure 5h). Finally, this difference is not likely to be caused by the electronic layer at step edges since it stretches away from the edges up to 100 nm, which is too far to be attributed to local dipoles [42]. Simultaneously the oxygen removal is likely to be initiated at step edges, as it was as postulated by Martinez et al. [43] for a similar $TiO_2(110)$ oxide. Hence for the severe reduction of $SrTiO_3(100)$ a gradient of the average cation valence across one terrace may be expected, which can contribute to the observed small decrease in the WF near the step edges. In terms of the absolute work function of TiO_2-terminated $SrTiO_3(100)$, the obtained value of 3.12(18) eV, averaged across a number of images, is close to this postulated by DFT (3.39 eV) for TiO_2 termination with oxygen vacancies in the surface layer [14]. The difference is most likely caused by the higher density of oxygen vacancies, due to the heavy thermal reduction.

Ambient air reoxidation of TiO and $SrTiO_3$

As the vast majority of applications of transition metal oxides is related to the oxygen activity and redox reactions on surfaces,
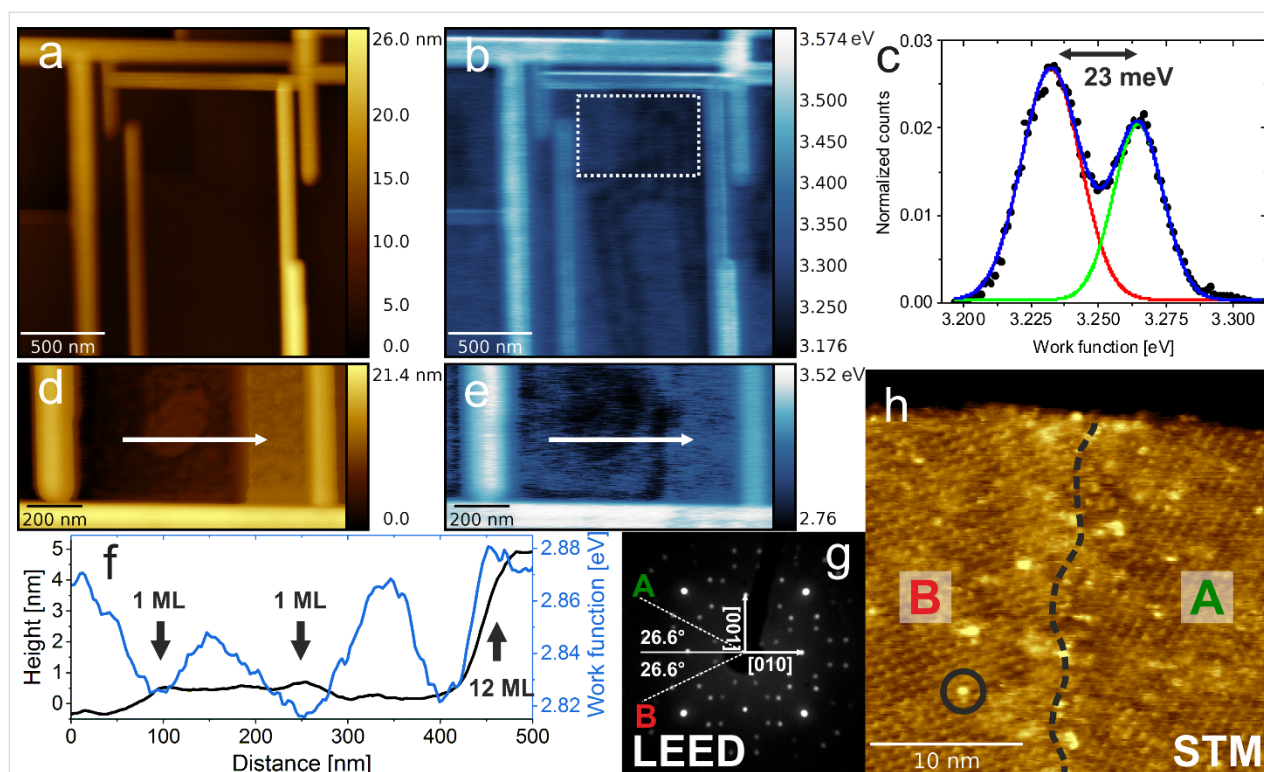
Figure 5: Characterization of the SrTiO$_3$(100) surface by KPFM. a) Topography of a TiO/SrTiO$_3$ structure ($\Delta f = -20$ Hz), b) corresponding work function map from KPFM, c) work function histogram from the selected area in b), d) and e) topography and work function of a different TiO/STO network ($\Delta f = -20$ Hz), showing the WF correlation with step edges. f) Topography and work function line profiles, extracted from d) and e). g) LEED pattern (100 eV beam energy) indicating the perfect ($\sqrt{5}\times\sqrt{5}$)R26.6° reconstruction with two equiprobable domains A and B. h) STM topography showing the concurrent presence of A and B domains, with defects marked in black.

the next experiment was aimed to study the work function dependence upon controlled reoxidation of reduced oxides.

Transition metal oxide nanostructures find manifold applications, especially in various (photo)catalytic processes, e.g., water splitting [1,44]. For industrial uses, the samples have to be exposed to ambient conditions, therefore it is necessary to investigate the impact of air exposure on electronic surface properties. Moreover, transition metal oxides are often regarded as promising materials for sensing applications, due to the strong response to gaseous pressures, especially oxygen and water [45]. The tool of choice that provides information on the subtle changes in the work function is KPFM, which has been employed for research on the photocatalytic activity of TiO$_2$-based doped and undoped nanofibers [46,47] and for the understanding of the operation of nanostructure electrochemical sensors [48].

Thus, we have focused on the systematic approach of the influence of ambient air on the work function of TiO and SrTiO$_3$(100). Figure 6a shows the topography and work function of representative TiO nanowire networks before and after ambient air exposure. Additionally, the impact of low temperature annealing (230 °C) in UHV is presented. After the venting of the vacuum chamber, the TiO nanowires still had a much higher work function than the SrTiO$_3$(100) surface; however, the absolute values for both materials increased. It is widely known that water molecules present in the ambient air form a dipole layer, which can give rise to an effective surface potential [49].

To reduce the impact of weakly interacting adsorbates, in the next step, the sample underwent in situ UHV annealing, which implicated a WF decrease of both TiO and SrTiO$_3$ by about 0.2–0.4 eV. To illustrate the experimental findings better, three histograms of reduced, air-oxidized and outgassed work functions are plotted in Figure 6b. It is immediately visible that the general three-peak nature of STO and lower and higher TiO values of the WF are preserved, however the offset changes, as illustrated in Figure 6c. The STO(100) work function increases by 0.9 eV due to air exposure, similar to the case of oxygen reoxidation [30]. A conclusion can be drawn that the main contribution of the work function increase is related to oxygen, which refills vacancies of the reduced ($\sqrt{5}\times\sqrt{5}$)R26.6° surface and locally oxidizes titanium cations to regain the 4+ valence state.
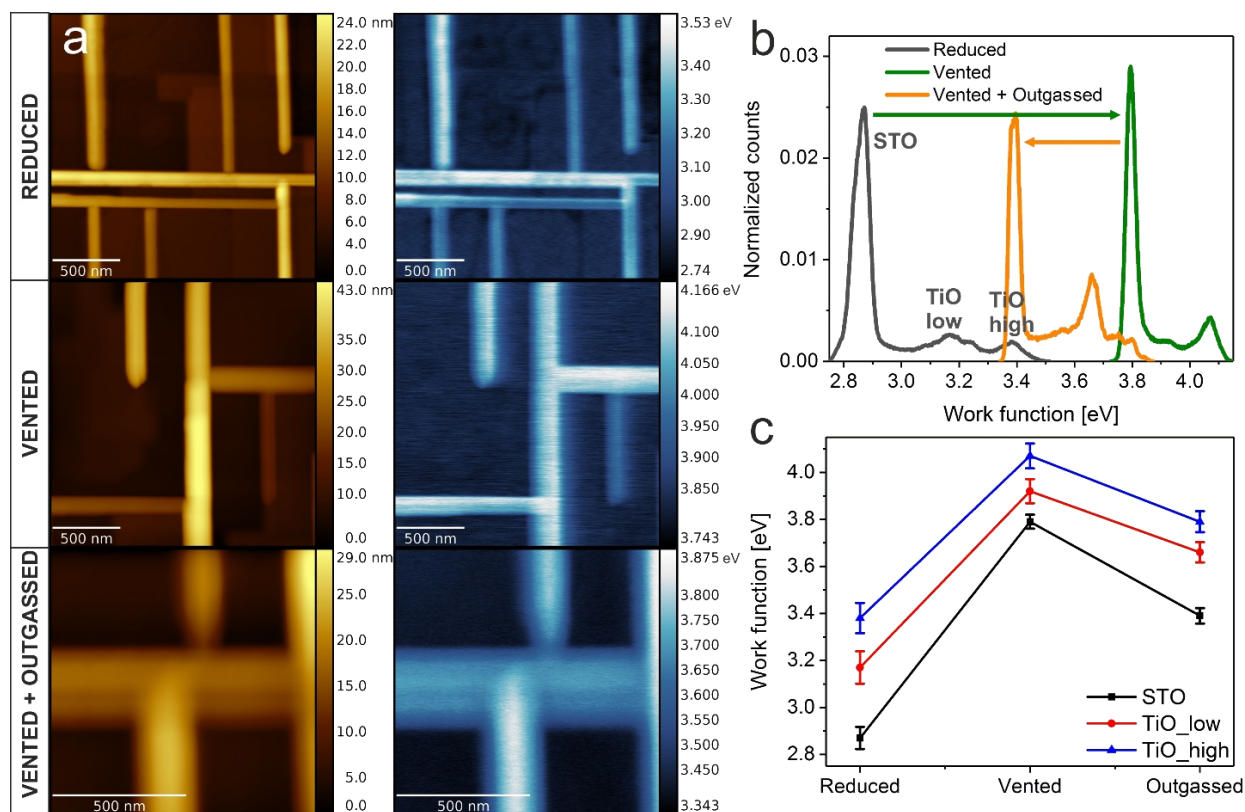
Figure 6: Influence of air exposure on the TiO/SrTiO$_3$ work function. a) KPFM topography and work function of a TiO/SrTiO$_3$ heterostructure (Δf = −40 Hz) after reduction (first row), exposed to ambient air (second row) and after annealing up to 230 °C (third row). b) Work function histograms of the presented cases. c) Evolution of the work function value for the SrTiO$_3$(100) surface (black), lower TiO facets (red) and higher (blue).

Vented TiO nanowires have a work function that is higher by 0.65 eV, independent of the face, which is almost 0.5 eV higher than in the case of pure oxygen (not shown). This is a footprint of the high catalytic activity of the TiO surface, which was previously postulated in the case of TiO/TiO$_2$ nanoparticles [44]. Reduced titania TiO$_{1.23}$ proves also to be a promising candidate for electrochemical water splitting [50]. As the catalytic activity of a crystalline rock-salt TiO phase has yet to be studied, this is a first indirect observation of the high potential of such a structure.

After in situ annealing to 230 °C, the work function of TiO nanowires drops by 0.2 eV, in contrast to the 0.35 eV decrease for the SrTiO$_3$(100) surface. A temperature of 230 °C was chosen to enable desorption of the most abundant adsorbates, also mimicking the typical operating temperatures of metal oxide gas sensors [51]. Numerical calculations suggest that H$_2$O and CO$_2$ species present in air saturate almost all free adsorption sites on TiO$_2$-terminated SrTiO$_3$(100) [52]. The low Redhead desorption temperature of H$_2$O (CO$_2$) of 233–283 K (428–523 K) calculated by Baniecki et al. [52] suggests that our

surface, which is predominantly TiO$_2$-terminated, is cleaned of those adsorbates after annealing, hence the 0.35 eV difference in the WF.

The lower response of TiO to annealing is a hint of the higher adsorption energy of the interacting gases. It suggests the chemisorption of H$_2$O and CO$_2$ and dissociation of their products, stemming from the high catalytic activity of the TiO phase.

To wrap up our experimental findings of the KPFM study of TiO and SrTiO$_3$(100) crystals, a comparison between the obtained work functions as well as the subject literature values is presented in Table 1. The first direct work function measurement of the cubic γ-phase of TiO yields 3.31(21) eV for the as-grown (reduced in UHV at 1150 °C) and 3.75(11) eV for vented and outgassed material, which is most likely close to the value for the pristine TiO crystal. To date, the only values for the TiO WF come from polycrystalline samples (films, nanoparticles) and from the laterally averaging method of UPS, thus this cannot be reasonably compared with our findings. The WF

Table 1: Comparison between the literature values and the obtained experimental results of TiO and SrTiO$_3$ work functions (WF).

Material	Sample	WF [eV]	Method	Ref.
TiO	TiO nanoparticles (14 nm)	3.01	UPS	[44]
	TiO thin polycrystalline film	≈4.5	UPS	[53]
	TiO cubic γ-phase (nanowires):			
	· reduced (UHV, 1150 °C)	3.31(21)	KPFM	this study
	· air-exposed	3.92(17)		
	· air-exposed and annealed	3.75(11)		
SrTiO$_3$	SrTiO$_3$(100)	4.13	XPEEM	[32]
	SrTiO$_3$(110)	4.32		
	SrTiO$_3$(111)	4.34		
	SrTiO$_3$(100)	4.2	UPS	[33]
	SrTiO$_3$(100) reduced at 900 °C	3.478(64)	KPFM	[30]
	TiO$_2$-terminated SrTiO$_3$(100)	4.2–4.3	macroscopic Kelvin probe	[54]
	SrO-terminated SrTiO$_3$(100)	2.5–3.0		
	SrTiO$_3$(100) (single crystal):			
	· reduced (UHV, 1150 °C)	3.12(18)	KPFM	this study
	· air-exposed	3.835(72)		
	· air-exposed and annealed	3.41(11)		
	SrTiO$_3$(100) BHF-etched, air-annealed (1000 °C)	≈10 meV	KPFM	[41]
	· $\phi_{TiO2} - \phi_{SrO}$ difference			
	SrTiO$_3$(100) BHF etched, air annealed (1300 °C)	≈0.5 eV	LEEM	[55]
	· $\phi_{TiO2} - \phi_{SrO}$ difference			

value obtained for the reduced SrTiO$_3$(100) surface of 3.12(18) eV follows the trend of a decreasing work function upon reduction and an increasing one due to reoxidation [30]. It is worth mentioning that substantial discrepancies between the measured WF for transition metal oxides, besides the different quality of the samples, could stem from the suboptimal conditions during preparation, e.g., holder materials can act as oxygen getters, influencing the reduction state of a sample [12].

Conclusion

We have presented a thorough study of the Kelvin probe force microscopy investigations on the electronic properties of cubic TiO formed on a SrTiO$_3$(100) single crystal surface. To our best knowledge, this is the first measurement of the crystalline TiO work function and its dependence on the gaseous pressure of air in comparison to the SrTiO$_3$(100) response. The rock-salt cubic γ-phase, with a high crystallographic order, has a work function of 3.31(21) eV with significant variations on the surface, which are related to the different facets exposed. The higher work function of TiO compared to STO(100) is accompanied with a higher conductivity, with an ohmic behavior, which was checked by simultaneous LC-AFM measurements. Full ambient venting results in a 0.6 eV increase in the TiO work function and is a hint of the ongoing catalyzed dissociation of CO$_2$ and H$_2$O present in ambient air. The work function of TiO decreases by 0.2 eV as a result of 230 °C UHV annealing, being a measure of the amount of weakly adsorbed species. Air exposure of the (√5×√5)R26.6° TiO$_2$-terminated SrTiO$_3$(100) sur-

face results in a 0.9 eV increase in the work function, which is similar to the increase observed for reoxidation in pure oxygen. Annealing induces a decrease of 0.4 eV as a result of the desorption of weakly bonded species.

Our study also contains an estimation of the FM-KPFM lateral resolution, which enabled reliable measurements of TiO nanowires separated by 40 nm, proving the suitability of the KPFM technique for the investigation of transition metal oxide structures, even with remarkable topographical variations.

In conclusion, the presented results acquired for crystalline TiO and SrTiO$_3$ phases provide important information on the work function values themselves but also on their interaction with air and operation upon elevated temperatures.

Experimental

We investigated Verneuil-grown epitaxy-ready-polished SrTiO$_3$(100) crystals, provided by the Crystec company. The crystals were mounted onto Omicron direct heating holders and introduced into the UHV chamber, with a base pressure of 5×10^{-10} mbar, maintained by the use of turbo-molecular, ion and sublimation pumps. In order to produce a TiO nanowire network on the surface of STO(100), the extremely low oxygen partial pressure (ELOP) method of perovskite decomposition was adapted (for more information see [12,26]). The SrTiO$_3$(100) single crystal ($10 \times 3 \times 0.5$ mm^3) sample was mounted on an n-doped Si(111) single crystal, which acted as

an oxygen getter, allowing extremely low effective oxygen partial pressures to be reached on the STO surface (below 10^{-20} mbar). As a result of the high-temperature reduction (1150 °C, 1 h) under such conditions, a macroscopic network of nanowires was formed. After slow cooling down to room temperature, the samples were transferred in situ to the microscope chamber of an Omicron RT STM/AFM system, where KPFM, LC-AFM and STM measurements were performed. KPFM, operating in FM mode, was used with a single-pass method, with three feedback loops maintaining the oscillation amplitude, phase and frequency shift [56]. The real oscillation amplitude was in the range of 10 nm. In order to obtain the CPD signal, an AC-modulated bias was applied to the bottom of the electrode, where a sample was mounted. The modulation frequency and amplitude were set to 315 Hz and 500 mV, respectively.

In order to ensure reproducible FM-KPFM results, two different types of AFM cantilevers were used: PPP-ContPt (PtIr-coated) and PtSi-FM (platinum silicide tips), both from Nanosensors. Such cantilevers are widely used as conducting tips in a contact mode AFM, allowing for a high lateral resolution in conductivity measurements. The remarkable mechanical stability of the selected cantilevers allowed for the noncontact mode measurements (with a Kelvin loop) using the very same tip, maintaining oscillations at the higher harmonics of the fundamental frequency ($\approx$75 kHz). Hence, in order to record current and CPD maps from the very same sample area, KPFM measurements were first performed with the soft cantilever forced to oscillate at higher harmonics, then the tip was retracted tens of nanometers from the surface, all feedback loops were turned down and a contact mode AFM scan was performed when approached with a single loop maintaining a deflection set point of 10–30 mV. The high conductivity of both TiO and STO materials enabled a low sample bias of +1 mV for the LC-AFM measurements to be used.

Real work function values were calculated from recorded CPD maps after calibration against a material of known work function, here highly oriented pyrolytic graphite (HOPG), which was annealed in situ up to 300 °C in order to remove water and other adsorbates. After each set of KPFM measurements, the HOPG surface was scanned employing the same experimental parameters and a V_{CPD}(HOPG) was obtained. Assuming a HOPG work function of ϕ_{HOPG} = 4.5 eV (subject literature values: 4.6 ± 0.1 eV [57], 4.4 ± 0.1 eV [58]), a work function of TiO/STO was evaluated by applying the equation: $\phi_{TiO/STO} = V_{CPD}(TiO/STO) - V_{CPD}(HOPG) + \phi_{HOPG}$.

Ambient air exposure was realized by venting the sample in the load-lock and then introducing it again into the UHV system.

Subsequent annealing up to 230 °C for 1 h hour enabled the estimation of the content of the weakly adsorbed species at the surface.

Acknowledgements

ORCID® iDs

Dominik Wrana - https://orcid.org/0000-0002-8239-0043
Karol Cieślik - https://orcid.org/0000-0002-1069-1840
Wojciech Belza - https://orcid.org/0000-0003-1959-3160
Christian Rodenbücher - https://orcid.org/0000-0001-8029-3066
Krzysztof Szot - https://orcid.org/0000-0001-8773-2754
Franciszek Krok - https://orcid.org/0000-0002-6931-3545

Preprint

A non-peer-reviewed version of this article has been previously published as a preprint doi:10.3762/bxiv.2019.12.v1

References

1. Imran, M.; Yousaf, A. B.; Zhou, X.; Jiang, Y.-F.; Yuan, C.-Z.; Zeb, A.; Jiang, N.; Xu, A.-W. *J. Phys. Chem. C* **2017,** *121,* 1162–1170. doi:10.1021/acs.jpcc.6b10274
2. Compton, R., Ed. *Electrode kinetics: reactions;* Elsevier: Amsterdam, Netherlands, 1987; Vol. 27.
3. Waser, R.; Dittmann, R.; Staikov, G.; Szot, K. *Adv. Mater. (Weinheim, Ger.)* **2009,** *21,* 2632–2663. doi:10.1002/adma.200900375
4. Yu, X.; Marks, T. J.; Facchetti, A. *Nat. Mater.* **2016,** *15,* 383–396. doi:10.1038/nmat4599
5. Wrana, D.; Kratzer, M.; Szajna, K.; Nikiel, M.; Jany, B. R.; Korzekwa, M.; Teichert, C.; Krok, F. *J. Phys. Chem. C* **2015,** *119,* 17004–17015. doi:10.1021/acs.jpcc.5b04384
6. Lin, Y.; Norman, C.; Srivastava, D.; Azough, F.; Wang, L.; Robbins, M.; Simpson, K.; Freer, R.; Kinloch, I. A. *ACS Appl. Mater. Interfaces* **2015,** *7,* 15898–15908. doi:10.1021/acsami.5b03522
7. Jöhr, R.; Hinaut, A.; Pawlak, R.; Sadeghi, A.; Saha, S.; Goedecker, S.; Such, B.; Szymonski, M.; Meyer, E.; Glatzel, T. *J. Chem. Phys.* **2015,** *143,* 094202. doi:10.1063/1.4929608
8. Fatayer, S.; Schuler, B.; Steurer, W.; Scivetti, I.; Repp, J.; Gross, L.; Persson, M.; Meyer, G. *Nat. Nanotechnol.* **2018,** *13,* 376–380. doi:10.1038/s41565-018-0087-1
9. Axt, A.; Hermes, I. M.; Bergmann, V. W.; Tausendpfund, N.; Weber, S. A. L. *Beilstein J. Nanotechnol.* **2018,** *9,* 1809–1819. doi:10.3762/bjnano.9.172
10. Batko, I.; Batkova, M. *Eur. Phys. J.: Appl. Phys.* **2012,** *58,* 20102. doi:10.1051/epjap/2012120102
11. Zerweck, U.; Loppacher, C.; Otto, T.; Grafström, S.; Eng, L. M. *Phys. Rev. B* **2005,** *71,* 125424. doi:10.1103/physrevb.71.125424
12. Wrana, D.; Rodenbücher, C.; Jany, B. R.; Kryshtal, O.; Cempura, G.; Kruk, A.; Indyka, P.; Szot, K.; Krok, F. *Nanoscale* **2019,** *11,* 89–97. doi:10.1039/c8nr04545c
13. Su, J.; Zou, X.; Chen, J.-S. *RSC Adv.* **2014,** *4,* 13979–13988. doi:10.1039/c3ra47757f

14. Zhong, Z.; Hansmann, P. *Phys. Rev. B* **2016,** *93,* 235116.
 doi:10.1103/physrevb.93.235116

15. Zhang, T.-F.; Tang, X.-G.; Huang, X.-X.; Liu, Q.-X.; Yiang, Y.-P.;
 Zhou, Q.-F. *Energy Technol.* **2016,** *4,* 633–640.
 doi:10.1002/ente.201500436

16. Ohtomo, A.; Hwang, H. Y. *Nature* **2004,** *427,* 423–426.
 doi:10.1038/nature02308

17. Song, Q.; Zhang, H.; Su, T.; Yuan, W.; Chen, Y.; Xing, W.; Shi, J.;
 Sun, J.; Han, W. *Sci. Adv.* **2017,** *3,* e1602312.
 doi:10.1126/sciadv.1602312

18. Yamashita, J. *J. Phys. Soc. Jpn.* **1963,** *18,* 1010–1016.
 doi:10.1143/jpsj.18.1010

19. Shu, G.; Wang, H.; Zhao, H.-X.; Zhang, X. *ACS Appl. Mater. Interfaces*
 2019, *11,* 3323–3333. doi:10.1021/acsami.8b17418

20. Xu, J.; Wang, D.; Yao, H.; Bu, K.; Pan, J.; He, J.; Xu, F.; Hong, Z.;
 Chen, X.; Huang, F. *Adv. Mater. (Weinheim, Ger.)* **2018,** *30,* 1706240.
 doi:10.1002/adma.201706240

21. Zhang, C.; Hao, F.; Gao, G.; Liu, X.; Ma, C.; Lin, Y.; Yin, Y.; Li, X.
 npj Quantum Mater. **2017,** *2,* 2. doi:10.1038/s41535-016-0006-3

22. Wang, D.; Huang, C.; He, J.; Che, X.; Zhang, H.; Huang, F.
 ACS Omega **2017,** *2,* 1036–1039. doi:10.1021/acsomega.7b00048

23. Shirotori, Y.; Sawada, K.; Ozawa, K.; Edamoto, K. *Thin Solid Films*
 2004, *464–465,* 76–79. doi:10.1016/j.tsf.2004.06.086

24. Pabón, B. M.; Beltrán, J. I.; Sánchez-Santolino, G.; Palacio, I.;
 López-Sánchez, J.; Rubio-Zuazo, J.; Rojo, J. M.; Ferrer, P.;
 Mascaraque, A.; Muñoz, M. C.; Varela, M.; Castro, G. R.;
 de la Fuente, O. R. *Nat. Commun.* **2015,** *6,* 6147.
 doi:10.1038/ncomms7147

25. Amano, S.; Bogdanovski, D.; Yamane, H.; Terauchi, M.;
 Dronskowski, R. *Angew. Chem., Int. Ed.* **2016,** *55,* 1652–1657.
 doi:10.1002/anie.201510479

26. Rodenbücher, C.; Meuffels, P.; Speier, W.; Ermrich, M.; Wrana, D.;
 Krok, F.; Szot, K. *Phys. Status Solidi RRL* **2017,** *11,* 1700222.
 doi:10.1002/pssr.201700222

27. Banus, M. D.; Reed, T. B.; Strauss, A. J. *Phys. Rev. B* **1972,** *5,*
 2775–2784. doi:10.1103/physrevb.5.2775

28. Szot, K.; Bihlmayer, G.; Speier, W. *Solid State Phys.* **2014,** *65,*
 353–559. doi:10.1016/b978-0-12-800175-2.00004-2

29. Rodenbücher, C.; Wrana, D.; Meuffels, P.; Rogala, M.; Krok, F.;
 Szot, K. *APL Mater.* **2018,** *6,* 066105. doi:10.1063/1.5028424

30. Wrana, D.; Rodenbücher, C.; Bełza, W.; Szot, K.; Krok, F.
 Appl. Surf. Sci. **2018,** *432,* 46–52. doi:10.1016/j.apsusc.2017.06.272

31. Zhong, Z.; Kelly, P. J. *EPL* **2008,** *84,* 27001.
 doi:10.1209/0295-5075/84/27001

32. Zagonel, L. F.; Bäurer, M.; Bailly, A.; Renault, O.; Hoffmann, M.;
 Shih, S.-J.; Cockayne, D.; Barrett, N. *J. Phys.: Condens. Matter* **2009,**
 21, 314013. doi:10.1088/0953-8984/21/31/314013

33. Chung, Y.-W.; Weissbard, W. B. *Phys. Rev. B* **1979,** *20,* 3456–3461.
 doi:10.1103/physrevb.20.3456

34. Sadewasser, S.; Glatzel, T.; Rusu, M.; Jäger-Waldau, A.;
 Lux-Steiner, M. C. *Appl. Phys. Lett.* **2002,** *80,* 2979–2981.
 doi:10.1063/1.1471375

35. Imanishi, A.; Tsuji, E.; Nakato, Y. *J. Phys. Chem. C* **2007,** *111,*
 2128–2132. doi:10.1021/jp0668403

36. Polak, L.; Wijngaarden, R. J. *Ultramicroscopy* **2016,** *171,* 158–165.
 doi:10.1016/j.ultramic.2016.09.014

37. Krok, F.; Sajewicz, K.; Konior, J.; Goryl, M.; Piatkowski, P.;
 Szymonski, M. *Phys. Rev. B* **2008,** *77,* 235427.
 doi:10.1103/physrevb.77.235427

38. Sadewasser, S.; Leendertz, C.; Streicher, F.; Lux-Steiner, M. C.
 Nanotechnology **2009,** *20,* 505503.
 doi:10.1088/0957-4484/20/50/505503

39. Jang, Y. H.; Cho, J. H. *J. Korean Phys. Soc.* **2016,** *69,* 783–788.
 doi:10.3938/jkps.69.783

40. Martirez, J. M. P.; Morales, E. H.; Saidi, W. A.; Bonnell, D. A.;
 Rappe, A. M. *Phys. Rev. Lett.* **2012,** *109,* 256802.
 doi:10.1103/physrevlett.109.256802

41. Gellé, F.; Chirita, R.; Mertz, D.; Rastei, M. V.; Dinia, A.; Colis, S.
 Surf. Sci. **2018,** *677,* 39–45. doi:10.1016/j.susc.2018.06.001

42. Sasahara, A.; Uetsuka, H.; Onishi, H. *Jpn. J. Appl. Phys., Part 1* **2004,**
 43, 4647–4650. doi:10.1143/jjap.43.4647

43. Martinez, U.; Hansen, J. Ø.; Lira, E.; Kristoffersen, H. H.; Huo, P.;
 Bechstein, R.; Lægsgaard, E.; Besenbacher, F.; Hammer, B.;
 Wendt, S. *Phys. Rev. Lett.* **2012,** *109,* 155501.
 doi:10.1103/physrevlett.109.155501

44. Chen, Z.; Zhong, W.; Liang, Z.; Li, W.; He, G.; Wang, Y.; Li, W.; Xie, Y.;
 He, Q. *J. Nanomater.* **2014,** *2014,* 298619. doi:10.1155/2014/298619

45. Henning, A.; Günzburger, G.; Jöhr, R.; Rosenwaks, Y.;
 Bozic-Weber, B.; Housecroft, C. E.; Constable, E. C.; Meyer, E.;
 Glatzel, T. *Beilstein J. Nanotechnol.* **2013,** *4,* 418–428.
 doi:10.3762/bjnano.4.49

46. Wu, M.-C.; Liao, H.-C.; Cho, Y.-C.; Tóth, G.; Chen, Y.-F.; Su, W.-F.;
 Kordás, K. *J. Mater. Chem. A* **2013,** *1,* 5715–5720.
 doi:10.1039/c3ta01011b

47. Wu, M.-C.; Liao, H.-C.; Cho, Y.-C.; Hsu, C.-P.; Lin, T.-H.; Su, W.-F.;
 Sápi, A.; Kukovecz, Á.; Kónya, Z.; Shchukarev, A.; Sarkar, A.;
 Larsson, W.; Mikkola, J.-P.; Mohl, M.; Tóth, G.; Jantunen, H.;
 Valtanen, A.; Huuhtanen, M.; Keiski, R. L.; Kordás, K.
 J. Nanopart. Res. **2014,** *16,* 2143. doi:10.1007/s11051-013-2143-y

48. Henning, A.; Rosenwaks, Y. KPFM of Nanostructured Electrochemical
 Sensors. In *Kelvin Probe Force Microscopy;* Sadewasser, S.;
 Glatzel, T., Eds.; Springer: Cham, Switzerland, 2018; pp 367–389.
 doi:10.1007/978-3-319-75687-5_12

49. Kim, H.; Kim, D.-W. *Appl. Phys. A: Mater. Sci. Process.* **2011,** *102,*
 949–953. doi:10.1007/s00339-011-6277-4

50. Swaminathan, J.; Subbiah, R.; Singaram, V. *ACS Catal.* **2016,** *6,*
 2222–2229. doi:10.1021/acscatal.5b02614

51. Wang, C.; Yin, L.; Zhang, L.; Xiang, D.; Gao, R. *Sensors* **2010,** *10,*
 2088–2106. doi:10.3390/s100302088

52. Baniecki, J. D.; Ishii, M.; Kurihara, K.; Yamanaka, K.; Yano, T.;
 Shinozaki, K.; Imada, T.; Kobayashi, Y. *J. Appl. Phys.* **2009,** *106,*
 054109. doi:10.1063/1.3169654

53. Greiner, M. T.; Chai, L.; Helander, M. G.; Tang, W.-M.; Lu, Z.-H.
 Adv. Funct. Mater. **2012,** *22,* 4557–4568. doi:10.1002/adfm.201200615

54. Susaki, T.; Makishima, A.; Hosono, H. *Phys. Rev. B* **2011,** *84,* 115456.
 doi:10.1103/physrevb.84.115456

55. Jobst, J.; Boers, L. M.; Yin, C.; Aarts, J.; Tromp, R. M.;
 van der Molen, S. J. *Ultramicroscopy* **2019,** *200,* 43–49.
 doi:10.1016/j.ultramic.2019.02.018

56. Krok, F.; Kolodziej, J. J.; Such, B.; Czuba, P.; Struski, P.;
 Piatkowski, P.; Szymonski, M. *Surf. Sci.* **2004,** *566–568,* 63–67.
 doi:10.1016/j.susc.2004.05.023

57. Melitz, W.; Shen, J.; Lee, S.; Lee, J. S.; Kummel, A. C.; Droopad, R.;
 Yu, E. T. *J. Appl. Phys.* **2010,** *108,* 023711. doi:10.1063/1.3462440

58. Jeong, H. K.; Yang, C.; Kim, B. S.; Kim, K.-j. *EPL* **2010,** *92,* 37005.
 doi:10.1209/0295-5075/92/37005

Ion mobility and material transport on KBr in air as a function of the relative humidity

Dominik J. Kirpal*, Korbinian Pürckhauer, Alfred J. Weymouth and Franz J. Giessibl

Full Research Paper

Address:
Institute of Experimental and Applied Physics, University of
Regensburg, 93040 Regensburg, Germany

Email:
Dominik J. Kirpal* - dominik.kirpal@ur.de

* Corresponding author

Abstract

Surfaces exposed to air can change their structure due to external influences such as chemical reactions or material exchange and movement. The adsorbed water layer that is present under ambient conditions plays an important role especially for highly soluble materials. Surface atoms can easily diffuse into the thin water layer and, when surface conditions are favorable, they can re-attach to the surface. We collected atomic force microscopy images of KBr surfaces in a humidity-controlled glove box at various relative humidities below 40%. By scratching and poking the surface with the AFM tip, we constructed energetically unfavorable holes or scratch sites and material accumulations and recorded the evolution of these defects as a function of the time. We observed an exponential decay of the size of the defects and material accumulations, and from this data we determined energy barriers to dissolution and aggregation of approximately 0.9 eV.

Introduction

Defining surface properties under ambient conditions is challenging as they are heavily influenced by the environment. In general, there are various contributing factors such as temperature, air pressure and air composition. Typically, air is composed of different gases, a small fraction of aerosols and water vapor. The relative humidity (RH) usually ranges from about 25% to 70%, depending on weather and season. A thin film of water molecules adsorbs on every surface exposed to humid gases [1-3].

The thickness of these water layers depends on many factors including the relative humidity, surface roughness, hydrophilicity or hydrophobicity, meniscus formation (as described later) and also air pressure and temperature [2]. In the case of freshly cleaved or dried surfaces the amount of adsorbed water also relates to the time of exposure to the humid air. The layer thickness ranges from partial coverage at very low humidities (RH < 10%) up to several nanometers near saturation. Arima et al. performed XPS measurements on potassium bromide (KBr)

thin films under UHV conditions ($4 \cdot 10^{-10}$ mbar) in order to determine the thickness as a function of the relative humidity [4]. They observed an increase of the coverage up to one monolayer at RH = 30%. This thickness remained constant up to a relative humidity of about 60%. A small increase up to RH = 80% and large increase up to 2 nm for higher humidities was recorded. It has to be taken into account that measurements at such low pressure rather relate to the outer atmosphere than to ambient conditions. However similar observations have been made by Asay et al. under ambient conditions, who showed on silicon oxide the growth of three monolayers up to RH = 30%, an additional layer forming by increasing RH to 60% and further growth of the water film up to 2.7 nm (ca. 10 monolayers) thickness at higher humidities [1].

On the atomic level, water and adsorbed molecules can arrange according to the surface structure and form ordered hydration layers that are also referred to "ice-like" [1,5-8]. The presence of water can have a large influence on the surface, especially for salt crystals. Investigations suggest that the presence of water and, as a consequence, the relative humidity have a direct influence on material transport and step movement [3,7]. The relationship between humidity, water coverage and movement speed, however, is complex.

In this study we investigated the surface of KBr, a salt crystal, by using frequency-modulation atomic force microscopy (FM-AFM) using a qPlus sensor [9-11]. The aim of our experiments is a qualitative and quantitative observation of the change and evolution of the KBr surface as a function of the relative humidity. Therefore, several artificial defects in the range of some to tens of nanometers were created and observed over a period of a few hours up to a few weeks while the relative humidity was kept within a certain range for each experiment.

Experimental

For the experiments we used a custom-designed AFM equipped with a qPlus sensor. The qPlus sensor is a stiff ($k = 1800$ N/m) self-sensing quartz sensor with a resonance frequency around $f_0 = 32$ kHz. It has enabled unprecedented results in low-temperature AFM, such as the imaging of single pentacene molecules by Gross et al. [12], intramolecular resolution of PTCDA at room temperature by Huber et al. [13], as well as the capability to perform non-destructive measurements on sensitive biological samples in air and in a liquid [14]. Moreover, it has been shown that a qPlus AFM is capable of observing material dissolution [7,15].

These studies show that the high stiffness is beneficial and allows one to use larger tips built from any appropriate tip material and to operate the AFM at small amplitudes without

risking jump to contact [7,16-19]. A small and sharp splinter of a smashed sapphire bulk crystal was used as a tip. Sapphire is a very hard material, it is hydrophobic with a contact angle to water above 80°[20], and it is chemically inert [21]. The high hardness allows us to create large artificial defects in our sample (as described later) without damaging the tip. Moreover, the hydrophobicity reduces capillary formation at the tip–sample contact area. Capillary condensation causes a locally enhanced presence of condensed water molecules [22], which might correspond to a much higher relative humidity near the apex. Furthermore, the water film and the water meniscus that forms around the tip–sample contact cause damping forces on the probe, which result in higher noise [7]. The hydrophobicity of sapphire reduces the meniscus effect. The impact that hydrophobicity or hydrophilicity of the tip material can have is demonstrated by Wastl et al. in [23], by comparing the rip-off distance of the meniscus for a sapphire and a silicon tip.

In order to observe a significant temporal evolution of the sample surface we chose KBr, a soft and easily soluble salt (650 g/L in H_2O at 20 °C) [24]. KBr crystallizes in the rock-salt structure with a lattice constant of $a = 660$ pm [25]. A clean and dry surface can be generated by cleaving the bulk crystal with a knife along the [100] direction. The surface shows large atomically flat terraces with heights ranging from one to a few atom layers. Steps, screw dislocations, small holes and islands can be observed. However, it was not possible to observe single atomic defects, as their life time is too short for the AFM imaging process [7].

The soft sample material allows us to generate large and deep artificial defects on the scale of some tens of nanometers in length and some nanometers in depth. We deliberately created two types of defects: poking holes and scratching holes. Poking holes are deep and narrow holes, created by poking the tip several nanometers into the surface. This results in a steep hole with a shape similar to the tip apex. The removed material mainly accumulates around the hole but partially attaches to the tip. Scratching holes are larger defects, created by poking the tip into the surface and then scanning quadratic or rectangular areas with a freely determined edge length, of typically some tens of nanometers. The result is an almost rectangular hole with the removed material accumulated around the defect and to a small extent attached to the tip. Most of the material accumulates at the turnaround points of the tip. The scratching technique creates larger and more reproducible holes than the poking of single points, since the shape of the tip becomes less important.

AFM enables high lateral resolution, although the imaging of structures with rough topographies is challenging. When scan-

ning rugged surfaces the back structure of the tip apex becomes more important. As the tip follows the surface while keeping the tip–sample interaction constant, side effects of the tip become more important for steep edges. The depicted structures show a convolution between the tip and sample. This may result in smeared out step edges in the images and, consequently, an amplification of convex structures such as material accumulations, as well as a reduction of concave structures [26,27] such as holes as shown in Figure 1. These artifacts can be minimized by using sharp tips with small tip angles ϕ, as defined in Figure 1. If we consider the apparent size of a surface feature with width *w* and height *h*, for a two-dimensional case, the measured cross-sectional area *A* of the elevation (+) or hole (−) is given by:

$$A = hw \pm h^2 \tan(\phi),\qquad(1)$$

and the measured volume *V* for circular structures having the real volume of $\pi h(w/2)^2$ is given by:

$$V = \pi h \left(\frac{w^2}{4} \pm \frac{wh}{2} \tan(\phi) + \frac{h^2}{3} \tan^2(\phi) \right).\qquad(2)$$

Thus, even if only the material from a hole ends up forming an elevation, the measured volume of the elevation is apparently larger than the volume of the hole.
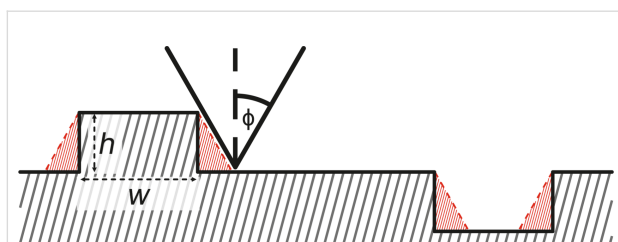

Figure 1: 1D schematic of the tip–sample convolution at islands and holes. Due to the tip geometry step edges appear smeared out. Consequently, accumulations appear to be larger and holes smaller. The red hatched areas show the misassigned volumes at step edges. This effect is more pronounced for large tip angles (blunt tips) compared to small angles (sharp tips).

The relative humidity in laboratories without air conditioning usually ranges from 25 to 60%. In order to provide a stable relative humidity for time periods up to some weeks, the microscope was placed into a glove-box. The humidity inside the box can be increased by evaporating water or decreased by using the drying effect of silica gel. With this setup, RH values below 2%

can be obtained. The desired humidity can be reached within a time scale ranging from some minutes up to a few hours. Without active influence the air humidity remains quite constant with a maximum rate of change of less than one percent per hour. The humidity was continuously measured and, if needed, adjusted during the measurement process.

All AFM experiments were performed in the frequency-modulation mode with a qPlus sensor with a resonance frequency of 29 to 33 kHz and a stiffness of $k = 1.8$ kN/m. Typical image parameters were an amplitude $A = 500$ pm and a frequency-shift set point of $\Delta f = +10$ to $+25$ Hz. Data and image processing was performed with MATLAB (The MathWorks, Inc.) and WSxM [28].

Results and Discussion
Initial experiments with poking holes

This experiment shall investigate qualitatively how the material transport rate changes with humidity RH in a range of 18.8% < RH < 35.1%. Several holes and accumulations of different size and shape were induced by poking the tip several nanometers into the surface. The defects initially have a conical shape with depths ranging from 1 to 18 nm and diameters between 100 and 200 nm. The depth of the defects is defined by the height difference between the lowest point of the defect and the surrounding terrace. The removed material aggregates around the artificial defect. The accumulations do not attach symmetrically but irregularly around the holes. This can be explained by the shape and angular orientation of the tip towards the surface. The consecutive images displayed in Figure 2 are 1.5 µm × 1.0 µm sections of the continuously scanned area and show the time evolution of the shape of the holes.

During this experiment the humidity changed over time. We can devide the experiment into three sections, defined by the relative humidity. The time evolution of the first section, 20.5% < RH < 25.0% for the first 27 h can be seen by comparing Figure 2a to Figure 2b. The first period shows a slow erosion of the accumulated material and a filling of the defects from the bottom. The accumulated material around both top structures and the middle left structure slightly decreases. For the other three structures a slight spread of the accumulated material can be observed. The lowest levels of the middle and bottom left defects get filled.

In the second section the relative humidity ranges from 25.0% to 35.1% within a time period of 46 h. Figure 2b and Figure 2c show the surface topography directly before and after this period. It can be observed that the accumulated material around the top right and the middle left structure has completely eroded. Also, for the other structures only a fraction of the

Figure 2: 1.5 μm × 1.0μm sections showing the time evolution of artificial defects and accumulations in three ranges of relative humidity. (a to b) 1st range: 20.5% < RH < 25.0%, t = 0–27 h); (b to c) 2nd range: 25.0% < RH < 35.1%, t = 27–73 h; (c to d) 3rd range: 18.5% < RH < 23.0%, image (c) was recorded directly after decreasing the humidity at t = 76 h). In image (a) the holes are denominated from A to F for depth comparison below in Figure 3. Measurement parameters: f_0 = 32893 Hz, A = 500 pm, Δf = 20 Hz.

$$\frac{\mathrm{d}\Delta z}{\mathrm{d}t} = \frac{1}{A_{\text{sub-hole}}} V_t = \frac{2\pi R_1 c_{V_t}}{\pi r_1^2}, \tag{3}$$

with $A_{\text{sub–hole}}$ being the area of the layer being filled. The r_1^{-2} relation shows why small and steep holes fill up faster than larger and shallow structures. For steep accumulations this results in a spreading of the material from the higher levels into the surrounding area, which can be observed in the experiment described in the next section.

In the third section the relative humidity ranges from 18.5% < RH < 23.0%. Figure 2c and Figure 2d show the time evolution within the next 145 h. The amount of accumulated material of the bottom right and the middle right structure has further decreased, yet less significant compared to the previous section. Only the lowest level of the middle and bottom holes have partially filled. The time evolution of the maximum depth is displayed in Figure 3. During the first period the steep holes (especially D and F) show significant a decrease in depth that continues (see D and F) or is enhanced (see E) for the second period. The third section only shows small changes.

initial volume is left. All holes appear to be less deep and show an increased diameter. This increase can be understood by considering a simple picture in which the additional energetic cost of a hole can be described by the length of its edge. This model is based on the Terrace Step Kink model as described in Ref. [29]. If we were to start with a defect that has the first layer removed in a circle with radius R_1 and a second (deeper) layer removed in a circle with radius $r_1 < R_1$, this would yield an energy term for the edge $E_1 \propto 2\pi R_1 + 2\pi r_1$. The defect now evolves, maintaining the total volume of the hole to a single-layer circular defect with radius R_2. Conservation of volume requires

$$R_2 = \sqrt{R_1^2 + r_1^2},$$

but now the corresponding energy of the edge is smaller,

$$E_2 \propto 2\pi R_2 = \pi \sqrt{R_1^2 + r_1^2} < E_1.$$

An illustrative drawing can be found in Supporting Information File 1, Figure S5. The material that is filling the smaller hole in the second layer is removed from the edge of the first layer. Therefore the dissolved volume per time v_t is proportional to the edge length $2\pi R_1$ with $V_t = 2\pi R_1 c_{V_t}$, where $[c_{V_t}]$ = m²/s is the material transport coefficient. This results in a depth change $d\Delta z/dt$:

Figure 3: Maximum depth of the observed holes over time. The poking holes to which the letters correspond is displayed in Figure 2 a). The blue highlighted area shows the second time period with RH > 25%. Only holes (B,C,F) are displayed, the full graph is displayed in Supporting Information File 1.

This experiment indicates that the material transport for steep structures is significantly enhanced driven by the energetically unfavorable form (large surface-to-volume ratio). A contribution of the relative humidity cannot be derived readily from this experiment. The tip–sample-convolution effect described above

appears to be a dominant factor. For that reason, further experiments were performed by scratching holes into the substrate.

Scratching holes at RH < 6%

In this experiment the surface was exposed to very dry air below RH < 6%. Therefore, a low coverage of the surface with water molecules is expected. When probing the surface at such low humidity, the mobility of ions is expected to be reduced.

A large rectangular defect with an edge length of about 80 nm × 60 nm with a depth of up to 4.3 nm (see Figure 4) was created with the scratching technique described above. The removed material accumulated in several nanometer thick and up to 7.0 nm high walls around the hole. The area was scanned only once every few days to minimize the effects of tip-induced material transport. In the seven days of observation the relative humidity was kept between 3.0% ≤ RH ≤ 5.5%.
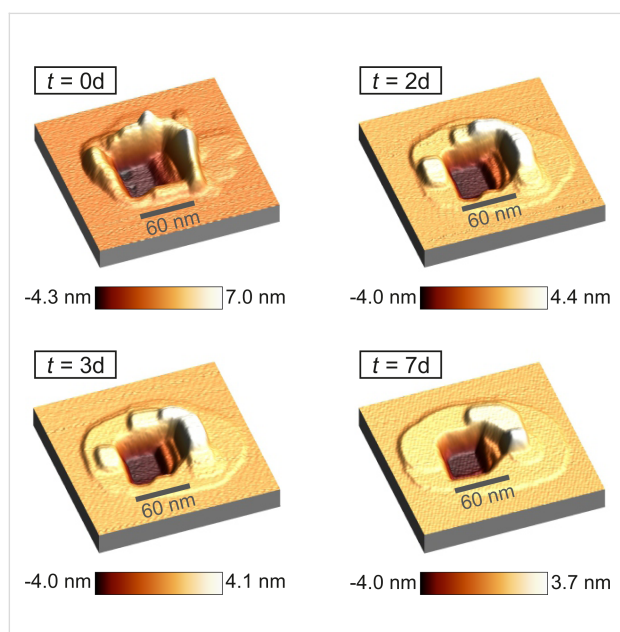

Figure 4: 200 nm × 200 nm 3D profile image of the generated scratching site directly taken after generating, after two, three and seven days at 3.0 < RH < 5.5%. The lowest levels of the hole fill until the second measurement, yet the maximum depth remains constant afterwards. The higher levels accumulated material erodes more quickly. A spread of the material around the defect can be observed. Measurement parameters: f_0 = 31785 Hz, A = 500 pm, Δf = 25 Hz.

In order to evaluate the size of the accumulation and the defect every measurement point that differs more than 165 pm (half an atomic step height) from the average height of the surrounding plain ($z = 0$) is referred as part of the hole or the accumulation. The volume is obtained by adding up the height of all corresponding measurement points multiplied with the size per point. The total volume of the hole or accumulation therefore can be expressed by

$$V_{\text{def/acc}} = \frac{A_{\text{scan}}}{N_{\text{p}}} \sum_{i_{\pm z > 165\,\text{pm}}} z_i, \tag{4}$$

where A_{scan} is the size of the total scan area and N_{p} is the number of measurement points.

Over a period of seven days significant changes of the studied structure can be observed. The accumulation erodes quite fast at the beginning and spreads out to the surrounding area. Initially, the defect was surrounded by walls which were up to 35 nm thick and up to 7 nm high. After two days the maximum height decreased to 4 nm and a single atom layer is spreading around the structure. At the defect a rounding of the corners can be observed. These processes continue over time.

Figure 5 shows the size and change rate for each image. It can be seen that the change of the material accumulation is much larger than that of the defect. This would mean a loss of material as the total change rates do not match. This can be due to the amplification/reduction effect of steep convex/concave structures as described above. Furthermore, this scan area is not a closed system and allows for material exchange with the surroundings. Also material gets removed by the tip. However, there is one important observation to be made: Slow material movement still takes place despite the very low humidity. The observed slower filling of the defect compared to the erosion of the accumulated material could be either a measurement artifact (assisted mobility) or a real physical effect. While in this example it is difficult to differentiate, further examples shown in this work all show a similar pattern that the accumulated material erodes quicker than the defect fills. This makes us conclude that it is indeed a real physical effect.
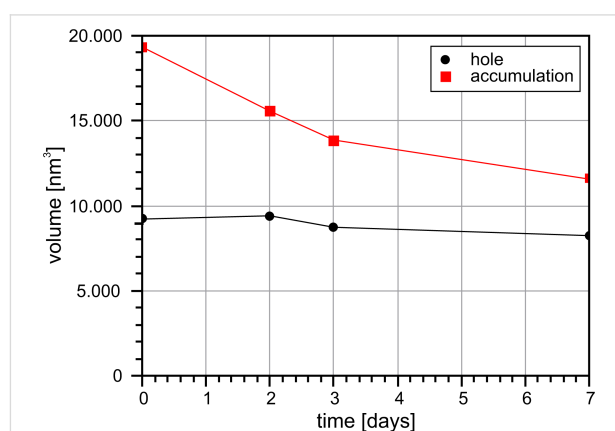

Figure 5: Volume of the hole and accumulation at 3.0% < RH < 5.5% within seven days. No significant change in the volume of the hole can be observed in this time period. The accumulation appears to be larger and show a higher material transport than the hole. However, these values are influenced by the tip–sample convolution.

Scratching holes at 12% < RH < 20%

In this experiment material transport was investigated at relative humidities from 12% ≤ RH ≤ 16% for 15 days and then it was linearly increased by about ΔRH = 1% per 19 h to investigate whether this affects the transport rate. The temperature was 20 ± 1 °C. A rectangular defect with edge lengths of about 95 nm × 80 nm and a maximum depth of 7.0 nm was created. The accumulation has an apparent initially volume of approximately 136000 nm² and the defect has an approximate volume of 72000 nm². The time evolution of the structure is shown in Figure 6 and Figure 7 (graph). It can be seen that after an initial settling time the accumulation, as well as the defect, get exponentially smaller, until the size drops below a certain value.

The phenomenon of an enhanced material transport directly after creating a structure can be explained by the sample material being ripped out of the crystal structure during the scratching process. Now, the material is likely no longer in a monocrystalline configuration like the bulk material. The material accumulation therefore is less stable and more mobile. This hypothesis explains the increased volume change during the first hours compared to the exponential decrease afterwards. Conversely, this results in an increased availability of material and a quicker filling of the hole.

The accumulated material erodes faster than the hole is filled. The accumulation completely eroded after about 12.5 days. At this time the volume of the hole has shrunk to 17% of its initial volume. About 2.5 days later we started to increase the relative humidity, marked by the blue dashed vertical line. The expo-
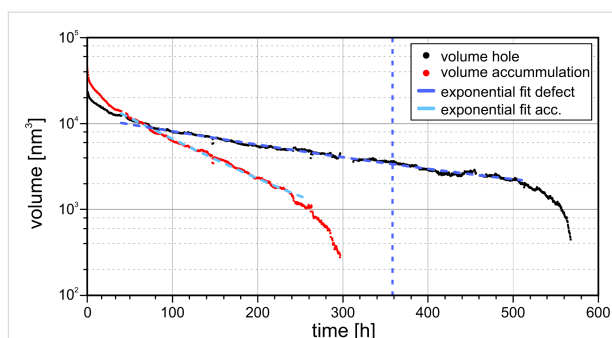
Figure 7: Time evolution of both defect and accumulation volume. After an initial settling time the logarithmically scaled size values show a linear behavior, which corresponds to an exponential decrease (see solution of differential Equation 5). The dashed blue vertical line corresponds to the point after which the relative humidity was increased linearly from RH = 12.9% to 19.9% until complete filling. The exponential behavior is not affected. When the structure volumes fall below a certain size (accumulation: t > 250 h, hole: t > 510 h) the transport rate increases and now corresponds to Eqaution Equation 10. Measurement parameters: f_0 = 29302 Hz, A = 500 pm, Δf = 10 Hz.

nential decrease of the hole did not significantly change with the increase of humidity, but rather when it fell below a certain size at approximately t = 510 h, when the humidity reached RH = 17.9%. When the hole completely filled, the relative humidity had reached 19.9%.

For a quantitative description of this behavior we consider the sample material to be able to take two different states: (1) In the bound state the K⁺/Br⁻-Ions are immobilized on the surface. This state is observed by the AFM technique as the surface topography. (2) In the second state the ions are dissolved in the
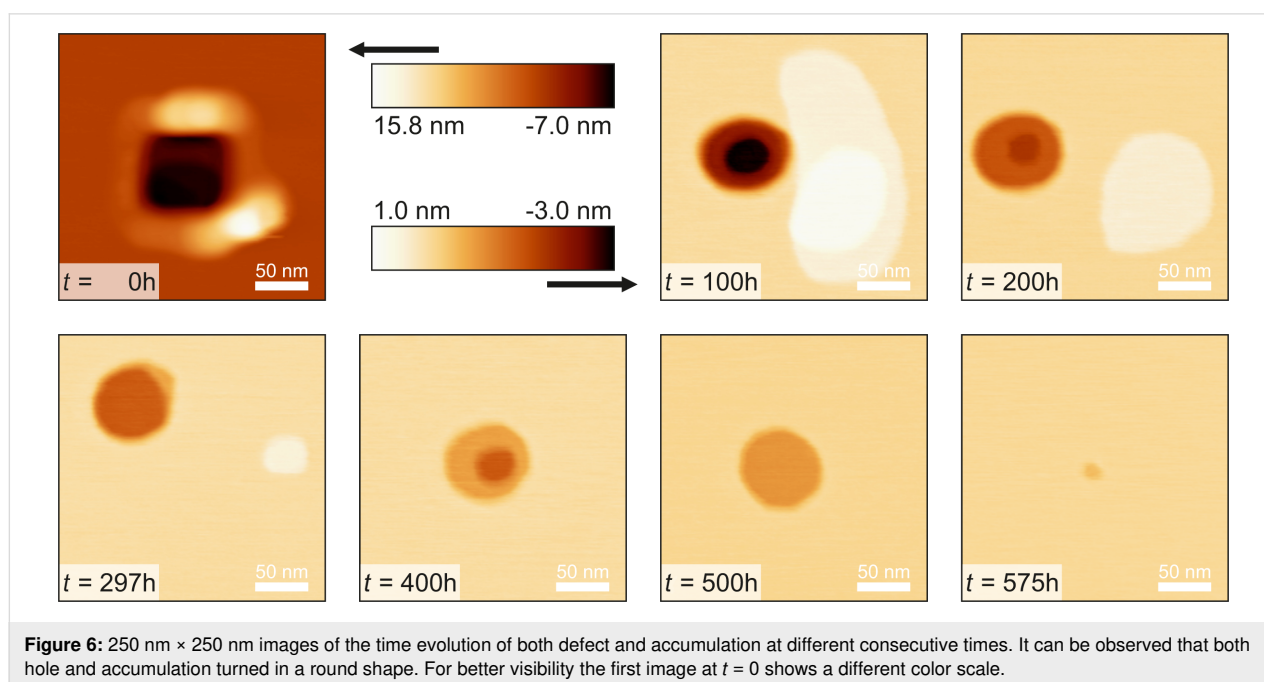
Figure 6: 250 nm × 250 nm images of the time evolution of both defect and accumulation at different consecutive times. It can be observed that both hole and accumulation turned in a round shape. For better visibility the first image at t = 0 shows a different color scale.

hydration layer or in a physiosorbed or precursor state [30], which shows a high mobility and cannot be imaged. The material from the accumulation over time changes from the first state into the second state and from the second state into the first state, attaching to the hole. These transitions require each atom to overcome an energy barrier E_b. The change rate can be expressed by

$$\frac{dN}{dt} = -\nu N \cdot \exp\left(-\frac{E_b}{k_B T}\right), \qquad (5)$$

with N being the size of the observed structure, ν the attempt frequency to overcome the energy barrier, k_B the Boltzmann constant and T the temperature. We assume an attempt rate of $\nu = 10^{13}$ s^{-1}, which is in the order of magnitude of a KBr phonon [31], equal for both transitions. This differential equation can be solved by an exponential decaying function of the form $N(t) = N_0 \cdot \exp(-t/\tau)$, with N_0 being the structure size at the time $t = 0$ (in this case the time after the initial enhanced transport) and $1/\tau$ the exponential decay rate. This allows us to calculate a value for the energy barrier from the recorded data, given by

$$E_b = k_B T \ln(\tau \nu). \qquad (6)$$

As we consider the exponential decay rate to be constant we obtain a value for the energy barrier of $E_{b,acc} = 875$ meV for the accumulation and $E_{b,def} = 895$ meV for the defect. The calculated values vary by less than 6.8% when ν is altered by one order of magnitude. If we calculate the barrier for the defect before and after the point of increasing the relative humidity separately our results differ by less than 2.6%.

To explain the non-exponential behavior as the accumulation and defect get smaller, a different model is required. In the model described above the ions dissolve or adsorb at any position of the interface of the structures, which then rearranges into the energetically more favorable round shape. For smaller sizes a further effect becomes dominant. As the step edges make up the highest energy cost of the surface configuration they are more reactive than the rest of the surface. The ions face a lower energy barrier and if the ratio between edge length and structure size is large enough the material transport is mainly driven by adsorption and dissolution at the step edges. To understand why that would lead to higher material transport, we consider a circular accumulation or defect with a total number of atoms N. With a radius r and interatomic spacing of a:

$$N = \pi \frac{r^2}{a^2} \Leftrightarrow r = \sqrt{N} \frac{a}{\sqrt{\pi}}. \qquad (7)$$

The number of atoms at the step edge N_e can be described by

$$N_e \approx \frac{2\pi r}{a} = 2\sqrt{\pi}\sqrt{N}. \qquad (8)$$

If material transport is confined to the edges, then (see Equation 5):

$$\frac{dN}{dt} = -\nu N_e \exp\left(\frac{-E_{b,e}}{k_B T}\right) = -2\nu\sqrt{\pi}\sqrt{N}\exp\left(\frac{-E_{b,e}}{k_B T}\right), \qquad (9)$$

with $E_{b,e}$ being the energy barrier height at the step edge. This yields a solution of the form

$$N(t) = \left(\sqrt{N_0} - c_e t\right)^2, \qquad (10)$$

with $c_e = \nu\sqrt{\pi}\exp(-E_{b,e}/k_B T)$, and explains the increased decay of the structure volumes as their size decreases.

Further measurements at a relative humidity in a similar range of 14.5% < RH < 18.5% are shown in Figure S6 in Supporting Information File 1. Several structures of different volumes were observed and show a similar behavior. The accumulated material erodes faster than the holes fill. Slow material transport (compared to the experiment at RH = 28%, next section) is taking place. The smallest structure fills within less than 200 h whereas no significant change in volume for the largest structures can be observed. These measurements are not included to this manuscript as they were created by poking but not with scratching. The measurement of the exact volumes therefore may be imprecise.

Scratching a hole at RH = 28%

In this experiment a scratching defect at *RH* = 28.1% and $T = 22$ °C was observed. A coverage between one and three molecular water layers is expected [1,4]. A quick first image was taken immediately after creation of the defect (see Supporting Information File 1, Figure S1). Already in this first image, the hole does not appear as a square, as it did in Figure 4, but rather it is already rounded.

The sample was then continuously scanned with a period of $t = 1050$ s = 17.5 min per frame, shown in Figure 8. Each measurement point was assigned to a certain atom layer and represents an area of 1 nm^2. For a quantitative analysis of the materi-
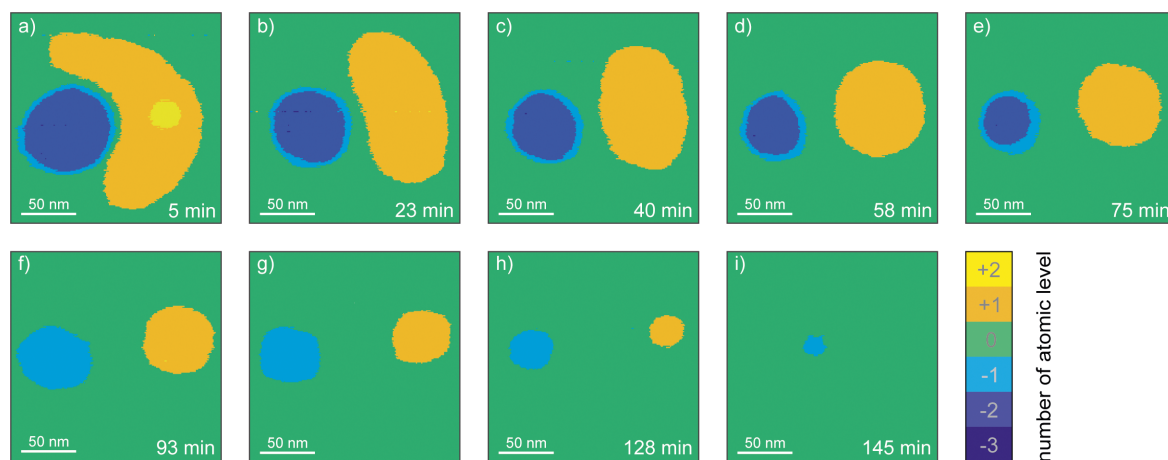
Figure 8: 200 nm × 200 nm sections of the time evolution of the scratching site at RH = 28.2%. Each image is measured within 17.5 min starting about 5 min after the creation. The initial rectangular scratching site adopts in a few minutes a circular form. Similarly the material accumulation erodes faster on the sharp margins and also adopts a circular form. The small second layer erodes after some minutes. The hole, already after a few minutes is largely two atomic layers deep. The accumulation completely erodes some minutes faster than the deepening. Measurement parameters: f_0 = 32873 Hz, A = 500 pm, Δf = 20 Hz.

al movement, the topographic images of this experiment were converted from the continuous height scale into a discrete scale.

The volume of the defect and the accumulation are shown as a function of time in Figure 9 and in Table S1 in Supporting Information File 1. Again, there is an exponential relationship until approx. minute 100. Regarding this time period, we applied the same analysis as we did earlier, and obtained the values for the transition energy barrier of $E_{b,acc}$ = 867 meV for the accumulation and $E_{b,def}$ = 874 meV for the hole.

The experiment at a relative humidity of 14.5% < RH < 18.5% in Figure S6 in Supporting Information File 1 (described in the previous section) show structures of different volumes, larger as well as smaller than the defect in this experiment. However, even the smallest hole (smaller than here) is filled in a time period that is one to two orders of magnitude longer. This observation supports the interpretation that in this experiment the material transport is dominantly affected by the relative humidity and is significantly increased compared to values below RH < 20%.

Conclusion

Our studies of defect healing and erosion of accumulations in various ranges of relative humidity have shown that the speed of the material movement depends on several factors including the relative humidity, and size and shape of the accumulation or defect. Directly after the scratching process the material that is ripped out of the crystal structure does not fully realign. Therefore, it is less stable and more mobile or more likely to dissolve in the water film. This leads to a short time period where the

Figure 9: Time course of the size and change rate of the observed defect (upper position) and accumulation (lower position) at RH = 28.2%. For larger structures the total size shows an (approximately) linear decrease on a logarithmic scale. The relative change describes the ratio between the transported material and the previous structure volume per each timestep of 1050 s. For larger structures this value stays roughly constant.

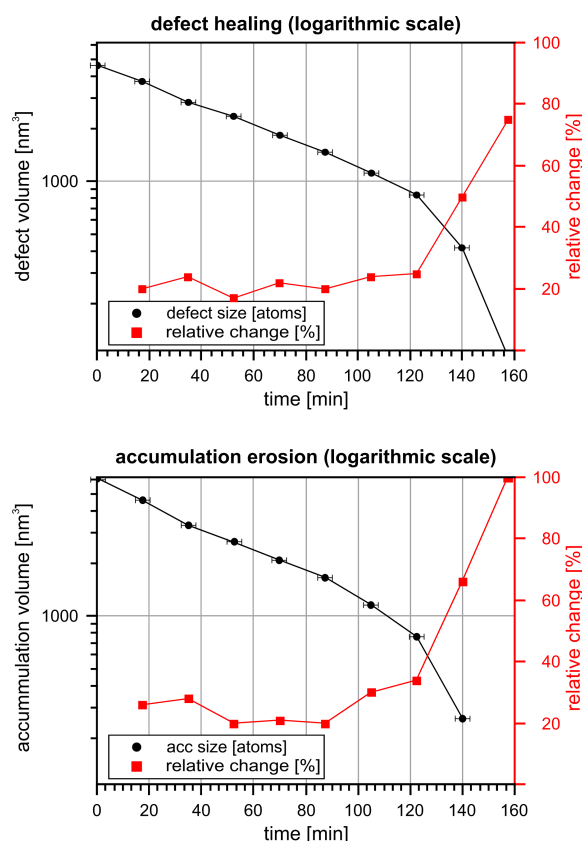transport rate is strongly enhanced. The relative humidity is one of the most important factors, but it has a non-linear effect on material transport. It has been shown that material transport is still possible at very low relative humidities. It also has been observed that artificially generated material accumulations are less stable than holes. Furthermore, small structures show a large surface compared to the volume and are, therefore, energetically less favorable. This results in the healing of small defects within a few hours to a few days, whereas larger defect may remain without significant changes over a period of some weeks.

Supporting Information

Supporting Information File 1
Additional experimental data.
[https://www.beilstein-journals.org/bjnano/content/supplementary/2190-4286-10-203-S1.pdf]

Acknowledgements

ORCID® iDs
Dominik J. Kirpal - https://orcid.org/0000-0001-5382-196X
Korbinian Pürckhauer - https://orcid.org/0000-0002-5687-7464
Alfred J. Weymouth - https://orcid.org/0000-0001-8793-9368
Franz J. Giessibl - https://orcid.org/0000-0002-5585-1326

References

1. Asay, D. B.; Kim, S. H. *J. Phys. Chem. B* **2005,** *109,* 16760–16763. doi:10.1021/jp053042o
2. Ewing, G. E. *Chem. Rev.* **2006,** *106,* 1511–1526. doi:10.1021/cr040369x
3. Luna, M.; Rieutord, F.; Melman, N. A.; Dai, Q.; Salmeron, M. *J. Phys. Chem. A* **1998,** *102,* 6793–6800. doi:10.1021/jp9820875
4. Arima, K.; Jiang, P.; Deng, X.; Bluhm, H.; Salmeron, M. *J. Phys. Chem. C* **2010,** *114,* 14900–14906. doi:10.1021/jp101683z
5. Hu, J.; Xiao, X.-D.; Ogletree, D. F.; Salmeron, M. *Science* **1995,** *268,* 267–269. doi:10.1126/science.268.5208.267
6. Miranda, P. B.; Xu, L.; Shen, Y. R.; Salmeron, M. *Phys. Rev. Lett.* **1998,** *81,* 5876–5879. doi:10.1103/physrevlett.81.5876
7. Wastl, D. S.; Weymouth, A. J.; Giessibl, F. J. *Phys. Rev. B* **2013,** *87,* 245415. doi:10.1103/physrevb.87.245415
8. Pürckhauer, K.; Kirpal, D.; Weymouth, A. J.; Giessibl, F. J. *ACS Appl. Nano Mater.* **2019,** *2,* 2593–2598. doi:10.1021/acsanm.9b00526
9. Giessibl, F. J. Device for contactless scanning of surface. DE DE19633546A1, Feb 26, 1998.
10. Giessibl, F. J. *Appl. Phys. Lett.* **1998,** *73,* 3956. doi:10.1063/1.122948
11. Giessibl, F. J. *Rev. Sci. Instrum.* **2019,** *90,* 011101. doi:10.1063/1.5052264
12. Gross, L.; Mohn, F.; Moll, N.; Liljeroth, P.; Meyer, G. *Science* **2009,** *325,* 1110–1114. doi:10.1126/science.1176210
13. Huber, F.; Matencio, S.; Weymouth, A. J.; Ocal, C.; Barrena, E.; Giessibl, F. J. *Phys. Rev. Lett.* **2015,** *115,* 066101. doi:10.1103/physrevlett.115.066101
14. Pürckhauer, K.; Weymouth, A. J.; Pfeffer, K.; Kullmann, L.; Mulvihill, E.; Krahn, M. P.; Müller, D. J.; Giessibl, F. J. *Sci. Rep.* **2018,** *8,* 9330. doi:10.1038/s41598-018-27608-6
15. Ichii, T.; Negami, M.; Sugimura, H. *J. Phys. Chem. C* **2014,** *118,* 26803–26807. doi:10.1021/jp5078505
16. Ooe, H.; Kirpal, D.; Wastl, D. S.; Weymouth, A. J.; Arai, T.; Giessibl, F. J. *Appl. Phys. Lett.* **2016,** *109,* 141603. doi:10.1063/1.4964125
17. Burnham, N. A.; Colton, R. J. *J. Vac. Sci. Technol., A* **1989,** *7,* 2906–2913. doi:10.1116/1.576168
18. Giessibl, F. J. *Phys. Rev. B* **1997,** *56,* 16010–16015. doi:10.1103/physrevb.56.16010
19. Giessibl, F. J.; Bielefeldt, H.; Hembacher, S.; Mannhart, J. *Appl. Surf. Sci.* **1999,** *140,* 352–357. doi:10.1016/s0169-4332(98)00553-4
20. Gorb, E. V.; Hosoda, N.; Miksch, C.; Gorb, S. N. *J. R. Soc., Interface* **2010,** *7,* 1571–1579. doi:10.1098/rsif.2010.0081
21. Pishchik, V.; Lytvynov, L. A.; Dobrovinskaya, E. R. *Sapphire;* Springer US: Boston, MA, U.S.A., 2009. doi:10.1007/978-0-387-85695-7
22. Wei, Z.; Zhao, Y.-P. *J. Phys. D: Appl. Phys.* **2007,** *40,* 4368–4375. doi:10.1088/0022-3727/40/14/036
23. Wastl, D. S.; Weymouth, A. J.; Giessibl, F. J. *ACS Nano* **2014,** *8,* 5233–5239. doi:10.1021/nn501696q
24. Haynes, W. M. *CRC Handbook of Chemistry and Physics,* 96th ed.; CRC Press, 2015.
25. Giessibl, F. J.; Binnig, G. *Ultramicroscopy* **1992,** *42–44,* 281–289. doi:10.1016/0304-3991(92)90280-w
26. Odin, C.; Aimé, J. P.; El Kaakour, Z.; Bouhacina, T. *Surf. Sci.* **1994,** *317,* 321–340. doi:10.1016/0039-6028(94)90288-7
27. Winzer, A. T.; Kraft, C.; Bhushan, S.; Stepanenko, V.; Tessmer, I. *Ultramicroscopy* **2012,** *121,* 8–15. doi:10.1016/j.ultramic.2012.07.002
28. Horcas, I.; Fernández, R.; Gómez-Rodríguez, J. M.; Colchero, J.; Gómez-Herrero, J.; Baro, A. M. *Rev. Sci. Instrum.* **2007,** *78,* 013705. doi:10.1063/1.2432410
29. Oura, K.; Katayama, M.; Zotov, A. V.; Lifshits, V. G.; Saranin, A. A. *Surface Science;* Springer: Berlin, Germany, 2003. doi:10.1007/978-3-662-05179-5
30. Brown, D. E.; Moffatt, D. J.; Wolkow, R. A. *Science* **1998,** *279,* 542–544. doi:10.1126/science.279.5350.542
31. Safron, S. A.; Duan, J.; Bishop, G. G.; Gillman, E. S.; Skofronick, J. G. *J. Phys. Chem.* **1993,** *97,* 1749–1757. doi:10.1021/j100111a008

Integration of sharp silicon nitride tips into high-speed SU8 cantilevers in a batch fabrication process

Nahid Hosseini[1], Matthias Neuenschwander[1], Oliver Peric[1], Santiago H. Andany[1], Jonathan D. Adams[1,2] and Georg E. Fantner[*1]

Abstract

Employing polymer cantilevers has shown to outperform using their silicon or silicon nitride analogues concerning the imaging speed of atomic force microscopy (AFM) in tapping mode (intermittent contact mode with amplitude modulation) by up to one order of magnitude. However, tips of the cantilever made out of a polymer material do not meet the requirements for tip sharpness and durability. Combining the high imaging bandwidth of polymer cantilevers with making sharp and wear-resistant tips is essential for a future adoption of polymer cantilevers in routine AFM use. In this work, we have developed a batch fabrication process to integrate silicon nitride tips with an average tip radius of 9 ± 2 nm into high-speed SU8 cantilevers. Key aspects of the process are the mechanical anchoring of a moulded silicon nitride tip and a two-step release process. The fabrication recipe can be adjusted to any photo-processable polymer cantilever.

Introduction

Atomic force microscopy (AFM) cantilevers have been developed for numerous applications since the invention of scanning probe microscopy (SPM) [1]. Quality and accuracy of an AFM image strongly depend on the tip geometry since the image topography is the convolution of the surface topography and the cantilever tip geometry [2]. More precisely, the resulting images suffer from the effect of dilation [3]. AFM images with tip artefacts are of reduced quality and can seriously mislead users [4]. New fabrication methods have enabled increased tip sharpness and uniformity, so that commercial AFM cantilevers now have a standard tip quality. A range of specialized AFM techniques require custom tip designs, including high-speed AFM [5,6], high-resolution electrochemical and nanoelectrical imaging [7,8], Raman spectroscopy [9], nanoindentation [10], nanomechanical machining [11], plasmonic applications [12,13] and microscale grapping [14].

In parallel with the development of AFM cantilevers made out of traditional materials (e.g., silicon, silicon nitride and silicon oxide), polymer cantilevers have gained attention due to their ease of fabrication, their versatility [15-19] and their potential for fabricating low spring constant cantilevers [20]. For instance, the microfabrication process of SU8 cantilevers has a high fabrication yield and an easy bottom-up recipe. Genolet et al. have shown AFM images of DNA-plasmid molecules using SU8 cantilevers [21]. SU8-based Hall effect sensor cantilevers have also been presented by Mouaziz and co-workers [22].

In addition, SU8 cantilevers have shown a performance of high-speed amplitude modulation AFM (HS-AM-AFM) enhanced by up to one order of magnitude due to their low mechanical quality factor (Q-factor) and hence their high mechanical bandwidth [23]. A tip made of SU8 or other structural polymers can be integrated into a polymer cantilever by moulding. Such tips have been prepared with acceptable radii for many imaging purposes [20]. However, the wear rate of SU8 is very high [24], which makes this and other polymers a nonideal tip material. Some attempts to coat SU8 cantilevers and tips with a more wear-resistant material (such as graphene) have been made [25], but yielded blunt tips (the tip radius increased by an order of magnitude).

Lee et al. have shown that hydrogel AFM cantilevers fabricated by replica moulding and UV curing have great potential for tuning the mechanical properties of the tip, its shape and the surface functionalization [26]. However, the fabrication of hydrogel probes requires processes that involve individual alignment and bonding [27].

The present work aims to overcome the primary limitation of polymer AFM cantilevers, namely the poor wear rate of polymer tips, by integrating a tip element made of a traditional tip material. The main concept of this work is to partially embed the tip into the cantilever body, such that the attachment between the tip and the polymer is of a mechanical nature. We have developed a batch fabrication process to integrate silicon nitride tips into SU8 cantilevers. The whole structure, except for the tip, is made of SU8 to benefit from the ease of fabrication and the high-speed imaging capability of cantilevers made of this polymer, while oxide-sharpened silicon nitride tips provide tip sharpness and tip wear-resistance. The tip is anchored securely by being partially embedded in the polymer cantilever. These probes therefore have the advantage of a fast mechanical response, and the tip is made from a material that is known and accepted in the field as suitable for high-quality tips.

Cantilever Fabrication

The cantilever is made of SU8 and the tip is entirely covered with low-stress silicon nitride (LSNT). Pyramidal tips are made based on an indirect tip fabrication process [28] by etching a mould into a 380 µm thick single-side polished silicon (100) wafer. Figure 1a shows the summarized process flow, outlining the important steps.

(i) A 20 nm LSNT thin film is layered onto a silicon (100) wafer by low-pressure chemical vapor deposition. Circular

Figure 1: Batch fabrication process of LSNT-tip SU8 cantilevers. (a) Summarized process flow. (b) SEM image of the LSNT and the silicon oxide layers where the silicon underneath has been etched (step iv). (c) SEM image of a single cantilever. The pyramidal tip consists of four {111}-planes and has a half-cone angle of 35°. It is aligned with the cantilever. (d) Optical photograph of the released cantilevers.

openings (20 μm diameter) are then cut into the layer by electron-beam lithography. The LSNT mask is dry-etched before the moulds are structured by anisotropic KOH (40% at 60 °C) etching. The formation of {111} facets results in four-sided pyramidal pits. The diameter of the circular openings defines the final height of the tips and can be tuned. (ii) The LSNT mask is removed in HF 50%. Afterwards, a 400 nm wet silicon oxide layer and a 100 nm LSNT layer are deposited on the wafer. The 400 nm silicon oxide layer improves the tip sharpness by oxidation sharpening [29]. Studies report a 30% decrease of the oxide thickness along the sharp silicon ridges after wet oxidation at 900–950 °C [30]. This decrease is due to an increase of the activation barrier of the interfacial reactions induced by the stress build-up in these areas [31]. Due to the nonlinear growth of the silicon oxide, the oxide layer becomes thinner at the inside corner of the pyramidal moulds than at the mould faces. The silicon oxide layer forms a concave curvature on each face of the four-sided pyramidal moulds, which is then projected onto the subsequent LSNT layer. (iii) The silicon oxide and the LSNT layers are patterned by photolithography to cover only the etched pits. (iv) Deep reactive ion etching (DRIE) is used to etch the silicon vertically and laterally (4 and 1 μm, respectively) in order to provide access for the SU8 polymer to fill the base of the tips in the subsequent steps. Figure 1b shows the SEM image of this step. (v) All SU8 (GM1050, GM1060 and GM1075, Gersteltec, Pully, Switzerland) structural layers, the cantilever beam and the three layers of the chip body are patterned by photolithography. A three-layer chip body with an offset between the successive layers is required especially for shorter cantilevers, so that the chip body does not obstruct the path of the laser for the optical readout. The thicknesses of the chip body layers are, from bottom to top, 30, 120 and 150 μm. The geometry of the SU8 beam defines the resonance frequency of the cantilever (f_0) and the spring constant (k). (vi) The process is designed for top release, so the wafer is treated with DRIE to create a freestanding SU8 beam with the embedded silicon nitride tip encased in a protective oxide. (vii) The release process is finalized by placing the wafer in KOH (23% at 90 °C) to separate the SU8 cantilevers from the wafer. The silicon oxide layer on the tips is then stripped using buffered hydrofluoric acid. The process is completed by titanium–gold (5–20 nm) sputtering on the chip-body side of the cantilevers. This layer serves as the reflective metal coating required for the optical beam deflection read out. Figure 1c and Figure 1d show the SEM and the optical images of the released cantilevers fabricated by this process.

Results

The primary goals of the fabrication of AFM cantilevers for general imaging purposes are to enhance the tip sharpness, improve the tip durability and to increase the detection speed

and sensitivity. The detection speed in amplitude-modulation mode is determined by the amplitude response time of the cantilever. The tapping-mode bandwidth is given by BW = $\pi f_0/Q$, where f_0 is the resonance frequency and Q is the Q-factor [32]. The resonance frequency for a rectangular cantilever with homogenous material properties and no external load is given by

$$f_0 = \frac{1.758}{\pi l^2} \sqrt{\frac{I}{A}} \sqrt{\frac{E}{\rho}},$$

where E is the elastic modulus, I the second moment of area, ρ the density and A the cross-sectional area of the cantilever beam. Thus, the resonance frequency depends on the properties of the cantilever material, which are presented as $\sqrt{E/\rho}$. On the other hand, $1/Q$ is strongly influenced by the intrinsic damping η_i of the cantilever material. Therefore, optimizing the ratio $\pi f_0/Q$ translates into optimizing the ratio $\eta_i \sqrt{E/\rho}$, which has been defined as material bandwidth product [23]. SU8 cantilevers have shown a high imaging speed due to the high material bandwidth product, which mainly results from the high intrinsic damping properties of the polymer. Such cantilevers have high resonance frequencies and low Q-factors for a given size and stiffness [23]. However, SU8 tips wear down quickly and become blunt when they encounter hard surfaces with high aspect ratio features [24]. The SU8 cantilever fabrication process that we have developed has overcome this issue by incorporating hard LSNT-tips into the process without sacrificing the high detection bandwidth of the polymer levers.

To quantify the tip sharpness, 20 randomly chosen LSNT-tip SU8 cantilevers have been tested with a polycrystalline titanium roughness sample. The images were taken using a NanoScope-V controller and a Multi-Mode-V AFM with a J scanner (Bruker) in tapping mode. The imaging conditions were as follows: scan size 2 μm, number of pixels 512 × 512, scan rate 1 Hz, free amplitude 123 nm and setpoint at 95% of the free amplitude.

With these parameters, we estimated the tip–sample forces using the Virtual Environment for Dynamic AFM (VEDA, nanohub.org/tools/veda) and obtained mean forces of 10 nN. Figure 2a shows an AFM image taken with one of the LSNT-tip SU8 cantilevers.

To evaluate the tip sharpness, the blind tip estimation algorithm [33] as implemented in the Gwyddion program [34,35] has been used. The blind tip estimation algorithm is used to estimate the sharpness of the tip from the image of a polycrystalline titanium tip characterizer sample of unknown geometry, with fea-

Figure 2: Tip sharpness and durability assessment of the LSNT-tip SU8 cantilevers using a polycrystalline titanium roughness sample in tapping mode. (a) The AFM image of the polycrystalline titanium roughness sample, used for the tip radius measurement. The average tip radius of 20 randomly chosen cantilevers is 9 nm. The image size is 2 × 2 µm at 512 × 512 pixels while the array dimension for the tip estimation is 55 × 55 pixels. The inset shows the result of the Gwyddion partial tip blind estimation extracted from the full image. (b, c) the tip radius evolution over 16 mm travelling distance shows negligible tip degradation.

tures significantly sharper than the tip under evaluation. The Gwyddion partial blind tip estimation algorithm iterates over the surface of the image to find the high points with the steepest slopes on the image. These points are subsequently used to estimate the radius of the tip 5 nm away from its apex by taking the average width of the tip along the two orthogonal axes, using the assumption that the evaluated tip must be sharper than the sharpest feature on the image of the specimen. To guarantee that the dilation of the specimen surface results exclusively from the tip geometry, the noise suppression threshold is set at 100 pm which is superior to the measured image noise of 40 pm. Additionally, borders of the image are also excluded from the estimation to prevent edge artefacts. The inset of Figure 2a shows the result of the Gwyddion partial tip estimation, which uses a limited number of the highest points on the image to estimate the sharpness of the tip. For the 20 cantilevers we evaluated, we obtained an average tip radius of 9 nm with a standard deviation of 2 nm.

We evaluated the tip durability in our work by uninterrupted imaging of the polycrystalline titanium roughness sample (tapping mode, scan size 2 µm, 512 × 512 pixels and scan rate 1 Hz). Figure 2b shows the partial blind estimation of the tip shape for the first and last images after 16 mm tip travel. No obvious degradation occurred. Figure 2c shows the evolution of the tip radius for more than 16 mm of tip travel (8 images).

To investigate the detection speed of the LSNT-tip SU8 cantilevers, we measured the detection bandwidth of the cantilever in tapping mode by measuring the 3 dB decrease of the tracking amplitude similar to the protocols described by Kokavecz et al. and Sulcheck and co-workers [36,37]. Figure 3a shows a comparison of the bandwidths of the individual cantilevers, namely the commercial RTESPA (Bruker AFM probes, Camarillo, CA, USA) with f_0 = 339 kHz, k = 48 N/m, Q = 592, planar dimensions of 125 × 40 µm and a thickness of 3.4 µm, and our LSNT-tip SU8 cantilever with f_0 = 328 kHz, k = 15 N/m, Q = 23, planar dimensions of 80 × 20 µm and a thickness of 7 µm. The detection bandwidth is 750 Hz and 50 kHz for the RTESPA and SU8 cantilevers, respectively.

Both cantilevers were designed for tapping-mode AFM imaging in air. We want to point out that based on our choice of planar geometries and thickness of the cantilevers, these two cantilevers were the most similar in terms of resonance frequency, however, their parameters are not an ideal match. Nevertheless, the drastically higher bandwidth of the SU8 cantilever is to be primarily attributed to the change in the materials properties. The LSNT-tip SU8 cantilever is more than 50 times faster than its silicon cantilever counterpart for a given resonance frequency. In order to evaluate the link between the tapping bandwidth and the image quality, an AFM calibration grating (1 µm pitch, 100 nm depth) was imaged with the RTESPA cantilever

Figure 3: Comparison of the tapping bandwidth between our tip-integrated SU8 cantilever and a commercial silicon cantilever (RTESPA). (a) The 3 dB drop of the surface tracking in tapping mode for RTESPA and the SU8 cantilever happens at 750 Hz and 50 kHz, respectively. RTESPA has f_0 = 339 kHz and Q = 592, and the LSNT-tip SU8 cantilever has f_0 = 328 kHz and Q = 23. (b) Amplitude error images of a 1 µm pitch reference sample taken by the RTESPA silicon cantilever and the LSNT-tip SU8 cantilever at scan rates of 1, 10, 20 and 30 Hz. The SU8 cantilever shows a better topography tracking ability compared to the RTESPA cantilever due to its higher tapping bandwidth. The scale bar is 500 nm.

(f_0 = 331 kHz, Q = 586) and the LSNT-tip SU8 cantilever (f_0 = 347 kHz, Q = 25) at scan rates of 1, 10, 20 and 30 Hz. The imaging was conducted with a Bruker Dimension FastScan AFM system at a scan size of 2 µm and a number of pixels of 512 × 512. Figure 3b shows the amplitude error images taken at different scan rates for these two cantilevers. A lower amplitude error contrast corresponds to a better tracking performance. While the silicon cantilever clearly tracks the sample poorly at a scan rate of 30 Hz, the SU8 cantilever detects the sample topography significantly better.

Discussion

The critical feature of any AFM cantilever is the tip. For general imaging, the quality of the tip is primarily determined by the tip radius and the wear rate of the tip. We need to comment that our tips have a decent sharpness compared to other silicon nitride moulded tips, but they are less sharp than the typical silicon tips that are commercially available with tip radii of less than 2 nm. However, even for the ultra-sharp tips, tip wear is unavoidable and a great concern for AFM users. The tip wear problem has been reported as early as 1991 [38]. By assuming that all of the imaging parameters are set correctly, tip wear can still occur due to abrasive wear, fracture and adhesive wear [39,40]. The presented cantilevers have proven a good tip sharpness, and provide the well-established wear-resistance of silicon nitride tips, supplemented with their good tracking bandwidth. We should also mention that our tips have a relatively large opening angle of 35°. On the one hand, the large opening angle limits the imaging capabilities on very rough samples. On the other hand, our tips are symmetric and have a clearly

defined geometry, which can be beneficial, for example for nanomechanical mapping of biological samples.

In general, SU8 cantilevers suffer from residual mean stress and residual stress gradients in the beam. These residual stresses can bend the cantilevers and cause issues with aligning the laser and approaching the sample. Keller et al. have shown that introducing a long hard bake after the SU8 development, and a modification of the SU8 photolithography baking profiles make it possible to fabricate 500 µm long cantilevers with less than 20 µm initial bending for 2 µm thick SU8 cantilevers [41]. Although our cantilevers are already relatively straight (due to their shorter length), a similar optimization of the process parameters could improve this issue further.

The cantilevers shown in Figure 1c have a peculiar shape with SU8 residues sticking out in a cross at the free end of the SU8 cantilever. This is due to the scattering of the light during photolithography of the cantilever patterning. Light travels through the SU8 polymer and reaches the bottom surface (LSNT) and is then reflected back to the parts of the non-exposed SU8. Except for its unusual shape, it does not bring any prominent problem in general AFM uses unless the cross is so large that it touches the sample, which we have not observed so far. One way to reduce this problem could be adjusting the exposure dose to values not higher than absolutely required.

The increased detection bandwidth of the SU8 cantilevers arises from the viscoelastic nature of the SU8 polymer resulting in a low Q-factor. This low Q-factor however comes at the price of

a low mechanical excitation efficiency when shaking the cantilever at resonance with a dither piezo. Hence the drive amplitude for these cantilevers has to be higher than that of traditional cantilevers. This gives rise to parasitic resonance peaks in the cantilever tune, which is well known for tapping-mode AFM in low-Q environments such as liquids. As with imaging in fluids, acquiring a thermal tune prior to the mechanical tune helps to find the correct resonance peak to use. The poor mechanical tune caused by the low Q-factor of the cantilever is aggravated by the fact that the chip body is also made of SU8 instead of a stiff conventional material. One technique to approach this challenge would be to make the cantilever chip body out of a SU8 nanocomposite with higher Young's modulus instead of pure SU8. For instance, M. Kandpal et al. [42] have shown that embedding ZnO nanoparticles into a pure SU8 matrix increases its Young's modulus from 8 to 30 GPa. The stiffer cantilever chip body will probably yield better mechanical tuning properties and hence an improved ease of use.

Conclusion

In this article, a batch fabrication process of LSNT-tip SU8 cantilevers has been presented. Tip sharpness measurements have been performed for 20 cantilevers, and reveal an average tip sharpness of 9 ± 2 nm. The tips are made of LSNT, a material known for its wear resistance, and no clear wear was observed after more than 16 mm of tip travel during the AFM imaging of a polycrystalline titanium roughness sample.

A suitable tip sharpness and a high wear resistance have been achieved along with a high tracking bandwidth of the fabricated LSNT-tip SU8 cantilevers. A comparison between a commercial silicon cantilever and the LSNT-tip SU8 cantilever reveals that the detection speed is improved by a factor of more than 50.

Acknowledgements

ORCID® iDs

Matthias Neuenschwander - https://orcid.org/0000-0001-8624-7343
Santiago H. Andany - https://orcid.org/0000-0003-2281-7612

References

1. Binnig, G.; Rohrer, H.; Gerber, C.; Weibel, E. *Phys. Rev. Lett.* **1982,** *49,* 57–61. doi:10.1103/physrevlett.49.57

2. Villarrubia, J. S.
   J. Vac. Sci. Technol., B: Microelectron. Nanometer Struct.–Process., Meas., Phenom. **1996,** *14,* 1518. doi:10.1116/1.589130

3. Villarrubia, J. S. *Surf. Sci.* **1994,** *321,* 287–300.
   doi:10.1016/0039-6028(94)90194-5

4. Schwarz, U. D.; Haefke, H.; Reimann, P.; Güntherodt, H.-J.
   J. Microsc. (Oxford, U. K.) **1994,** *173,* 183–197.
   doi:10.1111/j.1365-2818.1994.tb03441.x

5. Leitner, M.; Fantner, G. E.; Fantner, E. J.; Ivanova, K.; Ivanov, T.;
   Rangelow, I.; Ebner, A.; Rangl, M.; Tang, J.; Hinterdorfer, P. *Micron*
   2012, *43,* 1399–1407. doi:10.1016/j.micron.2012.05.007

6. Shibata, M.; Uchihashi, T.; Ando, T.; Yasuda, R. *Sci. Rep.* **2015,** *5,*
   8724. doi:10.1038/srep08724

7. Nellist, M. R.; Chen, Y.; Mark, A.; Gödrich, S.; Stelling, C.; Jiang, J.;
   Poddar, R.; Li, C.; Kumar, R.; Papastavrou, G.; Retsch, M.;
   Brunschwig, B. S.; Huang, Z.; Xiang, C.; Boettcher, S. W.
   Nanotechnology **2017,** *28,* 095711. doi:10.1088/1361-6528/aa5839

8. Velmurugan, J.; Agrawal, A.; An, S.; Choudhary, E.; Szalai, V. A.
   Anal. Chem. (Washington, DC, U. S.) **2017,** *89,* 2687–2691.
   doi:10.1021/acs.analchem.7b00210

9. Maouli, I.; Taguchi, A.; Saito, Y.; Kawata, S.; Verma, P.
   Appl. Phys. Express **2015,** *8,* 032401. doi:10.7567/apex.8.032401

10. Suriano, R.; Zandrini, T.; De Marco, C.; Osellame, R.; Turri, S.;
    Bragheri, F. *Nanotechnology* **2016,** *27,* 155702.
    doi:10.1088/0957-4484/27/15/155702

11. Yan, Y.; Geng, Y.; Hu, Z. *Int. J. Mach. Tools Manuf.* **2015,** *99,* 1–18.
    doi:10.1016/j.ijmachtools.2015.09.004

12. Umakoshi, T.; Saito, Y.; Verma, P. *Nanoscale* **2016,** *8,* 5634–5640.
    doi:10.1039/c5nr08548a

13. Sanders, A.; Zhang, L.; Bowman, R. W.; Herrmann, L. O.;
    Baumberg, J. J. *Part. Part. Syst. Charact.* **2015,** *32,* 182–187.
    doi:10.1002/ppsc.201400104

14. Kawashima, K.; Mineta, T.; Makino, E.; Kawashima, T.; Shibata, T.
    Electron. Commun. Jpn. **2015,** *98,* 30–36. doi:10.1002/ecj.11760

15. Seena, V.; Fernandes, A.; Pant, P.; Mukherji, S.; Ramgopal Rao, V.
    Nanotechnology **2011,** *22,* 295501.
    doi:10.1088/0957-4484/22/29/295501

16. Seena, V.; Nigam, A.; Pant, P.; Mukherji, S.; Rao, V. R.
    J. Microelectromech. Syst. **2012,** *21,* 294–301.
    doi:10.1109/jmems.2011.2175703

17. Johansson, A.; Calleja, M.; Rasmussen, P. A.; Boisen, A.
    Sens. Actuators, A **2005,** *123–124,* 111–115.
    doi:10.1016/j.sna.2005.03.025

18. Wang, X.; Ryu, K. S.; Bullen, D. A.; Zou, J.; Zhang, H.; Mirkin, C. A.;
    Liu, C. *Langmuir* **2003,** *19,* 8951–8955. doi:10.1021/la034858o

19. McFarland, A. W.; Poggi, M. A.; Bottomley, L. A.; Colton, J. S.
    Rev. Sci. Instrum. **2004,** *75,* 2756–2758. doi:10.1063/1.1777387

20. Genolet, G.; Brugger, J.; Despont, M.; Drechsler, U.; Vettiger, P.;
    de Rooij, N. F.; Anselmetti, D. *Rev. Sci. Instrum.* **1999,** *70,* 2398–2401.
    doi:10.1063/1.1149767

21. Genolet, G.; Despont, M.; Vettiger, P.; Anselmetti, D.; de Rooij, N. F.
    J. Vac. Sci. Technol., B: Microelectron. Nanometer Struct.–Process., Meas., Phenom. **2000,** *18,* 617. doi:10.1116/1.591248

22. Mouaziz, S.; Boero, G.; Popovic, R. S.; Brugger, J.
    J. Microelectromech. Syst. **2006,** *15,* 890–895.
    doi:10.1109/jmems.2006.879376

23. Adams, J. D.; Erickson, B. W.; Grossenbacher, J.; Brugger, J.;
    Nievergelt, A.; Fantner, G. E. *Nat. Nanotechnol.* **2016,** *11,* 147–151.
    doi:10.1038/nnano.2015.254

24. Sidler, K. Fabrication and characterization of SU-8 cantilevers with integrated tips designed for dip-pen nanolithography. Master's thesis, ETH Zurich, Switzerland. 2006. doi:10.3929/ethz-a-005177681
25. Martin-Olmos, C.; Rasool, H. I.; Weiller, B. H.; Gimzewski, J. K. *ACS Nano* **2013,** *7,* 4164–4170. doi:10.1021/nn400557b
26. Lee, J. S.; Song, J.; Kim, S. O.; Kim, S.; Lee, W.; Jackman, J. A.; Kim, D.; Cho, N.-J.; Lee, J. *Nat. Commun.* **2016,** *7,* 11566. doi:10.1038/ncomms11566
27. Kim, S.; Song, J.; Cho, S.-J.; Lee, J. *J. Microelectromech. Syst.* **2017,** *26,* 504–506. doi:10.1109/jmems.2017.2675946
28. Boisen, A.; Rasmussen, J. P.; Hansen, O.; Bouwstra, S. *Microelectron. Eng.* **1996,** *30,* 579–582. doi:10.1016/0167-9317(95)00314-2
29. Marcus, R. B.; Sheng, T. T. *J. Electrochem. Soc.* **1982,** *129,* 1278. doi:10.1149/1.2124118
30. Ravi, T. S.; Marcus, R. B.; Liu, D. *J. Vac. Sci. Technol., B: Microelectron. Nanometer Struct.–Process., Meas., Phenom.* **1991,** *9,* 2733. doi:10.1116/1.585680
31. Kao, D.-B.; McVittie, J. P.; Nix, W. D.; Saraswat, K. C. *IEEE Trans. Electron Devices* **1988,** *35,* 25–37. doi:10.1109/16.2412
32. Mertz, J.; Marti, O.; Mlynek, J. *Appl. Phys. Lett.* **1993,** *62,* 2344–2346. doi:10.1063/1.109413
33. Villarrubia, J. S. *J. Res. Natl. Inst. Stand. Technol.* **1997,** *102,* 425–454. doi:10.6028/jres.102.030
34. Gwyddion – Free SPM (AFM, SNOM/NSOM, STM, MFM, …) data analysis software. http://gwyddion.net (accessed Oct 31, 2019).
35. Nečas, D.; Klapetek, P. *Cent. Eur. J. Phys.* **2012,** *10,* 181–188. doi:10.2478/s11534-011-0096-2
36. Kokavecz, J.; Marti, O.; Heszler, P.; Mechler, Á. *Phys. Rev. B* **2006,** *73,* 155403. doi:10.1103/physrevb.73.155403
37. Sulchek, T.; Yaralioglu, G. G.; Quate, C. F.; Minne, S. C. *Rev. Sci. Instrum.* **2002,** *73,* 2928–2936. doi:10.1063/1.1488679
38. Hellemans, L.; Waeyaert, K.; Hennau, F.; Stockman, L.; Heyvaert, I.; Van Haesendonck, C. *J. Vac. Sci. Technol., B: Microelectron. Nanometer Struct.–Process., Meas., Phenom.* **1991,** *9,* 1309. doi:10.1116/1.585185
39. Bloo, M. L.; Haitjema, H.; Pril, W. O. *Measurement* **1999,** *25,* 203–211. doi:10.1016/s0263-2241(99)00004-4
40. Bhaskaran, H.; Gotsmann, B.; Sebastian, A.; Drechsler, U.; Lantz, M. A.; Despont, M.; Jaroenapibal, P.; Carpick, R. W.; Chen, Y.; Sridharan, K. *Nat. Nanotechnol.* **2010,** *5,* 181–185. doi:10.1038/nnano.2010.3
41. Keller, S.; Haefliger, D.; Boisen, A. *J. Micromech. Microeng.* **2010,** *20,* 045024. doi:10.1088/0960-1317/20/4/045024
42. Kandpal, M.; Sharan, C.; Poddar, P.; Prashanthi, K.; Apte, P. R.; Ramgopal Rao, V. *Appl. Phys. Lett.* **2012,** *101,* 104102. doi:10.1063/1.4748575

A review of demodulation techniques for multifrequency atomic force microscopy

David M. Harcombe[*], Michael G. Ruppert and Andrew J. Fleming

Abstract

This article compares the performance of traditional and recently proposed demodulators for multifrequency atomic force microscopy. The compared methods include the lock-in amplifier, coherent demodulator, Kalman filter, Lyapunov filter, and direct-design demodulator. Each method is implemented on a field-programmable gate array (FPGA) with a sampling rate of 1.5 MHz. The metrics for comparison include the sensitivity to other frequency components and the magnitude of demodulation artifacts for a range of demodulator bandwidths. Performance differences are demonstrated through higher harmonic atomic force microscopy imaging.

Introduction

Atomic force microscopy (AFM) [1] has enabled innovation in nanoscale engineering since it was invented in 1986 by Binnig and co-workers. Atomic-scale topographical resolution is achieved by sensing the interaction between a sharp microcantilever probe and the sample [2]. Initial operation was in constant-force contact-mode, where a static deflection is maintained through a constant contact force [3].

In dynamic imaging modes [4], the cantilever is driven at, or near, a resonance frequency, which establishes the requirement for demodulation in AFM. In intermittent-contact constant-

amplitude AFM [5], a constant cantilever oscillation amplitude is maintained by feeding back the demodulated fundamental amplitude of the deflection signal. The imaging of delicate biological samples [6-8] is particularly suited to intermittent-contact AFM [9] when tip–sample contact is gentle.

Environmental damping has a large effect on the quality factor (Q) of the cantilever. Values can range from as low as $Q \approx 1$ in liquid [10], up to $Q \approx 10,000$ in ultra-high vacuum [11]. This affects the mechanical bandwidth of the cantilever according to the expression $f_{-3\mathrm{dB}} = f_0/2Q$, where f_0 is the fundamental reso-

nance frequency. Assuming all other components in the *z*-axis feedback loop are also working at high speed [3], a low quality factor can demand a fast demodulator [12].

Multifrequency AFM (MF-AFM) is a major field within dynamic mode AFM. It involves studying multiple frequency components in the cantilever oscillation during tip–sample interactions [13]. Observing higher eigenmodes of the cantilever [14], higher harmonics of the fundamental resonance [15] and intermodulation products [16] have been shown to provide further nanomechanical sample information. These include properties such as sample elasticity, stiffness and adhesiveness [17], which are mapped simultaneously with the topography. Acquiring these observables requires the accurate demodulation of amplitude and phase of multiple frequency components.

Small interaction forces associated with higher-harmonic AFM have been imaged in free air [18] as well as liquid [19]. This has lead to relatively large biological objects being imaged including viruses [20] and cells [21]. Multimodal AFM, where two or more resonance frequencies are driven, has theoretical foundations for determining secondary sample properties such as Young's modulus [13,22]. Applications include the imaging of secondary properties of proteins [23] and polymers [24]. Intermodulation AFM actively drives the cantilever slightly below and above resonance with a two-tone drive. Compared to higher-harmonic AFM, this technique has more enhanced nonlinear interactions [25]. Intermodulation products present in the cantilevers motion have been shown to be sensitive to material and chemical contrast [16,26], leading to enhanced nanomechanical insights [27]. Regardless of which MF-AFM technique is performed, the demodulator is an essential component for acquiring observables to characterize the sample.

Previously, the authors conducted an in-depth comparison of conventional and novel demodulation techniques for single-frequency amplitude-modulation atomic force microscopy [28]. It was found that conventional high-speed non-synchronous demodulators are incompatible with MF-AFM, due to the lack of robustness against unwanted frequency components [28]. These include the peak-hold [12], peak detector [29] and RMS-to-DC [30] conversion demodulators. In contrast, synchronous demodulators have been shown to provide accurate estimates in the presence of other frequency components [28]. As a result, MF-AFM experiments usually employ multiple lock-in amplifiers in parallel. However, this introduces an inherent bandwidth limitation as high-frequency mixing products must be low-pass filtered [28,31].

Motivated by improving high-speed MF-AFM demodulation capabilities, a multifrequency Kalman filter was developed

[32]. It outperformed a commercially available lock-in amplifier in terms of both tracking bandwidth and noise performance. However, a major disadvantage of the Kalman filter is its implementation complexity. This heavily limits the achievable sampling rate and ability to track a large number of signals. To alleviate this issue, the Lyapunov filter [33] was established, which is computationally more efficient than the Kalman filter while achieving similar performance [34]. This was extended to a multifrequency Lyapunov filter, which has seen success in higher-harmonic AFM for both amplitude and phase-contrast imaging [35,36]. A limitation, common to both the Kalman and the Lyapunov filter, is a fixed 1st-order response, which has motivated the development of techniques for the direct design of the demodulator frequency response [37,38].

This article aims to provide a rigorous experimental comparison of MF-AFM demodulation techniques. This includes the conventional lock-in amplifier and coherent demodulator, as well as the recently proposed Kalman filter, Lyapunov filter and direct-design method. For a fair comparison, each system is implemented on the same FPGA platform with a common sample rate. The sensitivity to unwanted frequency components for both low and high bandwidths is assessed along with implementation complexity. A final experimental comparison is conducted through higher-harmonic AFM imaging for both low and high tracking bandwidths.

Multifrequency AFM Modulation and Demodulation Fundamentals
Cantilever deflection signal model
A single component of the cantilever deflection signal is modeled as a sine wave with carrier frequency f_i, time-varying amplitude $A_i(t)$ and phase $\phi_i(t)$, that is of the form

$$y_i(t) = A_i(t)\sin\big(\omega_i t + \phi_i(t)\big). \tag{1}$$

For a better readability, explicit time-dependencies on the amplitude $A(t)$ and phase $\phi(t)$ are dropped from this point onward. By extension, a deflection signal consisting of multiple frequencies is given by

$$y(t) = \sum_{i=1}^{n} y_i(t) = \sum_{i=1}^{n} A_i \sin\big(\omega_i t + \phi_i\big), \tag{2}$$

where $i = 1, 2, \ldots, n$ denotes the *i*-th modeled frequency. An alternative representation of a single signal component is of the linearly parameterized form

$$y_i(t) = x_{2i-1}\cos(\omega_i t) + x_{2i}\sin(\omega_i t), \qquad (3)$$

where x_{2i-1} and x_{2i} represent quadrature and in-phase components respectively. This is convenient for MF-AFM, as the time-varying amplitude and phase of each frequency can be recovered by the output equations

$$A_i = \sqrt{x_{2i-1}^2 + x_{2i}^2},$$
$$\phi_i = \arctan\left(\frac{x_{2i-1}}{x_{2i}}\right). \qquad (4)$$

Modulation

An amplitude-modulated signal (double-sideband full carrier) is obtained by mixing a modulating signal $y_m(t)$ at a frequency $\omega_m = 2\pi f_m$ with a carrier signal $y_i(t)$. The modulating signal oscillates at a frequency that is significantly slower than the carrier frequency ω_i. Figure 1a illustrates a cantilever driven at multiple frequencies being amplitude-modulated by a sample topography. In MF-AFM, the cantilever deflection signal contains frequency components originating from the fundamental resonance mode, as well as from higher eigenmodes and/or harmonics. If for simplicity we assume unity amplitudes, then amplitude-modulation of a distinct frequency component at ω_i is described by

$$\begin{aligned} y_m(t) \times y_i(t) &= \left[1 + M\sin(\omega_m t)\right] \times \sin(\omega_i t + \phi) \\ &= \sin(\omega_i t) + \frac{M}{2}\cos\left[(\omega_i - \omega_m)t + \phi\right] \\ &\quad - \frac{M}{2}\cos\left[(\omega_i + \omega_m)t + \phi\right]. \end{aligned} \qquad (5)$$

Here, M is the modulation index, which for AM signals is the ratio of the peak value of the modulated signal relative to the carrier. Equation 5 shows that the modulation process creates distinct frequencies components at f_i and $f_i \pm f_m$. The latter components are termed the upper and lower sidebands and are centered symmetrically around the carrier frequency as illustrated in Figure 1b. As the modulating frequency increases, the sidebands move away from the carrier up until the limit where the left sideband is at DC and the right sideband is at $2f_i$. The scenario where $f_m > f_i$ is not of practical interest, as the amplitude changes would need to be faster than the cantilever oscillation frequency.

Demodulation

Demodulation is the process of estimating the modulating signal (sample) associated with a carrier frequency. Demodulators can be classified as either synchronous or non-synchronous. Non-synchronous methods do not require a reference oscillator.
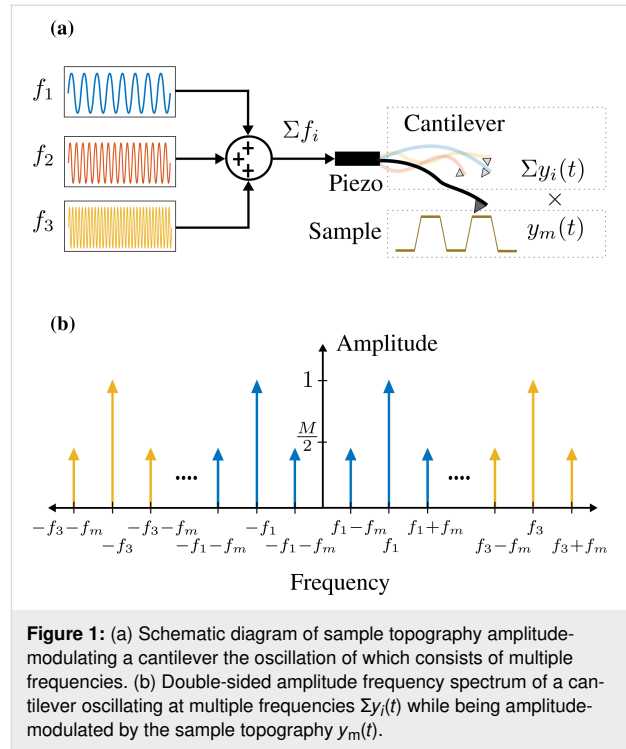
Figure 1: (a) Schematic diagram of sample topography amplitude-modulating a cantilever the oscillation of which consists of multiple frequencies. (b) Double-sided amplitude frequency spectrum of a cantilever oscillating at multiple frequencies $\Sigma y_i(t)$ while being amplitude-modulated by the sample topography $y_m(t)$.

However, these methods are incompatible with MF-AFM, due to their inability to reject unwanted frequency components [28]. For this reason, these techniques are not discussed in this article. Synchronous demodulation techniques employ a reference oscillator and can be categorized as either open-loop or closed-loop, depending on whether they use feedback to estimate parameters. Open-loop demodulators include the lock-in amplifier and coherent demodulator, while closed-loop methods include the Kalman filter, Lyapunov filter, and direct-design demodulator.

Performance metrics

In a previous work [28], the performance of single-frequency AFM demodulators was assessed by measuring the magnitude of demodulation artifacts and the sensitivity to measurement noise. However, multifrequency AFM applications require an additional metric due to the large number of potentially closely spaced frequencies. For example, higher-harmonic imaging with single-frequency excitation results in small harmonic amplitudes that must be estimated in the presence of both noise and much larger fundamental and/or harmonic components [19,36]. The performance of the demodulator in this regard can be quantified by a metric herein referred to as the off-mode rejection (OMR).

OMR is defined as the gain ratio between a modeled carrier frequency f_i and another frequency f_j as visualized in Figure 2. It can be evaluated by

$$\text{OMR}_{f_i f_j} = \frac{\left| G\left(2\pi f_i \right) \right|}{\left| G\left(2\pi f_j \right) \right|}, \qquad (6)$$

where $G(2\pi f)$ is the demodulator frequency response. Additionally, implementation complexity is qualitatively discussed. It is assessed according to the maximum achievable sampling rate, timing requirements and computational scalability when modeling additional channels.

Figure 2: Visualization of off-mode rejection in the frequency domain for a demodulator magnitude frequency response |$G(2\pi f)$| at f_i with respect to f_j.
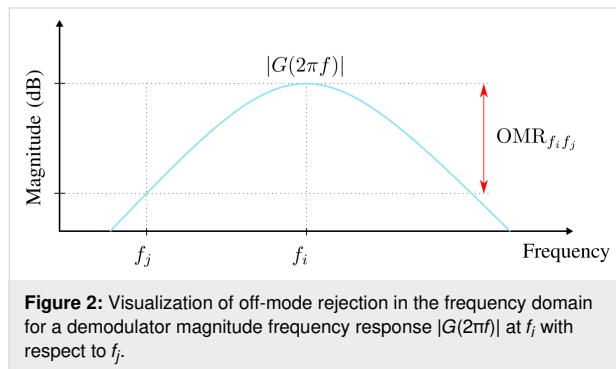
Review of Multifrequency Demodulation Methods
Lock-in amplifier

The multifrequency lock-in amplifier (LIA) [28,39-41] operates by multiplying an input signal described by Equation 2 with parallel in-phase and quadrature sinusoids tuned to frequencies the amplitude and phase of which are of interest. For simplicity, consider an ideal input signal consisting of a single sinusoid with a frequency ω_i, applied to a lock-in amplifier tuned to ω_i. During the mixing process, the following intermediate signals are generated

$$\begin{aligned} y_I\left(t \right) &= y\left(t \right) \times \sin\left(\omega_i t \right) \\ &= \frac{1}{2} A_i \left[\cos\left(\phi_i \right) - \cos\left(2\omega_i t + \phi_i \right) \right] \end{aligned} \qquad (7)$$

and

$$\begin{aligned} y_Q\left(t \right) &= y\left(t \right) \times \sin\left(\omega_i t \right) \\ &= \frac{1}{2} A_i \left[\sin\left(\phi_i \right) + \sin\left(2\omega_i t + \phi_i \right) \right]. \end{aligned} \qquad (8)$$

From Equation 7 and Equation 8 it can be seen that in addition to the desired amplitude and phase, mixing products are generated at twice the carrier frequency $2\omega_i$. If the input contains more than one sinusoid and/or a noise process, further unde-

sired frequency components are present in the intermediate signals. These high-frequency mixing components and noise terms are removed by employing a low-pass filter, the cut-off frequency of which is determined by making a trade-off between tracking bandwidth and $2\omega_i$ ripple suppression [28]. Additionally, lock-in amplifiers should always be AC-coupled as any residual DC offset in the input signal (Equation 2) will generate a mixing component at ω_i.

The functional block diagram of the multifrequency lock-in amplifier is shown in Figure 3. Here, it can be seen that multiple frequencies are tracked by running several lock-in amplifiers in parallel, with each oscillator tuned to a specific frequency ω_i. The required components for digital implementation of each lock-in amplifier are a direct digital synthesizer (DDS) to generate the sine and cosine mixing signals, two multipliers, two low-pass filters and an output block. The output block, which calculates amplitude and phase, is described by Equation 4, meaning the square-root and arctan functions are required. Typically the phase is calculated by using either a polynomial approximation [42] or the CORDIC algorithm [43].

Figure 3: Functional block diagram of the multifrequency lock-in amplifier implementation. The zoom-box displays the functional block diagram of a single lock-in amplifier.
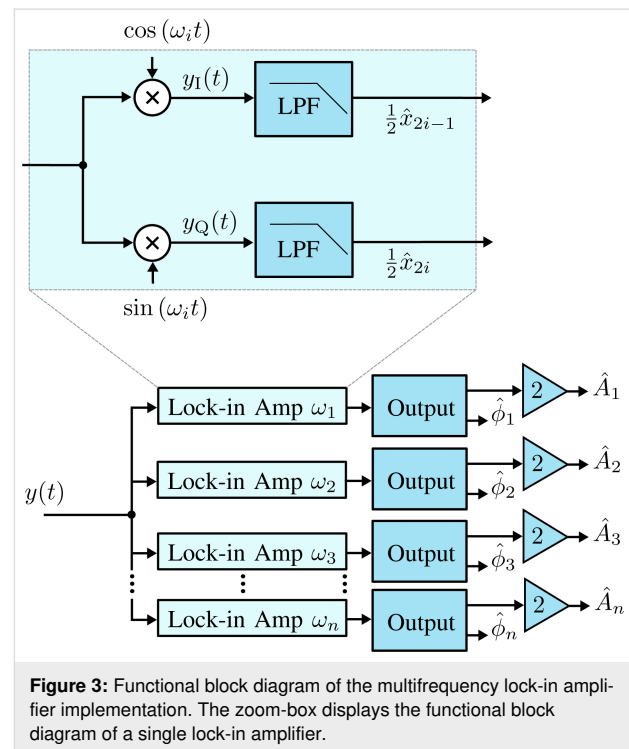
Coherent demodulator

The multifrequency coherent demodulator is a digital demodulation method based on mixing and precise integration over a fixed time window [28,44-47]. Conceptually, it is a digital lock-in amplifier that utilizes mixing with in-phase and quadrature sinusoids

$$y_{\text{I}}(t) = y(t) \times \sin(\omega_i t),$$
$$y_{\text{Q}}(t) = y(t) \times \cos(\omega_i t), \qquad (9)$$

and implements low-pass filtering of mixing products and any other additional unwanted frequency components through precise fixed-length numerical integration [45]. If the input signal is a pure sinusoid (Equation 1) and the integration period T is chosen to be an integer multiple of the drive signal period, $T = mT_i$, the integrals over $y_{\text{I}}(t)$ and $y_{\text{Q}}(t)$ evaluate exactly to the in-phase and quadrature states

$$\frac{1}{2} x_{2i-1} = \frac{1}{mT_i} \int_0^{mT_i} y_{\text{I}}(t),$$
$$\frac{1}{2} x_{2i} = \frac{1}{mT_i} \int_0^{mT_i} y_{\text{Q}}(t). \qquad (10)$$

The functional block diagram of the multifrequency coherent demodulator is shown in Figure 4. It requires the same components as the lock-in amplifier, although the method in which the low-pass filter is implemented is different. Advanced implementation details can be found in the literature [28,45]. Practitioners should pay strong attention to timing considerations, otherwise the desired low-pass filtering effect will not occur.

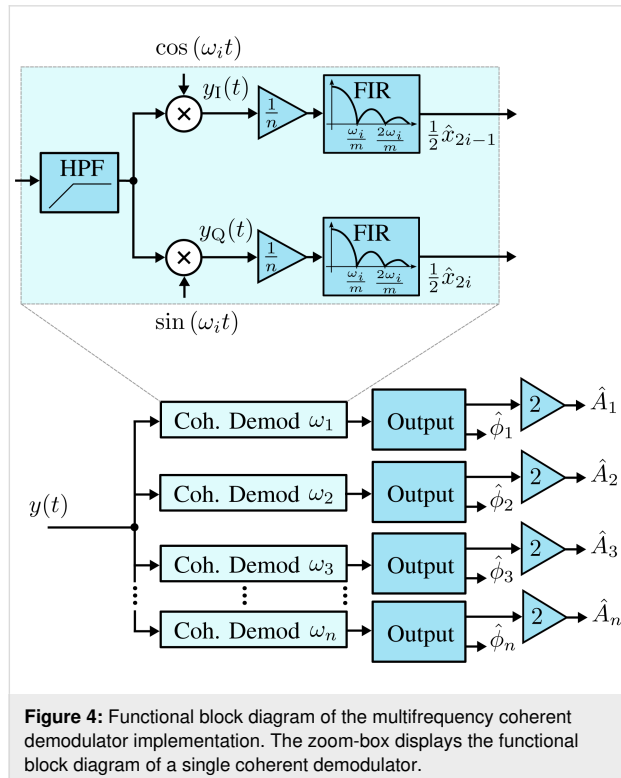**Figure 4:** Functional block diagram of the multifrequency coherent demodulator implementation. The zoom-box displays the functional block diagram of a single coherent demodulator.

For Equation 10 to hold, the integration period must be an integer multiple of the sampling period, $nT_s = mT_i$, where n is the number of samples in the integration. Since an arbitrary sample-to-carrier frequency ratio F_s/f_i is rarely an integer, this condition is hard to meet. Therefore, a practical solution is to find the smallest n such that $nT_s \leq mT_i \leq (n + 1)T_s$ and perform a partial integration over the last sampling interval [45]. Such precise control over the integration period is achievable in digital systems, although the implementation of this method is still challenging.

The discrete-time integration in Equation 10 yields a very useful finite impulse response (FIR) filter, the frequency response of which is a sinc(·) function with zeros occurring at integer multiples of the oscillation frequency [28]. Unlike the lock-in amplifier, this allows the coherent demodulator to achieve low-noise output estimates at high tracking bandwidths since it strongly rejects $2f_i$ mixing products [28]. In addition, this zeroing characteristic can provide strong attenuation of unwanted harmonics and intermodulation products. This has lead to the multifrequency coherent demodulator being successfully applied to intermodulation AFM [26,27].

Kalman filter

The Kalman filter [48] has seen practical application in many fields including inertial navigation [49], robotics [50], and economics [51]. The Kalman filter uses a recursive algorithm to minimize the error between modeled and measured information to estimate an unknown process variable. Specifically, if the modeling and measurement noise processes have a Gaussian distribution, the Kalman filter produces an optimal estimate of a variable in the least-squares sense by minimizing the variance [52]. Fundamental to its operating principle, the Kalman filter utilizes a linear model of system dynamics and feedback of the state variables to update the Kalman gains, which controls the tracking bandwidth.

When the time-varying system is discretized for $t = kT_s$, where T_s is the sampling period, the process model of the Kalman filter is established as

$$\mathbf{x}_{k+1} = \mathbf{A}_k \mathbf{x}_k + w_k,$$
$$y_k = \mathbf{C}_k \mathbf{x}_k + v_k,$$
$$E\left[\mathbf{w}_k \mathbf{w}_k^T\right] = \mathbf{Q}_k,$$
$$E\left[\mathbf{v}_k \mathbf{v}_k^T\right] = R_k, \qquad (11)$$
$$E\left[\mathbf{w}_k \mathbf{v}_k^T\right] = 0,$$

where w_k and v_k are the process noise and measurement noise with respective covariance matrices $\mathbf{Q}_k$ and R_k. The state and output matrix are described by

$$
\begin{aligned}
\mathbf{A}_k &= I_{2n+1}, \\
\mathbf{C}_k &= \begin{bmatrix} \cos\theta_{1,k} & \sin\theta_{1,k} & \dots & \cos\theta_{n,k} & \sin\theta_{n,k} \end{bmatrix},
\end{aligned}
\tag{12}
$$

where I_{2n+1} is the identity matrix of dimension $2n + 1$, n is the number of modeled frequencies, $\theta_{i,k} = \omega_i k T_s$. In this representation, quadrature $x_{2i-1,k}$ and in-phase $x_{2i,k}$ states are assumed to be random variables describing the states of Equation 3.

The parameters $\mathbf{Q}_k$ and R_k dictate the amount of uncertainty in the model and the measurement noise, respectively. To simplify tuning of the filter during operation it is recommended to fix R_k such that it reflects the standard deviation σ of the Gaussian noise in the input signal from the sensor $y(t)$ ($R = \sigma^2$). This leaves $\mathbf{Q}_k$ as the only tuning variable that directly influences the Kalman gains and sets the tracking bandwidth.

The functional block diagram of the Kalman filter implementation is shown in Figure 5, it follows the standard recursive algorithm equations [53,54]. The prediction step is computed as

$$
\begin{aligned}
\hat{\mathbf{x}}_{k|k-1} &= \mathbf{A}_k \hat{\mathbf{x}}_{k-1|k-1}, \\
\mathbf{P}_{k|k-1} &= \mathbf{A}\mathbf{P}_{k-1|k-1}\mathbf{A}^{\mathbf{T}} + \mathbf{Q}_k,
\end{aligned}
\tag{13}
$$

where $\mathbf{P}_{k|k-1}$ denotes the predicted covariance matrix. This is followed by the Kalman gain and state measurement updates

$$
\begin{aligned}
\mathbf{K}_k &= \mathbf{P}_{k|k-1}\mathbf{C}_k^{\mathbf{T}}(\mathbf{C}_k\mathbf{P}_{k|k-1}\mathbf{C}_k^{\mathbf{T}} + \mathbf{R}_k)^{-1} \\
\hat{\mathbf{x}}_{k|k} &= \hat{\mathbf{x}}_{k|k-1} + \mathbf{K}_k\left(\mathbf{y}_k - \mathbf{C}\hat{\mathbf{x}}_{k|k-1}\right).
\end{aligned}
\tag{14}
$$
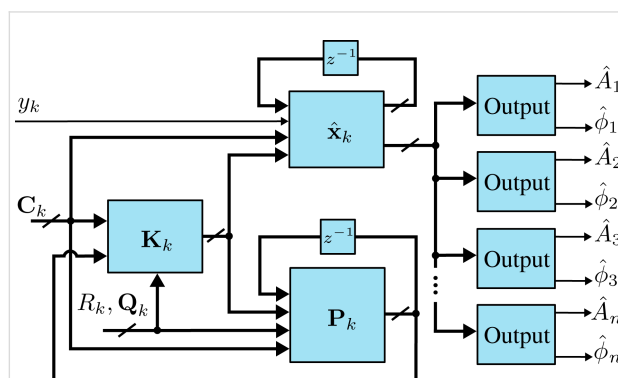
Figure 5: Functional block diagram of the Kalman filter implementation.

Lastly, the covariance matrix is updated according to

$$
\mathbf{P}_{k|k} = \left(\mathbf{I} - \mathbf{K}_k\mathbf{C}_k\right)\mathbf{P}_{k|k-1}\left(\mathbf{I} - \mathbf{K}_k\mathbf{C}_k\right)^{\mathbf{T}} + \mathbf{K}_k\mathbf{R}_k\mathbf{K}_k^{\mathbf{T}},
\tag{15}
$$

which is in Joseph form, i.e., it is naturally symmetric and positive definite. These properties can be exploited in the implementation to reduce memory and computation requirements. In addition, it is the most numerically stable form of the covariance matrix and remains convergent and non-deterministic for any selection of $\mathbf{Q}_k$ and R_k[53].

Specific amplitude and phase of a modeled frequency ω_i are shown to be recovered by employing the output equations in Equation 4. Although this method is simple to tune in real-time, a disadvantage is the fixed 1st-order response. Also, the Kalman filter equations have a complexity of $\mathcal{O}(n^3)$ for n modeled frequencies resulting in significant computational requirements beyond three modeled frequencies. This system representation has seen success in tracking power system voltage phasors [55] and more recently high-speed AFM [31,32].

Lyapunov filter

The Lyapunov filter [33,35,36] also uses a model-based feedback approach to obtain amplitude and phase of signals at desired frequencies. Under certain conditions, the Lyapunov filter has been shown to be equivalent to the Kalman filter [33]. However, the Lyapunov filter uses a tunable scalar gain γ instead of updating covariance matrix and Kalman gain equations. This gives the Lyapunov filter a computational complexity of $\mathcal{O}(n)$ as additional frequencies are modeled, a significant improvement over the Kalman filter.

A key property of the Lyapunov filter is exponential convergence of the estimated states [56], with the tunable loop gain γ governing the speed of convergence. The multifrequency Lyapunov filter is implemented as parallel linear observers tuned to a particular frequency ω_i, as depicted in Figure 6. An error signal is generated by feeding back an estimate of the input signal as per Equation 2, obtained from the parameterized states of each individual filter. Regulation of this error through feedback leads to the much desired suppression of the high-frequency mixing components.

The update law for the Lyapunov filter [33,36] for multiple frequencies is written as

$$
\begin{aligned}
\dot{\hat{\mathbf{x}}} &= \boldsymbol{\Gamma}\mathbf{C}^T\left[y(t) - \hat{y}(t)\right], \\
\hat{y}(t) &= \mathbf{C}\hat{\mathbf{x}},
\end{aligned}
\tag{16}
$$

Figure 6: Functional block diagram of the multifrequency Lyapunov filter implementation. The zoom-box displays the functional block diagram of a single Lyapunov filter.
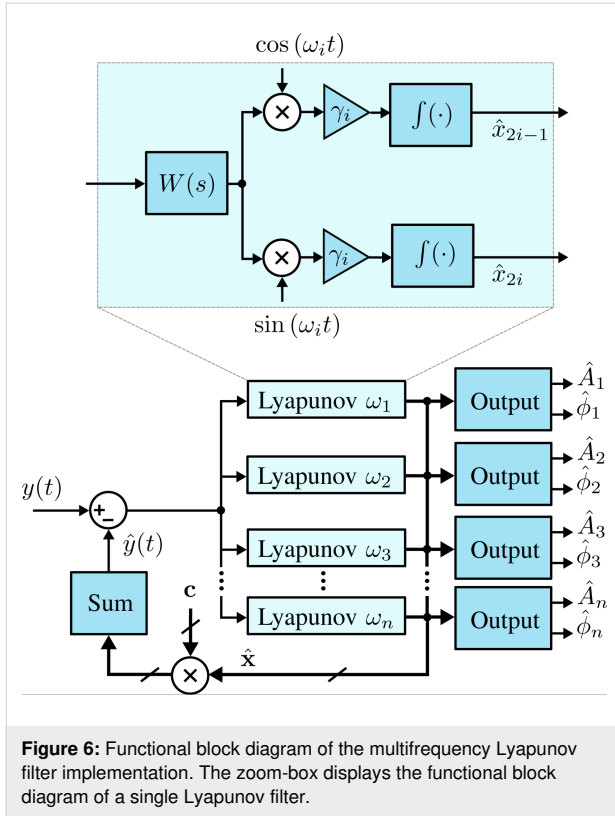
where

$$
\mathbf{\Gamma} = \begin{bmatrix} \gamma_1 & & & \\ & \gamma_1 & & 0 \\ & & \ddots & \\ & 0 & & \gamma_n \\ & & & & \gamma_n \end{bmatrix} \tag{17}
$$

and

$$
\mathbf{C} = \begin{bmatrix} \cos(\omega_1 t) & \sin(\omega_1 t) \dots \cos(\omega_n t) & \sin(\omega_n t) \end{bmatrix}. \tag{18}
$$

In this form, $\hat{y}(t)$ represents the estimated input signal and the amplitude A_i and phase ϕ_i estimates are found by applying Equation 4 to each quadrature and in-phase pair of $\hat{\mathbf{x}}$. A key property to ensure exponential convergence of $\hat{\mathbf{x}}$ to $\mathbf{x}$ is to guarantee that $\mathbf{C}$ is persistently excited [56]. Convergence is shown for the single-frequency filter in [33] and can easily be extended for the multifrequency case. Furthermore, exponential convergence of $\hat{\mathbf{x}}$ means that $\hat{A}$ and $\hat{\phi}$ also converge. This system representation has been shown to perform similarly to the Kalman filter [28], which is advantageous given its imple-

mentation simplicity. Recently, it has been used for higher-harmonic AFM for both amplitude and phase-contrast imaging [35,36].

Direct-design method

The direct-design method [37] also utilizes model-based feedback to obtain the amplitude and phase of signals at desired frequencies. However, intrinsic to its design methodology is the ability to implement an arbitrary filter response with a specified filter order and linearity in the bandpass region. For example, a demodulator can be implemented the frequency response of which resembles a Butterworth or Chebyshev filter with a desired filter bandwidth and order. This alleviates the limited 1st-order response of the Kalman and Lyapunov filters, creating stronger rejection of unwanted frequency components. This occurs while maintaining benefits such as low noise and low computational complexity.

In order to obtain an arbitrary demodulator response, consider the functional block diagram in Figure 7, where the integrator of the Lyapunov filter is replaced by the transfer function $F(s)$. In this form, the direct-design demodulator follows a modulated–demodulated control loop [57] with a unity plant. This method differs from the Lyapunov filter as it does not set the pre-filter to $W(s) = 1$, instead it utilizes $W(s)$ as part of the design of a desired closed-loop response. In the original work

Figure 7: Functional block diagram of the multifrequency direct-design filter implementation. The zoom-box displays the functional block diagram of a single direct-design filter.
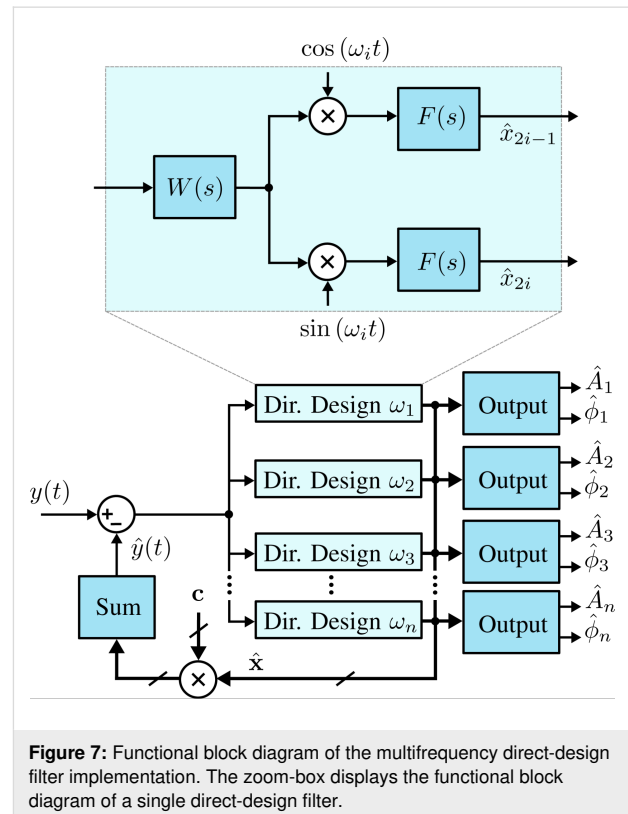
[37] on the direct-design method, a useful and relatively simple design methodology is detailed. Firstly, $F(s)$ is set as

$$F(s) = \frac{\gamma}{s}, \tag{19}$$

meaning the closed-loop equivalent transfer function is

$$\tilde{F}(s) = \frac{B(s)}{A(s)} = \frac{1}{2}\left[F(s+j\omega) + F(s-j\omega) \right]. \tag{20}$$

The pre-filter $W(s) = P(s)/L(s)$ is then found according to the pole-assignment equation

$$A_{\mathrm{d}}(s) = L(s)A(s) + P(s)B(s) \tag{21}$$

to achieve a specified closed-loop response.

For example, to implement a 2nd-order bandpass Butterworth prototype, the closed-loop transfer function is

$$G_{\mathrm{d}}(s) = \frac{B_{\mathrm{d}}(s)}{A_{\mathrm{d}}(s)} = \frac{b_2 s^2}{s^4 + a_3 s^3 + a_2 s^2 + a_1 s + a_0}. \tag{22}$$

Here, b_2 and A_i are the filter coefficients the values of which are calculated based on the chosen filter order and bandwidth around the modeled frequency ω_i. As the desired closed-loop polynomial has five coefficients, the coefficients of the pre-filter $W(s)$ are of the form

$$W(s) = \frac{P(s)}{L(s)} = \frac{p_1 s + p_0}{l_2 s^2 + l_1 s + l_0}, \tag{23}$$

and are able to be obtained by solving Equation 21.

The existing literature on direct-design demodulation techniques [37,38] is concerned with single-frequency applications.

However, this article demonstrates the performance advantages that can also be achieved in multifrequency applications.

Summary

Table 1 compares the multifrequency demodulation techniques discussed in this section. Two distinct categories of synchronous demodulators can be seen; those that employ low-pass filtering of mixing products in open-loop configurations and those that use closed-loop model-based feedback to regulate the error. As shown in a previous work [28], the closed-loop methods are able to maintain very high tracking bandwidths, achieving single-cycle convergence ($f_{-3\mathrm{dB}} \approx f_{\mathrm{i}}$) with optimal noise performance.

Results and Discussion
Experimental setup
The multifrequency demodulation techniques detailed in the previous section were implemented on a Xilinx Kintex-7 KC705 evaluation board (model: XC7K325T) paired with a DC-coupled high-speed 4DSP input/output (I/O) card (model: FMC151). The FPGA clock is synchronized with the high-speed I/O card at 240 MHz. The I/O card has a two-channel 14-bit analog-to-digital converter (ADC) and a two-channel 16-bit digital-to-analog converter (DAC), which sample at 250 MHz and 800 MHz, respectively. All demodulation methods were run at a nominal sampling frequency of $F_{\mathrm{s}} = 1.5$ MHz.

Implementation
Because of the high complexity, the sampling rate off the Kalman filter implementation was set to $F_{\mathrm{s}} = 1.5$ MHz, which was the maximum achievable for three modeled frequencies employing floating point precision to ensure covariance matrix stability and a computationally optimized implementation [32].

The Lyapunov filter and direct-design method achieve sampling rates of $F_{\mathrm{s}} = 7$ MHz for three modeled frequencies. This is due to the reduced complexity compared to the Kalman filter, floating point precision was also used to implement these methods.

Table 1: Summary of multifrequency demodulation estimation methods.

method	tuning	configuration	order	references
lock-in amplifier	low-pass filter	open-loop	specified n	[28,39-41]
coherent demodulator	number of hold cycles	open-loop	specified n	[28,44-47,58]
Kalman filter	$\mathbf{Q}_k$	closed-loop	1st	[28,31,32,48,53]
Lyapunov filter	$\mathbf{\Gamma}$	closed-loop	1st	[28,33,35,36,59]
direct-design method	desired poles	closed-loop	specified n	[37,38]

The open-loop methods include the lock-in amplifier and coherent demodulator, which are able to achieve $F_s = 120$ MHz for three modeled frequencies. In contrast to the closed-loop methods, the open-loop methods are compatible with pipelined fixed-point implementation, which results in significantly increased maximum sampling rates and reduced FPGA resource usage. A large number of modeled frequencies are possible.

In addition to processing requirements, the implementation complexity may also be increased by timing requirements. For example, the fixed-length numerical integration of the coherent demodulator results in sinc($\cdot$) frequency responses the zeros of which are related to F_s/f_i. This results in a limited number of possible high-bandwidth configurations. At low bandwidths, there is much more flexibility in achieving a desired bandwidth as the ($N + 1$)-FIR filter is longer. Here, the group delay ($N/2$) introduced should be considered with respect to the phase margin of the z-axis feedback loop.

Off-mode rejection

Each multifrequency demodulator was assessed by applying a single-tone sine sweep of the carrier frequency ω_i on an input signal described by Equation 1. For each demodulator, an amplitude magnitude frequency response of all three channels was recorded as the input carrier frequency was swept from DC to 750 kHz with a constant amplitude A_i. The three channels were configured to model carrier frequencies of 50, 150, and 300 kHz. In this experiment, the noise floor is dictated by a residual DC offset, which is present due to the finite resolution of the DAC. However, as each demodulation technique was analyzed by using the same hardware, the relative OMR differences are a good indication of each methods performance.

The open-loop methods have the benefit of being easily configured to a desired filter order. For this experiment they are of 4th order, which for low-bandwidth settings in Figure 8 creates very steep roll-offs for the lock-in amplifier (Figure 8a,b) and coherent demodulator (Figure 8e,f). When compared to the

fixed 1st-order Kalman filter (Figure 8i,j) and Lyapunov filter (Figure 8m,n), the open-loop methods achieve stronger attenuation around the modeled carrier frequency.

The difference between the lock-in amplifier and coherent demodulator is the method used to employ the low-pass filter for suppressing mixing products. In this experiment, the lock-in amplifier utilizes a Butterworth filter, which generates a maximally flat frequency response around the modeled carrier frequency. Conversely, the coherent demodulator employs fixed-length numerical integration resulting in a sinc($\cdot$) envelope in its frequency response [28]. This leads to strong OMR at regular intervals at sinc($\cdot$) zero locations. However, there is less rejection in-between zeros compared to the Butterworth response.

In contrast to the open-loop methods, the Kalman and Lyapunov filters operate in a closed-loop configuration resulting in state cross-coupling during feedback. As seen in Figure 8 for the Kalman filter (Figure 8i–l) and the Lyapunov filter (Figure 8m–p), this leads to each channel zeroing frequency components corresponding to the other modeled channels. The direct-design method alleviates the fixed 1st-order frequency response of the Kalman and Lyapunov filters. In Figure 8, the direct-design method (Figure 8q–t) performance is shown when configured to a 2nd-order Butterworth filter. The higher filter order results in greater suppression of broadband noise and other frequency components around the modeled carrier frequency when compared to the other closed-loop methods.

Table 2 examines the channel-to-channel OMR performance of each multifrequency demodulator for the 300 kHz channel. It is clear that the open-loop demodulators have a significant performance decrease as the tracking bandwidth increases. The poor OMR is caused by insufficient roll-off of each frequency response with respect to the other modeled frequencies f_1 and f_2. This occurs despite the coherent demodulator rejecting its own $2f_i$ mixing products. In contrast, the closed-loop Kalman filter, Lyapunov filter and direct-design methods benefit from cross-coupling zeros across all bandwidths allowing them to maintain

Table 2: Channel-to-channel off-mode rejection for the $f_3 = 300$ kHz channel.

method	Bandwidth 0.1%f_i		Bandwidth 1%f_i		Bandwidth 10%f_i		Bandwidth 50%f_i	
	$\text{OMR}_{f_3f_1}$ (dB)	$\text{OMR}_{f_3f_2}$ (dB)	$\text{OMR}_{f_3f_1}$ (dB)	$\text{OMR}_{f_3f_2}$ (dB)	$\text{OMR}_{f_3f_1}$ (dB)	$\text{OMR}_{f_3f_2}$ (dB)	$\text{OMR}_{f_3f_1}$ (dB)	$\text{OMR}_{f_3f_2}$ (dB)
lock-in amplifier	−43.8	−44.0	−42.2	−42.8	−39.5	−29.0	−14.2	−3.1
coherent demodulator	−45.6	−46.3	−40.5	−40.0	−36.4	−27.8	−14.3	−4.6
Kalman filter	−44.0	−44.1	−53.0	−52.1	−47.8	−49.7	−42.6	−47.0
Lyapunov filter	−41.7	−40.5	−52.8	−53.1	−44.8	−46.2	−46.1	−47.4
direct-design method	−41.6	−46.7	−42.3	−43.5	−47.2	−46.0	−51.7	−52.3
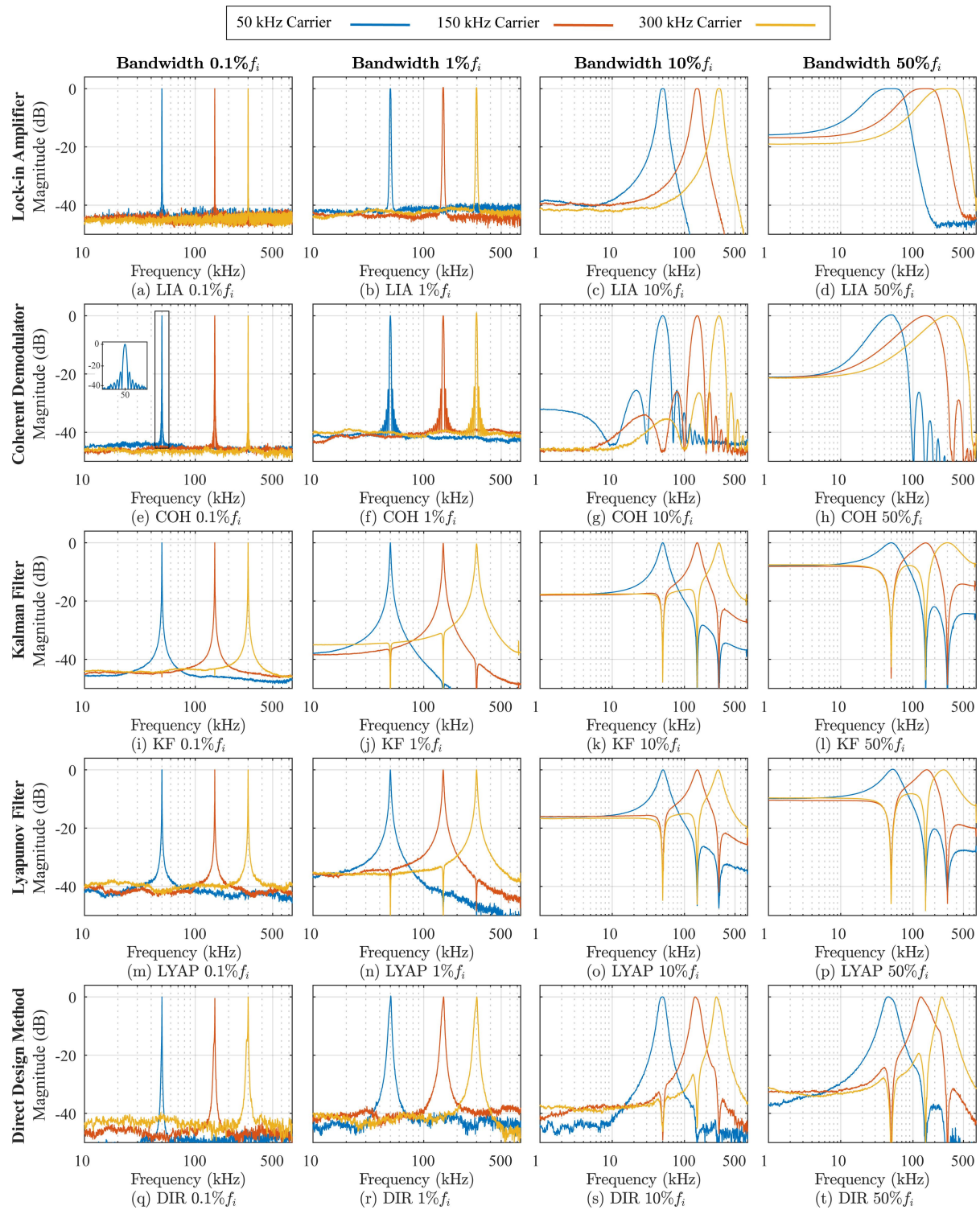
Figure 8: Experimental off-mode rejection results. Here each multifrequency demodulator is on a single row and the tracking bandwidths are adjusted per column with settings of 0.1%f_i, 1%f_i, 10%f_i and 50%f_i. For each system the three modeled carrier frequencies are $f_1 = 50$kHz (blue), $f_2 = 150$ kHz (red) and $f_3 = 300$ kHz (yellow).

a strong OMR. The ability to precisely resolve the zeros is limited by the DAC resolution. However, the performance distinction between open-loop and closed-loop methods is clear.

Time-domain estimation analysis

Amplitude estimation performance of the three-channel multi-frequency demodulators was investigated when a three-tone

sinewave was applied as an input signal described by Equation 2. Here, A_1 = 500 mV, A_2 = 100 mV, A_3 = 50 mV, f_1 = 50 kHz, f_2 = 150 kHz, and f_3 = 300 kHz. Figure 9 shows the amplitude estimation error ($\hat{A}_i / A_i \times 100\%$) in the time-domain and amplitude estimate power spectral density (PSD) for both low (1%f_i) and high (50%f_i) tracking bandwidth settings.

When the three-tone sinewave is applied, the performance of each demodulator at low bandwidths is shown to be similar. Each channel is able to estimate the amplitude of its modeled frequency, while strongly attenuating the other frequency components present in the input signal.

At high bandwidths, closed-loop demodulators benefit from cross-coupling zeros at the modeled frequencies. Compared to the open-loop methods, this results in significantly less estimation error as seen in Figure 9. In Figure Figure 9a, the lock-in amplifier 50 kHz estimate contains mixing products at $2f_i$ = 100 kHz in the time-domain, shown as distinct peaks in the PSD. In contrast, the coherent demodulator in Figure 9b strongly attenuates the mixing products. The performance difference is due to the Butterworth filter not sufficiently attenuating the mixing products, while the sinc(·) envelope contains a zero at $2f_i$. However, both open-loop methods poorly estimate the 150 kHz and 300 kHz input signals at high tracking bandwidths due to weak OMR. The PSD reveals that the large estimation errors consist of intermodulation products, which arise from the input multiplying stage.

AFM imaging

The lock-in amplifier and Lyapunov filter were compared through an MF-AFM imaging experiment where they estimate a signal in the presence of undesirable frequency components. These demodulators were chosen as they are the most simple methods to implement in their respective configurations. This experiment further investigated open-loop and closed-loop demodulator performance at low and high tracking bandwidths.

When compared to bimodal AFM, higher-harmonic AFM [15,60] has inherently greater demodulation challenges. Strong OMR is required as higher harmonics are separated by nf_0, much closer than the approx. $6f_0$ second eigenmode spacing [61]. In addition, harmonic content from tip–sample interactions scales with approx. $1/n^2$[13]. Therefore, the signals of interest are detected in the presence of a much larger fundamental resonance frequency, emphasizing the need for strong noise sensitivity from the demodulator.

Higher-harmonic AFM imaging was performed using an NT-MDT NTEGRA AFM on the second harmonic amplitude. The chosen cantilever (Budget Sensor TAP190G) has a funda-

mental resonance frequency of 156.75 kHz. The sample is a blend of polystyrene (PS) and polyolefin elastomer (LDPE) available from Bruker (PS-LDPE-12M). Due to the different elastic moduli of the PS and LPDE regions, the sample is used for evaluating imaging methods that are sensitive to elasticity.

Higher-harmonic amplitude images were obtained by the lock-in amplifier and Lyapunov filter on the second harmonic. Each demodulator was configured to track 313.50 kHz. In addition, the Lyapunov filter contained a channel modeling the fundamental resonance frequency. Although the cantilever is actively driven at its fundamental resonance frequency, during imaging its deflection signal contains additional frequency components. These include higher harmonics and intermodulation products excited by non-linear tip–sample forces during contact.

Second-harmonic amplitude images captured by both demodulators at low (1 kHz) and high (60 kHz) tracking bandwidths are shown in Figure 10. At low bandwidths, the lock-in amplifier (Figure 10e) and the Lyapunov filter (Figure 10c) perform comparably as demonstrated in a previous work [36]. However, at high bandwidths the lock-in amplifier image has large artifacts when compared to the Lyapunov filter. This is due to the different OMR achieved by each system with respect to the fundamental resonance frequency. Through channel cross-coupling, the Lyapunov filter is guaranteed to contain a zero at the desired location of 156.75 kHz.

In contrast, the lock-in amplifier insufficiently attenuates the fundamental resonance frequency. The PSD of the raw data from a single scan line (Figure 10g), taken from the image in Figure 10f, reveals that the estimate contains large intermodulation products. These signal components are aliased due to the low AFM sampling frequency (F_s = 256 Hz), resulting in the low-frequency artifacts seen in Figure 10f.

Conclusion

This article compares the performance of traditional and recently proposed demodulators for MF-AFM. These include conventional open-loop methods such as the lock-in amplifier and coherent demodulator, and closed-loop methods such as the Kalman filter, the Lyapunov filter and the direct-design method. The sensitivity of each demodulator to unwanted frequency components was assessed for low and high tracking bandwidths. Additionally, higher-harmonic AFM imaging was conducted for both low and high tracking bandwidths to further compare demodulator performance.

Open-loop demodulation schemes attenuate the high-frequency mixing component at $2f_i$ by employing a low-pass filter. The lock-in amplifier provides flexibility to implement a desired
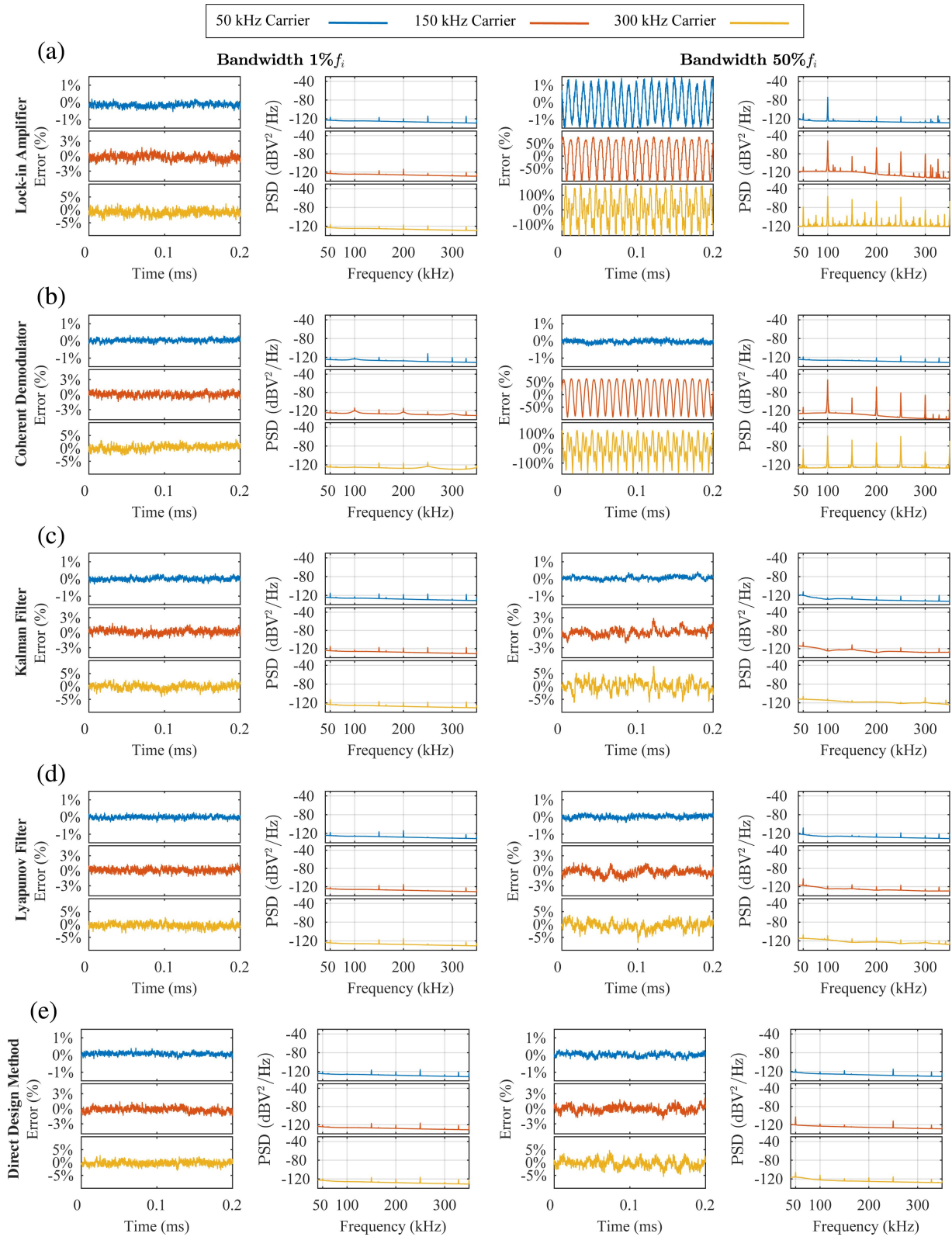
Figure 9: Experimental amplitude estimation error and power spectral density of amplitude estimation for the (a) lock-in amplifier, (b) coherent demodulator, (c) Kalman filter, (d) Lyapunov filter and (e) direct-design method for low (1%f_i) and high (50%f_i) tracking bandwidths. The input signal is described by Equation 2, where A_1 = 500 mV, A_2 = 100 mV, A_3 = 50 mV and f_1 = 50 kHz, f_2 = 150 kHz and f_3 = 300 kHz.

(a) Topography 2D.

(b) Topography 3D.

(c) LYAP $\hat{A}_{HH2}$ at 1 kHz.

(d) LYAP $\hat{A}_{HH2}$ at 60 kHz.

(e) LIA $\hat{A}_{HH2}$ at 1 kHz.

(f) LIA $\hat{A}_{HH2}$ at 60 kHz.

(g) PSD of raw data from a single scan line in the image (f).
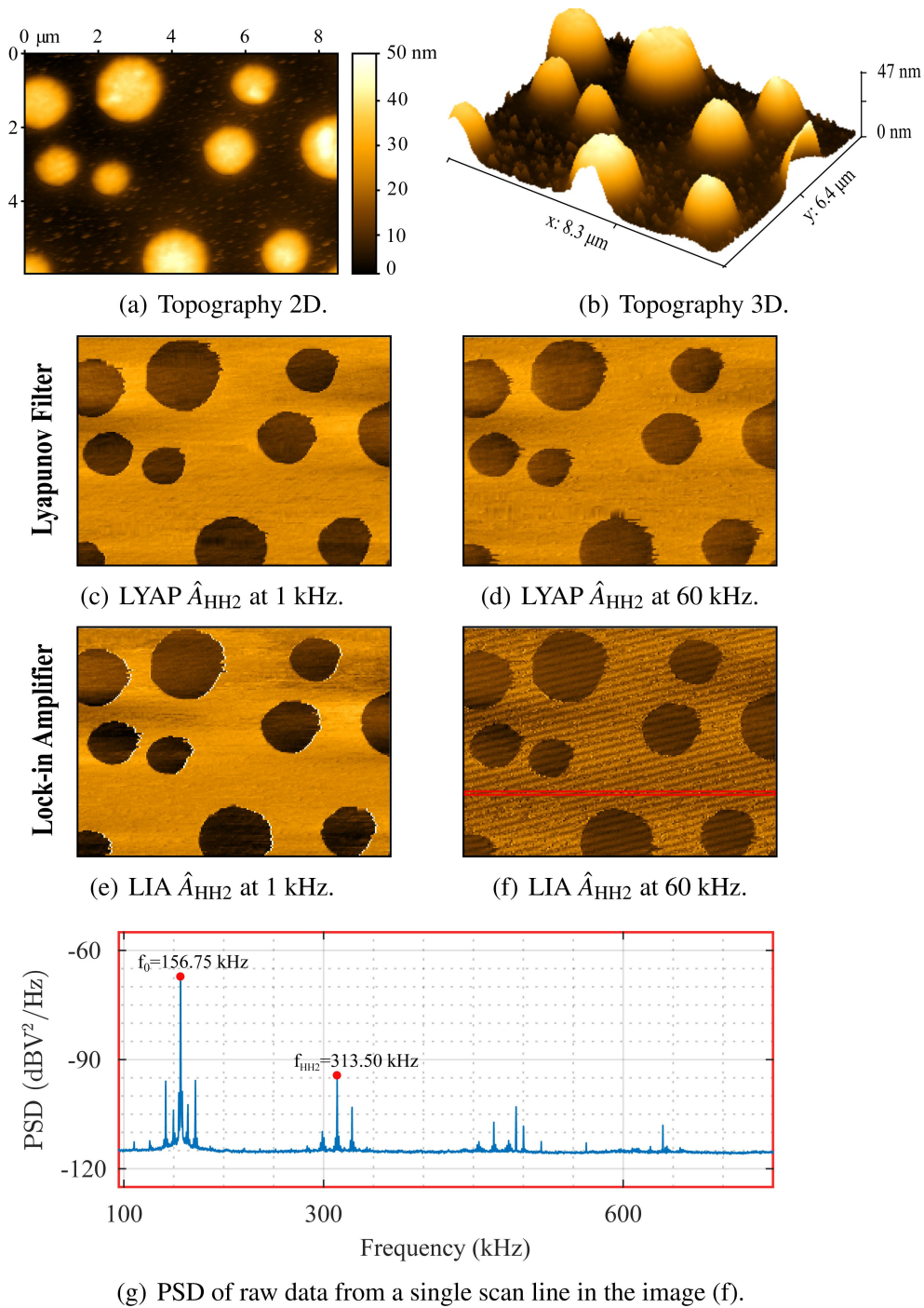
Figure 10: Higher-harmonic amplitude AFM imaging performed with the fundamental mode of a TAP190G cantilever on a PS/LPDE polymer blend. Images shown are the (a,b) topography in nanometers at 3 kHz, with parallel second-harmonic amplitude estimates from the (c,d) lock-in amplifier and (e,f) Lyapunov filter at tracking bandwidths of 1 kHz and 60 kHz. The PSD (g) is shown for the raw data of a single scan line from the image in (f).

filter response and order. Conversely, the coherent demodulator contains a sinc(·) envelope as it performs numerical integration over a fixed-length time window. Both demodulators excel at low bandwidths due to steep roll-offs, while having poor OMR at high tracking bandwidths. Although the lock-in amplifier implementation is simpler, the coherent demodulator

sinc(·) lobes are advantageous for higher harmonic and intermodulation AFM.

The closed-loop Kalman filter, Lyapunov filter and direct-design method employ internal feedback of the estimated states to reject the mixing products. This allows them to maximize the

Table 3: Summary of MF-AFM applications and required demodulator properties. Note: f_0 is the fundamental resonance frequency and f_i is the demodulated frequency.

MF-AFM application	application characteristics		demodulator properties	
	frequency spacing	number of channels	tracking bandwidth	off-mode rejection
intermodulation	very small $(f_i/f_0 \ll 1)$	40+	very low $(\ll 1\% f_0)$	very important
higher harmonic	medium $(f_i/f_0 \approx 1)$	10+	low $(1\% f_0)$	important
higher mode	large $(f_i/f_0 \gg 1)$	1–5	user choice $(\geq 1\% f_0)$	less important

tracking bandwidth without introducing additional noise in the amplitude estimate [28]. An added benefit of this approach is cross-coupling zeros occurring at modeled frequencies, which was demonstrated to reduce estimation artifacts. The direct-design method alleviates the limited 1st-order response of the Kalman and Lyapunov filters. When configured to a 2nd-order Butterworth response, it achieved an increased roll-off which increases broadband noise suppression while still maintaining strong OMR performance.

Table 3 is provided as a reference of MF-AFM application characteristics and required demodulator properties. A recommendation for which demodulator is most suited to three major MF-AFM applications is given as follows:

Intermodulation AFM: This MF-AFM application tracks a large number of closely spaced intermodulation products [16]. As each signal of interest has a frequency separation of the order of 100 Hz, a very low bandwidth and a very strong OMR are essential. The requirement to track up to 40+ signals is most suited to a computationally inexpensive open-loop method. The coherent demodulator is recommended for intermodulation AFM, since the sinc(·) response of each channel can be configured to zero other intermodulation products [58].

Higher-harmonic AFM: This MF-AFM application tracks integer multiples of the cantilever fundamental resonance frequency, resulting in frequency spacing of the order of the fundamental resonance frequency, which ranges between 100 and 300 kHz. Since each harmonic is in the presence of a much larger fundamental resonance frequency, a low tracking bandwidth and a strong OMR is required. The open-loop lock-in amplifier and coherent demodulator are recommended at low tracking bandwidths. While the closed-loop Lyapunov filter and direct-design method are recommended if a higher tracking bandwidth is desired. This is because the closed-loop methods have the added benefit of zeroing the large fundamental resonance frequency and other harmonics.

Higher-mode AFM: This MF-AFM application tracks the fundamental resonance frequency and higher resonance modes. Frequency content of interest is typically separated by 500 kHz or more, depending on the cantilever geometry. This provides flexibility to the user to operate at either a low or high tracking bandwidth. At low tracking bandwidths, the lock-in amplifier is recommended, as it is of lower complexity than the coherent demodulator, which offers little benefit for widely spaced signals. At high tracking bandwidths, a closed-loop method is recommended as they achieve single-cycle convergence $(f_{-3\mathrm{dB}} \approx f_i)$ with optimal noise performance. Also, each channel has the added benefit of zeroing other resonant modes. The Lyapunov filter and direct-design method are preferred over the Kalman filter, as they are significantly easier to implement.

ORCID® iDs

David M. Harcombe - https://orcid.org/0000-0002-9866-5806
Michael G. Ruppert - https://orcid.org/0000-0003-2286-4929
Andrew J. Fleming - https://orcid.org/0000-0001-7132-8458

References

1. Binnig, G.; Quate, C. F.; Gerber, C. *Phys. Rev. Lett.* **1986,** *56,* 930–933. doi:10.1103/physrevlett.56.930
2. Rabe, U.; Janser, K.; Arnold, W. *Rev. Sci. Instrum.* **1996,** *67,* 3281–3293. doi:10.1063/1.1147409
3. Abramovitch, D. Y.; Andersson, S. B.; Pao, L. Y.; Schitter, G. A tutorial on the mechanisms, dynamics, and control of atomic force microscopes. In *2007 American Control Conference,* 2007; pp 3488–3502.
4. García, R.; Perez, R. *Surf. Sci. Rep.* **2002,** *47,* 197–301. doi:10.1016/s0167-5729(02)00077-8
5. García, R. *Amplitude Modulation Atomic Force Microscopy;* Wiley-VCH Verlag GmbH: Weinheim, Germany, 2010. doi:10.1002/9783527632183
6. Möller, C.; Allen, M.; Elings, V.; Engel, A.; Müller, D. J. *Biophys. J.* **1999,** *77,* 1150–1158. doi:10.1016/s0006-3495(99)76966-3
7. Kodera, N.; Yamamoto, D.; Ishikawa, R.; Ando, T. *Nature* **2010,** *468,* 72–76. doi:10.1038/nature09450
8. Chiaruttini, N.; Redondo-Morata, L.; Colom, A.; Humbert, F.; Lenz, M.; Scheuring, S.; Roux, A. *Cell* **2015,** *163,* 866–879. doi:10.1016/j.cell.2015.10.017

9. Zhong, Q.; Inniss, D.; Kjoller, K.; Elings, V. B. *Surf. Sci.* **1993,** *290,* L688–L692. doi:10.1016/0039-6028(93)90582-5

10. Tamayo, J.; Humphris, A. D. L.; Miles, M. J. *Appl. Phys. Lett.* **2000,** *77,* 582–584. doi:10.1063/1.127051

11. Lübbe, J.; Tröger, L.; Torbrügge, S.; Bechstein, R.; Richter, C.; Kühnle, A.; Reichling, M. *Meas. Sci. Technol.* **2010,** *21,* 125501. doi:10.1088/0957-0233/21/12/125501

12. Ando, T.; Kodera, N.; Takai, E.; Maruyama, D.; Saito, K.; Toda, A. *Proc. Natl. Acad. Sci. U. S. A.* **2001,** *98,* 12468–12472. doi:10.1073/pnas.211400898

13. García, R.; Herruzo, E. T. *Nat. Nanotechnol.* **2012,** *7,* 217–226. doi:10.1038/nnano.2012.38

14. Martínez, N. F.; Lozano, J. R.; Herruzo, E. T.; Garcia, F.; Richter, C.; Sulzbach, T.; Garcia, R. *Nanotechnology* **2008,** *19,* 384011. doi:10.1088/0957-4484/19/38/384011

15. Stark, R. W.; Heckl, W. M. *Rev. Sci. Instrum.* **2003,** *74,* 5111–5114. doi:10.1063/1.1626008

16. Platz, D.; Tholén, E. A.; Pesen, D.; Haviland, D. B. *Appl. Phys. Lett.* **2008,** *92,* 153106. doi:10.1063/1.2909569

17. García, R.; Proksch, R. *Eur. Polym. J.* **2013,** *49,* 1897–1906. doi:10.1016/j.eurpolymj.2013.03.037

18. Hillenbrand, R.; Stark, M.; Guckenberger, R. *Appl. Phys. Lett.* **2000,** *76,* 3478–3480. doi:10.1063/1.126683

19. Raman, A.; Trigueros, S.; Cartagena, A.; Stevenson, A. P. Z.; Susilo, M.; Nauman, E.; Contera, S. A. *Nat. Nanotechnol.* **2011,** *6,* 809–814. doi:10.1038/nnano.2011.186

20. Preiner, J.; Tang, J.; Pastushenko, V.; Hinterdorfer, P. *Phys. Rev. Lett.* **2007,** *99,* 046102. doi:10.1103/physrevlett.99.046102

21. Cartagena-Rivera, A. X.; Wang, W.-H.; Geahlen, R. L.; Raman, A. *Sci. Rep.* **2015,** *5,* 11692. doi:10.1038/srep11692

22. Forchheimer, D.; Borysov, S. S.; Platz, D.; Haviland, D. B. *Nanotechnology* **2014,** *25,* 485708. doi:10.1088/0957-4484/25/48/485708

23. Herruzo, E. T.; Perrino, A. P.; Garcia, R. *Nat. Commun.* **2014,** *5,* 3126. doi:10.1038/ncomms4126

24. Benaglia, S.; Amo, C. A.; García, R. *Nanoscale* **2019,** *11,* 15289–15297. doi:10.1039/c9nr04396a

25. Platz, D.; Tholén, E. A.; Hutter, C.; von Bieren, A. C.; Haviland, D. B. *Ultramicroscopy* **2010,** *110,* 573–577. doi:10.1016/j.ultramic.2010.02.012

26. Forchheimer, D.; Forchheimer, R.; Haviland, D. B. *Nat. Commun.* **2015,** *6,* 6270. doi:10.1038/ncomms7270

27. Thorén, P.-A.; de Wijn, A. S.; Borgani, R.; Forchheimer, D.; Haviland, D. B. *Nat. Commun.* **2016,** *7,* 13836. doi:10.1038/ncomms13836

28. Ruppert, M. G.; Harcombe, D. M.; Ragazzon, M. R. P.; Moheimani, S. O. R.; Fleming, A. J. *Beilstein J. Nanotechnol.* **2017,** *8,* 1407–1426. doi:10.3762/bjnano.8.142

29. Ando, T. *Nanotechnology* **2012,** *23,* 062001. doi:10.1088/0957-4484/23/6/062001

30. Kitchin, C.; Counts, L. *RMS to DC Conversion Application Guide,* 1st ed.; Analog Devices, 1986.

31. Ruppert, M. G.; Karvinen, K. S.; Wiggins, S. L.; Reza Moheimani, S. O. *IEEE Trans. Control Syst. Technol.* **2016,** *24,* 276–284. doi:10.1109/tcst.2015.2435654

32. Ruppert, M. G.; Harcombe, D. M.; Moheimani, S. O. R. *IEEE/ASME Trans. Mechatronics* **2016,** *21,* 2705–2715. doi:10.1109/tmech.2016.2574640

33. Ragazzon, M. R. P.; Ruppert, M. G.; Harcombe, D. M.; Fleming, A. J.; Gravdahl, J. T. *IEEE Trans. Control Syst. Technol.* **2018,** *26,* 765–772. doi:10.1109/tcst.2017.2692721

34. Ruppert, M. G.; Harcombe, D. M.; Ragazzon, M. R. P.; Moheimani, S. O. R.; Fleming, A. J. Frequency Domain Analysis of Robust Demodulators for High-Speed Atomic Force Microscopy. In *2017 American Control Conference (ACC),* 2017.

35. Harcombe, D. M.; Ruppert, M. G.; Ragazzon, M. R.; Fleming, A. J. Higher-harmonic AFM imaging with a high-bandwidth multifrequency Lyapunov filter. In *2017 IEEE International Conference on Advanced Intelligent Mechatronics (AIM),* 2017; pp 725–730.

36. Harcombe, D. M.; Ruppert, M. G.; Ragazzon, M. R. P.; Fleming, A. J. *Beilstein J. Nanotechnol.* **2018,** *9,* 490–498. doi:10.3762/bjnano.9.47

37. Ruppert, M. G.; Harcombe, D. M.; Moore, S. I.; Fleming, A. J. Direct Design of Closed-loop Demodulators for Amplitude Modulation Atomic Force Microscopy. In *2018 Annual American Control Conference (ACC),* 2018; pp 4336–4341.

38. Moore, S. I.; Ruppert, M. G.; Harcombe, D. M.; Fleming, A. J.; Yong, Y. K. *IEEE/ASME Trans. Mechatronics* **2019,** *24,* 1861–1870. doi:10.1109/tmech.2019.2928592

39. Cosens, C. R. *Proc. Phys. Soc., London* **1934,** *46,* 818–823. doi:10.1088/0959-5309/46/6/310

40. Michels, W. C.; Curtis, N. L. *Rev. Sci. Instrum.* **1941,** *12,* 444–447. doi:10.1063/1.1769919

41. Morris, E. D., Jr.; Johnston, H. S. *Rev. Sci. Instrum.* **1968,** *39,* 620–621. doi:10.1063/1.1683462

42. Lyons, R. G. *Understanding Digital Signal Processing,* 1st ed.; Addison-Wesley Longman Publishing Co., Inc.: Boston, MA, U.S.A., 1996.

43. Volder, J. E. *IRE Trans. Electron. Comput.* **1959,** *EC-8,* 330–334. doi:10.1109/tec.1959.5222693

44. Kokavecz, J.; Tóth, Z.; Horváth, Z. L.; Heszler, P.; Mechler, Á. *Nanotechnology* **2006,** *17,* S173–S177. doi:10.1088/0957-4484/17/7/s12

45. Abramovitch, D. Y. Coherent Demodulation with Reduced Latency Adapted for use in Scanning Probe Microscopes. U.S. Patent US20100128342A1, May 27, 2010.

46. Abramovitch, D. Y. Low latency demodulation for Atomic Force Microscopes, Part I efficient real-time integration. In *Proceedings of the 2011 American Control Conference,* 2011; pp 2252–2257.

47. Abramovitch, D. Y. Low Latency Demodulation for Atomic Force Microscopes, Part II: Efficient Calculation of Magnitude and Phase. In *IFAC Proceedings Volumes,* 2011; pp 12721–12726.

48. Kalman, R. E. *J. Basic Eng.* **1960,** *82,* 35–45. doi:10.1115/1.3662552

49. Grewal, M. S.; Henderson, V. D.; Miyasako, R. S. *IEEE Trans. Autom. Control* **1991,** *36,* 3–13. doi:10.1109/9.62283

50. Chen, S. Y. *IEEE Trans. Ind. Electron.* **2012,** *59,* 4409–4420. doi:10.1109/tie.2011.2162714

51. Harvey, A. C. *Forecasting, Structural Time Series Models and the Kalman Filter;* Cambridge University Press: Cambridge, United Kingdom, 1990.

52. Anderson, B.; Moore, J. *Optimal Filtering;* Prentice-Hall, 1979.

53. Brown, R. G.; Hwang, P. Y. *Introduction to Random Signals and Applied Kalman Filtering,* 3rd ed.; John Wiley & Sons, 1985.

54. Simon, D. *Optimal State Estimation;* John Wiley & Sons, Inc.: Hoboken, NJ, U.S.A., 2006. doi:10.1002/0470045345

55. Girgis, A.; Daniel Hwang, T. *IEEE Trans. Power Appar. Syst.* **1984,** *PAS-103,* 2943–2951. doi:10.1109/tpas.1984.318297

56. Ioannou, P. A.; Sun, J. *Robust Adaptive Controls;* Docer Publications, Inc.: Mineola, NY, U.S.A., 2012.

57. Karvinen, K. S.; Moheimani, S. O. R. *Mechatronics* **2014,** *24,* 661–671.
doi:10.1016/j.mechatronics.2013.11.011

58. Tholén, E. A.; Platz, D.; Forchheimer, D.; Schuler, V.; Tholén, M. O.;
Hutter, C.; Haviland, D. B. *Rev. Sci. Instrum.* **2011,** *82,* 026109.
doi:10.1063/1.3541791

59. Ragazzon, M. R. P.; Gravdahl, J. T.; Fleming, A. J. On Amplitude
Estimation for High-Speed Atomic Force Microscopy. In *2016 Annual
American Control Conference (ACC),* 2016; pp 2635–2642.

60. Stark, M.; Stark, R. W.; Heckl, W. M.; Guckenberger, R.
Appl. Phys. Lett. **2000,** *77,* 3293–3295. doi:10.1063/1.1325404

61. García, R.; Magerle, R.; Perez, R. *Nat. Mater.* **2007,** *6,* 405–411.
doi:10.1038/nmat1925

Implementation of data-cube pump–probe KPFM on organic solar cells

Benjamin Grévin[*], Olivier Bardagot and Renaud Demadrille

Abstract

An implementation of pump–probe Kelvin probe force microscopy (pp-KPFM) is reported that enables recording the time-resolved surface potential in single-point mode or over a 2D grid. The spectroscopic data are acquired in open *z*-loop configuration, which simplifies the pp-KPFM operation. The validity of the implementation is probed by measurements using electrical pumping. The dynamical photoresponse of a bulk heterojunction solar cell based on PTB7 and PC$_{71}$BM is subsequently investigated by recording point-spectroscopy curves as a function of the optical power at the cathode and by mapping 2D time-resolved images of the surface photovoltage of the bare organic active layer.

Introduction

Many emerging photovoltaic technologies rely on the use of thin film materials displaying structural and/or chemical heterogeneities at the µm or nm scale. This is the case for solution-processed organic donor–acceptor blends called bulk heterojunctions (BHJ), for polycrystalline direct bandgap semiconductors such as CdTe, $CuIn_xGa_{(1-x)}Se_2$ and Cu_2ZnSnS_4 and for hybrid organic–inorganic perovskite solar cells. Whatever material used, improving the performance of the solar cell requires a precise understanding of the relationship of the structural,

chemical and optoelectronic properties of the device. Especially, a universal problem in third-generation photovoltaics consists in identifying the sources of carrier loss by the recombination of photogenerated charge carriers.

This has prompted the development of new time-resolved extensions of electrostatic force microscopy (EFM) and Kelvin probe force microscopy (KPFM). Time-resolved EFM (trEFM) has been used to map photoinduced charging rates (i.e., the time

needed to reach an electrostatic equilibrium after illumination) in organic donor–acceptor blends with sub-ms time resolution [1]. Subsequent works have shown that sub-µs time resolution can be achieved by acquiring the full information on the cantilever oscillation, leading to the development of fast trEFM [2] and general-mode KPFM [3].

Contrary to feedback-free electrostatic methods [4,5], conventional KPFM relies on a closed feedback loop that compensates the tip–sample contact potential difference (CPD). It is thus inherently a rather "slow technique". Kelvin controllers typically operate with time constants of a few to tens of ms. To implement time-resolved KPFM, a first method consists in increasing the detection bandwidth by using the so-called heterodyne mode [6-9] or dissipative electrostatic force modulation [10,11].

To probe the photocarrier lifetime in photovoltaic materials, another option consists in analyzing the dependence of the time-averaged KPFM compensation potential (or surface potential (SP)) on the frequency modulation (f_{mod}) of an illumination source. The first demonstration of light intensity-modulated KPFM (IM-KPFM) was carried out in 2008 by Takihara et al. on polycrystalline Si solar cells [12], and it has been recently applied to organic [13,14] and nanocrystal-based [15] solar cells. However, there are some disadvantages to using this technique. First, at specific frequencies, the excitation signal used to generate charge carriers can interfere [16] with the cantilever oscillation or the ac voltage applied for the detection of the CPD. Errors in the surface photovoltage (SPV) measurement caused by photoinduced changes in the capacitance gradient [17] can also be a problem. Upon modulated illumination, the KPFM loop indeed measures the time-averaged value of the instantaneous SP weighted by the capacitance gradient [17] instead of the time-averaged SP. This may lead to a frequency-dependent overestimation of the average SP and consequently generate errors in the mathematical fit performed on the SP(f_{mod}) curves, which is done to calculate the SPV decay-time constants. Last, the analysis of IM-KPFM data becomes a complex matter when the photocharging time is not negligible compared to the light pulse duration. In this case, numerical simulations are necessary to properly analyze the spectroscopic SP(f_{mod}) curves [18].
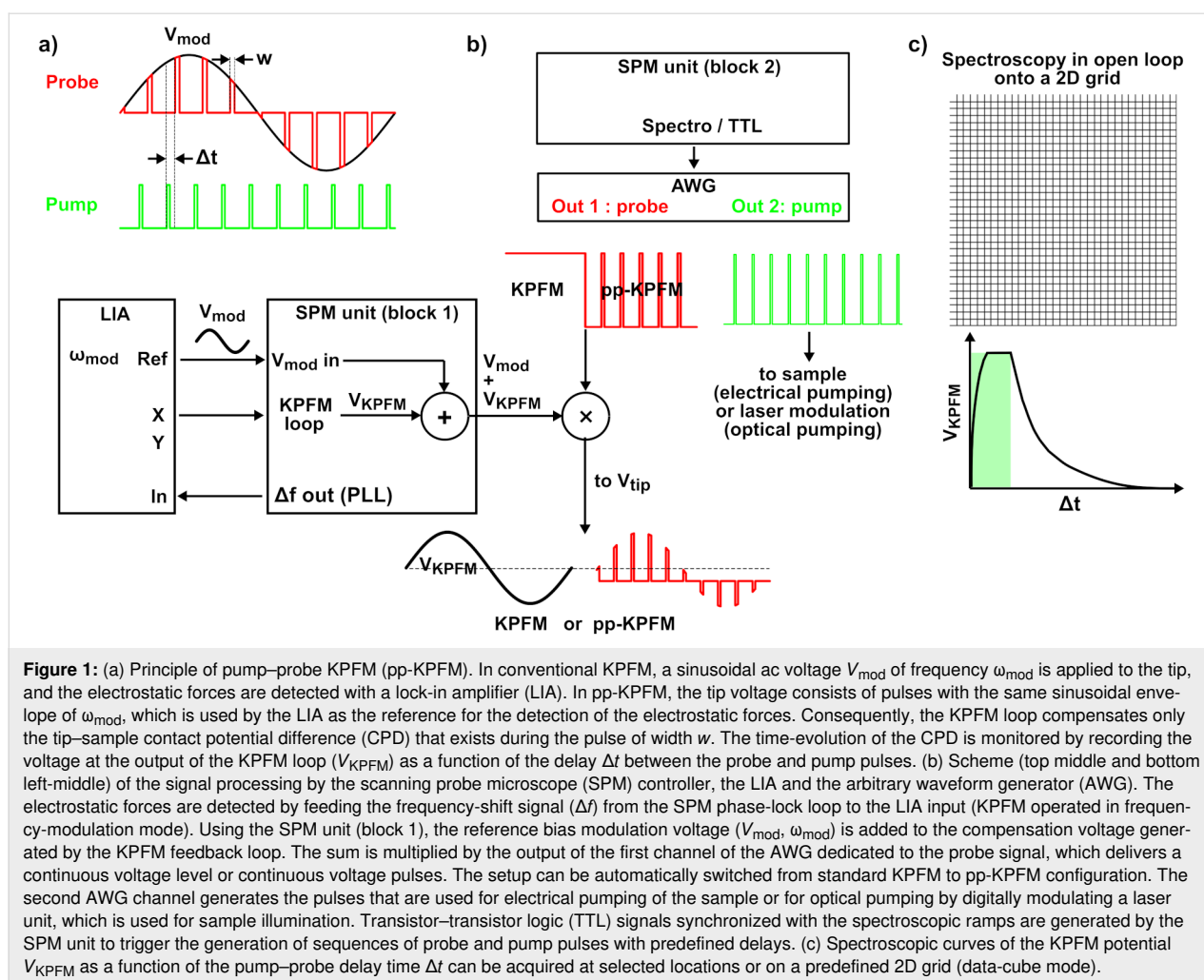
When investigating organic donor–acceptor (D–A) blends, both capacitive effects and photocharging dynamics shall be taken into account, which renders the interpretation of IM-KPFM data even more difficult. Upon illumination, the capacitive junction formed by the cantilever tip and the conducting substrate onto which the organic layer is deposited is indeed reduced due to photogenerated carriers [19]. As a first approximation, this effect can be understood by assuming that there are no perma-

nent charges in the "dark" (i.e., unilluminated) state of the organic layer considered as an undoped semiconductor. In "real" samples trapped carriers and electrostatic dipoles at the donor–acceptor interfaces contribute to the global electrostatic landscape probed by KPFM in the dark state [20]. The photocharging dynamics can be understood as follows. After exciton splitting and dissociation of the charge transfer states at the D–A interfaces, the photogenerated carriers experience a drift-diffusion limited by the carrier mobility [21]. Internal electric fields due to band bending at the D–A interfaces and at the organic/substrate interface play a key role in this process. In an open-circuit configuration occurring in KPFM experiments, the charges will move until the internal electric fields are compensated. Then the charge motion stops and the charge recombination balances the photogeneration. At this stage, the electrostatic landscape probed by KPFM reaches an equilibrium state.

Pump–probe Kelvin probe force microscopy (pp-KPFM) is a promising alternative to IM-KPFM. It is a priori not prone to capacitive artefacts, and it offers the possibility to probe directly and independently both the photocharging rate and the SPV decay. As introduced by Murawski et al. [22], in pp-KPFM the modulated bias voltage, which is used for the detection of electrostatic forces with a lock-in amplifier (LIA), is restricted to a finite time window (*w*, Figure 1a). Consequently, the counter potential generated by the KPFM loop compensates only the CPD that exists during this time window. By recording the KPFM signal as a function of the delay time Δt between the time window during which the ac modulation is applied (i.e., the probe) and the signal used to generate SP transients (the pump), one can track the SP evolution as a function of time.

The pump can be either an electrical (voltage pulse) or an optical (light pulse) signal. The first configuration was used by Murawski et al. to demonstrate the ability of pp-KPFM to probe the charge dynamics in organic field effect transistors (OFETs) at a µs temporal resolution [23]. For that purpose, they recorded successive images of the SP in the active channel of an OFET device, each of them being acquired at a different delay between the probe and a voltage pulse applied to the drain electrode of the transistor. In a later study, Schumacher et al. [24] used optical pumping in a pp-KPFM approach to probe the photocarrier lifetime in GaAs samples grown at low temperature.

In organic BHJ solar cells, electron donor and acceptor materials are processed to form two interpenetrated networks phase-segregated at the 10 nm scale. Consequently, if one aims at investigating the interplay of the morphology and the photocarrier dynamics in BHJs (and by extension in other nanostruc-

Figure 1: (a) Principle of pump–probe KPFM (pp-KPFM). In conventional KPFM, a sinusoidal ac voltage V_{mod} of frequency ω_{mod} is applied to the tip, and the electrostatic forces are detected with a lock-in amplifier (LIA). In pp-KPFM, the tip voltage consists of pulses with the same sinusoidal envelope of ω_{mod}, which is used by the LIA as the reference for the detection of the electrostatic forces. Consequently, the KPFM loop compensates only the tip–sample contact potential difference (CPD) that exists during the pulse of width *w*. The time-evolution of the CPD is monitored by recording the voltage at the output of the KPFM loop (V_{KPFM}) as a function of the delay Δt between the probe and pump pulses. (b) Scheme (top middle and bottom left-middle) of the signal processing by the scanning probe microscope (SPM) controller, the LIA and the arbitrary waveform generator (AWG). The electrostatic forces are detected by feeding the frequency-shift signal (Δf) from the SPM phase-lock loop to the LIA input (KPFM operated in frequency-modulation mode). Using the SPM unit (block 1), the reference bias modulation voltage (V_{mod}, ω_{mod}) is added to the compensation voltage generated by the KPFM feedback loop. The sum is multiplied by the output of the first channel of the AWG dedicated to the probe signal, which delivers a continuous voltage level or continuous voltage pulses. The setup can be automatically switched from standard KPFM to pp-KPFM configuration. The second AWG channel generates the pulses that are used for electrical pumping of the sample or for optical pumping by digitally modulating a laser unit, which is used for sample illumination. Transistor–transistor logic (TTL) signals synchronized with the spectroscopic ramps are generated by the SPM unit to trigger the generation of sequences of probe and pump pulses with predefined delays. (c) Spectroscopic curves of the KPFM potential V_{KPFM} as a function of the pump–probe delay time Δt can be acquired at selected locations or on a predefined 2D grid (data-cube mode).

tured photovoltaic materials), it is necessary to probe SP transients upon pulsed illumination at a high spatial resolution. Similar to the study of OFETs [23], a first option may consist in recording successive sequences of pp-KPFM images of the same sample area using a variable pump–probe delay time. However, at room temperature, as usually defined for studies of solar cells, it is hardly possible to record a stack of images while keeping exactly the same tip–sample relative positioning because of thermal drift and piezo creep. To avoid lateral misalignment artefacts, a better option is to record a matrix of spectroscopic curves of the pp-KPFM signal on a 2D grid. In this work, we explore the performance of such a spectroscopic pp-KPFM approach in data-cube mode. We show how topographic artefacts can be avoided by implementing an automated sequence that allows for performing the scan with a standard KPFM configuration and acquiring the spectroscopic pp-KPFM curves with an open *z*-loop. The implementation is validated by carrying out test measurements by electrical pumping of reference substrates. Moreover, the technique is applied to characterize BHJ solar cells by optical pumping. To

this end, point-spectroscopy curves are recorded on the device cathode as a function of the optical power using various values of the pump–probe time delay. Furthermore, the mapping of 2D time-resolved images of the bare active organic layer is employed. The results demonstrate that the SPV dynamics are dominated by trap-delayed processes in the investigated system. Current limitations and upcoming improvements of the chosen approach for pp-KPFM are finally discussed.

pp-KPFM Implementation

The experiments were performed on the basis of noncontact AFM (nc-AFM) under ultrahigh vacuum (UHV) with a beam deflection setup operated in frequency-modulation (FM) mode at room temperature. In the following, we only describe the general setup that has been used to implement data-cube pump–probe-KPFM (Figure 1b and Figure 1c). Additional technical information is provided in the experimental section.

We kept the standard SPM controller configuration for frequency-modulation KPFM (FM-KPFM). Here, the electrostatic
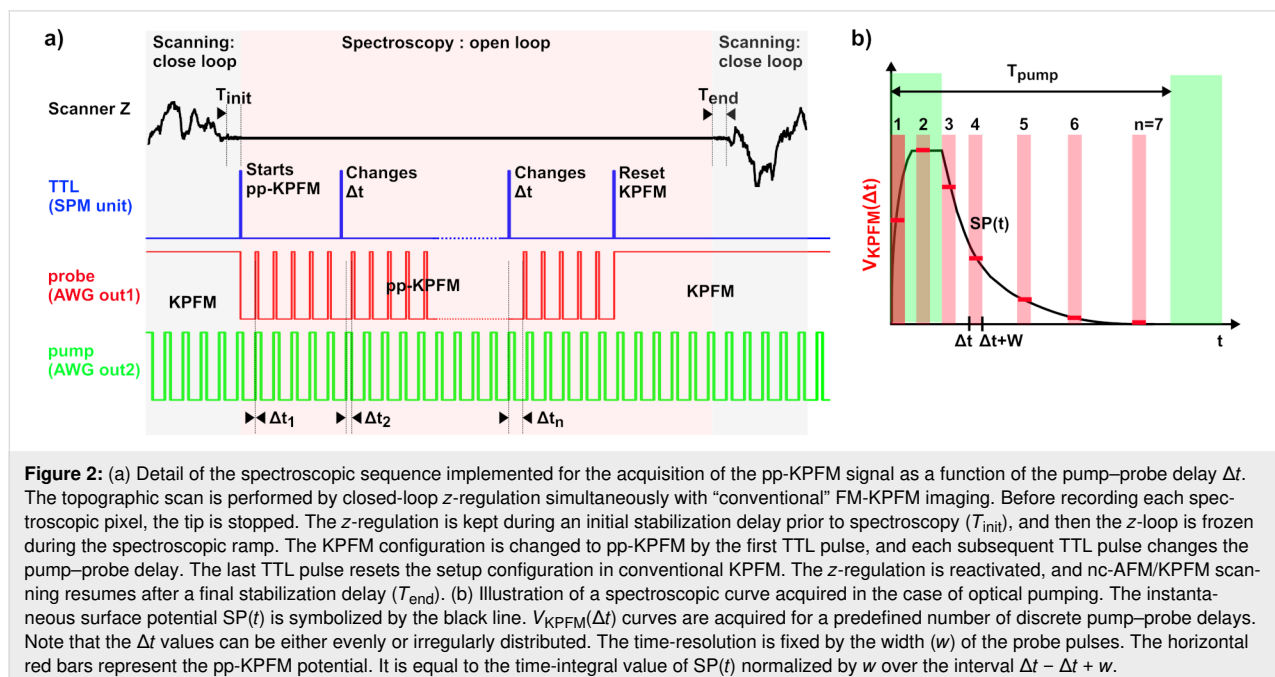
forces are detected by demodulating the modulated component (ω_{mod}) of the frequency-shift signal (Δf) with the LIA. The reference bias modulation voltage (V_{mod}, ω_{mod}) and the compensation voltage generated by the KPFM feedback loop (V_{KPFM}) are internally summed by the SPM unit.

To generate the modulated bias for pp-KPFM, a pseudo multiplication is performed on this voltage sum by using a fast analog switch, the TTL input of which is driven by one of the two outputs of a programmable AWG. In pp-KPFM, the CPD is only detected during the time window defined by the probe pulses. Murawski et al. have shown that this can generate artefacts in the z-regulation [22], since for any given pump–probe delay, the time-averaged CPD differs from the one probed and compensated by the KPFM loop. In our case, a similar issue occurs since the compensation bias is only applied during the probe-time window, keeping in mind that the multiplication by the pump train pulses is applied to the sum of V_{mod} and V_{KPFM}. As a result, the electrostatic forces are not compensated during the time interval between the probe pulses, and the z-feedback can be affected by the time-variable electrostatic force field. To minimize topographic artefacts, a first option may consist in using a dual set of KPFM compensation loops operated at different modulation frequencies [22]. The first loop would be used for pp-KPFM and the second to compensate the time-averaged component of the electrostatic potential.

In this work, we propose an alternative method that consists in operating the KPFM in standard mode (closed-loop z-regulation and sinusoidal bias modulation) for the topographic analysis and in switching the setup configuration to pp-KPFM with an open z-loop for the spectroscopic acquisition of $V_{KPFM}(\Delta t)$ curves (Figure 1b and Figure 2). Great care was taken to stabilize the setup before spectroscopic acquisition in open-loop configuration in order to minimize the impact of the z-drift on the KPFM potential. The residual z-drift less was smaller than 0.4 nm over a time lapse of 40 s, see Figure S1 in Supporting Information File 1. Switching the controller configuration from standard KPFM to pp-KPFM was done by synchronizing the AWG unit with the spectroscopic ramps of the SPM controller by means of TTL pulses and by using predefined sequences of pulses and continuous-wave (cw) dc signals stored in the memory of the AWG. Note that in this configuration, the KPFM potential probed during the topographic acquisition yields a time-averaged value of the SP since the pump signal is permanently applied to the sample. A further refinement, not shown in Figure 2, consists in switching also the pump signal to a cw level during the topographic acquisition, basically given by an "on" or "off" state. This can be done for the purpose of specific tests described hereafter. However, for optical pumping, it is preferable to keep the pump permanently in a modulated configuration as shown in Figure 2 to maintain a continuous time-averaged optical power on the cantilever to avoid thermal detuning effects.

Finally, one must keep in mind that pp-KPFM does not exactly probe the instantaneous SP but its time-averaged value over the time window defined by the probe pulse. This point is illustrated in Figure 2b. Moreover, we underline that in our approach the series of discrete pump–probe delay values used for

Figure 2: (a) Detail of the spectroscopic sequence implemented for the acquisition of the pp-KPFM signal as a function of the pump–probe delay Δt. The topographic scan is performed by closed-loop z-regulation simultaneously with "conventional" FM-KPFM imaging. Before recording each spectroscopic pixel, the tip is stopped. The z-regulation is kept during an initial stabilization delay prior to spectroscopy (T_{init}), and then the z-loop is frozen during the spectroscopic ramp. The KPFM configuration is changed to pp-KPFM by the first TTL pulse, and each subsequent TTL pulse changes the pump–probe delay. The last TTL pulse resets the setup configuration in conventional KPFM. The z-regulation is reactivated, and nc-AFM/KPFM scanning resumes after a final stabilization delay (T_{end}). (b) Illustration of a spectroscopic curve acquired in the case of optical pumping. The instantaneous surface potential SP(t) is symbolized by the black line. $V_{KPFM}(\Delta t)$ curves are acquired for a predefined number of discrete pump–probe delays. Note that the Δt values can be either evenly or irregularly distributed. The time-resolution is fixed by the width (w) of the probe pulses. The horizontal red bars represent the pp-KPFM potential. It is equal to the time-integral value of SP(t) normalized by w over the interval $\Delta t - \Delta t + w$.

the spectroscopic acquisition can be distributed either uniformly or irregularly within the time window defined by the pump period (see Figure 2b). The second configuration can be used to reduce the spectroscopic acquisition time by using less data points to probe the parts of the time-domain where the SP evolves more slowly.

Organic BHJ Solar Cells

In this work, PTB7:PC$_{71}$BM BHJ photovoltaic thin films have been used as test samples (Figure 3) for pp-KPFM experiments. In the following, a few concepts of organic photovoltaics are presented. For a comprehensive introduction to this field, the reader may refer to [25].
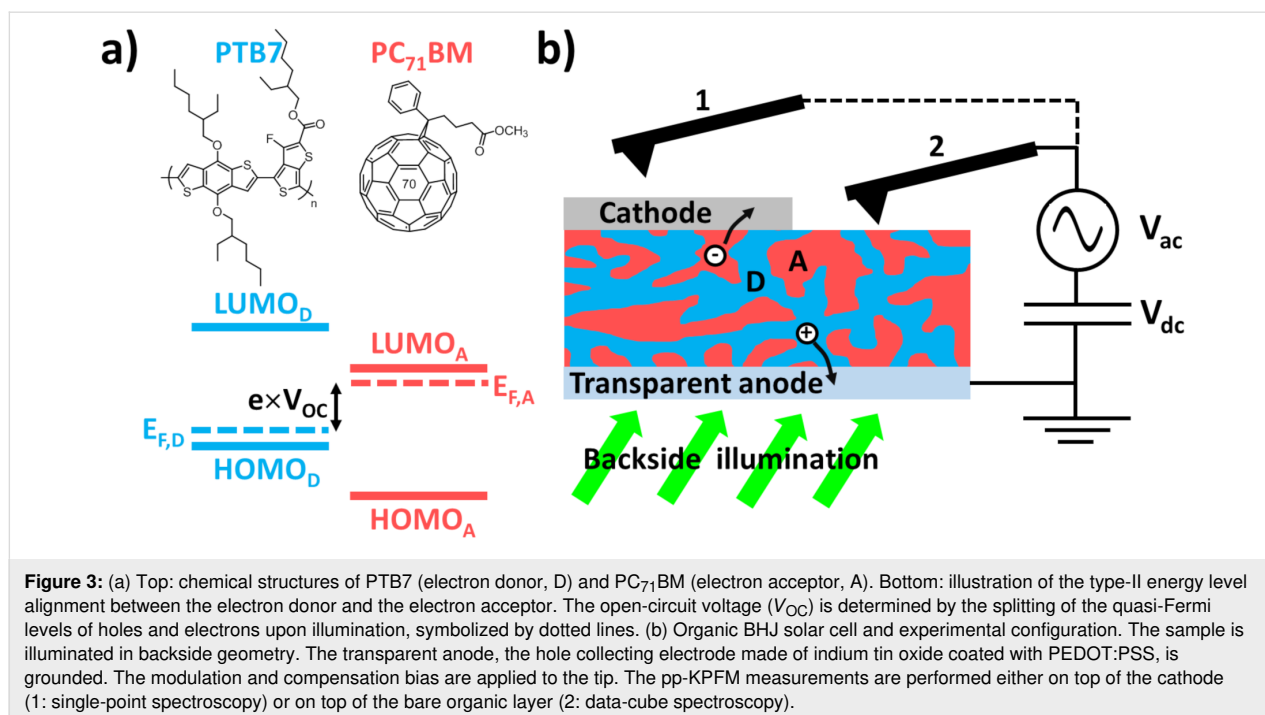
Solution-processed organic solar cells [25] rely on the combination of electron donor (D) and acceptor (A) π-conjugated polymers and/or molecules that display a type-II energy offset between their highest occupied molecular orbital (HOMO) and lowest unoccupied molecular orbital (LUMO) levels. These energetic offsets enable to dissociate singlet excitons into Coulomb-bound electron–hole pairs also called charge transfer states (CTs). These can either recombine in pairs at the D–A interfaces or split up into free charges. The latter can eventually reach the collection electrodes of the device. Here, the low-bandgap polymer PTB7 was used as the donor and the fullerene derivative PC$_{71}$BM as the acceptor.

In the BHJ configuration [26], the D and A materials should form two interpenetrated networks phase-segregated at the 10 nm scale, to maximize the donor–acceptor interfacial area where the excitons are dissociated and to overcome the short-exciton diffusion length. The vast majority of solution-processed D–A blends actually display more complex morphologies. For instance, they can feature a three-component organization in two (relatively) "pure" phases (i.e., donor-enriched and acceptor-enriched sub-networks), and a third one where donor and acceptor molecules are finely intermixed at the sub-10 nm scale [27]. Further complexity is added by the fact that radically different morphologies can be obtained depending of the solvent and additives used for the film deposition from solution.

The use of PTB7:PC$_{71}$BM is widely documented. It is now well established that films of good morphology, namely with a nano-scale phase separation, can be obtained from solutions containing 1,8-diiodooctane (DIO) as solvent additive [28-30]. Adding a small amount of DIO indeed prevents the formation of large PC$_{71}$BM aggregates and favors the formation of an intermixed morphology at the scale of a few tens of nm during film casting and drying.

In BHJs, the photogenerated carriers recombine in a nongeminate manner by electron–hole annihilation at the D–A interfaces. Here, we do not discuss the losses by exciton relaxation or by pairwise recombination of the CT state. The free carriers can also be trapped in tail states [25] before recombining with free unpaired counter charges. This slower recombination process is called a trap-assisted or trap-delayed recombination.

Figure 3: (a) Top: chemical structures of PTB7 (electron donor, D) and PC$_{71}$BM (electron acceptor, A). Bottom: illustration of the type-II energy level alignment between the electron donor and the electron acceptor. The open-circuit voltage (V_{OC}) is determined by the splitting of the quasi-Fermi levels of holes and electrons upon illumination, symbolized by dotted lines. (b) Organic BHJ solar cell and experimental configuration. The sample is illuminated in backside geometry. The transparent anode, the hole collecting electrode made of indium tin oxide coated with PEDOT:PSS, is grounded. The modulation and compensation bias are applied to the tip. The pp-KPFM measurements are performed either on top of the cathode (1: single-point spectroscopy) or on top of the bare organic layer (2: data-cube spectroscopy).

Results and Discussion
pp-KPFM upon electrical pumping

The ability to perform time-resolved measurements using this pp-KPFM implementation was validated by a series of single-point spectroscopy measurements applying electrical pumping on a highly oriented pyrolytic graphite (HOPG) substrate. The sample was electrically connected to the AWG by mounting the HOPG substrate onto a sample holder designed with in situ electrical contacts. The pump signal generated by the AWG was transmitted through a coaxial cable (air side) connected to a twisted pair (vacuum side) through an intermediate UHV feedthrough.

Figure 4 presents the results of two measurements carried out with different pump and probe signals (note that two different cantilevers were used for these two tests). In the first example

(Figure 4a and Figure 4b), a 50 kHz square-wave signal with a 200 mV amplitude and a 50% duty ratio was used for the pump. The probe width was set to 500 ns, and the pump–probe delay was incremented 40 times by steps of 500 ns during the spectroscopic acquisition. The pp-KPFM spectrum reproduces fairly well the shape of the pump signal, demonstrating that a time-resolution at least as good as 1 μs can be achieved with this setup. The slight overestimation of the pulse amplitude (213 mV instead of 200 mV) originates from an impedance mismatch effect. This has been confirmed by comparing the KPFM loop response (in standard mode) to the dc bias applied from the AWG or internally added to the tip by the SPM unit (see Figure S2 in Supporting Information File 1).

A pulse signal of 200 Hz and an amplitude of 500 mV featuring a sub-ms potential rise and a slower decay were used as the
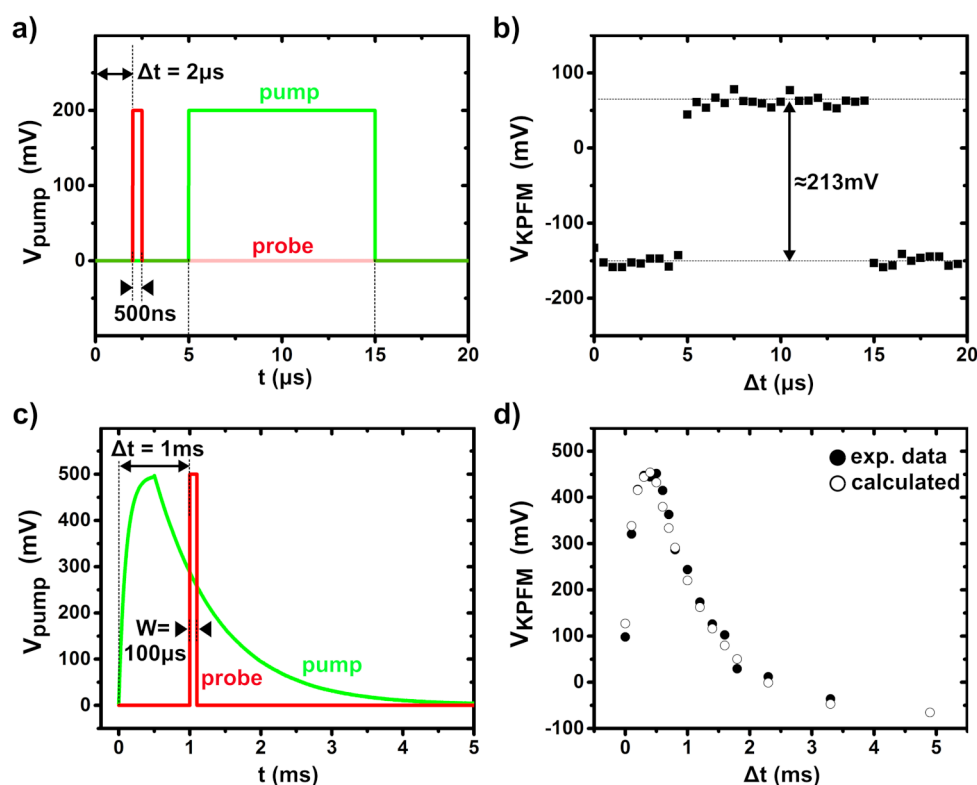

Figure 4: (a, b) pp-KPFM single-point spectroscopy of an electrical square-wave signal of 10 μs (pump, amplitude 200 mV, period 20 μs). (a) Plot of the pump and probe signals as a function of time for Δt = 2 μs. The pump signal was recorded using the oscilloscope. NB: the *y*-scale is shown for the pump only. The probe-time window was set to 500 ns. (b) KPFM compensation potential as a function of Δt. 40 delay values evenly distributed within the time window of 20 μs as defined by the pump signal period were used to record that spectrum. The integration time per pixel was 4 s. (c, d) pp-KPFM single-point spectroscopy measurement of a "surge pulse" of 5 ms (pump, amplitude 500 mV). (c) Plot of the pump and probe signals as a function of time for Δt = 1 ms. The probe window was set to 100 μs. (d) KPFM compensation potential (average of 5 spectra) as a function of Δt (filled circles). 17 delay values irregularly distributed within the time window of 5 ms were used. The integration time per pixel was set to 1 s, preceded by a pre-integration time of 2 s. The open circles represent calculated values obtained by integrating the pump signal over the probe-time window and by applying a correction factor to correct the impedance mismatch. The calculated data have been shifted along the *y*-axis to ease the comparison with the experimental results. This *y*-shift with respect to the zero baseline results from the difference of the tip–substrate work function.

pump for the second test (Figure 4c and Figure 4d). Also here, an excellent agreement was obtained between the pump and pp-KPFM signals. More precisely, the pp-KPFM spectrum (filled circles in Figure 4d) matches the values calculated by integrating the pump signal over the time windows defined by the probe (open symbols in Figure 4d).

Here, we stress that to achieve a proper pp-KPFM measurement, it is crucial to set a suitable time constant for the KPFM feedback loop and an adequate integration time per pixel. The signal-to-noise (*S/N*) ratio dramatically decreases when switching from KPFM to pp-KPFM due to a reduction of the bandwidth [22]. This effect demands a reduction of the loop gain and an increase of the integration time. Namely, the KPFM loop needs sufficient time to adapt and track the SP changes that occur when changing the pump–probe delay. A pre-integration time during which the KPFM potential is not recorded shall precede the acquisition of each spectroscopic pixel. The pre-integration time can be set by repeating several times the same pump-probe delay in the probe's pulse sequence (ex: $\Delta t_1 = \Delta t_2 = \Delta t_3$ in Figure 2a). This procedure was used to process the data shown in Figure 4d, and it has been systematically applied for pp-KPFM measurements using optical pumping.

pp-KPFM upon optical pumping of the organic solar cell

The PTB7:PC$_{71}$BM blend forming the active layer of the solar cell was processed from a chlorobenzene/DIO (CB/DIO) mixture (see Experimental section) with the aim to obtain an optimized nanoscale morphology [28]. The global performance deduced from macroscopic electrical characterization (Figure S3 in Supporting Information File 1) remains however below the state-of-the-art for PTB7:PC$_{71}$BM-based devices. We will describe later that an imperfect morphology may be the origin of the reduced performance.

In a first step, the dynamic photoresponse of the device upon optical pumping was investigated by point spectroscopy at the cathode. This experimental configuration is labeled "1" in Figure 3b. It was chosen for an initial examination of the pp-KPFM operation using optical pumping, because the *S/N* ratio could be increased at will by averaging several successive spectroscopic curves. In this configuration, the cathode defines an equipotential level. In other words, the dynamic SP photoresponse is not position-dependent. Furthermore, here, the SPV

can be directly compared to the open-circuit voltage deduced from the macroscopic electrical characterization.

Figure 5a shows a measurement of the SPV performed by applying a long cw light pulse (515 nm) to the sample. The calculated SPV of about 650 mV at 48 mW·cm^{-2} and 515 nm is close to the open-circuit voltage of 680 mV upon one sun illumination as deduced from the electrical characterization. The SPV approximately displays a logarithmic dependence on the illumination intensity (Figure 5b), with a slope equal to ca. 1.5 $k_B T \cdot q^{-1}$ (k_B: Boltzmann constant, q: electron charge). This suggests that trap-delayed processes constitute a significant pathway for photocarrier recombination in this sample [31]. These measurements were also performed to confirm the validity of pp-KPFM operations on this system. More precisely, we probed the ability of pp-KPFM to yield a proper SP measurement. For that purpose, the setup configuration was switched from standard KPFM to pp-KPFM mode within the spectroscopic ramp (Figure 5a), and two successive light pulses were applied. The first and the second light pulse occurred during KPFM and pp-KPFM, respectively. For clarity, we underline that there is no variable pump–probe delay. The pump channel is only used to apply dc levels corresponding to the on and off states of the illumination source. In other words, in this test, pp-KPFM is not used to perform a time-resolved measurement as a function of Δt. It is rather used to monitor a SP at two different levels of illumination, namely in a dark state and under cw illumination. Neglecting noise, both configurations yielded identical SP levels in the dark and upon cw illumination. However, as expected, the noise level increases for pp-KPFM, and a much longer time delay is needed to stabilize the compensation potential upon turning on and off the illumination. As noted above, this urged us to use pre-integration delays when performing measurements of the pp-KPFM signal as a function of Δt.

Time-resolved pp-KPFM measurements were carried out at the cathode (Figure 6) as a function of the illumination intensity and by using two different pump–probe delay sequences. The operating parameters are detailed in the caption of Figure 6. The experimental data were analyzed by modeling the SPV decay after light pulse extinction with a stretched exponential function (time constant: τ_d, stretch exponent: β) and by integrating over the probe-time window (w). It can be shown that for given Δt, the pp-KPFM potential in the "decay part" of the curve can be expressed as (see Supporting Information File 1):

$$V_{\text{pp-KPFM}}(t) = (V_I - V_D) \times \frac{t_d}{w \times \beta} \times \left(\gamma \left[\frac{1}{\beta}, \left(\frac{\Delta t + w - t_0}{t_d} \right)^\beta \right] - \gamma \left[\frac{1}{\beta}, \left(\frac{\Delta t - t_0}{t_d} \right)^\beta \right] \right) + V_D \qquad (1)$$
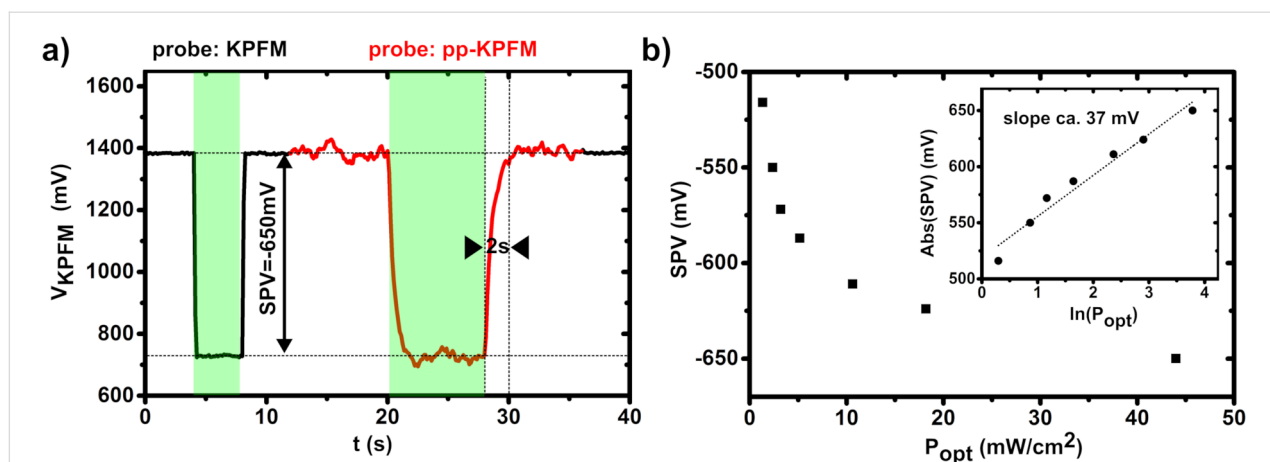
Figure 5: (a) Plot of the KPFM compensation potential measured at the solar cell cathode as a function of time (spectroscopic sequence of 320 pixels, 125 ms per pixel). The probe signal configuration is automatically switched from standard KPFM to pp-KPFM (pulses of 250 µs, repetition frequency of 200 Hz) at t = 12 s and set back to standard KPFM at t = 36 s. The illumination state is switched twice from dark to cw illumination. First illumination sequence: 4 s < t < 8 s, second sequence: 20 s < t < 28 s, P_{opt} = 48 mW·cm^{-2} at 515 nm). (b) Plot of the surface photovoltage (SPV) as a function of the optical power P_{opt}. The SPV is calculated as the difference between the KPFM potential values measured (standard KPFM configuration) at cw illumination and in the dark. Inset: plot of the SPV (in absolute value) as a function of the natural logarithm of the optical power.

Here, V_D and V_I correspond to the dark-state SP and the SP value at the end of the light pulse ($t = t_0$), respectively. If the pulse duration exceeds the photocharging time, V_I will be equal to the SP value measured upon cw illumination (V_{cw}). γ represents the unnormalized lower-half Euler gamma function (see Supporting Information File 1).

Obviously, a trade-off between the time-resolution (limited by the probe-time window) and measurement of the full SPV dynamics must be found. In Figure 2a, a pump pulse of 40 ms is applied. Here, several tens of ms are needed to recover completely the dark-state SP after pulse extinction. Using a pump signal with a shorter period (5 ms instead of 40 ms, Figure 2b) increases the temporal resolution, but does not allow the system to return fully to its initial electrostatic state between the light pulses. However, it is important to note that the data acquired using these two different sequences display an excellent consistency. At the irradiance maximum (P_{opt} = 193 mW·cm^{-2}, Figure 6a and Figure 6b), the decay-time constants, stretch exponents and dark-state SP values extracted from both curves are identical within the error bars. The agreement between both data sets is unambiguous when plotting the two data sets in the same graph with a common normalized origin (Figure S5 in Supporting Information File 1).

As expected, the magnitude of the SPV decreases when reducing the optical power (Figure 6). However, the decay-time constant is barely fluence-dependent, which indicates that the underlying dynamics originate from trap-delayed processes [25]. Most likely, a broad distribution of states exists in which the photocarriers are trapped for longer or shorter periods as in-

dicated by stretch exponents lower than 0.7 required for fitting of the spectroscopic curves (with the exception of the data in Figure 6f). These traps can be partially filled by applying a continuous white light background in addition to the pump pulse, which results in a significant reduction of the effective decay-time constant (see Figure S6 in Supporting Information File 1). However, these experimental conditions do not fulfil the requirements of a small perturbation measurement [32], and the SPV dynamics remain most likely dominated by trap-release processes.

Due to the limited time-resolution, the photocharging dynamics could not be addressed as accurately as the SPV decay dynamics. Aquiring all information at once would require using smaller probe-to-pump duty ratios. This could be done by keeping the same pump period while reducing the probe-time window. This was not possible in practice because of an insufficient S/N ratio. Some interesting observations can nevertheless be made. The photocharging time, i.e., the time needed to reach an electrostatic equilibrium upon illumination, appears to depend strongly on the pump fluence. More precisely, the photopotential builds up more slowly when decreasing the optical power. At the lowest fluence applied (P_{opt} = 2.4 mW·cm^{-2}), the photocharging time even exceeds the pulse duration within the second sequence (Figure 6f). The physics of the photocharging dynamics are based on a drift-diffusion process limited by the carrier mobility. Hence, our data (Figure 6) indicate that the effective carrier mobility strongly depends on the photocarrier concentration, which is inversely proportional to the optical power. Such a situation has been reported for different organic blends [33-35]. In some models,
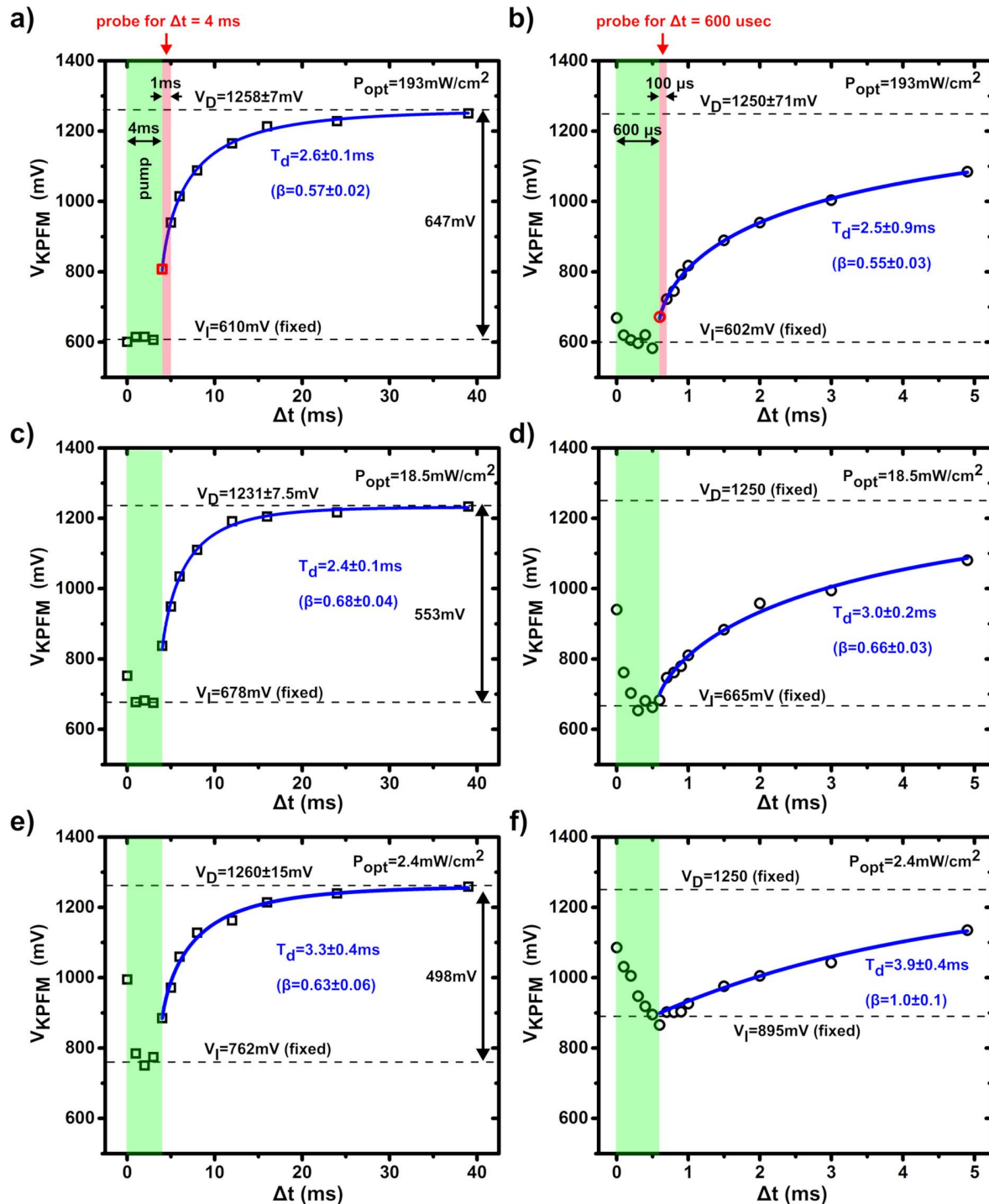
Figure 6: (a–f) Spectroscopic curves (average of 5 acquisitions) of the pp-KPFM compensation potential as a function of Δt measured at the solar cell cathode. The data were acquired using three different illumination intensities (peak power of the pump pulses): (a, b)193 , (c, d) 18.5 and (e, f) 2.4 mW·cm^{-2}. Two different pump–probe delay sequences were used. Open squares and open circles represent data of the first and second sequence, respectively. (a, c, e) First sequence: 4 ms pump pulses repeated at 25 Hz, 1 ms probe-time window, post-data acquisition delay of 2 s, integration time 1 s. (b, d, f) Second sequence: 600 µs pump pulses repeated at 200 Hz, 100 µs probe-time window, post-data acquisition delay of 2 s, integration time 1 s. The time intervals corresponding to the pump (a–f) and the probe (a, b) signals (shown only for one given delay) are highlighted by half-transparent green and red rectangles, respectively. Note that the time (t) and delay (Δt) scales coincide since the delays are defined with respect to the time origin t = 0 s. However, each data point represents a measurement of the SP integrated during the pump–time window. The solid blue lines represent the results of the numerical curve fits performed to extract the SPV decay-time constants (τ_d). For the fit, the V_I values were fixed at the value reached upon illumination. V_D, τ_d , β were free variables, with the exception of the data in (d) and (f), that were adjusted with fixed V_D values.

traps are the source of this concentration-dependent mobility of the photocarriers [36].

We now focus on the photoresponse of the phase-segregated organic blend, i.e., the photoactive layer of the device without the cathode electrode, given by configuration 2 in Figure 3b. The surface morphology of the PTB7:PC$_{71}$BM blend (Figure 7a) is consistent with that reported for samples processed under similar conditions [37,38].

The nc-AFM topographic images (Figure 7a) display a rather uniform contrast indicating that the donor and acceptor species have been finely mixed. However, specific contrasts in the KPFM potential images recorded in the dark (Figure 7b) reveal compositional and/or morphological variations at the 100 nm scale. In BHJ blends, the dark-state electrostatic contrast reflects permanent charge distributions [20], which originate from unevenly distributed electrostatic dipoles at the D−A interfaces [39] or from permanently trapped charge carriers. Obviously, if the blend composition or the morphology of the donor and acceptor sub-networks vary, the interface dipoles fluctuate as well (in direction and magnitude).

Prior to pump–probe KPFM spectroscopy, the BHJ photoresponse was investigated by differential SPV imaging (Figure 8) [40]. Here, a 2D matrix of spectroscopic curves of the KPFM potential is recorded as a function of time in a standard KPFM configuration with an open *z*-loop. During the spectroscopic ramp, the cw illumination is switched on. Images of the SP in the dark and upon illumination, as well as their difference (i.e., the SPV) can be reconstructed by simple data processing. The results are presented in Figure 8. The topographic and dark-state potential images reproduce fairly well the ones observed by the standard imaging process (compare in particular the

histograms in Figure 7c and Figure 8d). The SPV is in average equal to −370 mV (Figure 8h), which is less than the SPV measured on the cathode using the same optical power (−625 mV for P_{opt} = 18.5 mW·cm^{-2}, see Figure 5b). This difference is not surprising, other reports [13] have already shown that the SPV probed by KPFM on the bare surface of BHJs is smaller than the open-circuit voltage [20]. More remarkable is the existence of strong correlations between the contrast in the dark-state SP and SPV images (compare Figure 8c and Figure 8g). This confirms that the local phase composition (and/or morphology) varies and has a deep impact on the opto-electronic properties of the D–A blend.

Time-resolved pp-KPFM measurements in data-cube mode were performed at roughly the same sample area using two different pump–probe sequences. Spectroscopic pp-KPFM curves and 2D images recalculated from these are presented in Figure 9. To facilitate a comparison to the differential SPV images, dashed contours indicating the same sample area have been drawn in Figure 8 and Figure 9b, Figure 9d and Figure 9f. These contours correspond also to the scan area shown in Figure 9i, Figure 9k and Figure 9m.

Compared to the single-point spectroscopy measurements, 2D pp-KPFM spectroscopic imaging presents an additional degree of difficulty, especially in terms of acquisition time. To maintain a reasonable *S/N* ratio, higher probe-to-pump duty ratios were used (4% and 5% for the first and the second sequence, respectively). The pump–probe delays were set to focus on the SPV decay regime. Note that even under these conditions, several tens of hours were needed to acquire each set of images. The data shown in Figure 9a–g were acquired with pump pulses of 500 μs (P_{opt} = 18.5 mW·cm^{-2}) repeated at 200 Hz and a probe-time window of 200 μs. Figure 9a shows two spectros-
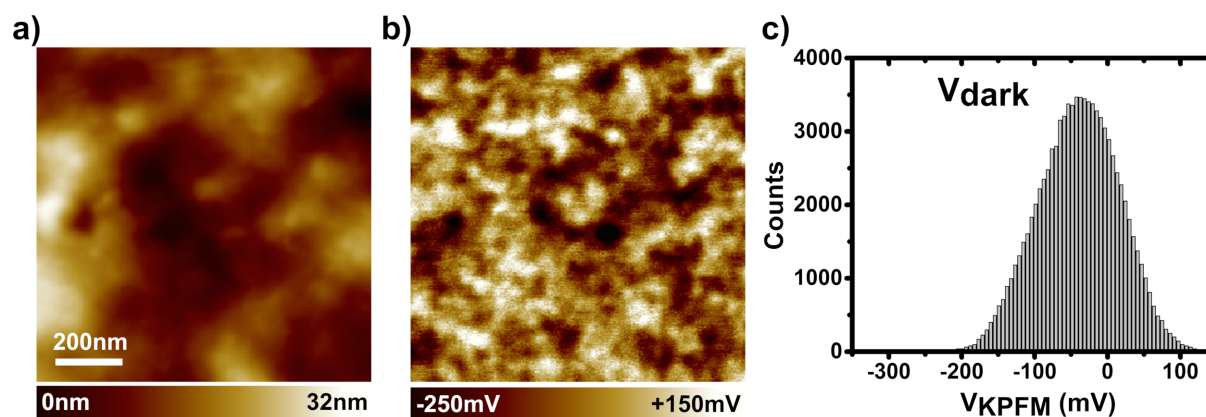

Figure 7: (a) Topographic (nc-AFM, UHV, 300 K) and (b) KPFM compensation potential images (1 μm × 1 μm, 300 × 300 pixels) of the PTB7:PC$_{71}$BM blend recorded in the dark (standard KPFM configuration). (c) Histogram of the KPFM potential values.
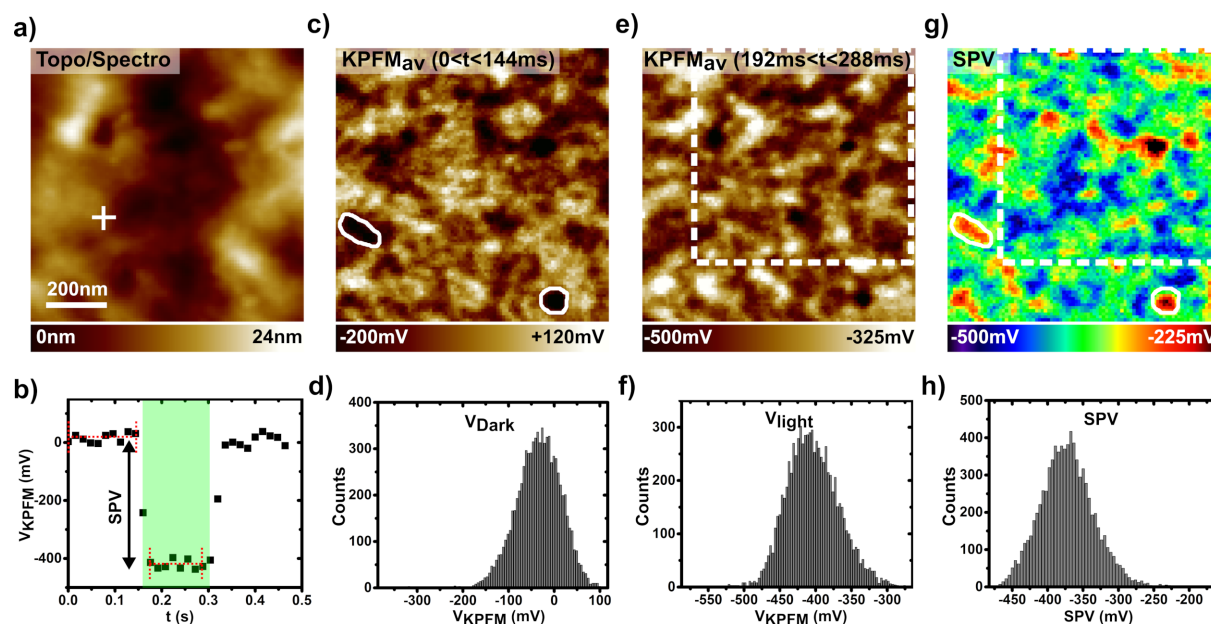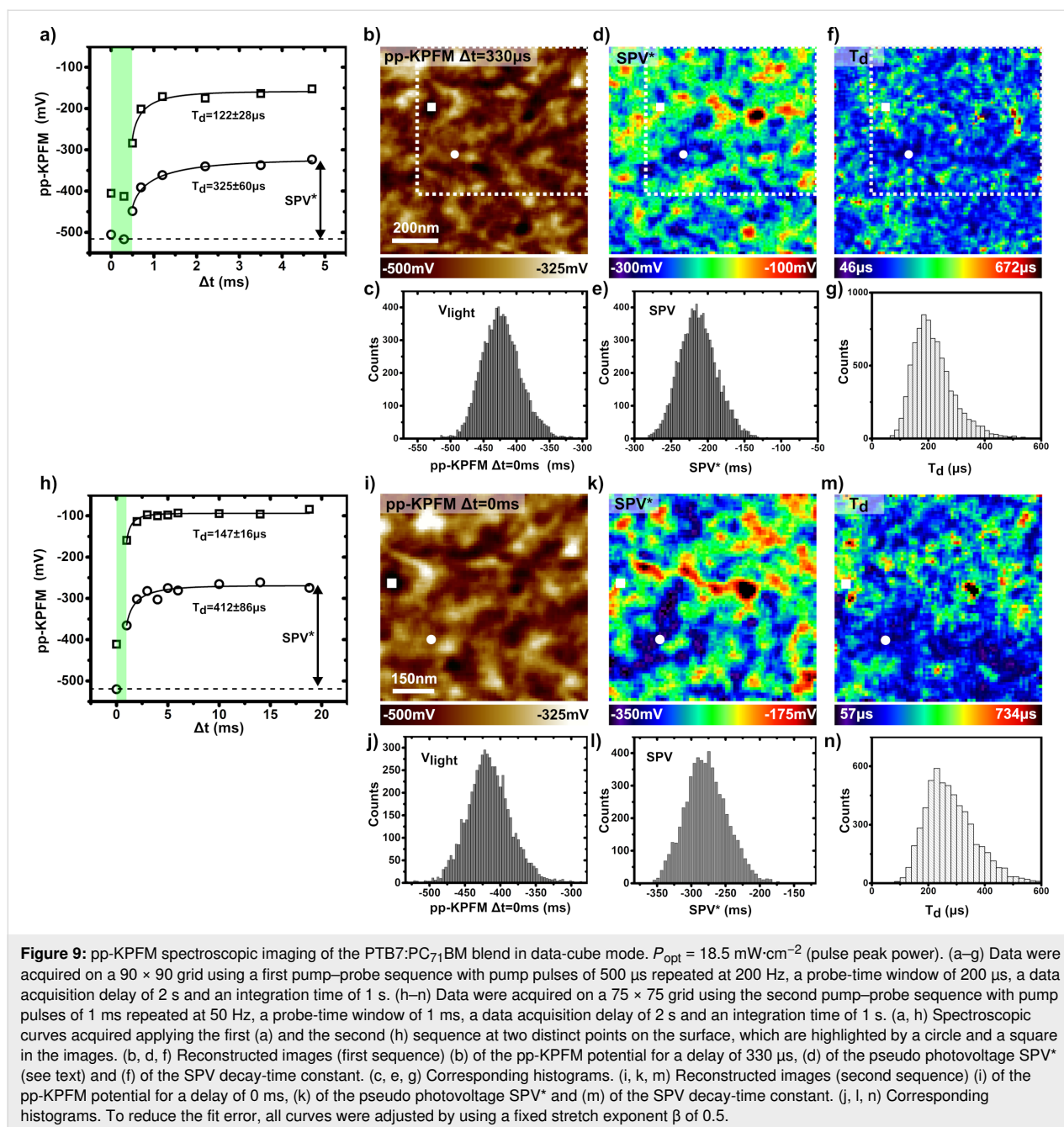
Figure 8: (a, c, e, g) nc-AFM/KPFM images of the PTB7:PC$_{71}$BM blend (1 μm × 1 μm, 90 × 90 pixels) acquired during a differential SPV imaging experiment (P_{opt} = 18.5 mW·cm^{-2}). (a) Topographic image. (b) Spectroscopic curve of the KPFM potential as a function of time (30 pixels, each 6 ms long), recorded at the location indicated by a cross in (a). The dark-state SP and SP upon cw illumination are calculated by averaging the data points for 0 < *t* < 144 ms and 192 < *t* < 288 ms, respectively. These time windows are highlighted by red dotted lines. (c) Calculated dark-state SP (V_{dark}) image. (d) Histogram of the V_{dark} values. (e) Calculated image of the SP under illumination (V_{light}). (f) Histogram of the V_{light} values. (g) Calculated image of the SPV. (h) Histogram of the SPV values. The white solid contours in (c) and (g) highlight the existence of strong correlations between the contrast in the dark-state potential and the SPV images. The dotted rectangles in (e) and (g) indicate the sample area highlighted in Figure 9a–c and displayed in Figure 9e–g.

copic curves acquired with this sequence at different points on the surface highlighted by a square and a circle in the related spectroscopic images.

Figure 9b displays the spectroscopic image of the compensation potential for a delay Δ*t* = 300 μs, which falls within the light pulse. The contrast and the potential levels (histogram in Figure 9c) are in excellent agreement with the ones obtained by differential SPV imaging under cw illumination (compare Figure 8e, Figure 8f and Figure 9b, Figure 9c). This confirms that the photocharging time is smaller than the pulse duration, in line with the results of point spectroscopy on the cathode. In a second step, one can also map a "pseudo surface photovoltage" (SPV*) image by calculating the difference between the signals measured for Δ*t* = 300 and 4.7 ms. It turns out that the SPV* (Figure 9d) and the SPV images (Figure 8g) display a similar contrast. The SPV* image however has a smaller magnitude (in average −214 mV instead of −370 mV). According to single-point spectroscopy, the potential cannot fully return to its dark-state level within a pump period of 5 ms. However, we also note that the decay-time constants obtained from the curves recorded at the bare layer are reduced by one order of magnitude compared the values acquired at the cathode. The 2D map of the SPV decay-time constants is presented in Figure 9f, and

the corresponding histogram is shown in Figure 9g. At this stage, the existence of correlations between the dynamical contrasts and the ones in the dark-state SP and SPV channels seems rather unclear.

The pp-KPFM spectroscopic mapping using a longer pump periodicity yields further insights (Figure 9). The contrast of the potentiometric images (Figure 9i and Figure 9k) matches perfectly the one obtained before. Furthermore, the values of the SPV decay-time constant are consistent, although slightly higher, with the ones deduced from the measurement with the shorter pump period. A correspondence can be established between the contrast in both dynamical images. A closer examination reveals that the areas where the SPV decays the fastest correspond mainly to the ones were the SPV is more negative. The rather slow SPV decay is similar to the lifetime of long-lived trap populations reported for other BHJs [41]. The measurements on the cathode already indicated that the SPV decays reflect the trap-release dynamics. Thus, it is likely that the compositional and/or morphological heterogeneities generating the dark-state SP and SPV contrast play also a key role in the photocarrier trapping process. A reasonable (yet to be definitely confirmed) scenario could invoke the existence of non-percolating PC$_{71}$BM clusters acting as trapping centers. Such

Figure 9: pp-KPFM spectroscopic imaging of the PTB7:PC$_{71}$BM blend in data-cube mode. P_{opt} = 18.5 mW·cm^{-2} (pulse peak power). (a–g) Data were acquired on a 90 × 90 grid using a first pump–probe sequence with pump pulses of 500 µs repeated at 200 Hz, a probe-time window of 200 µs, a data acquisition delay of 2 s and an integration time of 1 s. (h–n) Data were acquired on a 75 × 75 grid using the second pump–probe sequence with pump pulses of 1 ms repeated at 50 Hz, a probe-time window of 1 ms, a data acquisition delay of 2 s and an integration time of 1 s. (a, h) Spectroscopic curves acquired applying the first (a) and the second (h) sequence at two distinct points on the surface, which are highlighted by a circle and a square in the images. (b, d, f) Reconstructed images (first sequence) (b) of the pp-KPFM potential for a delay of 330 µs, (d) of the pseudo photovoltage SPV* (see text) and (f) of the SPV decay-time constant. (c, e, g) Corresponding histograms. (i, k, m) Reconstructed images (second sequence) (i) of the pp-KPFM potential for a delay of 0 ms, (k) of the pseudo photovoltage SPV* and (m) of the SPV decay-time constant. (j, l, n) Corresponding histograms. To reduce the fit error, all curves were adjusted by using a fixed stretch exponent β of 0.5.

an imperfect morphology would be consistent with the relatively low macroscopic performance of this device compared to established PTB7:PC$_{71}$BM devices (Figure S3, Supporting Information File 1).

Finally, some questions remain open and will require further investigations. Firstly, the origin of the difference between the SPV decay-time constants determined in the bare layer and the cathode measurements remains unclear. To address this point, statistical measurements at several sample areas would be needed to check if the sample properties are homogeneous or if

they display strong variations at the mesoscopic scale. Indeed, sample parts with longer trap-release times may exist, which would contribute to the global SPV decay dynamics probed on the cathode. Secondly, the difference between the SPV magnitudes probed by differential and pp-KPFM 2D imaging is still unexplained. This difference decreases significantly when increasing the pump period (see the histograms in Figure 9). However, even at the longest pump period, the dark-state level is not recovered completely. This is puzzling since such an effect was neither observed for the point-spectroscopy measurements on the cathode, nor for the pp-KPFM measurements

using electrical pumping. A comparison of the differences of these three experimental configurations may yield further insights. Optical pumping of the bare organic layers presents a specificity. Both the tip–sample capacitance and the KPFM *S/N* ratio are susceptible to significant changes with varying illumination state. Upon illumination, the charge carrier density increases leading not only to a reduction of the tip–sample capacitive junction but also to an increase in the KPFM *S/N* ratio. Regarding the basic operating principles of pp-KPFM, it is unclear why photoinduced capacitive changes shall affect the measurement of the dark-state potential only. An illumination-dependent *S/N* ratio may be a better explanation similar to previous observations by Murawski et al., who have shown [22] that the electrostatic contrast cannot be fully measured for very small electrical pumping cycles. Here, the *S/N* ratio becomes too low to perform stable pp-KPFM experiments at a useful bandwidth. To verify this hypothesis, further experiments and developments are needed. In particular, we plan to increase the *S/N* ratio by using a heterodyne scheme [6] instead of the standard frequency-modulation mode for the KPFM operation.

Conclusion

We have introduced an alternative approach to pp-KPFM based on the acquisition of spectroscopic curves of the KPFM compensation potential as a function of the pump–probe delay using an open-loop configuration. This configuration simplifies the operation of pp-KPFM, since it allows for avoiding topographic artefacts without the need to use a second compensation loop. Single-point spectroscopy measurements performed on HOPG (under electrical pumping) and on an organic solar cell cathode (under optical pumping), confirmed the validity of this implementation. In addition, we demonstrated that spectroscopic pp-KPFM can be used in data-cube mode enabling the acquisition of 2D images of the SPV dynamics of organic BHJs. In the investigated PTB7:PC$_{71}$BM blend, the SPV decay dynamics were found to be dominated by trap-release processes at the time scale of a few hundreds of μs to a few ms. The resolution of this pp-KPFM approach is however not limited to these slow dynamics. A temporal resolution as good as 1 μs was already obtained using electrical pumping, and further developments are in progress to perform ns-resolved measurements. This will be done by implementing a multiplication stage generating the probe signal and by modifying the electric circuit for fast operation upon electrical pumping with a correct circuit impedance matching.

Last, by comparing the results of pp-KPFM and of differential SPV imaging performed on the bare organic layer, an underestimation effect in the measurement of the SPV has been evidenced. These results stress the need to quantify properly the

dependence of the *S/N* ratio of the pp-KPFM potential on the illumination state when investigating photovoltaic materials. For that purpose, future works will be devoted to increasing the sensitivity of spectroscopic pp-KPFM, for instance by using a heterodyne or a side-band detector. Further insights will also be gained by comparing different kinds of photovoltaic materials, for which the illumination-dependence of the *S/N* ratio may be different. In particular, we plan to investigate silicon-based devices, hybrid perovskite thin films and single crystals as well as type-II van der Waals heterojunctions based on transition metal dichalcogenides.

Experimental
Nc-AFM and pp-KPFM

Noncontact-AFM (nc-AFM) experiments were performed with a ScientaOmicron VT-AFM setup in UHV at room temperature (RT) driven by a Matrix SPM control unit. Pt/Ir-coated silicon cantilevers (EFM, Nanosensors, resonance frequency in the 45–115 kHz range) were annealed in situ to remove atmospheric contaminants. Topographic imaging was realized in FM mode (FM-AFM) with negative frequency shifts of a few Hz and vibrational amplitudes of a few tens of nm. KPFM measurements were carried out in single-pass mode using FM (FM-KPFM) with a peak-to-peak modulation bias V_{ac} of 0.9 V at 1140 Hz. The compensation voltage V_{dc} was applied to the cantilever (tip bias $V_{tip} = V_{dc}$). The CPD is therefore the negative of V_{dc}, hence $V_{tip} = V_{dc} = -CPD$ [39]. The KPFM data are presented as V_{dc} images also referred to as KPFM potential or SP images for simplicity. A lock-in amplifier (Signal Recovery 7280) was used to measure simultaneously the modulation of the frequency shift at the electrostatic excitation frequency. The 'in-phase' amplitude of the first harmonic is fed into the KPFM bias feedback loop of the SPM controller. A fast radiofrequency analog switch (ZASWA-2-50DRA+, Mini-circuits, switching time rated to 20 ns) was used to apply a "pseudo multiplication" on the sum of the KPFM compensation bias and the ac bias generated by the LIA output. The switch driver TTL input was connected to the first output channel of a programmable AWG (Keysight 33622A). That channel was dedicated to the generation of the probe signal. Note that in the "open state" the switch output is grounded.

Both probe and pump signals were generated by a programmable dual channel AWG (Keysight 33622A), which was synchronized with the scanning probe microscopy (SPM) unit by its external trigger input. The pulse sequences were programmed using the Keysight BenchLink Waveform Builder Pro software. Basically, the pulses consisted in a series of dual waveforms, each of them featuring a different delay between the two channels, which were repeated until a trigger event was sent to the AWG. The two channels are initially synchronized

after downloading the sequence to the unit by using the "sync arbs" function of the 33622A unit.

In optical pumping configuration, the second channel of the AWG was used to drive the digital-modulation input of a fiber-coupled PhoxXplus laser module operated at 515 nm (Omicron Laserage GmbH). Sample illumination was performed in back-side geometry using custom sample holders with on-board mirrors through an optical viewport of the UHV AFM chamber. The wavelength of 515 nm was selected since it falls within the UV–vis absorption bands of both $PC_{71}BM$ and PTB7. For each measurement, the optical power P_{opt} corresponding to the maximum pulse intensity during the modulated illumination is indicated in the corresponding figure caption (Figure 5, Figure 8, Figure 9). P_{opt} is defined per unit of surface by taking into account the laser beam diameter.

Image processing and processing of the spectroscopic data

The WsXM software [42] was used to process the SPM images. Semi-automated data processing routines were also developed using the batch processing options of the OriginPro software (OriginLab Corp.). These routines were employed to import the 2D spectroscopic data and to perform automated curve fit adjustments on the VKPFM(Δt) curves. A Gaussian smooth filter was applied to the spectroscopic images. The processed data display the same features as the raw data however at a slightly lower noise level.

Organic BHJ thin films processing, solar cell fabrication and characterization

The $PTB7:PC_{71}BM$ BHJ thin film was deposited on an indium thin oxide (ITO) substrate coated with PEDOT:PSS (a hole-conducting polymer) following the procedure published by Liang et al. [28]. PTB7 (Ossila, $M_w = 85$ kDa, PDI = 2.0) and $PC_{71}BM$ (Solenne BV, 99% purity) were used as received. A thin layer of filtered (0.45 μm) PEDOT:PSS (Baytron A14083, Clevios) was spin-coated onto the activated ITO surface at 5000 rpm for 25 s, 4000 rpm for 60 s and 4000 rpm for 1 s (≈30 nm) and annealed at 120 °C for 10 min under ambient conditions. The substrate was then transferred into an argon-filled glovebox for spin-coating of an active layer of the $PTB7:PC_{71}BM$ solution (1:1.5 weight ratio, 25 mg·mL^{-1} total concentration) in anhydrous chlorobenzene. The blend was stirred overnight at 50 °C for complete dissolution and cooled down to RT. Then, 3 vol % of 1,8-diiodooctane were added 2 min before deposition at 1500 rpm for 120 s and 1000 rpm for 1 s on a substrate preheated to 50 °C (110 ± 10 nm). The sample was finally loaded into a secondary vacuum deposition system (Kurt J. Lesker) for deposition of Ca (20 nm, 1.0 Å·s^{-1}) and Al (100 nm, 2.0 Å·s^{-1}) top electrodes (10.18 ± 0.1 mm^2).

The electrical characterization was performed in a glovebox. Current-density–voltage (J–V) curves were measured using a Keithley 2400 source measure unit. The photocurrent was measured under AM 1.5G illumination at 1000 W·m^{-2} using a Newport Thermal Oriel 91192 1000W solar simulator. The light intensity was calibrated using a monocrystalline silicon Oriel Newport 91150v VLSI reference solar cell certified by the National Renewable Energy Laboratory (NREL).

Supporting Information

Supporting Information File 1
Further experimental measurements, details of the pp-KPFM experiment, characterization of the solar cell device and derivation of the formula used to fit the pp-KPFM spectroscopy.
[https://www.beilstein-journals.org/bjnano/content/supplementary/2190-4286-11-24-S1.pdf]

ORCID® iDs

Benjamin Grévin - https://orcid.org/0000-0002-6494-8138
Olivier Bardagot - https://orcid.org/0000-0003-3306-7204
Renaud Demadrille - https://orcid.org/0000-0002-7455-5709

References

1. Cox, P. A.; Glaz, M. S.; Harrison, J. S.; Peurifoy, S. R.; Coffey, D. C.; Ginger, D. S. *J. Phys. Chem. Lett.* **2015,** *6,* 2852–2858. doi:10.1021/acs.jpclett.5b01360
2. Karatay, D. U.; Harrison, J. S.; Glaz, M. S.; Giridharagopal, R.; Ginger, D. S. *Rev. Sci. Instrum.* **2016,** *87,* 053702. doi:10.1063/1.4948396
3. Collins, L.; Belianinov, A.; Somnath, S.; Rodriguez, B. J.; Balke, N.; Kalinin, S. V.; Jesse, S. *Nanotechnology* **2016,** *27,* 105706. doi:10.1088/0957-4484/27/10/105706
4. Borgani, R.; Forchheimer, D.; Bergqvist, J.; Thorén, P.-A.; Inganäs, O.; Haviland, D. B. *Appl. Phys. Lett.* **2014,** *105,* 143113. doi:10.1063/1.4897966
5. Mascaro, A.; Miyahara, Y.; Enright, T.; Dagdeviren, O. E.; Grütter, P. *Beilstein J. Nanotechnol.* **2019,** *10,* 617–633. doi:10.3762/bjnano.10.62
6. Sugawara, Y.; Kou, L.; Ma, Z.; Kamijo, T.; Naitoh, Y.; Jun Li, Y. *Appl. Phys. Lett.* **2012,** *100,* 223104. doi:10.1063/1.4723697
7. Garrett, J. L.; Munday, J. N. *Nanotechnology* **2016,** *27,* 245705. doi:10.1088/0957-4484/27/24/245705
8. Garrett, J. L.; Tennyson, E. M.; Hu, M.; Huang, J.; Munday, J. N.; Leite, M. S. *Nano Lett.* **2017,** *17,* 2554–2560. doi:10.1021/acs.nanolett.7b00289
9. Weber, S. A. L.; Hermes, I. M.; Turren-Cruz, S.-H.; Gort, C.; Bergmann, V. W.; Gilson, L.; Hagfeldt, A.; Graetzel, M.; Tress, W.; Berger, R. *Energy Environ. Sci.* **2018,** *11,* 2404–2413. doi:10.1039/c8ee01447g
10. Miyahara, Y.; Topple, J.; Schumacher, Z.; Grütter, P. *Phys. Rev. Appl.* **2015,** *4,* 054011. doi:10.1103/physrevapplied.4.054011
11. Miyahara, Y.; Grütter, P. *Appl. Phys. Lett.* **2017,** *110,* 163103. doi:10.1063/1.4981937

12. Takihara, M.; Takahashi, T.; Ujihara, T. *Appl. Phys. Lett.* **2008**, *93,* 021902. doi:10.1063/1.2957468

13. Shao, G.; Glaz, M. S.; Ma, F.; Ju, H.; Ginger, D. S. *ACS Nano* **2014**, *8,* 10799–10807. doi:10.1021/nn5045867

14. Fernández Garrillo, P. A.; Borowik, Ł.; Caffy, F.; Demadrille, R.; Grévin, B. *ACS Appl. Mater. Interfaces* **2016**, *8,* 31460–31468. doi:10.1021/acsami.6b11423

15. Borowik, Ł.; Lepage, H.; Chevalier, N.; Mariolle, D.; Renault, O. *Nanotechnology* **2014**, *25,* 265703. doi:10.1088/0957-4484/25/26/265703

16. Sadewasser, S.; Nicoara, N.; Solares, S. D. *Beilstein J. Nanotechnol.* **2018**, *9,* 1272–1281. doi:10.3762/bjnano.9.119

17. Schumacher, Z.; Miyahara, Y.; Spielhofer, A.; Grutter, P. *Phys. Rev. Appl.* **2016**, *5,* 044018. doi:10.1103/physrevapplied.5.044018

18. Fernández Garrillo, P. A.; Grévin, B.; Borowik, Ł. *Beilstein J. Nanotechnol.* **2018**, *9,* 1834–1843. doi:10.3762/bjnano.9.175

19. Coffey, D. C.; Ginger, D. S. *Nat. Mater.* **2006**, *5,* 735–740. doi:10.1038/nmat1712

20. Grévin, B. Kelvin Probe Force Microscopy Characterization of Organic and Hybrid Perovskite Solar Cells. In *Kelvin Probe Force Microscopy: From Single Charge Detection to Device Characterization;* Sadewasser, S.; Glatzel, T., Eds.; Springer: Berlin, 2018; pp 331–365. doi:10.1007/978-3-319-75687-5_11

21. Stolterfoht, M.; Armin, A.; Philippa, B.; Neher, D. *J. Phys. Chem. Lett.* **2016**, *7,* 4716–4721. doi:10.1021/acs.jpclett.6b02106

22. Murawski, J.; Graupner, T.; Milde, P.; Raupach, R.; Zerweck-Trogisch, U.; Eng, L. M. *J. Appl. Phys.* **2015**, *118,* 154302. doi:10.1063/1.4933289

23. Murawski, J.; Mönch, T.; Milde, P.; Hein, M. P.; Nicht, S.; Zerweck-Trogisch, U.; Eng, L. M. *J. Appl. Phys.* **2015**, *118,* 244502. doi:10.1063/1.4938529

24. Schumacher, Z.; Spielhofer, A.; Miyahara, Y.; Grutter, P. *Appl. Phys. Lett.* **2017**, *110,* 053111. doi:10.1063/1.4975629

25. Heeger, A. J. *Adv. Mater. (Weinheim, Ger.)* **2014**, *26,* 10–27. doi:10.1002/adma.201304373

26. Yu, G.; Gao, J.; Hummelen, J. C.; Wudl, F.; Heeger, A. J. *Science* **1995**, *270,* 1789–1791. doi:10.1126/science.270.5243.1789

27. Razzell-Hollis, J.; Limbu, S.; Kim, J.-S. *J. Phys. Chem. C* **2016**, *120,* 10806–10814. doi:10.1021/acs.jpcc.6b02898

28. Liang, Y.; Xu, Z.; Xia, J.; Tsai, S.-T.; Wu, Y.; Li, G.; Ray, C.; Yu, L. *Adv. Mater. (Weinheim, Ger.)* **2010**, *22,* E135–E138. doi:10.1002/adma.200903528

29. Hedley, G. J.; Ward, A. J.; Alekseev, A.; Howells, C. T.; Martins, E. R.; Serrano, L. A.; Cooke, G.; Ruseckas, A.; Samuel, I. D. W. *Nat. Commun.* **2013**, *4,* 2867. doi:10.1038/ncomms3867

30. Liu, F.; Zhao, W.; Tumbleston, J. R.; Wang, C.; Gu, Y.; Wang, D.; Briseno, A. L.; Ade, H.; Russell, T. P. *Adv. Energy Mater.* **2014**, *4,* 1301377. doi:10.1002/aenm.201301377

31. Cowan, S. R.; Roy, A.; Heeger, A. J. *Phys. Rev. B* **2010**, *82,* 245207. doi:10.1103/physrevb.82.245207

32. Shuttle, C. G.; O'Regan, B.; Ballantyne, A. M.; Nelson, J.; Bradley, D. D. C.; de Mello, J.; Durrant, J. R. *Appl. Phys. Lett.* **2008**, *92,* 093311. doi:10.1063/1.2891871

33. Shuttle, C. G.; Hamilton, R.; Nelson, J.; O'Regan, B. C.; Durrant, J. R. *Adv. Funct. Mater.* **2010**, *20,* 698–702. doi:10.1002/adfm.200901734

34. Kniepert, J.; Lange, I.; Heidbrink, J.; Kurpiers, J.; Brenner, T. J. K.; Koster, L. J. A.; Neher, D. *J. Phys. Chem. C* **2015**, *119,* 8310–8320. doi:10.1021/jp512721e

35. Sun, L.; Sun, J.-X.; Xiong, C.-H.; Shi, X.-H. *Sol. Energy* **2016**, *135,* 308–316. doi:10.1016/j.solener.2016.06.004

36. Eng, M. P.; Barnes, P. R. F.; Durrant, J. R. *J. Phys. Chem. Lett.* **2010**, *1,* 3096–3100. doi:10.1021/jz1011803

37. Collins, B. A.; Li, Z.; Tumbleston, J. R.; Gann, E.; McNeill, C. R.; Ade, H. *Adv. Energy Mater.* **2013**, *3,* 65–74. doi:10.1002/aenm.201200377

38. Kim, W.; Kim, J. K.; Kim, E.; Ahn, T. K.; Wang, D. H.; Park, J. H. *J. Phys. Chem. C* **2015**, *119,* 5954–5961. doi:10.1021/jp510996w

39. Fuchs, F.; Caffy, F.; Demadrille, R.; Mélin, T.; Grévin, B. *ACS Nano* **2016**, *10,* 739–746. doi:10.1021/acsnano.5b05810

40. Almadori, Y.; Bendiab, N.; Grévin, B. *ACS Appl. Mater. Interfaces* **2018**, *10,* 1363–1373. doi:10.1021/acsami.7b14616

41. Shuttle, C. G.; Treat, N. D.; Douglas, J. D.; Fréchet, J. M. J.; Chabinyc, M. L. *Adv. Energy Mater.* **2012**, *2,* 111–119. doi:10.1002/aenm.201100541

42. Horcas, I.; Fernández, R.; Gómez-Rodríguez, J. M.; Colchero, J.; Gómez-Herrero, J.; Baró, A. M. *Rev. Sci. Instrum.* **2007**, *78,* 013705. doi:10.1063/1.2432410

Atomic-resolution imaging of rutile TiO$_2$(110)-(1 × 2) reconstructed surface by non-contact atomic force microscopy

Daiki Katsube[*,1,2], Shoki Ojima[2], Eiichi Inami[3] and Masayuki Abe[2]

Address:
[1]Graduate School of Engineering, Nagaoka University of Technology, 1603-1 Kamitomiokamachi, Nagaoka, Niigata 940-2188, Japan, [2]Graduate School of Engineering Science, Osaka University, 1-3 Machikaneyama, Toyonaka, Osaka 560-8531, Japan and [3]School of Systems Engineering, Kochi University of Technology, 185 Miyanokuchi, Tosayamada, Kami, Kochi 782-8502, Japan

Email:
Daiki Katsube[*] - d_katsube@vos.nagaokaut.ac.jp

* Corresponding author

Abstract

The structure of the rutile TiO$_2$(110)-(1 × 2) reconstructed surface is a phase induced by oxygen reduction. There is ongoing debate about the (1 × 2) reconstruction, because it cannot be clarified whether the (1 × 2) structure is formed over a wide area or only locally using macroscopic analysis methods such as diffraction. We used non-contact atomic force microscopy, scanning tunneling microscopy, and low-energy electron diffraction at room temperature to characterize the surface. Ti$_2$O$_3$ rows appeared as bright spots in both NC-AFM and STM images observed in the same area. High-resolution NC-AFM images revealed that the rutile TiO$_2$(110)-(1 × 2) reconstructed surface is composed of two domains with different types of asymmetric rows.

Introduction

Titanium dioxide (TiO$_2$) is a well-known photocatalyst and has been studied for applications in water splitting and the coating of materials [1]. To optimize the photocatalytic function, it is important to understand the reaction process, hence investigations of chemical and physical surface characteristics and the structure of the photocatalyst are necessary.

The rutile TiO$_2$(110) surface has often been the subject of atomic-level studies in the field of photocatalysis since the preparation of a clean surface is relatively easy. A well-known rutile TiO$_2$(110) surface is the (1 × 1) structure [2]. The (1 × 1) surface has been studied using low-energy electron diffraction (LEED) [3,4], surface X-ray diffraction [5], non-contact atomic force microscopy (NC-AFM) [6-9], scanning tunneling microscopy (STM) [10-12], transmission electron microscopy [13,14], and density functional theory (DFT) [15-19]. These studies have determined many surface properties such as structure, local defects, and adsorption sites.

The (1 × 1) surface transforms to the (1 × 2) surface by oxygen reduction in ultra-high vacuum (UHV) [2,20]. Several structural models for the (1 × 2) surface have been proposed [10,21-24]. Onishi and Iwasawa proposed a symmetric Ti_2O_3 model (Figure 1a) based on STM measurements [10], while Wang et al. proposed an asymmetric Ti_2O_3 model (Figure 1b) similar to the symmetric Ti_2O_3 model based on DFT calculations [24]. These two structural models have been widely accepted. Mochizuki et al. reported total reflection high-energy positron diffraction results for the (1 × 2) surface, which supported the asymmetric Ti_2O_3 model [25]. In contrast, our previous study using LEED and STM has revealed that the (1 × 2) LEED pattern was observed even if the (1 × 2) structure is formed only partially as shown in Figure 1c [20]. This indicates that real-space imaging with atomic resolution, i.e., STM and NC-AFM, would be helpful for a careful determination of the surface structure. It is necessary to observe the surface directly in order to find out whether the (1 × 2) structure is formed over a wide area. In real-space analysis at the atomic level, simultaneous NC-AFM and STM measurements in UHV at low temperature have revealed that the (1 × 2) chain on the (1 × 1) surface has an asymmetric structure [26]. However, in previous studies on the (1 × 2) surface formed over a wide area of a rutile $TiO_2(110)$ surface, the periodic line structure of the (1 × 2) surface was

considered to be a symmetric structure [10,22,27,28]. Therefore, it is still controversial whether or not the periodic (1 × 2) surface is a symmetric structure. The determination of the surface structure is crucial to understand the surface phenomena, such as adsorption, absorption, and decomposition in photocatalytic reactions.

In this study, we characterized the periodic structure of the rutile $TiO_2(110)$-(1 × 2) reconstructed surface using NC-AFM at room temperature. We confirmed by LEED and STM measurements that the (1 × 2) surface forms over a wide area of the rutile $TiO_2(110)$ surface. Ti_2O_3 rows were visualized as bright lines in both STM and NC-AFM images and were observed in the same area. High-resolution NC-AFM imaging revealed that the Ti_2O_3 rows are asymmetric structures.

Experimental
All experiments were conducted using our custom-built system combining NC-AFM, STM, and LEED operated in UHV at room temperature [29]. Nb-doped (0.05 wt %) rutile $TiO_2(110)$ substrates (Shinkosha Corp.) were used. A rutile $TiO_2(110)$-(1 × 2) reconstructed surface was prepared by iterating a surface cleaning process of Ar^+ sputtering (2 keV, Ar partial pressure of 3.0×10^{-4} Pa, ion current of ca. 1.1 µA,

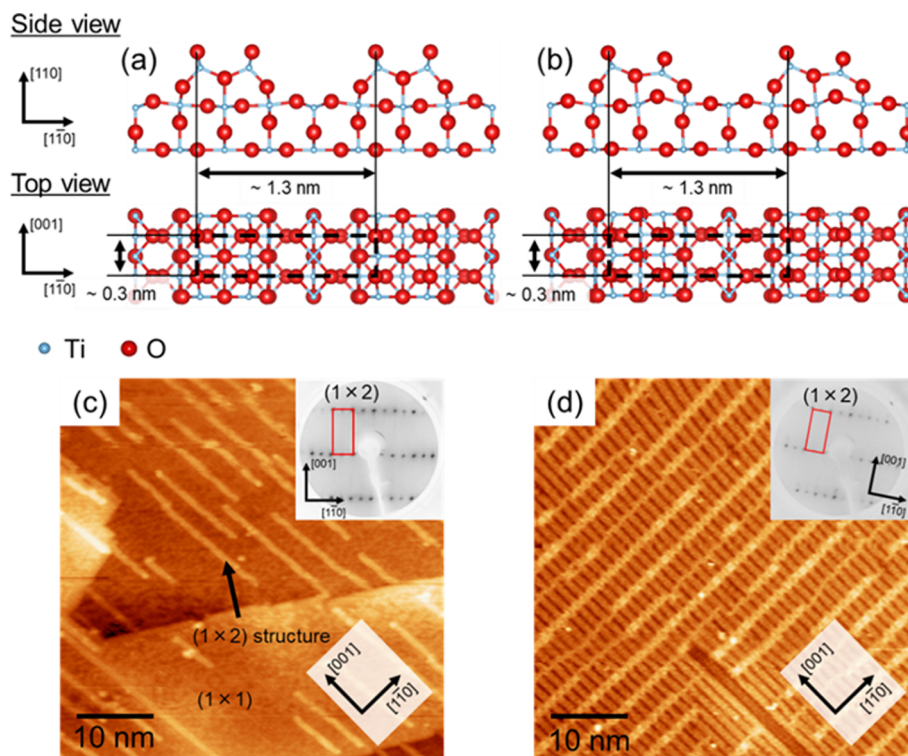**Figure 1:** Structural models of rutile $TiO_2(110)$-(1 × 2) reconstructed surface: (a) Symmetric Ti_2O_3 model [10] and (b) asymmetric Ti_2O_3 model [24]. Structural models were made with VESTA [39]. STM images and LEED patterns of the (1 × 2) structure is formed over a local area (c) and a wide area (d). Sample bias voltage and tunneling current were 1.5 V and 10 pA, respectively. LEED patterns were obtained with an energy of 100 eV.

10 min) and annealing (substrate temperature of ca. 1000 °C, 30 min). STM and NC-AFM imaging was performed using Pt-coated Si cantilevers (Budget Sensors, ElectriTAP190G). All cantilevers were cleaned by Ar^+ sputtering (0.6 keV, Ar partial pressure of 1.0×10^{-5} Pa, ion current of 0.05 μA, 5 min) before scanning. STM imaging was performed in constant-current mode without cantilever oscillation. NC-AFM feedback control was applied in frequency-modulation mode [30] with constant amplitude oscillation. The cantilever deflection was detected using an optical interferometer [31]. Since the electrostatic force due to the contact potential difference (CPD) between the tip and sample prevents high-resolution NC-AFM imaging, a bias voltage was applied to the sample to minimize the CPD.

Results and Discussion

Figure 2a shows a LEED pattern of a rutile $TiO_2(110)$-(1×2) reconstructed surface. The pattern shows two-fold spots in the $[1\bar{1}0]$ direction, confirming the formation of a (1×2) structure. However, in our previous study [20], we reported that a (1×2) LEED pattern also appears when the (1×2) chain is localized on the (1×1) surface. Thus, the surface was observed using STM to confirm that the (1×2) reconstructed structure was formed over a wide area of the rutile $TiO_2(110)$ surface (Figure 2b,c). It can be clearly seen that the (1×2) structure was formed over a wide area (200×200 nm^2) of the surface. Some local structures such as single links, double links, and line defects, which have been reported in previous studies [22,27,28,32], are evident on the (1×2) surface in Figure 2c. These results confirmed that the (1×2) surface prepared in this study is the same surface as in the previous studies [22,27,28,32].

Figure 3 shows STM and NC-AFM images and the height profiles obtained from the same surface area. Since STM and NC-AFM use different feedback signals (interaction force for NC-AFM and tunneling current for STM), the surface structure sometimes results in different contrasts in both images. In Figure 3, white squares and circles indicate line defects and protrusions, which are considered to be adsorbates or contamination. A line defect was imaged as a likely vacancy by STM and a protrusion by NC-AFM. By using these defects as markers, the height profiles from STM and AFM along the same lines are compared in Figure 3c and Figure 3d (A–A′ in Figure 3c and B–B′ in Figure 3d, respectively). For each profile, the positional relationship between the periodic lines and the defect is the same. Previous studies have reported STM imaging visualizing Ti_2O_3 rows with a bright contrast [22,24,26,28]. Based on these earlier results, the periodic lines with bright contrast in the NC-AFM image can be identified as Ti_2O_3 rows. STM and NC-AFM provided different geometry information on the line defect. The line defects could be due to be sub-surface defects because of the geometry of the reflected top surface obtained in NC-AFM imaging using the interaction between the tip and the sample surface as a feedback signal. To identify the line defects, it is necessary to combine DFT and STM and to investigate the bias dependence of simultaneous NC-AFM and STM images. This will be discussed elsewhere since the main subject of this article is the periodic line structure on the rutile $TiO_2(110)$-(1×2) reconstructed surface.

Our NC-AFM and STM imaging in the same area identified the Ti_2O_3 rows on the rutile $TiO_2(110)$-(1×2) reconstructed surface. However, the NC-AFM and STM images in Figure 3 could not reveal whether or not the Ti_2O_3 rows are symmetric because the tip was too dull to resolve inside the Ti_2O_3 rows. To investigate the structure of the Ti_2O_3 rows, the rutile $TiO_2(110)$-(1×2) reconstructed surface was observed with high-resolution NC-AFM imaging using a sharp tip. Figure 4
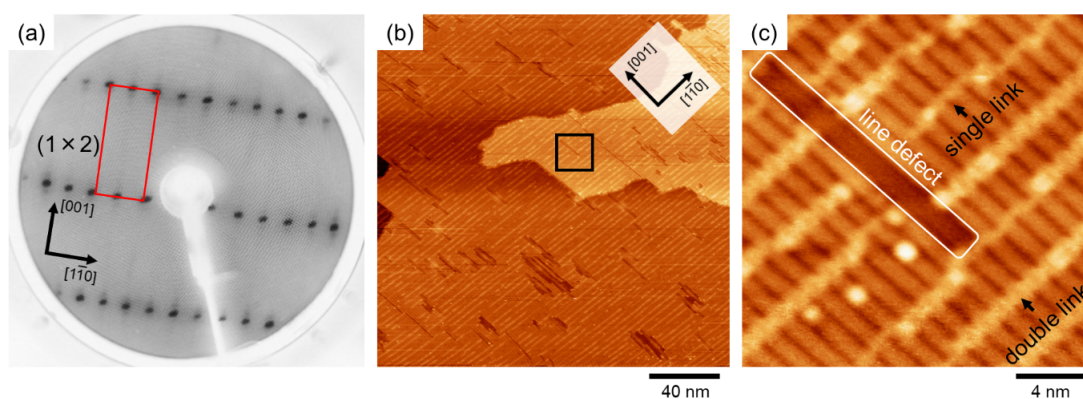

Figure 2: (a) LEED pattern of rutile $TiO_2(110)$-(1×2) reconstructed surface. The electron beam energy was 100 eV. (b), (c) STM image of rutile $TiO_2(110)$-(1×2) reconstructed surface (200×200 nm^2 for (b), 20×20 nm^2 for (c)). The sample bias and current set point were 1.5 V and 10 pA, respectively.
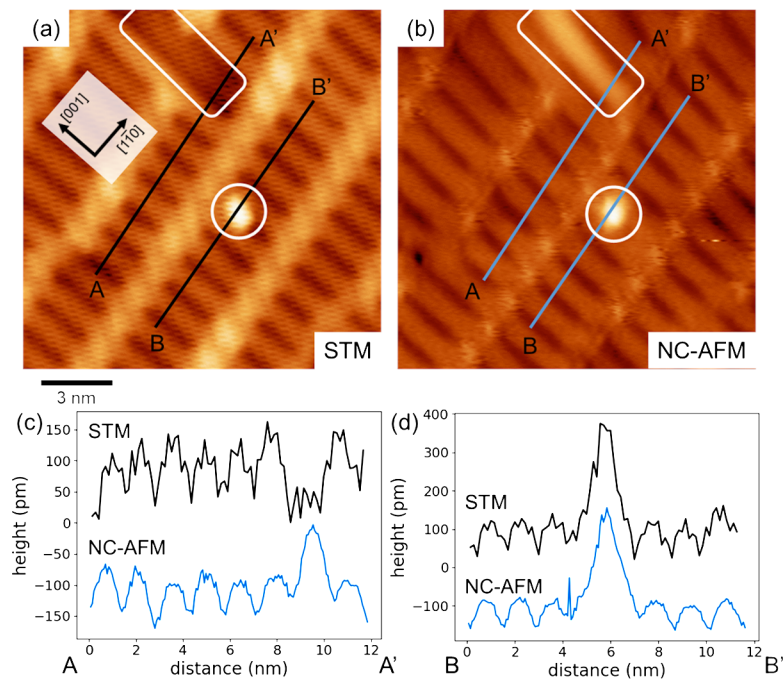
Figure 3: (a) STM and (b) NC-AFM images of a rutile TiO_2(110)-(1 × 2) reconstructed surface. (c, d) Height profiles along black (STM) and blue (NC-AFM) lines in the images. The STM and NC-AFM images were obtained using a Pt-coated Si cantilever with a resonance frequency of f_0 = 154.1 kHz and a spring constant of k = 27.05 N/m. In (a), STM imaging was performed without cantilever oscillation and the parameters sample bias and current set point were 1.5 V and 50 pA, respectively. In (b), the measurement parameters were Δf = −7.9 Hz, A = 16.5 nm, and V_s = 500 mV. The white circles and rectangles in (a) and (b) indicate the same structure at the same position.
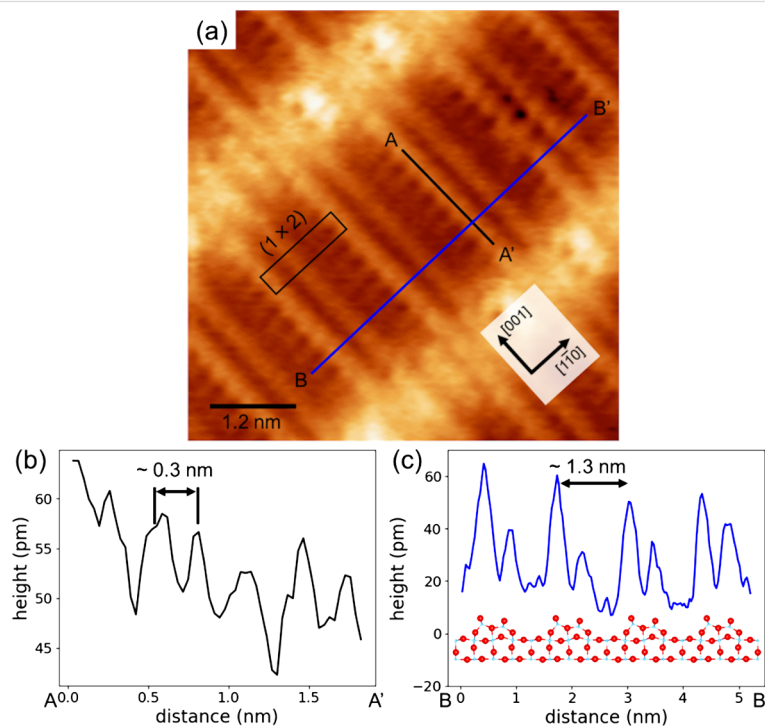
Figure 4: (a) High-resolution NC-AFM image of a rutile TiO_2(110)-(1 × 2) reconstructed surface. The height profiles in (b) and (c) correspond to the black and blue lines in (a), respectively. The NC-AFM image was obtained using a Pt-coated cantilever with a resonance frequency of f_0 = 154.1 kHz and a spring constant of k = 27.05 N/m. The measurement parameters were Δf = −38.1 Hz, A = 9.8 nm, and V_s = 350 mV. The asymmetric Ti_2O_3 model is included with the height profile in (d) for comparison of the surface geometry and the model.

shows a high-resolution NC-AFM image and height profiles. In the NC-AFM image in Figure 4a, twin resolved Ti_2O_3 rows are confirmed. From the height profiles (Figure 4b,c), the pitches of Ti_2O_3 in the [001] and [1$\bar{1}$0] directions were evaluated to be ca. 0.3 nm and ca. 1.3 nm, respectively. These distances correspond to the lattice constant of the (1 × 2) structure. These results confirm that Ti_2O_3 rows were observed with atomic resolution. The height profile in Figure 4c shows that Ti_2O_3 twin rows are asymmetric, with the left-side rows being higher. These results show that the Ti_2O_3 rows of rutile $TiO_2(110)$-(1 × 2) reconstructed surface have an asymmetric structure, and thus support the structural model by Wang et al. (Figure 1b) [24].

The image contrast in NC-AFM and STM depends on the structure and the state of the tip apex [7,9,33,34]. Also, deformation of the surface structure sometimes occurs due to interactions between the tip apex and the sample surface [35]. To address the possibility that the asymmetric contrast in the NC-AFM image in Figure 4a is caused by these artifacts, we confirmed the surface asymmetry by changing the AFM tip. By repeating the measurements, NC-AFM images with two types of the different domains were obtained at several times. Figure 5 shows a constant-height mode NC-AFM image (raw data) of a rutile $TiO_2(110)$-(1 × 2) reconstructed surface and a height profile. There is a case in which the tip apex asymmetry causes an unexpected local image pattern, i.e., dimers of the same height would be imaged at different heights due to the tip apex asymmetry. We obtained NC-AFM images with two types of asymmetric contrast for during repeated NC-AFM imaging. Two types of Ti_2O_3 rows, with either the left side or the right side in a higher position, are shown in the NC-AFM image and height profile in Figure 5, indicating that the asymmetric image is not

caused by an asymmetric tip apex structure. The other possibility to be considered is interactions between the tip and the sample surface that cause a deformation of the surface structure. In this case, a non-conservative force induced by surface structure deformations acts between the tip and the sample surface [36,37] and the signal should be observed as an energy dissipation. In the case of surface deformation, a dissipation signal range of 0.3–0.4 eV/cycle on the deformation site has been reported [37,38]. However, our dissipation images showed almost no contrast variation within a range of 0.12 ± 0.11 eV/cycle. This means that the effect of the tip-induced surface deformation is negligibly small, and that the high-resolution NC-AFM images reflect the intrinsic surface structure. These results clearly suggest that the observed asymmetric contrast in the NC-AFM images are attributed to the asymmetric structure of the periodic Ti_2O_3 rows. Additionally, the (1 × 2) surface has a multi-domain structure with either the left or the right side in a higher position.

Conclusion

In summary, we characterized the rutile $TiO_2(110)$-(1 × 2) reconstructed surface using NC-AFM, STM, and LEED at room temperature. In NC-AFM imaging, Ti_2O_3 rows on the (1 × 2) surface were imaged with high contrast, as confirmed by STM and NC-AFM images obtained in the same area. High-resolution NC-AFM imaging revealed that the Ti_2O_3 rows of the rutile $TiO_2(110)$-(1 × 2) reconstructed surface have an asymmetric structure. Additionally, we found two domains of asymmetric rows with either the right side or the left side in a higher position. We believe information on the geometry of the rutile $TiO_2(110)$-(1 × 2) reconstructed surface is useful for understanding surface phenomena, such as adsorption, absorption, and decomposition in photocatalytic reactions.
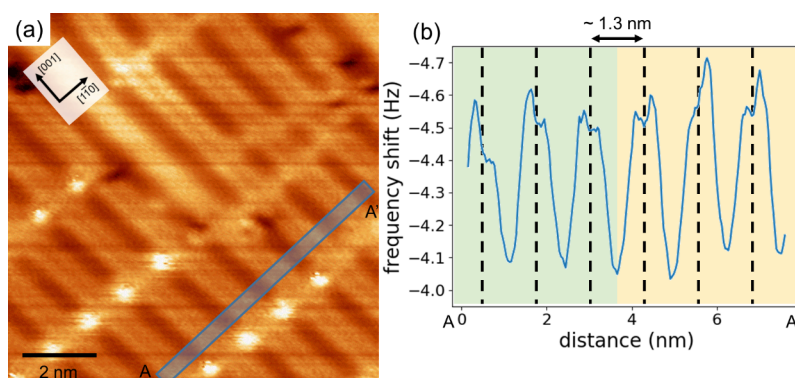

Figure 5: Area exhibiting two types of asymmetric Ti_2O_3 rows. (a) High-resolution constant height mode NC-AFM image (raw data) of rutile $TiO_2(110)$-(1 × 2) reconstructed surface and (b) averaged line profile corresponding to the blue square in the NC-AFM image. The NC-AFM image was obtained using a Pt-coated cantilever with a resonance frequency of f_0 = 154.9 kHz and a spring constant of k = 27.05 N/m. The measurement parameters were A = 10.9 nm, and V_s = 850 mV. The green and yellow regions in (b) indicate Ti_2O_3 rows with the left side and the right side in higher positions, respectively.

Funding

ORCID® iDs

Daiki Katsube - https://orcid.org/0000-0001-8879-0163
Eiichi Inami - https://orcid.org/0000-0002-2167-8510
Masayuki Abe - https://orcid.org/0000-0001-5619-3911

References

1. Fujishima, A.; Zhang, X.; Tryk, D. A. *Surf. Sci. Rep.* **2008,** *63,* 515. doi:10.1016/j.surfrep.2008.10.001
2. Diebold, U. *Surf. Sci. Rep.* **2003,** *48,* 53. doi:10.1016/s0167-5729(02)00100-0
3. Bennett, R. A.; Poulston, S.; Stone, P.; Bowker, M. *Phys. Rev. B* **1999,** *59,* 10341. doi:10.1103/physrevb.59.10341
4. Lindsay, R.; Wander, A.; Ernst, A.; Montanari, B.; Thornton, G.; Harrison, N. M. *Phys. Rev. Lett.* **2005,** *94,* 246102. doi:10.1103/physrevlett.94.246102
5. Charlton, G.; Hoowes, P. B.; Nicklin, C. L.; Steadman, P.; Taylor, J. S. G.; Muryn, C. A.; Harte, S. P.; Mercer, J.; McGrath, R.; Norman, D.; Turner, T. S.; Thornton, G. *Phys. Rev. Lett.* **1997,** *78,* 495. doi:10.1103/physrevlett.78.495
6. Fukui, K.-i.; Onishi, H.; Iwasawa, Y. *Phys. Rev. Lett.* **1997,** *79,* 4202. doi:10.1103/physrevlett.79.4202
7. Enevoldsen, G. H.; Foster, A. S.; Christensen, M. C.; Lauritsen, J. V.; Besenbacher, F. *Phys. Rev. B* **2007,** *76,* 205415. doi:10.1103/physrevb.76.205415
8. Yurtsever, A.; Sugimoto, Y.; Abe, M.; Morita, S. *Nanotechnology* **2010,** *21,* 165702. doi:10.1088/0957-4484/21/16/165702
9. Yurtsever, A.; Fernández-Torre, D.; González, C.; Jelínek, P.; Pou, P.; Sugimoto, Y.; Abe, M.; Pérez, R.; Morita, S. *Phys. Rev. B* **2012,** *85,* 125416. doi:10.1103/physrevb.85.125416
10. Onishi, H.; Iwasawa, Y. *Surf. Sci.* **1994,** *313,* L783. doi:10.1016/0039-6028(94)91146-0
11. Diebold, U.; Anderson, J. F.; Ng, K.-O.; Vanderbilt, D. *Phys. Rev. Lett.* **1996,** *77,* 1322. doi:10.1103/physrevlett.77.1322
12. Minato, T.; Sainoo, Y.; Kim, Y.; Kato, H. S.; Aika, K.-i.; Kawai, M.; Zhao, J.; Petek, H.; Huang, T.; He, W.; Wang, B.; Wang, Z.; Zhao, Y.; Yang, J.; Hou, J. G. *J. Chem. Phys.* **2009,** *130,* 124502. doi:10.1063/1.3082408
13. Shibata, N.; Goto, A.; Choi, S.-Y.; Mizoguchi, T.; Findlay, S. D.; Yamamoto, T.; Ikuhara, Y. *Science* **2008,** *322,* 570. doi:10.1126/science.1165044
14. Chang, T.-Y.; Tanaka, Y.; Ishikawa, R.; Toyoura, K.; Matsunaga, K.; Ikuhara, Y.; Shibata, N. *Nano Lett.* **2014,** *14,* 134. doi:10.1021/nl403520c
15. Ramamoorthy, M.; Vanderbilt, D.; King-Smith, R. D. *Phys. Rev. B* **1994,** *49,* 16721. doi:10.1103/physrevb.49.16721
16. Hameeuw, K. J.; Cantele, G.; Ninno, D.; Trani, F.; Iadonisi, G. *J. Chem. Phys.* **2006,** *124,* 024708. doi:10.1063/1.2136158
17. Perron, H.; Domain, C.; Roques, J.; Drot, R.; Simoni, E.; Catalette, H. *Theor. Chem. Acc.* **2007,** *117,* 565. doi:10.1007/s00214-006-0189-y
18. Çelik, V.; Ünal, H.; Mete, E.; Ellialtıoğlu, Ş. *Phys. Rev. B* **2010,** *82,* 205113. doi:10.1103/physrevb.82.205113
19. Matsunaga, K.; Tanaka, Y.; Toyoura, K.; Nakamura, A.; Ikuhara, Y.; Shibata, N. *Phys. Rev. B* **2014,** *90,* 195303. doi:10.1103/physrevb.90.195303
20. Ojima, S.; Katsube, D.; Yamashita, H.; Miyato, Y.; Abo, S.; Abe, M. *Jpn. J. Appl. Phys.* **2019,** *58,* SIIA10. doi:10.7567/1347-4065/ab19a3
21. Møller, P. J.; Wu, M.-C. *Surf. Sci.* **1989,** *224,* 265. doi:10.1016/0039-6028(89)90915-1
22. Pang, C. L.; Haycock, S. A.; Raza, H.; Murray, P. W.; Thornton, G.; Gülseren, O.; James, R.; Bullett, D. W. *Phys. Rev. B* **1998,** *58,* 1586. doi:10.1103/physrevb.58.1586
23. Park, K. T.; Pan, M.; Meunier, V.; Plummer, E. W. *Phys. Rev. B* **2007,** *75,* 245415. doi:10.1103/physrevb.75.245415
24. Wang, Q.; Oganov, A. R.; Zhu, Q.; Zhou, X.-F. *Phys. Rev. Lett.* **2014,** *113,* 266101. doi:10.1103/physrevlett.113.266101
25. Mochizuki, I.; Ariga, H.; Fukaya, Y.; Wada, K.; Maekawa, M.; Kawasuso, A.; Shibata, T.; Asakura, K.; Hyodo, T. *Phys. Chem. Chem. Phys.* **2016,** *18,* 7085. doi:10.1039/c5cp07892j
26. Reticcioli, M.; Setvin, M.; Hao, X.; Flauger, P.; Kresse, G.; Schmid, M.; Diebold, U.; Franchini, C. *Phys. Rev. X* **2017,** *7,* 031053. doi:10.1103/physrevx.7.031053
27. Pieper, H. H.; Venkataramani, K.; Torbrügge, S.; Bahr, S.; Lauritsen, J. V.; Besenbacher, F.; Kühnle, A.; Reichling, M. *Phys. Chem. Chem. Phys.* **2010,** *12,* 12436. doi:10.1039/c0cp00160k
28. Yim, C. M.; Pang, C. L.; Thornton, G. *Surf. Sci.* **2016,** *650,* 71. doi:10.1016/j.susc.2015.04.022
29. Katsube, D.; Yamashita, H.; Abo, S.; Abe, M. *Beilstein J. Nanotechnol.* **2018,** *9,* 686. doi:10.3762/bjnano.9.63
30. Albrecht, T. R.; Grütter, P.; Horne, D.; Ruger, D. *J. Appl. Phys.* **1991,** *69,* 668. doi:10.1063/1.347347
31. Ruger, D.; Mamin, H. J.; Guethner, P. *Appl. Phys. Lett.* **1989,** *55,* 2588. doi:10.1063/1.101987
32. Mezhenny, S.; Maksymovych, P.; Thompson, T. L.; Diwald, O.; Stahl, D.; Walck, S. D.; Yates, J. T., Jr. *Chem. Phys. Lett.* **2003,** *369,* 152. doi:10.1016/s0009-2614(02)01997-8
33. Enevoldsen, G. H.; Pinto, H. P.; Foster, A. S.; Jensen, M. C. R.; Kühnle, A.; Reichling, M.; Hofer, W. A.; Lauritsen, J. V.; Besenbacher, F. *Phys. Rev. B* **2008,** *78,* 045416. doi:10.1103/physrevb.78.045416
34. Sweetman, A.; Jarvis, S.; Danza, R.; Moriarty, P. *Beilstein J. Nanotechnol.* **2012,** *3,* 25. doi:10.3762/bjnano.3.3
35. Sugimoto, Y.; Pou, P.; Custance, Ó.; Jelínek, P.; Morita, S.; Pérez, R.; Abe, M. *Phys. Rev. B* **2006,** *73,* 205329. doi:10.1103/physrevb.73.205329
36. Iwata, K.; Yamazaki, S.; Tani, Y.; Sugimoto, Y. *Appl. Phys. Express* **2013,** *6,* 055201. doi:10.7567/apex.6.055201
37. Arai, T.; Inamura, R.; Kura, D.; Tomitori, M. *Phys. Rev. B* **2018,** *97,* 115428. doi:10.1103/physrevb.97.115428
38. Onoda, J.; Yabuoshi, K.; Miyazaki, H.; Sugimoto, Y. *Phys. Rev. B* **2017,** *96,* 241302(R). doi:10.1103/physrevb.96.241302
39. Momma, K.; Izumi, F. *J. Appl. Crystallogr.* **2011,** *44,* 1272. doi:10.1107/s0021889811038970

Current measurements in the intermittent-contact mode of atomic force microscopy using the Fourier method: a feasibility analysis

Berkin Uluutku and Santiago D. Solares[*]

Full Research Paper

Address:
The George Washington University, Department of Mechanical and Aerospace Engineering, 800 22nd St. NW, Suite 3000, Washington, DC 20052, USA

Email:
Santiago D. Solares[*] - ssolares@gwu.edu

* Corresponding author

Abstract

Atomic force microscopy (AFM) is an important tool for measuring a variety of nanoscale surface properties, such as topography, viscoelasticity, electrical potential and conductivity. Some of these properties are measured using contact methods (static contact or intermittent contact), while others are measured using noncontact methods. Some properties can be measured using different approaches. Conductivity, in particular, is mapped using the contact-mode method. However, this modality can be destructive to delicate samples, since it involves continuously dragging the cantilever tip on the surface during the raster scan, while a constant tip–sample force is applied. In this paper we discuss a possible approach to develop an intermittent-contact conductive AFM mode based on Fourier analysis, whereby the measured current response consists of higher harmonics of the cantilever oscillation frequency. Such an approach may enable the characterization of soft samples with less damage than contact-mode imaging. To explore its feasibility, we derive the analytical form of the tip–sample current that would be obtained for attractive (noncontact) and repulsive (intermittent-contact) dynamic AFM characterization, and compare it with results obtained from numerical simulations. Although significant instrumentation challenges are anticipated, the modelling results are promising and suggest that Fourier-based higher-harmonics current measurement may enable the development of a reliable intermittent-contact conductive AFM method.

Introduction

Conductive atomic force microscopy (C-AFM), a contact-mode technique, has been extensively utilized to investigate local electrical properties of nanoscale systems, such as organic solar cells [1-7], semiconductors [8-10], and metals [11-13]. C-AFM has been used to characterize local charge transport characteristics [4,6] and to obtain detailed information about local charge mobility [5,7]. However, contact-mode AFM techniques, where the probe continuously interacts with the surface in a repulsive

manner, can be destructive to soft samples [14-16]. In fact, C-AFM has been deliberately used as an imprinting tool in the past [17,18]. For the cases where the sample is rather delicate, intermittent-contact mode (ICM) imaging, where the tip and the sample interact briefly at the bottom of each cantilever oscillation, can be a less destructive technique [16,19,20], and this could be advantageous also for performing current measurements on such samples. Additionally, scanning tunnelling microscopy (STM) applications may also benefit from current measurements during which the tip oscillates above the surface, although in the noncontact regime. Specifically, STM measurements are modulated based on the observed tunnelling current, which has an exponential dependence on the tip–sample distance [21]. Therefore, any unexpected contact with the surface may lead to a current spike and severely perturb the controller for a period of time, during which the tip apex structure could be damaged further due to additional tip–sample impacts. However, if a noncontact oscillatory current measurement mode is used, where the control variable is not the instantaneous value of the current, these unexpected tip–sample impacts may be more benign and may not perturb the measurement as drastically as in traditional STM approaches.

Intermittent-contact current measurement within AFM has already been discussed in the literature. A notable example is the work by Fein et al. where injected voltage pulses were investigated using a custom-made, low-frequency, high-stiffness cantilever [22]. Another example is the work of Vecchiola et al. where a "pulsed force" microscopy approach was implemented, rather than traditional ICM-AFM [23]. Although the end result was intermittent-contact characterization, due to the nature of the force pulses the probe jumped from contact point to contact point rather than exhibiting a constant, nearly resonant intermittent-contact oscillation (the oscillation frequencies used were much smaller than the resonance frequency of the cantilever).

In this paper, we propose the use of Fourier analysis to implement ICM current measurements. Fourier analysis is commonly used in ICM-AFM experiments due to the periodic nature of the cantilever excitation and response. For example, in amplitude-modulation AFM (AM-AFM), the most common ICM-AFM method, a lock-in amplifier is used to track the cantilever response near the fundamental frequency [20]. Similarly, bimodal AFM, which involves the excitation of the cantilever at two frequencies, also uses lock-in amplifiers or phase-locked loops to control or observe each frequency response [24,25]. More elaborate Fourier analysis techniques have also been implemented [26], such as in the work of Stark et al. where time-resolved transient forces between the AFM probe and the sample were obtained from the experimental data [27]. This approach was enhanced by Sahin et al. through a "torsional

harmonic cantilever" [28], which combined flexural and torsional oscillations in a way that reduced cross-contamination of the signals used to reconstruct the tip–sample force. We have also reported numerical simulations of this method, providing analysis software that enables estimations of the accuracy of the method under different conditions [29]. Fourier analysis has also been implemented for AFM force reconstructions within the so-called intermodulation AFM method, developed by Haviland and co-workers, where the cantilever is typically excited simultaneously at two different frequencies, while various intermodulation products are recorded with a collection of lock-in amplifiers [30,31]. More recently, Borgani et al. used Fourier analysis to investigate non-linear conductance in C-AFM measurements, acquiring current–voltage responses at every scan point without sacrificing scanning speed [32].

In order to explore the various phenomena involved in dynamic current measurements, this manuscript discusses three different cases: (i) a noncontact dynamic current measurement where the cantilever follows an ideal sinusoidal trajectory, (ii) a similar case, but considering a more realistic trajectory where the tip oscillation is perturbed by the presence of the sample, and (iii) an intermittent-contact case where a Hertzian contact interaction is established with the sample and interrupted again during each cantilever oscillation. In the Results section, these three cases are simulated and the results are compared with the equations derived later in the current section. Practical and instrumentation challenges for the proposed methods in the context of real SPM experiments are summarised in the Discussion section, such as data acquisition difficulties when multiple weak signals at high frequencies are measured. Possible solutions are also discussed in some cases, although some of these challenges are significant and have not yet been overcome. In the remainder of this section we will derive Fourier space expressions for the measured current for each case analysed.

Case 1: Dynamic noncontact current measurement with ideal sinusoidal tip trajectory

Consider an AFM tip oscillating over a surface with a perfect cosine trajectory, without impacting the surface (Figure 1). In this case the distance between the AFM tip and the surface can be written as

$$d = h + A\cos\left(2\pi f \tau\right), \qquad (1)$$

where d is the instantaneous tip–sample distance, h is the equilibrium tip position, A is the oscillation amplitude, f is the oscillation frequency and τ is time. Since there is no tip–surface con-

tact, we consider a tunnelling current between the tip and the surface, which we approximate with an exponential function of the distance [21],

$$J = \sigma e^{-Kd},\qquad(2)$$

where σ is a linear scaling parameter and K provides the rate of exponential decay.
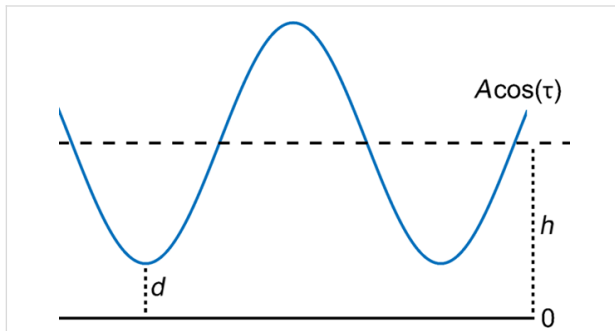

Figure 1: Illustration of a tip trajectory with a perfect sinusoidal shape in the noncontact dynamic AFM mode. The blue line represents the tip motion about the equilibrium position of the cantilever, while the solid black line represents the surface position, fixed at reference point zero. h is the cantilever rest position and d is the instantaneous tip–sample distance.

Inserting Equation 1 into Equation 2 we obtain an expression for the tunnelling current with respect to time:

$$
\begin{aligned}
J &= \sigma e^{-K\left[h + A\cos(\tau)\right]} \\
&= \sigma e^{-Kh} e^{-KA\cos(2\pi f \tau)} \\
&= \sigma e^{-Kh} e^{KA\cos(2\pi f \tau + \pi)}.
\end{aligned}
\qquad(3)
$$

We expect to have maximum tunnelling current at the bottom of the oscillation, where the cosine is at its minimum (this is where the tip and sample are closest). Likewise, the lowest value of the current occurs when the cosine reaches its maximum value. Since the oscillation phase reference is arbitrary, it is convenient to replace the time variable as follows:

$$2\pi f \tau + \pi = 2\pi f t,\qquad(4)$$

$$J = \sigma e^{-Kh} e^{KA\cos(2\pi f t)}.\qquad(5)$$

Note that the left-hand side of Equation 4 depends on the variable τ, whereas the right-hand side depends on t. Expressions such as the right-hand side of Equation 5 can be expanded with a Fourier cosine series using the modified Bessel functions of the first kind (of different orders) as the Fourier coefficients [33]:

$$e^{z\cos(\theta)} = I_0(z) + 2\sum_{k=1}^{\infty} I_k(z)\cos(\theta).\qquad(6)$$

We apply this expansion to our current equation and obtain:

$$J = \sigma e^{-Kh}\left[I_0(AK) + 2\sum_{k=1}^{\infty} I_k(AK)\cos(2\pi f k t)\right].\qquad(7)$$

In order to be able to more intuitively analyse the result, we take the Fourier transform of the series in Equation 7:

$$F\{J\} = \sigma e^{-Kh}\left[I_0(AK)\delta(w) + \sum_{k=1}^{\infty} I_k(AK)\left[\delta(w \pm kf)\right]\right].\qquad(8)$$

We will return to this expression in order to analyse and visualize it in the Results section.

Case 2: Dynamic noncontact current measurement with realistic tip trajectory

A real AFM tip trajectory exhibits perturbations due to the tip–sample forces, which have been treated analytically by Dürig [34-36] and investigated further by several other researchers [37-39]. The perturbed tip trajectory can be expressed as a Fourier cosine series:

$$\psi = \sum_{n=1}^{\infty} a_n \cos(2\pi n f t).\qquad(9)$$

Here the cantilever response consists of the principal frequency oscillation plus its higher harmonics, with the a_n values representing the amplitudes of those harmonics. For instance, a_1 corresponds to the fundamental frequency of the cantilever response, which is typically tracked using a lock-in amplifier and modulated during a standard dynamic AFM experiment. As outlined in the work of Hembacher and co-workers [37], the a_n values correspond to higher harmonics of the cantilever oscillation, as indicated in Equation 10, where the tip–sample interaction force exhibits short range compared to the full cantilever oscillation:

$$a_n = \frac{2}{\pi k}\frac{1}{1-n^2}\frac{A^n}{\prod_{i=1}^{n}(2i-1)}\int_{-1}^{1}\frac{d^n F(z+Au)}{dz^n}\left(1-u^2\right)^{n-0.5}du.\qquad(10)$$

The a_n values decrease rapidly with increasing n in conventional dynamic mode applications [note that in Equation 10 the a_n values are proportional to the inverse of $(1 - n^2)$]. The analysis of the cantilever trajectory and its higher harmonic responses are discussed in detail in [34-39]. The higher harmonics (i.e., $a_2, a_3, \ldots$) have also been measured in dynamic AFM experiments [40,41].

For our cantilever trajectory we will use Equation 9, since a tip–sample force perturbation is present. Since we are still considering a noncontact case, we will use the tunnelling current model from Equation 3. The tip–sample distance is:

$$d = h + \psi = h + \sum_{n=1}^{\infty} a_n \cos\left(2\pi n f t\right). \qquad (11)$$

We treat this expression in a similar manner as for the previously analysed ideal case and obtain the following current expression in the time domain:

$$
\begin{aligned}
J &= \sigma e^{K\psi} e^{-Kh} \\
&= \sigma e^{-Kh} \prod_{n=1}^{\infty} \left[e^{K a_n \cos(2\pi f n t)} \right] \\
&= \sigma e^{-Kh} \prod_{n=1}^{\infty} \left[I_0\left(a_n K\right) + 2 \sum_{k=1}^{\infty} I_k\left(K a_n\right) \cos\left(2\pi f n t\right) \right].
\end{aligned}
\qquad (12)
$$

We can again easily apply the Fourier transform to find the frequency-domain representation of the tunnelling current. In this case, however, although it is trivial to obtain the Fourier transform of the Fourier series, we have an infinite number of different Fourier series multiplied with one another. These multiplications in the time domain correspond to convolutions in the frequency domain:

$$
\begin{aligned}
F(J) &= \sigma e^{-Kh} \left[I_0\left(a_1 K\right) \delta(w) + 2\sum_{k=1}^{\infty} I_k\left(a_1 K\right) \delta\left(w \pm k f\right) \right] \\
&\quad * \left[I_0\left(a_2 K\right) \delta(w) + 2\sum_{k=1}^{\infty} I_k\left(a_2 K\right) \delta\left(w \pm 2 k f\right) \right] * \ldots \\
&\quad * \left[I_0\left(a_n K\right) \delta(w) + 2\sum_{k=1}^{\infty} I_k\left(a_n K\right) \delta\left(w \pm n k f\right) \right] * \ldots
\end{aligned}
\qquad (13)
$$

This infinite number of convolutions between infinite series may look intimidating at first glance. However, we note that the infinite series in Equation 13 consist of delta functions at different frequencies, multiplied by their respective coefficients. Convolution of a given function with a delta function yields

only a time shift in the convolved function, without changing the original shape of the function. For instance,

$$\cos(t) * \delta(t - a) = \int_{-\infty}^{\infty} f(\zeta) \delta(t - a - \zeta) \, d\zeta = \cos(t - a).$$

Furthermore, we know that the coefficients of the aforementioned delta functions correspond to modified Bessel functions of the first kind, which increase in order with every consecutive term in the infinite series. The zeroth-order modified Bessel function of the first kind approaches unity when its argument approaches zero. Higher-order modified Bessel functions of the first kind approach zero when their argument approaches zero (see Figure 2). Combining this knowledge with the knowledge of rapidly decreasing values of a_n, we can conclude that the higher harmonics of the current will approach a delta function with a coefficient equal to unity at 0 Hz, which has no effect on convolution operations:

$$
\begin{aligned}
&\lim_{z \to 0} I_0(z) = 1 \text{ hence } \lim_{n \to \infty} I_0(a_n) = 1, \\
&\lim_{z \to 0} I_{k>0}(z) = 0 \text{ hence } \lim_{n \to \infty} I_{k>0}(a_n) = 0, \qquad (14) \\
&f(x) * \delta(w) = f(x) \text{ and } f(x) * 0 = 0.
\end{aligned}
$$

Thus, we can conclude that only the first few harmonics will contribute significantly. Intuitively, it is also expected that the higher harmonics should not contribute significantly to the final convolution based on their a_n values approaching zero with increasing n.
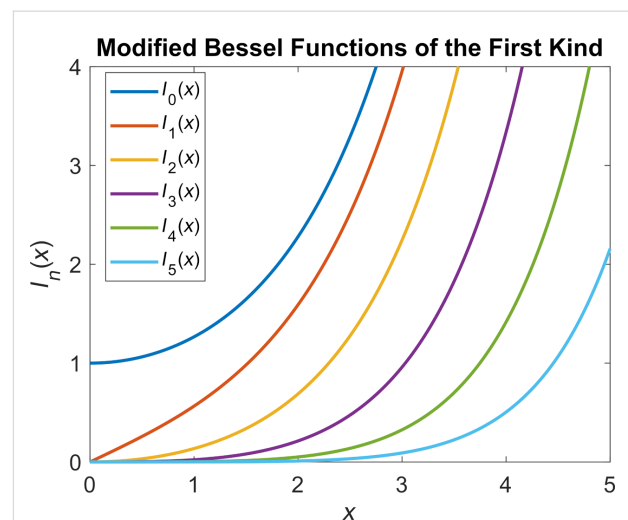

Figure 2: Modified Bessel functions of the first kind of different orders. While the zeroth-order function approaches unity at the origin, higher-order functions approach zero quite steeply. Higher-order functions converge to zero more quickly than their lower-order counterparts as the origin is approached from the right.

Case 3: Dynamic intermittent-contact current measurement with realistic tip trajectory

Here we consider a tip trajectory such that intermittent tip–sample repulsive contact occurs, for which a much larger current is expected from the conduction (contact) sections of the trajectory than from the tunnelling (noncontact) sections of the trajectory. During the conduction phase, we will treat the current as being proportional to the contact area, as a first approximation, as in an Ohmic contact, and will neglect the small tunnelling current for simplicity. Using the Hertzian contact model [42] for the repulsive interaction and considering surface indentation, we can write the current as:

$$I(d) = \begin{cases} 0, & d > 0 \\ C \cdot A, & d \le 0, \text{ where } A = |d| R \dfrac{1}{\pi} \end{cases}, \quad (15)$$

where d is the tip–sample distance, C is a conduction proportionality constant, and R is the AFM tip radius. The overall setting we have described is represented in Figure 3.

Although frequency-domain analysis has provided useful insight and mathematical convenience for the previous two cases considered, it is more challenging to perform here due to the piecewise expression for the current. We can address this issue using the square wave function (sq) to represent the indentation, *In*, as follows:

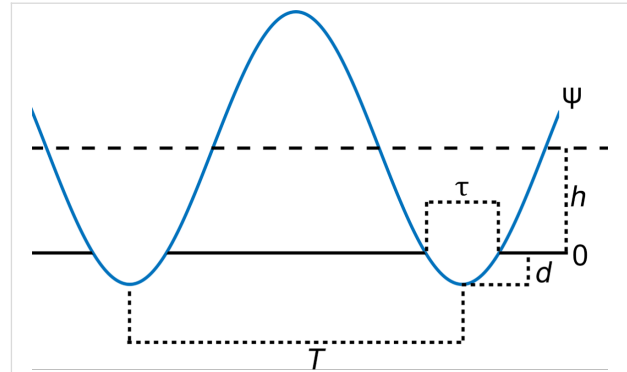$$In = -d \cdot \text{sq}(\tau, T) = -(h + \psi) \cdot \text{sq}(\tau, T), \quad (16)$$

Figure 3: Illustration of the intermittent-contact interaction case. The blue line represents ψ, the trajectory of the tip about the equilibrium position of the cantilever, while the solid black line represents the surface position, fixed at reference point zero. *h* is the cantilever rest position, *T* is the fundamental period of the tip trajectory, *d* is the indentation, and τ is the contact time.

where ψ is the tip trajectory, and sq(τ,T) is the square wave function with period T and duty cycle τ, ranging from zero to unity and with a duty cycle centred around zero time [43]. It is clear that τ, the duty cycle of the square wave function, corresponds to the effective interaction time between the tip and the sample. Upon introduction of sq(τ,T), which has a well-defined Fourier transform, our indentation will automatically be zero whenever there is a positive tip–sample distance (see Figure 4). We can now define the current as

$$I(In) = In \cdot C \cdot R \cdot \frac{1}{\pi} \quad (17)$$

and take its Fourier transform:

$$\begin{aligned}
F\{I\} &= \left[-h\delta(w) - \frac{1}{2}\sum_{k=1}^{\infty}\left(a_k\delta(w\pm kf)\right) \right] \\
&\quad * \left[\tau f\delta(w) + \sum_{n=1}^{\infty}\left(\frac{1}{n\pi}\sin(\pi f n\tau)\delta(w\pm nf)\right) \right] \\
&= \left\{ -h\delta(w) * \left[\tau f\delta(w) + \sum_{n=1}^{\infty}\left(\frac{1}{n\pi}\sin(\pi f n\tau)\delta(w\pm nf)\right) \right] \right\} \\
&\quad + \left\{ -\frac{1}{2}a_1\delta(w\pm f) * \left[\tau f\delta(w) + \sum_{n=1}^{\infty}\left(\frac{1}{n\pi}\sin(\pi f n\tau)\delta(w\pm nf)\right) \right] \right\} \\
&\quad + \left\{ -\frac{1}{2}a_2\delta(w\pm 2f) * \left[\tau f\delta(w) + \sum_{n=1}^{\infty}\left(\frac{1}{n\pi}\sin(\pi f n\tau)\delta(w\pm nf)\right) \right] \right\} \\
&\quad + \ldots \\
&\quad + \left\{ -\frac{1}{2}a_k\delta(w\pm kf) * \left[\tau f\delta(w) + \sum_{n=1}^{\infty}\left(\frac{1}{n\pi}\sin(\pi f n\tau)\delta(w\pm nf)\right) \right] \right\} + \ldots
\end{aligned} \quad (18)$$

In the above equation, two terms (in brackets) are being convoluted. The first term corresponds to the tip trajectory and the second term comes from the introduction of the square pulse. One can see that the contribution coming from the square pulse function has a sinc-shaped envelope on the coefficients of the delta functions, $(1/n\pi)\cdot\sin(\pi f n \tau)$. Examination of the term coming from the trajectory reveals that it can be separated into two components: a zero frequency (DC) contribution and a harmonics contribution. The DC contribution corresponds to the term containing $\delta(w)$ and the harmonics contribution corresponds to the terms containing $\delta(w \pm nf)$ inside the summation. Due to the additive property of the convolution, this operation can be performed one component at a time. This means that individual components of the motion can be convolved with the term originating from the square wave function and summed up afterwards. The zero-frequency contribution will yield a comb of delta functions with a sinc envelope on their coefficients, coming from the square wave function, while each of the delta functions deriving from the harmonics of the motion will lead to a shifted comb of delta functions with rescaled coefficients governed by a sinc envelope. This is demonstrated in Equation 19 and Equation 20. Equation 19 shows the expansion of the term coming from the DC contribution in the trajectory. As the equation shows, convolving the contribution of the rectangular pulse with the 0 Hz part of the trajectory only rescales the former. Equation 20 illustrates the convolution of the square pulse contribution with the first harmonic coming from the trajectory. This operation both rescales and shifts the square pulse contribution by the frequency of the first harmonic.

$$-h\delta(w)*\left[\tau f\delta(w)+\sum_{n=1}^{\infty}\left(\frac{1}{n\pi}\sin(\pi f n\tau)\delta(w\pm nf)\right)\right]$$
$$=-h\tau f\delta(w)-h\sum_{n=1}^{\infty}\left(\frac{1}{n\pi}\sin(\pi f n\tau)\delta(w\pm nf)\right), \quad (19)$$

$$-\frac{1}{2}a_1\delta(w+f)*\left[\tau f\delta(w)+\sum_{n=1}^{\infty}\left(\frac{1}{n\pi}\sin(\pi f n\tau)\delta(w\pm nf)\right)\right]$$
$$=\frac{1}{2}a_1\left[\tau f\delta(w+f)+\sum_{n=1}^{\infty}\frac{1}{n\pi}\sin(\pi f n\tau)\delta(w\pm nf+f)\right]. \quad (20)$$

Based on the above, we conclude that the current will consist of a linear combination of shifted combs of delta functions with a sinc envelope governing the coefficients of each comb. With rapidly decreasing a_n values, higher-frequency harmonics will become negligible quite rapidly. However, unlike in the noncontact (tunnelling) case, the a_n values are directly involved in the current expression, without being "processed" inside of a

modified Bessel function (in this case they are coefficients of delta functions). Therefore, the contribution of the higher harmonics is expected to be more significant in this case.
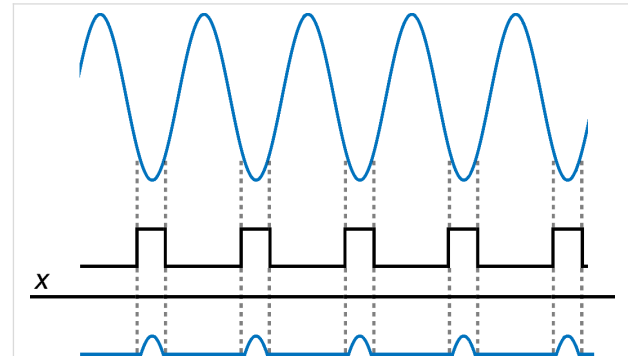

Figure 4: Illustration of the derivation of the indentation. The upper blue line represents the tip–sample distance. Multiplying that function with a square pulse function (black line) with duty cycle equal to the contact time, and changing sign, yields the indentation, represented by the lower blue line.

One can see from Equation 18 that the effective interaction time between the tip and the sample, τ, has a significant effect on the current profile. The consideration of the role of τ in Equation 18 leads to the conclusion that increasing τ increases the current magnitude and narrows the sinc envelope. Narrowing of the sinc envelope suggests more quickly decaying harmonics. This is reasonable, since increases in the contact time should lead to smoother variations in the current, which would reduce the need for very high frequency components in its Fourier transform. More quickly decaying harmonics suggest that it would be more difficult to measure a large number of them accurately, but due to the above reasons, fewer harmonics should be necessary for a proper reconstruction of the current. One can also conclude that knowledge of the tip–sample contact time would be useful in the characterization of the current profile, while, similarly, knowledge of the current as a function of time would aid in understanding the effective tip–sample contact time, which may also provide useful information regarding the mechanics of the interaction [44].

Results

In order to visualise the analytical results derived for the first case considered, we evaluate Equation 8 for a cantilever frequency of 70 kHz and an amplitude of 100 nm, with the lowest point of the trajectory being 1 nm above the surface. A tunnelling current in the form of Equation 2 is considered, with 1000-fold decay between a distance of 0 and 1 nm from the surface. As can be seen from Figure 5, the calculated frequency peaks on the power spectrum (calculated using the derived equation) match those calculated by taking the Fourier transform of the current.
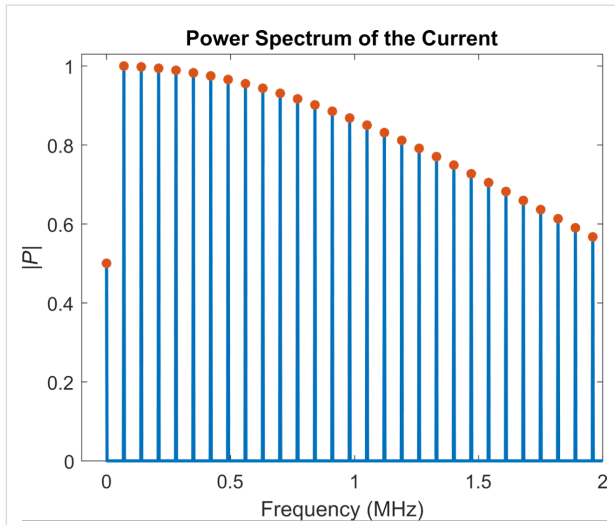
Figure 5: Normalised power spectrum of the current obtained for the noncontact, ideal-trajectory case. The blue lines indicate the power spectrum obtained via Fourier transform of the current, while the orange dots correspond to the predicted peaks from Equation 8. The first 50 elements of the infinite sum in Equation 8 were used for evaluating the equation. The results are in agreement with each other. Both the power spectrum and the predicted peaks are normalized. The figure also shows that the first harmonic (70 kHz), is the strongest peak in the spectrum, although the decay of the higher harmonic values is not rapid. Our calculations show that the peaks diminish to ca. 20% of the maximum peak value at a frequency of approximately 3.2 MHz, which roughly corresponds to the 46th harmonic.

In order to demonstrate the second case, we performed a numerical simulation for a dynamic AFM experiment that operates in the attractive tip–sample interaction regime. For this we have integrated the equation of motion of a spring–mass–dashpot model (Equation 21), customarily used to model dynamic AFM [45], where m_{eff} is the effective mass of the cantilever, f_0 its natural frequency, k its stiffness and Q its quality factor:

$$m_{eff}\ddot{x} + \frac{2\pi f_0 m}{Q}\dot{x} + kx = F_{excitation} + F_{interaction}. \quad (21)$$

$F_{excitation}$ is the sinusoidal driving force and the tip–sample interaction force, $F_{interaction}$, is based on the Hamaker equation [42]. The simulation parameters are provided in Table 1.

In the power spectrum of the cantilever response (Figure 6), one can observe that the a_n values decrease rather rapidly, such that only the first peak contributes significantly. Therefore, the frequency representation of the tunnelling current obtained for the numerical simulation is very close to the representation based on including only one cosine term in Equation 12 (Figure 7).
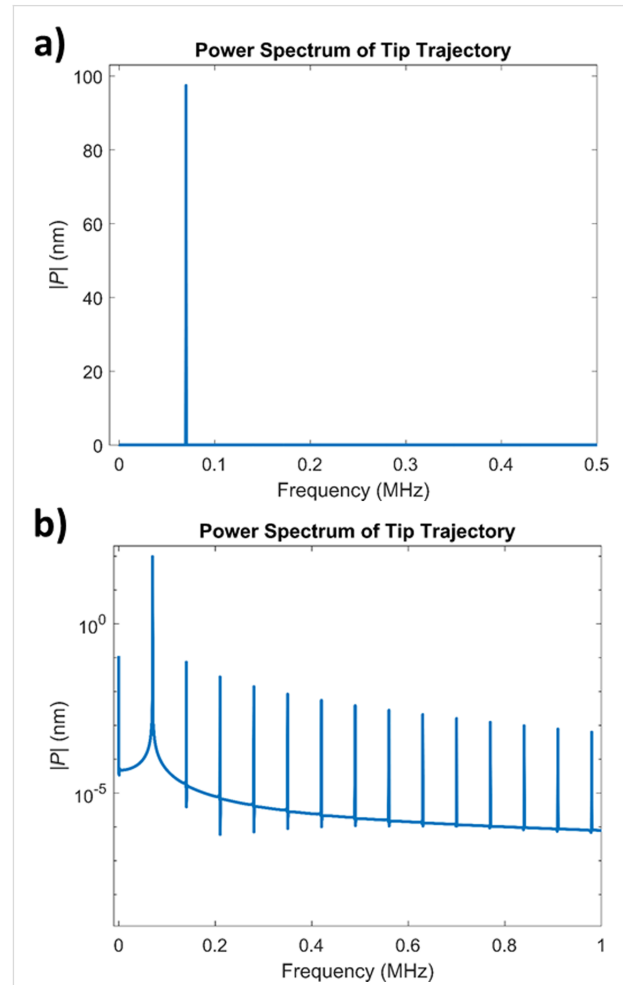

Figure 6: a) Power spectrum of the cantilever trajectory. The higher harmonic amplitudes are very small compared to the first harmonic amplitude, and their peaks are not visible in the spectrum with linear vertical axis. However, they are ever present and can be seen in a logarithmic plot (b), where the second harmonic is almost 1000 times smaller than the first harmonic.

Table 1: Simulation parameters for the spring–mass–dashpot AFM model in the attractive imaging regime (i.e., without tip–sample contact). The tip–sample interaction forces are modelled using the Hamaker equation for the case of a sphere interacting with a flat surface [42]. The imaging parameters are selected to resemble day-to-day large-amplitude experiments. The cantilever properties are similar to those of commercial cantilevers (e.g., BudgetSensors, ElectriMulti75-G conductively coated KPFM cantilevers). The Hamaker constant is chosen within the range appropriate for materials used in AFM experiments [46].

quality factor	spring constant	natural frequency	tip radius	Hamaker constant	free oscillation amplitude	resting tip distance
100	3 N/m	70 kHz	90 nm	60×10^{-20} J	100 nm	98 nm

A calculation based on including two cosine terms in Equation 12 (that is, considering the first two harmonics of the cantilever response), also predicts the power spectrum of the current accurately, and the result is only negligibly different from the single-cosine calculation, due to the rapid decrease of the higher harmonics in the tip trajectory (also plotted in Figure 7). In contrast, the magnitude of the higher harmonics of the current does not decrease rapidly. Figure 7 shows that the magnitude of the first few harmonics is very close to the magnitude of the fundamental harmonic. This suggests that a significant number of harmonics should be detectable in an experimental setting (provided that the fundamental harmonic is detectable), and that they need to be included in order to have a valid reconstruction of the current.
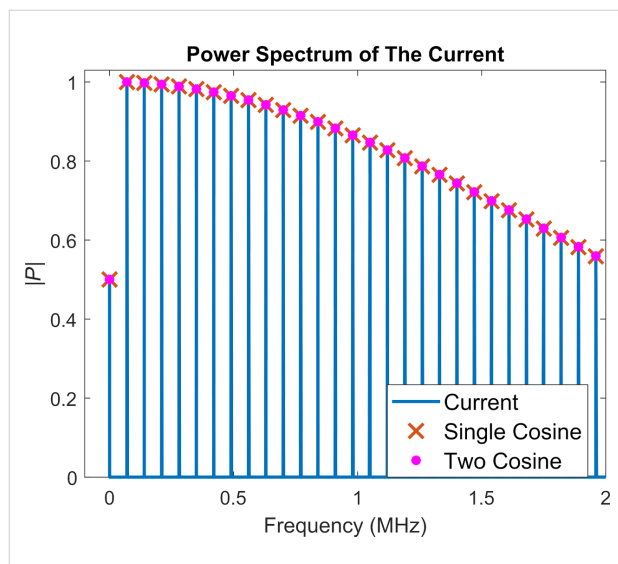

Figure 7: Power spectrum of the current from analytical calculations and numerical cantilever simulations for a noncontact case with attractive tip–sample forces. The blue lines correspond to the calculated power spectrum from the numerical simulation and the orange crosses correspond to the prediction from Equation 13, for the case where only one cosine term is included in Equation 12. The agreement between the two results is very good, as expected, since the higher harmonics of the tip trajectory decrease very rapidly. Pink dots are used to represent the two-cosine analytical prediction. Due to the rapid decrease of the higher harmonic amplitudes of the tip trajectory, the single- and two-cosine results fall almost on top of each other and are visually indistinguishable. The average difference between the single- and two-cosine calculations for the first 50 harmonics is 0.18%. Both calculations are normalised.

The numerical simulation for case 3 is similar to that of case 2, except that only repulsive forces are considered, which are based on the Hertzian contact model (for simplicity, the attractive forces are not included). The simulation parameters can be found in Table 2. Here we first consider (i) an unperturbed cantilever trajectory, whereby the cantilever indents the surface without experiencing any tip–sample forces, and (ii) a more realistic oscillation based on the spring–mass–dashpot model of Equation 21. For a proper comparison we use the same oscillation amplitude in both cases. Figure 8 depicts the power spectrum of the realistic cantilever trajectory (Figure 8a), along with a comparison of the power spectrum of the current for the two oscillation trajectories (Figure 8b). As explained in the Introduction section, unlike the first two cases considered, here the higher harmonics of the cantilever trajectory play a more prominent role, and there are clear differences in the current calculated for the ideal and for the more realistic case. Additionally, as expected, a sinc-shaped envelope can be observed in the power spectrum of the current, whereby the amplitude of the harmonics does not follow a monotonic trend.

Reconstruction of the tip–sample current should be possible if one can record its power spectrum. It is of course desirable to be able to record as many harmonics as possible, although this may not always be possible, in part due to signal-to-noise ratio limitations for very high frequencies or for frequencies near the nodes in the power spectrum (see Figure 8), and in part due to the fact that recording additional harmonics also requires additional instrumentation (i.e., lock-in amplifiers). Figure 9 illustrates the reconstruction of the current for the intermittent-contact simulation for one tip–sample impact, for different numbers of harmonics included in the reconstruction. As expected, including a larger number of harmonics leads to a current trace that is closer to the actual current. As can be seen in the figure, inclusion of 25 harmonics, whereby the 25th harmonic would still be within the range of frequencies that can be typically observed in AFM with relatively standard instrumentation (for sufficiently strong signals), already provides a very good reconstructed current (for reference, consider that the 4th eigenmode of a rectangular cantilever, which has been included in previous multifrequency AFM experiments [47], falls in the same range as the 30th harmonic). Furthermore, improvements in the recon-

Table 2: Simulation parameters for the spring–mass–dashpot AFM model in the intermittent-contact imaging regime. For simplicity, no attractive forces are considered. The repulsive interaction is modelled using the Hertzian contact model. The simulation parameters are selected to resemble those of day-to-day intermittent contact AFM experiments. The cantilever parameters are the same as given in Table 1.

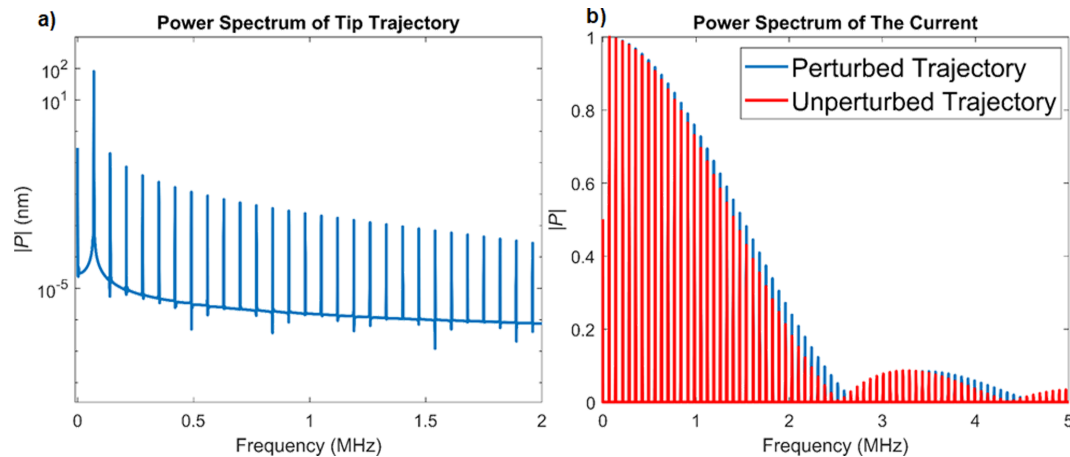| quality factor	spring constant	natural frequency	tip radius	effective elastic modulus	free oscillation amplitude	resting tip distance
100	3 N/m	70 kHz	90 nm	10 GPa	100 nm	80 nm

Figure 8: a) Power spectrum of the tip trajectory for the realistic simulation with the Hertzian repulsive interaction (the simulation parameters are provided in Table 2). The higher harmonic amplitudes of the tip oscillation are much smaller than the first harmonic amplitude but do nonetheless influence the current response. b) Comparison of the power spectrum of the current for the realistic numerical simulation with the power spectrum of the unperturbed, single-cosine trajectory. The single-cosine trajectory is designed to have the same frequency and maximum indentation as the realistic trajectory. Although the higher-harmonic amplitudes in the realistic tip trajectory are quite small compared to the first harmonic amplitude (a), the spectra of the current differ for the two trajectories considered. Both spectra exhibit the expected sinc envelope shape, with the envelope being wider when the realistic tip trajectory is considered.
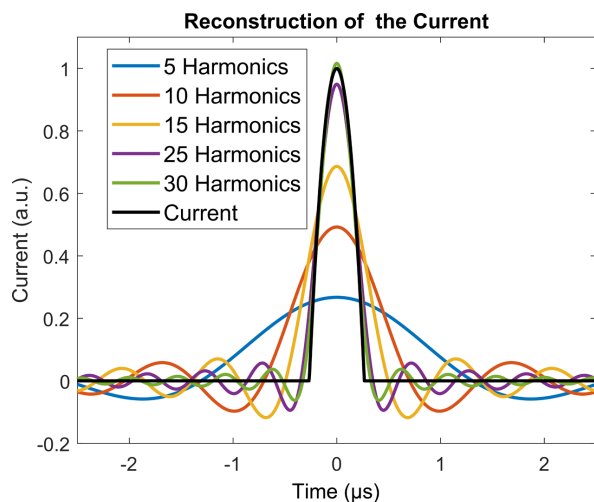

Figure 9: Current output obtained from the intermittent-contact simulation (black trace) and reconstruction of the current from different numbers of harmonics. As expected, inclusion of a larger number of harmonics in the reconstruction yields more accurate results. In this particular example, inclusion of 25 harmonics already leads to a very good reconstruction of the current. Since the behaviour of the harmonics coefficients as a function of frequency is not arbitrary, but rather expected to exhibit a sinc-shaped envelope, it may be possible to estimate a large number of higher harmonic amplitudes from a sparse collection of harmonics measured over a wide frequency range, such that a more accurate reconstruction is achieved.

struction may be possible due to the fact that the shape of the power spectrum envelope may be known, as is the case for Equation 13 and Equation 18, or could be approximated from the experimental data. Specifically, during an experiment it may

be possible to approximate the shape of the envelope if one has knowledge of the amplitude of a sparse collection of harmonics over a wide frequency range. With this information, one could predict the amplitude of the harmonics that have not been recorded and carry out a more accurate reconstruction of the current. It should be noted that this is possible due to the fact that all Fourier coefficients in the reconstructions discussed are real, such that if the fundamental harmonic is assigned a phase of zero, then all other harmonics should have a phase of either zero or π (see Equation 18).

Discussion

In the previous sections we have presented a Fourier description of tunnelling and conduction current in noncontact and intermittent-contact dynamic AFM scenarios, in the context of the development of an intermittent-contact conductive AFM technique. For the noncontact case, the exponential dependence of the current with respect to the tip–sample distance led to a power spectrum for the current which contained a collection of increasing orders of modified Bessel functions of the first kind. When a repulsive interaction was considered, we again obtained a collection of harmonics in the power spectrum, although this time their coefficients were characterized by a sinc-shaped envelope, which emerges from the intermittent-contact nature of the interaction, whereby only the conductive current was considered to be significant and the tunnelling current was neglected. In all cases we obtained good agreement between the analytical expressions derived and the numerical simulations conducted, which suggests that a Fourier-based reconstruction

of the current may be feasible. Nevertheless, it is important to point out anticipated challenges in the experimental implementation of the proposed method, which can be significant. We expect these challenges to arise from probe-related phenomena, data acquisition limitations, noise, the electrical nature of the sample, or some combination of all these factors.

With regards to probe challenges, it is well known that conductive tips can wear out rather easily, especially at the very apex and most especially in the case where coated tips are used, as opposed to solid conductive tips. In conventional C-AFM, small wear of the tip coating may not be as detrimental as it would be in an intermittent-contact experiment, because in the former case electrical tip–sample contact may also be established on the sides of the tip apex, particularly if indentation is significant during the experiment. However, indentation during an ICM-AFM experiment may be smaller and thus the tip contact region may be much smaller, especially under low-impact conditions. For example, in our Hertzian model simulation, the indentation is only around 0.6 nm, which limits the tip–sample contact area. In the noncontact case, the contrast is governed by the very apex of the tip, such that damage in that region may be even more problematic. Of course, the use of solid metallic tips is an alternative, although they may be more costly and the variety of parameters and geometries for which they are available is not as wide as for coated tips. In fact, coated tips can be easily fabricated starting with any non-conductive tip.

Electrical noise is anticipated to also introduce challenges. Although classical C-AFM can be affected by noise as well, the expected current magnitude in this mode of imaging should be larger than for ICM-AFM for the reasons described above, such that the current signal-to-noise ratio for the latter may be smaller. Furthermore, the current oscillations in C-AFM are of very low frequency. In contrast, ICM-AFM would involve the measurement of small currents at much higher frequencies, which would require an amplifier suitable for those conditions. Suitable instruments for experiments with relatively high conductance materials do exist (e.g., FEMTO DHPCA-100, trans-impedance amplifier [48]), which could, for example, record currents in the nanoampere regime at frequencies near 1 MHz. For experiments conducted on materials with significantly lower conductivity, different approaches need to be taken. It is possible that the use of several amplifier stages, in contrast to the use of a single trans-impedance amplifier in most conventional C-AFM setups, could improve time resolution [49]. Since the current spectrum is not expected to exhibit arbitrary frequencies, additional lock-in amplifiers can also be used. Previous researchers have provided creative examples of measurements performed on very small currents at high frequencies. For example, radio-frequency systems have been used in STM

applications, such as in the work of Manassen et al. who report measurements of ca. 0.25 nA tunnelling currents at 500 MHz [50]. Such RF-STM measurements are described in detail in the work of Kemiktarak and co-workers [49]. Generally speaking, the above examples suggest that the proposed measurements could be feasible, although the equipment requirements may be considerable, since the systems would need to be replicated for each Fourier component measured simultaneously.

Creative signal processing strategies may also be necessary. For example, one possible partial solution may be the use of comb-filtering approaches similar to the implementation used by Legleiter et al. in their scanning probe acceleration microscopy (SPAM) method [51], although this would only be beneficial for harmonics that rise significantly above the noise floor, and not for those that are near the nodes of the sinc envelope. Another possible solution is the use of time averaging of the peak magnitudes at the expected harmonic frequencies, as is done in some spectroscopy procedures, for random noise to cancel itself out while physical peaks persist. Additional algorithms and smoothing could also be implemented here [52-54]. As can be seen in Figure 8b, the maximum signal intensity decreases to around 20% of the highest harmonic amplitude at close to 2 MHz in our intermittent-contact realistic example, which corresponds to the 30th harmonic. Therefore, even with a 20% noise floor, a significant number of frequency peaks may still be available for a reasonable signal reconstruction (see Figure 9). Furthermore, since the overall shape of the power spectrum is not expected to be arbitrary, it may be possible to approximate its envelope shape from a sparse collection of harmonics, as described in the Results section.

An interesting source of electrical noise, which we have observed during our initial experiments, is shaker-piezo noise. In most AFM setups, the shaker piezo is located in very close proximity to the AFM cantilever, in order to be able to perform its duties and provide the required excitation to drive the cantilever. However, a shaker piezo with a relatively high voltage amplitude (up to 10 V in our case) acts like an antenna and creates a clear peak at the oscillation frequency in the measured current. This noise is not trivial to filter out due to its location being right at the principal frequency, where we also expect our strongest current peak. This noise may also cause high-gain current amplifiers to overload and may dominate all other current signals, and this issue would be ever present regardless of the application and regardless of the type of tip used. This might be eliminated through alternate cantilever excitation methods, such as laser-based thermal excitation, although existing commercial devices with this type of excitation cannot always provide reliable and sufficiently strong excitation suitable for all types of AFM probes. This has, in fact, been the case when we have

attempted to drive solid platinum probes in our laboratory, for which our thermal excitation did not impart a sufficiently large oscillation amplitude for a proper application of intermittent-contact AFM methods. Addressing this challenge may require either developments in excitation systems or probe developments. Other excitation approaches, such as magnetic excitation, may also be problematic due to the use of alternating current to drive the cantilever, which would also lead to antenna effects.

The electrical properties of the sample may play an important role in the feasibility of the proposed method. For example, in this introductory theoretical work we have treated the conductive properties of the sample as those of an Ohmic material, where the carrier response to the electric field is "immediate". However, many materials exhibit responses that depend on the timescales of the application of the electrical interactions (e.g., on the timescale of the contact time in our case). The characterization of such materials may lead to additional challenges, where for some frequencies the carriers may not be able to respond fast enough to the intermittent interaction. Examples of such materials, which are often characterized with C-AFM, are those used in photovoltaics, which have very particular capacitive, dielectric, and impedance properties, such that the timescale of the applied bias voltage can strongly influence the result [55,56]. One additional material-related challenge, is that in some materials the measured current is already very small (this is also the case in tunnelling experiments, regardless of the material). For example, in our experiments with conductive polymers we often observe current magnitudes on the order of tens of picoamperes in C-AFM measurements. Frequency-based, amplified data acquisition systems for measurements involving a large number of harmonics have already been developed, such as for the intermodulation AFM method, which uses a battery of lock-in amplifiers [30,31], but the amplification in that case is much smaller than what would be required for ICM-AFM.

In addition to the above challenges, which may not represent an exhaustive list, there are challenges that stem from the dynamics and mechanics of an intermittent-contact operation. Besides the fact that electrical contacts would be intermittent, the nature of the contact would also be time-dependent within the contact time. This is because the indentation is constantly varying. Furthermore, the approximation of the contact area (in order to be able to make estimates of conductivity) can be very challenging for hard materials, where constant evolution of the probe geometry may occur, as well as for soft (e.g., viscoelastic [57,58]) materials, for which the indentation depends very strongly not only on the tip–sample force, but also on the rate of application of that force.

Clearly the challenges are numerous and addressing them requires significant developments and investigations, but nevertheless, we believe this is an important and potentially fruitful area of research that we have begun to explore experimentally and for which we expect to report relevant results in the near future. We also encourage related developments by other researchers.

Conclusion

We have presented a possible method to obtain electrical property information from a sample surface using the intermittent-contact mode of AFM and Fourier analysis, considering also noncontact dynamic AFM cases. We have derived the expected current response in the frequency domain, which is in the form of harmonics of the principal frequency and discussed its shape and the significance of the various contributing terms. With the proposed models, non-measured spectral components may also be approximated. This may enable parameter-based estimation rather than model-free current reconstruction. The results suggest that reconstruction of the tip–sample current from such harmonics response is in principle feasible. However, we have also pointed out important anticipated experimental challenges that need to be addressed before realising the proposed goal.

ORCID® iDs

Berkin Uluutku - https://orcid.org/0000-0002-7286-8787
Santiago D. Solares - https://orcid.org/0000-0003-0895-8160

References

1. Noh, H.; Diaz, A. J.; Solares, S. D. *Beilstein J. Nanotechnol.* **2017,** *8,* 579–589. doi:10.3762/bjnano.8.62
2. O'Dea, J. R.; Brown, L. M.; Hoepker, N.; Marohn, J. A.; Sadewasser, S. *MRS Bull.* **2012,** *37,* 642–650. doi:10.1557/mrs.2012.143
3. Pingree, L. S. C.; Reid, O. G.; Ginger, D. S. *Adv. Mater. (Weinheim, Ger.)* **2009,** *21,* 19–28. doi:10.1002/adma.200801466
4. Pingree, L. S. C.; Reid, O. G.; Ginger, D. S. *Nano Lett.* **2009,** *9,* 2946–2952. doi:10.1021/nl901358v
5. Reid, O. G.; Munechika, K.; Ginger, D. S. *Nano Lett.* **2008,** *8,* 1602–1609. doi:10.1021/nl080155l
6. Kamkar, D. A.; Wang, M.; Wudl, F.; Nguyen, T.-Q. *ACS Nano* **2012,** *6,* 1149–1157. doi:10.1021/nn204565h
7. Dante, M.; Peet, J.; Nguyen, T.-Q. *J. Phys. Chem. C* **2008,** *112,* 7241–7249. doi:10.1021/jp712086q

8. Chen, Y. J.; Chan, S. C.; Liu, R.; Toh, S. L.; Ji, R. Nano-electric studies on advanced semiconductor devices by conductive AFM. In *2017 IEEE 24th International Symposium on the Physical and Failure Analysis of Integrated Circuits (IPFA),* IEEE, 2017; pp 1–4. doi:10.1109/ipfa.2017.8060085

9. Trenkler, T. *J. Vac. Sci. Technol., B: Microelectron. Nanometer Struct.–Process., Meas., Phenom.* **1998,** *16,* 367. doi:10.1116/1.589812

10. Olbrich, A.; Ebersberger, B.; Boit, C. *Appl. Phys. Lett.* **1998,** *73,* 3114–3116. doi:10.1063/1.122690

11. Farha Al-Said, S. A.; Hassanien, R.; Hannant, J.; Galindo, M. A.; Pruneanu, S.; Pike, A. R.; Houlton, A.; Horrocks, B. R. *Electrochem. Commun.* **2009,** *11,* 550–553. doi:10.1016/j.elecom.2008.12.031

12. Li, L. H.; Xing, T.; Chen, Y.; Jones, R. *Adv. Mater. (Weinheim, Ger.)* **2014,** *1,* 1300132. doi:10.1002/admi.201300132

13. Beinik, I.; Kratzer, M.; Wachauer, A.; Wang, L.; Piryatinski, Y. P.; Brauer, G.; Chen, X. Y.; Hsu, Y. F.; Djurišić, A. B.; Teichert, C. *Beilstein J. Nanotechnol.* **2013,** *4,* 208–217. doi:10.3762/bjnano.4.21

14. Zhong, Q.; Inniss, D.; Kjoller, K.; Elings, V. B. *Surf. Sci. Lett.* **1993,** *290,* L688–L692. doi:10.1016/0167-2584(93)90906-y

15. Alexeev, A.; Loos, J.; Koetse, M. M. *Ultramicroscopy* **2006,** *106,* 191–199. doi:10.1016/j.ultramic.2005.07.003

16. Vuppu, A. K.; Garcia, A. A.; Vernia, C. *Biopolymers* **1997,** *42,* 89–100. doi:10.1002/(sici)1097-0282(199707)42:1<89::aid-bip8>3.0.co;2-y

17. Farina, M.; Ye, T.; Lanzani, G.; di Donato, A.; Venanzoni, G.; Mencarelli, D.; Pietrangelo, T.; Morini, A.; Keivanidis, P. E. *Nat. Commun.* **2013,** *4,* 2668. doi:10.1038/ncomms3668

18. Jiang, G.; Baba, A.; Advincula, R. *Langmuir* **2007,** *23,* 817–825. doi:10.1021/la061817u

19. Liu, L.; Xi, N.; Li, G.; Chen, H. Atomic Force Microscope-Based Nanorobotic System for Nanoassembly. *Nano Optoelectronic Sensors and Devices;* Elsevier: Amsterdam, Netherlands, 2012; pp 51–79. doi:10.1016/b978-1-4377-3471-3.00004-6

20. Moreno-Herrero, F.; Colchero, J.; Gómez-Herrero, J.; Baró, A. M. *Phys. Rev. E* **2004,** *69,* 031915. doi:10.1103/physreve.69.031915

21. Morita, S., Ed. *Roadmap of Scanning Probe Microscopy;* NanoScience and Technology; Springer Berlin: Berlin, Germany, 2007. doi:10.1007/978-3-540-34315-8

22. Fein, A.; Zhao, Y.; Peterson, C. A.; Jabbour, G. E.; Sarid, D. *Appl. Phys. Lett.* **2001,** *79,* 3935–3937. doi:10.1063/1.1424473

23. Vecchiola, A.; Chrétien, P.; Delprat, S.; Bouzehouane, K.; Schneegans, O.; Seneor, P.; Mattana, R.; Tatay, S.; Geffroy, B.; Bonnassieux, Y.; Mencaraglia, D.; Houzé, F. *Appl. Phys. Lett.* **2016,** *108,* 243101. doi:10.1063/1.4953870

24. Garcia, R.; Proksch, R. *Eur. Polym. J.* **2013,** *49,* 1897–1906. doi:10.1016/j.eurpolymj.2013.03.037

25. Kawai, S.; Glatzel, T.; Koch, S.; Such, B.; Baratoff, A.; Meyer, E. *Phys. Rev. B* **2010,** *81,* 085420. doi:10.1103/physrevb.81.085420

26. Garcia, R.; Herruzo, E. T. *Nat. Nanotechnol.* **2012,** *7,* 217–226. doi:10.1038/nnano.2012.38

27. Stark, M.; Stark, R. W.; Heckl, W. M.; Guckenberger, R. *Proc. Natl. Acad. Sci. U. S. A.* **2002,** *99,* 8473–8478. doi:10.1073/pnas.122040599

28. Sahin, O.; Magonov, S.; Su, C.; Quate, C. F.; Solgaard, O. *Nat. Nanotechnol.* **2007,** *2,* 507–514. doi:10.1038/nnano.2007.226

29. Solares, S. D.; Hölscher, H. *Nanotechnology* **2010,** *21,* 075702. doi:10.1088/0957-4484/21/7/075702

30. Tholén, E. A.; Platz, D.; Forchheimer, D.; Schuler, V.; Tholén, M. O.; Hutter, C.; Haviland, D. B. *Rev. Sci. Instrum.* **2011,** *82,* 026109. doi:10.1063/1.3541791

31. Platz, D.; Tholén, E. A.; Pesen, D.; Haviland, D. B. *Appl. Phys. Lett.* **2008,** *92,* 153106. doi:10.1063/1.2909569

32. Borgani, R.; Gilzad Kohan, M.; Vomiero, A.; Haviland, D. B. *Phys. Rev. Appl.* **2019,** *11,* 044062. doi:10.1103/physrevapplied.11.044062

33. Abramowitz, M.; Stegun, I. A. *Handbook of Mathematical Functions with Formulas, Graphs, and Mathematical Tables;* Dover Publications Inc., 1965.

34. Dürig, U. *Appl. Phys. Lett.* **1999,** *75,* 433–435. doi:10.1063/1.124399

35. Dürig, U. *Surf. Interface Anal.* **1999,** *27,* 467–473. doi:10.1002/(sici)1096-9918(199905/06)27:5/6<467::aid-sia519>3.0.co;2-7

36. Dürig, U. *New J. Phys.* **2000,** *2,* 5. doi:10.1088/1367-2630/2/1/005

37. Hembacher, S.; Giessibl, F. J.; Mannhart, J. *Science* **2004,** *305,* 380–383. doi:10.1126/science.1099730

38. Giessibl, F. J. *Surf. Interface Anal.* **2006,** *38,* 1696–1701. doi:10.1002/sia.2392

39. Wright, C. A.; Solares, S. D. *Appl. Phys. Lett.* **2012,** *100,* 163104. doi:10.1063/1.3703767

40. Santos, S.; Barcons, V.; Font, J.; Verdaguer, A. *Beilstein J. Nanotechnol.* **2014,** *5,* 268–277. doi:10.3762/bjnano.5.29

41. Stark, R. W.; Heckl, W. M. *Rev. Sci. Instrum.* **2003,** *74,* 5111–5114. doi:10.1063/1.1626008

42. Israelachvili, J. *Intermolecular and Surface Forces,* 3rd ed.; Academic Press, 2011. doi:10.1016/c2009-0-21560-1

43. Smith, S. W. *The Scientist & Engineer's Guide to Digital Signal Processing,* 1st ed.; California Technical Publishing, 1997.

44. Tamayo, J.; García, R. *Langmuir* **1996,** *12,* 4430–4435. doi:10.1021/la960189l

45. García, R.; Pérez, R. *Surf. Sci. Rep.* **2002,** *47,* 197–301. doi:10.1016/s0167-5729(02)00077-8

46. Leite, F. L.; Bueno, C. C.; Da Róz, A. L.; Ziemath, E. C.; Oliveira, O. N., Jr. *Int. J. Mol. Sci.* **2012,** *13,* 12773–12856. doi:10.3390/ijms131012773

47. Solares, S. D.; An, S.; Long, C. J. *Beilstein J. Nanotechnol.* **2014,** *5,* 1637–1648. doi:10.3762/bjnano.5.175

48. FEMTO® Messtechnik GmbH. Variable Gain High Speed Current Amplifier DHPCA-100. https://www.femto.de/en/products/current-amplifiers/variable-gain-up-to-200-mhz-dhpca/34-schneller-stromverstaerker-mit-einstellbarer-versta erkung-dhpca-100-2 (accessed Feb 20, 2020).

49. Kemiktarak, U.; Ndukum, T.; Schwab, K. C.; Ekinci, K. L. *Nature* **2007,** *450,* 85–88. doi:10.1038/nature06238

50. Manassen, Y.; Hamers, R. J.; Demuth, J. E.; Castellano, A. J., Jr. *Phys. Rev. Lett.* **1989,** *62,* 2531–2534. doi:10.1103/physrevlett.62.2531

51. Legleiter, J.; Park, M.; Cusick, B.; Kowalewski, T. *Proc. Natl. Acad. Sci. U. S. A.* **2006,** *103,* 4813–4818. doi:10.1073/pnas.0505628103

52. Člupek, M.; Matějka, P.; Volka, K. *J. Raman Spectrosc.* **2007,** *38,* 1174–1179. doi:10.1002/jrs.1747

53. Barton, S. J.; Ward, T. E.; Hennelly, B. M. *Anal. Methods* **2018,** *10,* 3759–3769. doi:10.1039/c8ay01089g

54. Chen, H.; Xu, W.; Broderick, N.; Han, J. *J. Raman Spectrosc.* **2018,** *49,* 1529–1539. doi:10.1002/jrs.5399

55. Chen, B.; Yang, M.; Priya, S.; Zhu, K. *J. Phys. Chem. Lett.* **2016,** *7,* 905–917. doi:10.1021/acs.jpclett.6b00215

56. Yang, K. J.; Hu, C. *IEEE Trans. Electron Devices* **1999,** *46,* 1500–1501. doi:10.1109/16.772500
57. López-Guerra, E. A.; Eslami, B.; Solares, S. D. *J. Polym. Sci., Part B: Polym. Phys.* **2017,** *55,* 804–813. doi:10.1002/polb.24327
58. López-Guerra, E. A.; Solares, S. D. *Beilstein J. Nanotechnol.* **2017,** *8,* 2230–2244. doi:10.3762/bjnano.8.223